Understanding interpretation limitations due to MT inversion variability: examples from the Mount Isa Province, Queensland, Australia

Janelle Simpson

In fulfilment of the requirement for the degree of Doctor of Philosophy in the subject of Geophysics

Submitted to the Department of Earth Sciences,

School of Physical Sciences, Faculty of Sciences

University of Adelaide

Adelaide, November 2019

SUB CRUCE LUMEN
THE UNIVERSITY
of ADELAIDE

AUDAX AT FIDELIS
Queensland
Government

ABSTRACT

Exploration undercover presents a significant challenge and relies heavily on the effective interpretation of geophysical data. Magnetotelluric (MT) surveying is an ideal method for characterising these covered terranes because it provides resolution from the shallow cover into the deep earth. Undercover terranes often lack constraining information, creating a significant impediment for translating geophysical features into geological interpretations. This thesis presents advances for understanding MT inversion uncertainty to produce better geological interpretations in data-poor areas.

The project area is along strike from major Pb-Zn-Ag deposits at Mount Isa and George Fischer, and includes the location of a proposed suture between the Mount Isa Province and the North Australian Craton. The structure is interpreted from potential field data by previous workers but is not observable in outcrop. The prospective Proterozoic packages are concealed beneath 200-1200 m of Phanerozoic cover and consequently exploration success in this area has been very poor. The project dataset contains 1600 audiomagnetotelluric (AMT; 10^{-4} to 10^{0} seconds) and broadband MT (BBMT; 10^{-2} to 10^{3} seconds) sites; with approximate survey dimensions of 90 km north-south with line spacing of 5 km, and 150 km east-west with inter-site spacing of 2 km. The project area has scarce geological and geophysical information, and there is an inadequate understanding of the macro-scale geological structure. Three studies were undertaken with the aim of creating a new geological interpretation for the area. These studies were based on quantifying inversion variability and integration of information during interpretation.

One study presents a workflow to objectively assess the variability of models produced during 3D magnetotelluric inversion. The workflow uses a sequential inversion methodology to examine model variability while minimising the computational demand of 3D inversion. The results highlight the high degree of variability permissible in 3D MT inversion models and reinforce the clear impact inversion parameterisation has on the inversion models. Our method allows objective differentiation between well- and poorly-constrained features.

The second study integrates the results of 3D magnetotelluric inversion and variability analysis from the previous study, with deep crustal seismic and potential field data to refine our understanding of the southern Mount Isa Province. A new crustal-scale west-dipping feature is identified that is adjacent to a major change in crustal thickness and associated with a major change in crustal resistivity (that extends at least 400 km to the north). There is additionally a conductor located on or just above the interface and significant changes in the potential field response corresponding to both upper crustal and lower crustal depths. The structure is spatially associated with a low-resistivity feature (interpreted to be due to fluid movement or alteration), extends into the shallow crust and represents a possible exploration target.

The third study is focused on resolving the depth to basement and basin morphology of the Neoproterozoic-Mesozoic cover basins in the project area. Resolving the depth to basement from MT data is inherently difficult due to the data's insensitivity to the top of a resistive package (such as crystalline basement rocks). We used a combination of 1D probabilistic inversion, 2D deterministic inversion and synthetic modelling of downhole resistivity data to produce the final interpretation. The interpretation includes the base of the Eromanga Basin, an intra-Georgina Basin low-resistivity layer and depth to basement, all of which have associated error estimates.

Understanding variability in geophysical inversion is integral to the construction of a well-supported geological interpretation. This is especially true for areas where constraining information is limited or absent. We demonstrate that an understanding of data resolution and model uncertainty enables interpretation of new, worthwhile geological information from MT inversion even in data-poor greenfield terranes. Our new interpretation de-risks mineral exploration and provide new insights into crustal structures important for exploration targeting.

CONTENTS

LIST OF FIGURES

LIST OF TABLES

THESIS DECLARATION

I certify that this work contains no material which has been accepted for the award of any other degree or diploma in my name, in any university or other tertiary institution and, to the best of my knowledge and belief, contains no material previously published or written by another person, except where due reference has been made in the text. In addition, I certify that no part of this work will, in the future, be used in a submission in my name, for any other degree or diploma in any university or other tertiary institution without the prior approval of the University of Adelaide and where applicable, any partner institution responsible for the joint-award of this degree.

I acknowledge that copyright of works published within this thesis resides with the copyright holder(s) of those works.

I give permission for the digital version of my thesis to be made available on the web, via the University's digital research repository, the Library Search and also through web search engines, unless permission has been granted by the University to restrict access for a period of time.

I acknowledge the support I have received for my research through the provision of an Australian Government Research Training Program Scholarship.

Signed Date 6th June 2019

ACKNOWLEDGEMENTS

First and foremost, I would like to thank Paul Donchak, Brad John and Graham Heinson for their support in getting this project off the ground. Without their assistance none of this work would have been possible.

Thanks to my colleagues at the GSQ for their ongoing support and interest in my work. A special thanks to Vlad and Courteney for their various late night chats about all things magnetotelluric.

A special thanks to the HDR geology students at the Queensland University of Technology for letting me gate-crash their postgraduate seminars.

I would also like to thank all the people who were willing to read various drafts of this manuscript and offer feedback and comments – it was much appreciated.

Finally I would like to thank my friends and family for believing in me more than I believe in myself. Your endless support was crucial in getting this PhD over the line.

This project was carried out with the support of the Geological Survey of Queensland, part of the Department of Natural Resources, Mines and Energy, Queensland Government.

CHAPTER ONE

INTRODUCTION

1.1 Objectives and contributions

Geophysical inversion relies on subjective inputs to provide a solution to a non-unique and underdetermined problem. These inputs are often limited to inversion parameterisation or *a priori* constraints. Such inputs do not eliminate the possibility of producing an inversion which matches the observed data, but that has limited relationship to the underlying geology.

A variety of approaches exist for managing inversion ambiguity. These primarily fall into two categories: constrained inversion, which limits the range of possible inversion results; or probabilistic inversion, which aims to quantify the range of possible inversion outcomes. Difficulties arise where there is limited independent information available to constrain inversion, or computational requirements of inversion are significant. Utilising the available geological information in conjunction with analysis of inversion variability provides an alternative pathway to producing a geologically robust interpretation.

The overarching aim of the project was to produce a new interpretation and models in an under-explored area of the Mount Isa Province, a Proterozoic base metal province. The project area for this study is along strike from the major Pb-Zn-Ag deposits at Mount Isa and George Fischer. The prospective Proterozoic packages are concealed beneath a shallow-moderate thickness of Phanerozoic cover. Consequently, exploration success in this area has been very poor. A magnetotelluric survey with over 1600 sites was collected by the Geological Survey of Queensland in 2014-2015 and is the primary dataset for the study.

Geologically, there are two main aims for the Ph.D. study: better define the depth to Proterozoic basement to de-risk mineral exploration; and improve the understanding of the deep structure of the project area, and any implications for mineral exploration.

Geophysically, the main aim of the thesis is to find new ways integrating the uncertainty of inversion modelling and geological interpretation such that resulting interpretations are sensitive to the limitations the data.

Key research question:

Given the inherently non-unique nature of MT inversion products; what methods can be employed in poorly understood, data-poor greenfields terranes to create geological interpretations commensurate with data limitations?

Sub questions:

1. How can inversion variability be quantified in 3D MT inversion?
2. Can the dependence between inversion features and inversion parameterisation be assessed?
3. What are the large-scale structures of the southern Mount Isa Province?
4. Can downhole resistivity be used in synthetic modelling to aid more accurate interpretation of cover basin geology from an MT inversion?
5. What is the morphology of Georgina Basin between the Toko Syncline and Bourke River Structural Belt in southwest Queensland?

The aims of this thesis encompass two different scale questions. Understanding **regional-camp** scale (crustal-scale) variability related to the tectonic architecture; and understanding **deposit** scale variability in cover thickness. These goals align with the mineral system approach outlined by McCuaig and Hronsky (2014), which emphasises the importance of understanding geological processes at a range of scales to improve exploration targeting (Figure 1.1).

MT data are ideally suited to this style of integrated, multi-scale study as they yield information at a range of scales; from small, high-resolution studies (e.g. Lindsey et al., 2017) to whole-of-continent studies (e.g. Neska, 2016). The MT dataset utilised is located in the southern part of the Mount Isa Province, Queensland Australia. The prospective sequences of the Mount Isa Province in the project area are entirely concealed by sedimentary cover, leading to a historically low rate of exploration success (Figure 1.2). This thesis contributes to an improved understanding of both the tectonic architecture, and cover depths. Research in this area will aid explorers to better focus their work programs leading to improved exploration outcomes.

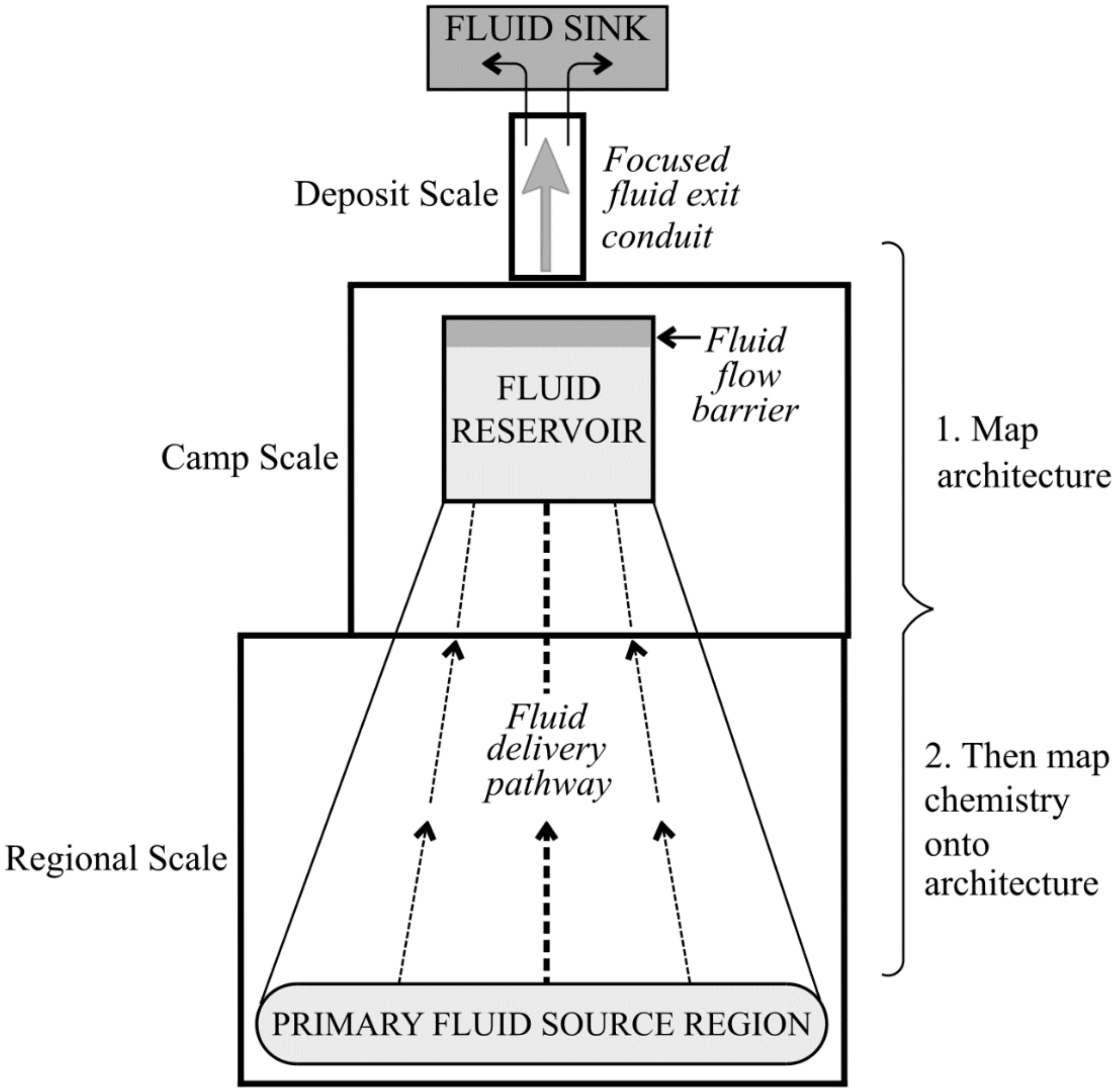

Figure 1.1. Summary of the ore genesis process after McCuaig and Hronsky (2014) showing the importance of understanding geological systems at a range of scales.

1.1.1 Structure of this manuscript

Chapters' two to four in this thesis present three interrelated studies which have an overarching goal of creating a new geological interpretation for the project area (Figure 1.2). Chapter two presents a workflow to objectively assess the variability of models produced during 3D magnetotelluric inversion. The workflow is applied to the project dataset to produce a suite of models for interpretation. Interpretation of the model suite is presented in Chapter three. Consideration of the sources of model variability and reliability of individual inversion features is presented in Chapter two and further expanded in Chapter three.

Chapter three integrates the results of 3D magnetotelluric inversion and variability analysis with other geophysical data to produce a new interpretation of the crustal-scale structures in the project area. A long-lived west dipping structure which pre-dates the Leichhardt Superbasin, but was potentially active during its deposition is identified. The structure is spatially associated with a low-resistivity feature (interpreted to be due to fluid movement or alteration), extends into the shallow crust and represents a possible exploration target.

Chapter four is focused on resolving shallow geological structures with a focus on depth to basement and basin morphology of the Neoproterozoic-Mesozoic cover basins in the project area. This chapter presents synthetic modelling together with 1D and 2D inversion results for the high frequency component of the project dataset. An interpretation is presented which includes the base of the Eromanga Basin, an intra-Georgina Basin low-resistivity layer and depth to basement, all of which have associated error estimates.

1.2 Overview of geophysical inversion

This section aims to introduce the challenges of the non-unique nature of geophysical inversion and the concept of model space (see Parker, 1994 for a detailed description of inverse theory). A brief overview of the inversion routines used in this thesis is also provided. The 3D ModEM inversion code used for the crustal scale inversions, while 1D SimPEG, 2D Occam, Occam 1D and rj-McMC are used for the cover study. WinGLink 2D used to verify the results of Occam 2D and also to complement the 3D crustal inversions. More detail for each of the inversion codes can be found in their respective papers (Brodie and Jiang, 2018; Cockett et al., 2015; Constable et al., 1987; deGroot-Hedlin and Constable, 1990; Kelbert et al., 2014; Rodi and Mackie, 2001). All the inversion codes discussed here assume that the Earth can be accurately represented by an isotropic model.

1.2.1 General geophysical inverse theory

The inherent non-unique nature of geophysical inversion is a well-known issue (Parker, 1994). This problem arises because of the ill-posed, or under-determined, nature of geophysical inversion and the effect of data errors. The general non-linear relationship between geophysical data and model parameters representing the physical properties and structure of the Earth is

$$d_i = F_i(m_{1,} m_2 \dots m_M) + e_i, \qquad i = 1, 2, \dots, N \tag{1.1}$$

where F_i is the forward function which predicts the data (d_i) for given values of a model, m_j and the error (e_i) in the prediction. The inverse problem is to solve for unknown model parameters (m_j) based on the observed data (d_i) (Chave and Jones, 2012).

Equation 1.1 components can be written in matrix notation

$$\boldsymbol{m} = (m_1 , m_2 \dots m_M)^T \tag{1.2}$$

$$\boldsymbol{d} = (d_1 , d_2 \dots d_N)^T \tag{1.3}$$

$$\boldsymbol{e} = (e_1\,, e_2 \dots\, e_N)^T \tag{1.4}$$

where the superscript T indicates the matrix transpose, *allowing* the equation 1.1 to be simplified to

$$\boldsymbol{d} = F(\boldsymbol{m}) + \boldsymbol{e} \tag{1.5}$$

In the case where **e** = **0**, the solution to equation 1.5 is simply

$$\boldsymbol{m} = \ F^{-1}(\boldsymbol{d}) \tag{1.6}$$

In reality, the existence of an exact solution to this problem is rarely available when the data contains errors ($e \neq 0$). Classically this is remedied by redefining a solution to be a model whose predictions match the data as closely as possible in some pre-defined sense, rather than matching exactly. Such a solution always exists; however, it may be non-unique or unstable (Rodi and Mackie, 2012).

Geophysical inversion has two essential elements:

1. Data misfit which measures the difference between the observed geophysical data and predicted data from an inversion model
2. Regularisation which evaluates an inversion model's adherence to prior knowledge and assumptions

Mathematically the data misfit ($\phi_d(\boldsymbol{m})$) can be defined as

$$\phi_d(\boldsymbol{m}) = \ \frac{1}{2}\ \|W_d(F(\boldsymbol{m}) - d_{obs})\|_2^2 \tag{1.8}$$

The predicted data is calculated by the forward operator ($F(\boldsymbol{m})$), and d_{obs} are the measured data. W_d is usually a diagonal matrix whose elements are equal to $W_{d_{ii}} = \ 1/e_i$, where e_i is an estimate of the errors at the ith datum. More generally, Wd may be non-diagonal with the off-diagonal terms representing estimates of the covariance of errors on the data.

Regularisation ($\phi_m(\boldsymbol{m})$) is defined as

$$\phi_m(\boldsymbol{m}) = \ \frac{1}{2}\ \left\|W_m(\boldsymbol{m} - \boldsymbol{m_{ref}})\right\|_2^2 \tag{1.9}$$

where W_m is a matrix which contains the assumptions or prior knowledge. In most cases, this is a measure of smoothness and deviation from the prior model (Cockett et al., 2015). Geological constraint can be added to the regularisation in the form of a prior model ($\boldsymbol{m_{ref}}$). Other methods for adding geological constraints include the introduction of breaks in smoothing parameters (de Groot-Hedlin and Constable, 2004; Smith et al., 1999), and variation in model mesh parameterisation (Tietze and Ritter, 2013).

A geophysical inversion is then formulated as an optimisation problem with a trade-off parameter, β (also called a regression parameter, regularisation parameter or Tikhonov parameter and may be denoted as λ) (Cockett et al., 2015)

$$\phi(\boldsymbol{m}) = \phi_d(\boldsymbol{m}) + \beta\phi_m(\boldsymbol{m}) \tag{1.10}$$

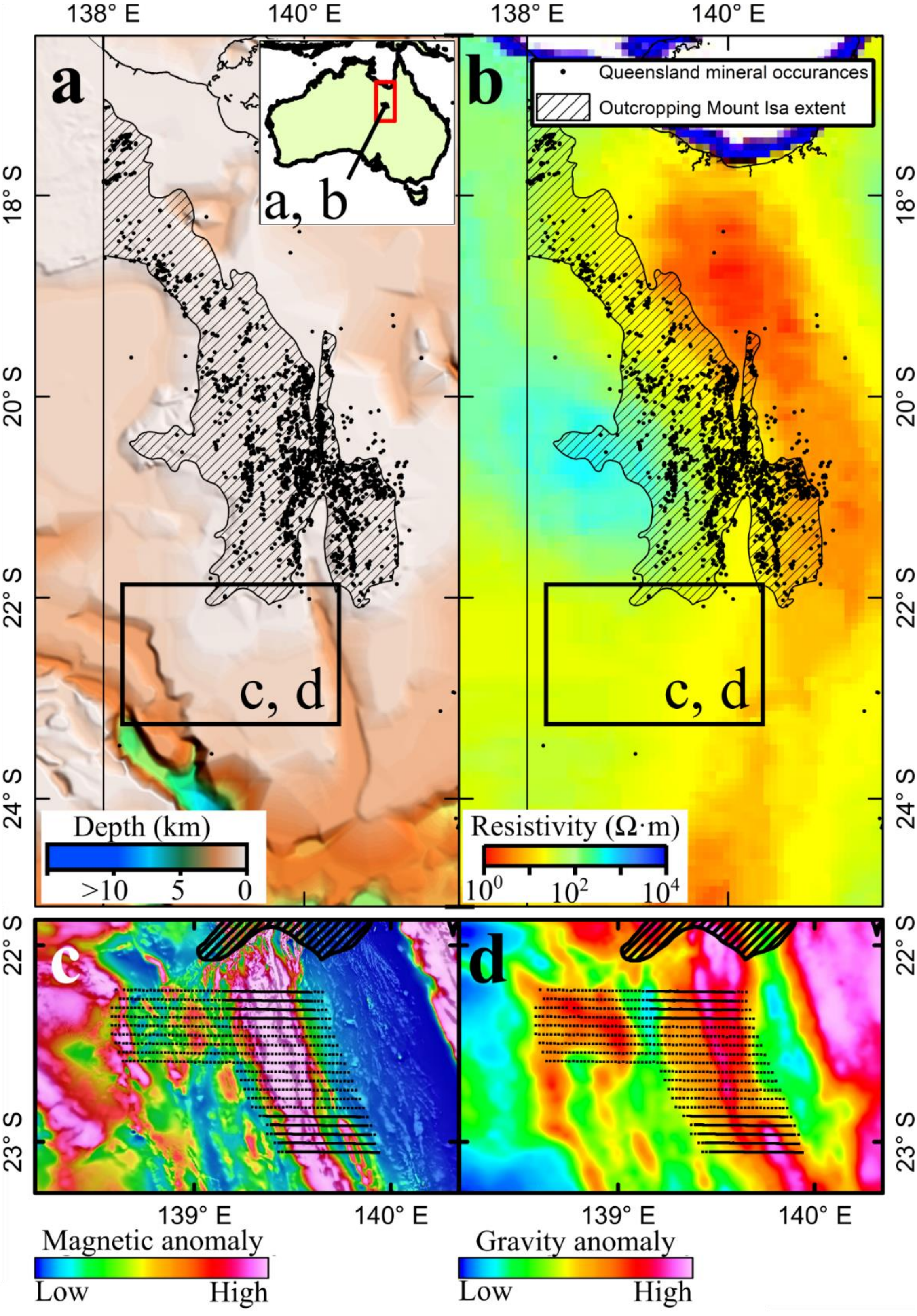

Figure 1.2. Regional context of the study area. a) the location of the project area (black box), with relation to the outcropping extent of the Mount Isa Province (hatched) and known mineral occurrences (black points), displayed over the OZ SEEBASE cover depth model (de Vries et al., 2006). Notice the strong correlation between the location of known mineral occurrences and the outcropping extent of the Mount Isa Province. b) Location of regional resistivity structure (53km depth slice; Wang et al., 2014) relative to the project area, known mineral occurrences and the outcropping extent of the Mount Isa Province. c) Total magnetic intensity magnetic data for the project area showing the location of the MT stations. d) Isostatically corrected Bouguer gravity data for the project area, also showing the location of MT stations. The magnetic and gravity data in the project area both display the strongly north-south geological character which typifies much of the Mount Isa Province.

Implementation of a geophysical inversion requires discretisation of the model into a mesh, with each mesh block representing a volume of constant resistivity for MT inversion (Cockett et al., 2015). An appropriate mathematical routine is also needed to solve the optimisation problem. Differences in selecting and implementing these choices in a geophysical inversion can give rise to significant variations in the final inversion routine.

A standard approach to geophysical inversion is to minimise both data misfit and regularisation simultaneously. This method produces a sub-set of 'model space' in which an inversion can search for solutions, where 'model space' is defined as the total range of models which fit a given dataset within the error tolerance. The most widely used approach to solving ill-posed, non-linear inverse problems in geophysics is damped least-squares estimation (Rodi and Mackie, 2012).

Iterative gradient based least squares minimisation algorithms make direct use of the sensitivity, or Jacobian, matrix relating to data and model perturbations. The Jacobian aids efficient exploration of model space, particularly in cases where model space is large.

1.2.2 Inversion codes used in this thesis

1.2.2.1 Occam (1D and 2D)

Occam inversion (Constable et al., 1987; deGroot-Hedlin and Constable, 1990) runs as a two-stage process. Initially, the inversion minimises data misfit, $\phi_d(\boldsymbol{m})$. When a specified misfit is achieved the inversion then reduces the model norm (a measure of roughness contained in $\phi_m(\boldsymbol{m})$) while maintaining the misfit. β is not fixed in this process but is determined during the inversion.

The Occam approach produces the smoothest model possible for a given misfit. This process can be computationally expensive but in a 1D and 2D inversion is not prohibitive. While a minimum structure model may be desirable for examining the minimum amount of structure required by the data, where local geology is known to have resistivity discontinuities, this method of inversion may not produce the most geologically reasonable model.

1.2.2.2 1D SimPEG

SimPEG 1D (Cockett et al., 2015) uses a deterministic approach and gradient-based optimisation with inversion regularisation defined as

$$\phi_m(\boldsymbol{m}) = \frac{1}{2}\left(\alpha_s\left\|W_s(\boldsymbol{m}-\boldsymbol{m}_{ref})\right\|^2 + \alpha_z\|W_z(\boldsymbol{m})\|^2\right) \qquad (1.11)$$

W_s is a diagonal matrix containing information about the length scales of the model, and the W_z matrix approximates the derivative of the model with depth (Cockett et al., 2015). Users can input the weighting parameters (α_s, α_z) and a reference model ($\boldsymbol{m}_{ref}$), as well as β in equation 1.10. High α_s will generate a model close to the reference model while a high α_z will generate smooth models. β is not designated as a fixed value but may instead be assigned a starting value and cooling schedule. This creates an inversion which initially suppresses additional structure but gradually prioritises minimising data misfit at the expense of adding extra (possibly excess) model structure as it progresses.

1.2.2.3 rj-McMC MT1D – reverse jump multichain Monte Carlo 1D inversion

The rj-McMC MT1D code uses trans-dimensional Markov chain Monte Carlo techniques to perform 1D magnetotelluric inversion via Bayesian inference (Brodie and Jiang, 2018). The trans-dimensional approach allows the number of layers to be an inversion parameter, rather than being fixed for an inversion. Inversion can be performed using either impedance tensor data or derived apparent resistivity and phase data.

Rj-McMC MT1D is the only probabilistic inversion routine used in this thesis. A user specified number of inversion chains progress through a burn in period to establish an ensemble of acceptable models (relative to noise estimates). From these models, a single model is randomly selected by each chain and inversion makes modifications of the model. The computed response for the new model is compared to the observed to data and accepted or rejected based on data fit. The inversion routine allows variation in the resistivity of model layers, depth to interfaces and number of interfaces (new interface added or existing one removed).

The inversion routine produces a probability distribution of resistivity vs. depth and automatically generates change point peaks for use in interpretation. A suite of statistics are also produced for examination.

1.2.2.4 WinGLink - 2D non-linear conjugate gradient

The WinGLink implementation of 2D non-linear conjugate gradient inversion (Rodi and Mackie, 2001) focuses on minimising misfit for a given Lagrange multiplier (λ, or β in equation 1.10) which is kept fixed for the inversion. The user must predetermine an appropriate λ to balance minimising both the data misfit and regularisation.

This inversion process is computationally less intensive than the Occam methodology, but it introduces a more subjective element to the inversion process through selection of an appropriate lambda. While this can work in favour of resolving discontinuous geological features through allowing higher model roughness, it can also introduce more model artefacts or under-constrained features to the final model.

1.2.2.5 3D ModEM

This thesis uses the non-linear conjugate gradient implementation of ModEM. This is simply a 3D implementation of the WinGLink code by Rodi and Mackie (2001). One modification was made in that it does not have a fixed λ (Egbert and Kelbert, 2012; Kelbert et al., 2014; Meqbel and Ritter, 2015), instead, the user specifies the starting λ and a cooling factor similar to SimPEG (β in equation 1.10).

1.2.3 Limitations of inversion

In addition to the limitations of inversion mentioned in the previous section, EM-techniques' are characterised by decreasing vertical and horizontal resolution with depth. This can lead to difficulties in resolving deeper structure, regardless of how inversions are parameterised.

3D MT inversions are subject to further limitations due to their significant computational requirement (Siripunvaraporn, 2012). This computational demand effectively limits both scale and discretisation of inversion models produced. A staged approach to inversion has been suggested to minimise the computational time required to produce a 3D inversion (Lindsey and Newman, 2015) and work is ongoing by the MT community to better optimise 3D inversion routines (Siripunvaraporn, 2012).

1.2.4 Approaches to quantifying inversion variability

In recent years, geophysical inversion methodologies have been proposed which aim to quantify the range of models which fit a given dataset. This work is typically restricted to gravity and magnetic inversion (e.g. Jessell et al., 2010; Lindsay et al., 2014; Wellmann et al., 2010). This is an active area of research for MT, however development of new inversion algorithms (Brodie and Jiang, 2018; Chen et al., 2012; Conway et al., 2018; Grandis et al., 1999; Rosas-Carbajal et al., 2015; Xiang et al., 2018) and approaches (Schnaidt and Heinson, 2015) which enable quantification of inversion uncertainty are typically limited to 1D and 2D implementations. A primary cause for this limitation is computational timeframes for MT inversion. Computational times for 3D MT inversion are already high, and the extra demand for a Monte Carlo style search of model space, for example, would make the process of 3D MT inversion computationally prohibitive.

1.2.5 Other considerations and challenges for MT inversion

Consideration of what the observed data can resolve is of utmost importance during parameterisation of an inversion starting model. The spatial resolution and aperture of the collected data are critical factors in determining the resolving power of the data. The depth extent of the data sensitivity is limited by the frequency band of the observed MT responses and the local resistivity structure; while the station geometry governs lateral sensitivity.

An inescapable dilemma with MT inversion is that resistivity variations can affect the data but not be well determined by them (Rodi and Mackie, 2012). This issue manifests predominantly in two ways: resistivity features appearing outside the bounds of the dataset being inverted and subtle resistivity variations which cannot be resolved due to the data errors. Ideally, good experimental design and the use of *a priori* information can assist with minimising the effect of these issues. However, it is unlikely they can be eliminated. Instead, these resolution limitations should be identified and assessed to ensure they are not introducing model artefacts during inversion and that the final inversion product is not being over-interpreted.

1.3 MT theory

The MT method is a passive geophysical technique which uses natural variation in the Earth's magnetic and electric fields to investigate subsurface variations in resistivity. Variations in the Earth's electromagnetic fields are caused by global thunderstorm activity at high frequencies and interaction between solar winds and the Earth's magnetosphere and ionosphere at low frequencies (Figure 1.3). In the frequency domain, horizontal electric (**E**) fields are related to horizontal magnetic (**H**) fields by the MT impedance tensor (**Z**)

$$\boldsymbol{E} = \begin{pmatrix} E_x \\ E_y \end{pmatrix} = \boldsymbol{ZH} = \begin{pmatrix} Z_{xx} & Z_{xy} \\ Z_{yx} & Z_{yy} \end{pmatrix} \begin{pmatrix} H_x \\ H_y \end{pmatrix} \tag{1.12}$$

where x is the north-south direction and y is the east-west direction. A detailed description of the MT method, including mathematical derivation, can be found in Chave and Jones (2012) and Simpson and Bahr (2005). The impedance tensor is usually displayed as variation in apparent resistivity and phase with period. Apparent resistivity is the average resistivity represented by a uniform half-space sounded at period, T (s). The phase represents the phase difference between the electric and magnetic fields; for a uniform half-space, the phase angle is 45°. Phase angles of less than 45° are indicative of the subsurface becoming more resistive with depth, and phases of greater than 45° indicate the resistivity is decreasing with depth.

MT data collect information in the time domain, which can be Fourier transformed to the frequency domain. Processed MT data contain a broad range of frequencies, facilitating investigation at a variety of depth-scales. MT data can be categorised as audio (AMT), broadband (BBMT) or long period (LP) data depending on the range of frequencies collected (Figure 1.3). Effective depth of penetration for MT data can be approximated using the skin depth equation

$$\delta(T) \approx 500\sqrt{T\rho_a} \tag{1.13}$$

where $\delta(T)$ is an estimate of the skin depth, T is the period (s), and ρ_a is the average resistivity of the crust at periods shorter than T. The skin depth is the depth, in a representative half-space, at which the EM fields are reduced to e^{-1} of their surface values. AMT data are used to investigate structures between the surface and a couple of kilometres depth, BBMT data are used to investigate shallow to deep crustal scale features, and long period data is used to study the deep crust and upper mantle.

Regional fields investigated by the MT method suffer from distortion generated by local currents and charge accumulations (Chave and Jones, 2012). The definition of local and regional are not strictly defined in this context and instead depend on the scale of features being investigated. These local effects produce a frequency independent distortion called static shift (Jones, 1988).

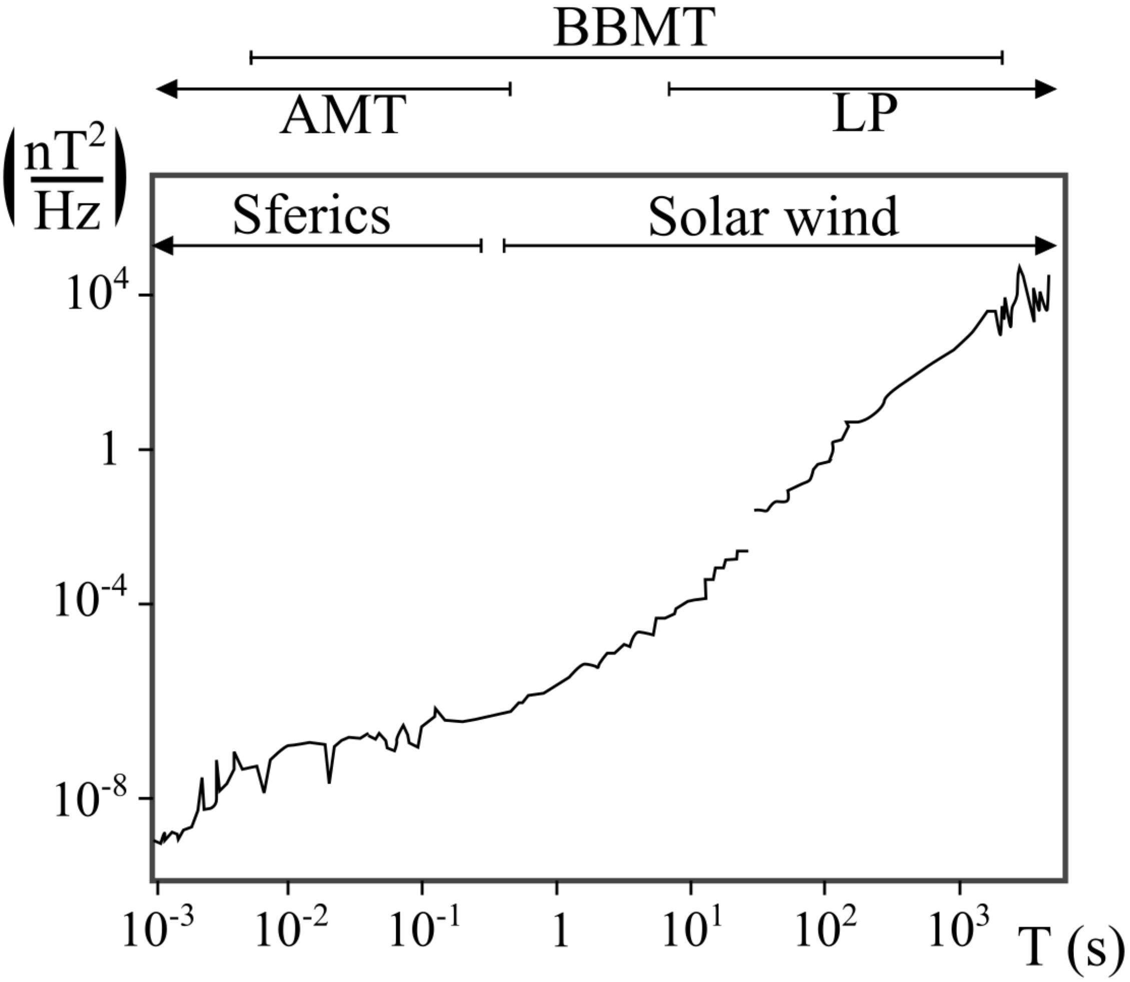

Figure 1.3. Sources of MT signal and signal strength depending on period, after Simpson and Bahr (2005). Typical bandwidths for the different categories of MT data are indicated at the top.

Static shift and other forms of distortion are problematic during data analysis and inversion (Jones, 2012). Distortion, including static shift, can be directly inverted for in 3D inversion (Meqbel et al., 2014). Some 2D inversion codes can be parameterised to invert for static shift (deGroot-Hedlin, 1991; Ogawa and Uchida, 1996), but otherwise it must be removed for 2D and 1D inversion. There are various methods for dealing with distortion, see Jones (2012) for a recent review.

The impedance tensor has three general forms (Table 1.1) which depend on the dimensionality of the Earth's resistivity distribution, called geoelectric dimensionality. Geoelectric dimensionally is a description of how electrical resistivity varies in the Earth (Figure 1.4). It is an inherent property of the Earth determined from the MT tensor and is often frequency dependent, with high-frequency data generally displaying 1D character, while lower frequency data are more commonly 2D or 3D (Rodi and Mackie, 2012). MT inversion algorithms make assumptions about the possible solutions for the impedance tensor based on dimensionality to reduce computational time (e.g. deGroot-Hedlin and Constable, 1990). If these assumptions are not correct (i.e. inverting 3D data with a 2D algorithm) inversion results will be unreliable. One-dimensional interpretation of 2D data is known to introduce "false conducting layers" and other artefacts, and 2D interpretation of 3D data can lead to underestimating of the total conductance (Jones and Garcia, 2003), and insertion of false features present off-profile (Ledo et al., 2002). While it is possible to invert 3D data with 2D inversion methods and achieve reasonable results, where possible 3D inversion methodologies should be used (Ledo, 2006; Ledo et al., 2002).

Table 1.1. General forms of the impedance tensor (Z) dependant on geoelectric dimensionality (modified after Thiel, 2008). Z_{TE} is the transverse electric mode with the electric field parallel to strike, and Z_{TM} is the transverse magnetic mode with the magnetic field parallel to strike. For Z_{xy} and Z_{yx} to represent Z_{TE} and Z_{TM}, respectively, the 2D MT data must be rotated so that the x-axis is parallel to geoelectric strike.

Dimensionality	**1D**	**2D**	**3D**
Tensor component	$Z_{xx} = Z_{yy} = 0$ $Z_{xy} = -Z_{yx}$	$Z_{xx} = Z_{yy} = 0$ $Z_{xy} \neq Z_{yx}$	$Z_{xx} \neq Z_{yy} \neq Z_{xy} \neq Z_{yx}$
Z	$\begin{pmatrix} 0 & Z_n \\ -Z_n & 0 \end{pmatrix}$	$\begin{pmatrix} 0 & Z_{TE} \\ Z_{TM} & 0 \end{pmatrix}$	$\begin{pmatrix} Z_{xx} & Z_{xy} \\ Z_{yx} & Z_{yy} \end{pmatrix}$

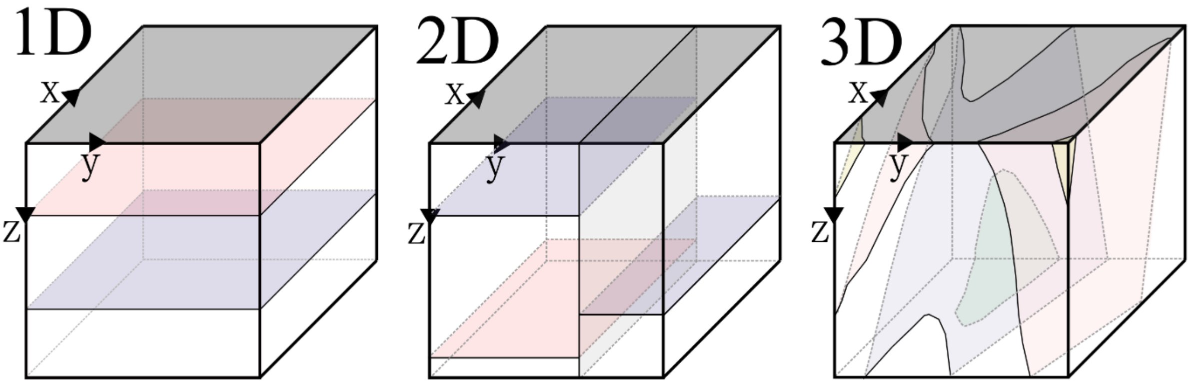

Figure 1.4. Diagrammatic examples of 1D, 2D and 3D structures. A 1D resistivity structure varies only with depth, a 2D resistivity structure varies with depth and one horizontal direction (y direction in figure), and a 3D resistivity structure varies in all horizontal and vertical directions.

1.3.1 Phase tensor

The phase tensor is a tool for MT data interpretation which is independent of static-shift and requires no assumption about the regional resistivity structure (Bibby et al., 2005; Booker, 2014; Caldwell et al., 2004). The phase tensor provides information regarding the geoelectric dimensionality and strike of an MT dataset, which is required for inversion, and also provides a way to monitor data quality (Booker, 2014). The MT phase tensor (ϕ) is defined by

$$\phi = \boldsymbol{X}^{-1}\boldsymbol{Y} = \begin{bmatrix} \phi_{xx} & \phi_{xy} \\ \phi_{yx} & \phi_{yy} \end{bmatrix} \qquad (1.14)$$

Where **X** and **Y** are the real and imaginary parts of **Z** (Caldwell et al., 2004). The phase tensor has three invariants, the maximum phase (ϕ_{max}), minimum phase (ϕ_{min}) and the skew angle (β)

$$\beta = \frac{1}{2}\tan^{-1}\left(\frac{\Phi_{xy} - \Phi_{yx}}{\Phi_{xx} + \Phi_{yy}}\right) \tag{1.15}$$

The phase tensor is fully defined based on these three invariants and the angle α

$$\alpha = \frac{1}{2}\tan^{-1}\left(\frac{\Phi_{xy} + \Phi_{yx}}{\Phi_{xx} - \Phi_{yy}}\right) \tag{1.16}$$

Where α expresses the tensor's dependence on a rotated coordinate system (Booker, 2014). The phase tensor expressed in terms of α, β, Φ_{max} and Φ_{min} is

$$\Phi = \boldsymbol{R}^T(\alpha - \beta)\begin{pmatrix}\Phi_{max} & 0 \\ 0 & \Phi_{min}\end{pmatrix}\boldsymbol{R}(\alpha - \beta) \tag{1.17}$$

where ***R*** is the rotation matrix (Bibby et al., 2005)

$$\boldsymbol{R}(\theta) = \begin{bmatrix}\cos\theta & \sin\theta \\ -\sin\theta & \cos\theta\end{bmatrix} \tag{1.18}$$

Analysis of β, Φ_{max} and Φ_{min} enables the geoelectric dimensionality and strike to be determined. In the 2D case, the geoelectric strike is equal to $\alpha - \beta$ which is often approximated to α. (Booker, 2014). Table 1.2 displays the theoretical values of the three invariants in a noise-free setting for the 1D, 2D and 3D case. In practice, due to noise levels $\beta \neq 0$ for 1D and 2D, and $\Phi_{max} \approx \Phi_{min}$ for 1D. This necessitates adoption of thresholds to categorise the dimensionality of MT data based on the phase tensor method (e.g. Robertson et al., 2015). It is important not to inflate thresholds applied to categorise the dimensionality of data as this can lead to 2D interpretation and inversion where it is not justified (Booker, 2014).

Table 1.2. Idealised values or relationships for the three invariant components of the phase tensor based on the dimensionality of the underlying Earth.

Dimensionality	**1D**	**2D**	**3D**
β	$\beta = 0$	$\beta = 0$	$\beta \neq 0$
Φ	$\Phi_{max} = \Phi_{min}$	$\Phi_{max} \neq \Phi_{min}$	$\Phi_{max} \neq \Phi_{min}$

The phase tensor can be plotted as an ellipse using the three invariants and α (Figure 1.5). This representation allows the user to visually assess geoelectric dimensionality and strike at numerous frequencies or sites simultaneously. While the phase tensor is a convenient way of determining the dimensionality of MT data, it is possible for data to appear 2D in cases where the underlying resistivity structure is 3D. To minimise this effect, the phase tensors should be analysed in concert with the induction vector (Booker, 2014), derived from a geomagnetic depth sounding.

1.3.2 Geomagnetic depth sounding

The geomagnetic depth sounding method involves measurement of the horizontal and vertical components of the Earth's magnetic field (***H***) over a period of days to a week or more (Chave and Jones, 2012). The vertical magnetic field is related to the horizontal magnetic field through the vertical magnetic transfer function (***T***):

$$H_z = \begin{pmatrix} T_{xz} \\ T_{yz} \end{pmatrix}^T \begin{pmatrix} H_x \\ H_y \end{pmatrix} \tag{1.19}$$

The effect of local distortion or static shift on the geomagnetic depth sounding is generally considered to be minor because it is not dependant on the electric field (Simpson and Bahr, 2005). At periods over 1000 s and in resistive environments, such as the Canadian shield distortion effects are possible (Chave and Smith, 1994; Zhang et al., 1993). MT data usually include the collection of the vertical magnetic field, allowing the magnetic transfer function, or tipper, to be calculated in addition to the impedance tensor.

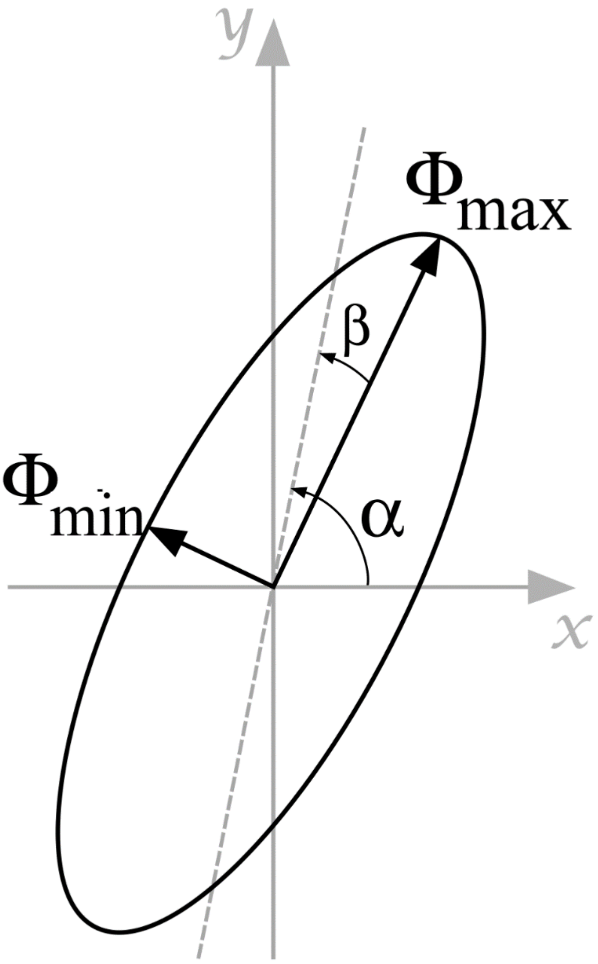

Figure 1.5. The MT phase tensor can be plotted graphically as an ellipse using the three invariants (the maximum phase (ϕmax), minimum phase (ϕmin) and the skew angle (β)), and the angle α. After Caldwell et al. (2004)

From the vertical transfer function, induction arrows can be plotted and point either towards (Parkinson, 1959) or away (Wiese, 1962) from low-resistivity bodies, depending on the convention used. Where structures are 1D, the induction vector is zero, and where structures are 2D the real and imaginary components of the induction arrow are parallel (Booker, 2014). Induction vectors for which the real and imaginary components are non-zero and not parallel, or for which the vector orientation changes with frequency, are an indicators of 3D resistivity structure.

1.4 Factors that affect crustal resistivity

This section describes the mechanisms of electrical resistivity in the Earth’s crust. Crystalline silicate rocks in a crustal environment are broadly resistive, with a bulk resistivity in the order of ~10^3 to 10^5 Ωm (Gough, 1986). An understanding of the sources of resistivity anomalies is needed to interpret features produced in MT inversion appropriately. Four main mechanisms are identified in the literature: ionic conduction; sulphide and iron concentrations; grain-boundary graphite; and semi-conduction by diffusing particles in silicate minerals. An overview of each mechanism is presented here, for a more detailed review of these processes refer to Evans (2012), Selway (2014) and Yang (2011).

1.4.1 Ionic conduction

Ionic conduction is the movement of charged particles in solution and occurs in saline fluids. Interconnected pathways are required to allow the movement of the charged particles and generate a resistivity anomaly. Ionic conduction is predominantly a near-surface process, involving connected fluids in porous sedimentary sequences (e.g. Tournerie and Chouteau, 2005). However, interconnected melts can also be a source of ionic conduction, a phenomenon which has been observed in areas of active volcanism or tectonism (Brasse, 2002; Hill et al., 2009). Ionic conduction can also lower resistivity in regions where fluids infiltrate shear zones or where metamorphic fluids are released from active dehydration reactions (Becken and Ritter, 2012; Selway, 2014).

1.4.2 Sulphide and iron concentrations

Sulphide minerals have low resistivity, leading some studies attribute low resistivity in cratonic environments to the presence of interconnected sulphides (Selway, 2014). Sulphides are expected to be stable to depths of the uppermost mantle; however, sulphur is not volumetrically abundant in the Earth's bulk composition (Allègre et al., 1995; McDonough and Sun, 1995). Consequently, while the presence of sulphides may explain spatially localised low-resistivity features, they are not expected to make a significant contribution to broad-scale regions of lowered resistivity in the lower crust and mantle.

Increased iron concentration in silicate minerals has also been associated with reduced resistivity. Iron concentrations vary in crustal rocks, with high iron concentrations producing a reduced resistivity response. In crustal rocks iron concentrations are linked to lithological variably, however in the mantle iron concentrations are lower and display little variability (Selway, 2014). Recent experiments suggest that a small amount of FeS powder added to finely ground olivine forms films on the grain boundaries. These films lower resistivity by more than an order of magnitude (Watson et al., 2010), however it does not appear common for natural samples to exhibit such films (Selway, 2014).

1.4.3 Grain-boundary graphite films

For graphite to cause significant resistivity anomalies, the lithosphere must contain sufficient carbon to form interconnected structures of a thickness greater than several nanometres (Selway, 2014). These often take the form of grain-boundary films and can develop at concentrations in the order of 100 ppm (Duba and Shankland, 1982). Graphite films have been observed on grain boundaries in many mid- to lower crustal samples (e.g. Mareschal et al., 1992). Analysis of xenoliths suggests that these kinds of grain-boundary films are stable only between 600 and 900 °C (Mathez, 1987).

1.4.4 Semi-conduction by diffusing particles in silicate minerals

Silicate minerals behave as resistors at surface pressures and temperatures. In the deeper crust, the elevated temperature and pressure enable them to act as semiconductors, where the charge carriers are diffusing particles (Selway, 2014). The Arrhenius relation defines conduction by diffusing species:

$$\sigma = \sigma_0 \cdot exp\left(\frac{-\Delta H}{RT}\right) \tag{1.20}$$

where σ_0 is the pre-exponential factor, ΔH is the activation enthalpy, R is the gas constant, and T is the absolute temperature. From this equation, composition and temperature will be the two most important factors controlling the electrical resistivity of silicate rocks.

The temperature must be sufficiently high to overcome the activation enthalpy of diffusion, and an increasing temperature will also increase the efficiency of diffusion (Selway, 2014). Hence, increased temperature leads to reduced resistivity. Temperature increases with depth in tectonically stable lithosphere in a predictable manner. Tectonic activity, plumes, and high concentrations of radiogenic elements can cause temperature profiles to deviate from these averages.

Experiments with anhydrous minerals such as olivine, garnet, orthopyroxene, clinopyroxene and plagioclase have concluded that hydrogen content is the most critical compositional parameter affecting resistivity in lithospheric conditions (Yang, 2011; Yang et al., 2012). Mineralogy, grain size, and magnesium number make a minor but important contribution to resistivity. Lower resistivity is observed in hydrated plagioclase, orthopyroxene, olivine and garnet than dry samples. Differential pressure loading may also enhance semiconduction in silicate rocks (Takeuchi and Nagao, 2013).

1.4.5 Other considerations

Other factors also contribute to resistivity variability in the crust. Graphite in high grade metasedimentary rocks (Boerner et al., 1996; Pous et al., 2004), along graphitized shear zones (Neska, 2016), or present in black shales (Korja, 2007; Schäfer et al., 2011) can cause localised low-resistivity anomalies at upper- and mid-crustal depths.

Recent work suggests that compositional variations other than sulphur, hydrogen, iron and graphite may contribute to low-resistivity features in crustal settings. Total alkaline ion concentration has been demonstrated to produce lowered resistivity in gneissic and granitic rocks, an effect which increases with temperate; i.e. at higher temperatures the same composition rocks had lower resistivity (Dai et al., 2018).

Lowered-resistivity in clay minerals due to surface conduction effects along the mineral grains is possible depending on the structure and composition of the clay (Choo et al., 2016; Kriaa et al., 2014).

1.5 Interpreting geology from resistivity

This section discusses geological factors which can lead to reduction of electrical resistivity, providing a foundation for interpreting the resistivity distributions produced in MT inversion in a geologically reasonable fashion. The most important factors to consider when understanding lithospheric resistivity structures depends on their depth. Interpretation should take into consideration the following rules of thumb:

1. Increased porosity in weathered rocks can produce reduced resistivity.

2. In the shallow crust, particularly in basin terranes, the effects of ionic conduction through porous or faulted rocks will be the dominant source of reduced resistivity.
3. In crystalline rocks with limited porosity, ionic conduction along planes of weakness, such as faults will produce zones of low resistivity. This effect is limited to the brittle crust.
4. Graphitic black shales, elevated iron concentrations in silicate minerals, and rare sulphides are potential sources of reduced resistivity in crystalline rocks.
5. In the mid-crust to upper mantle, the main considerations for interpreting resistivity will be variation in temperature, the presence of melt, and differences in hydrogen fertilisation.
6. Neotectonic stress fields and differential crustal thicknesses should be examined – in areas where non-uniform loading is occurring, regions experiencing higher pressures may have lower resistivity.

Hydrogen behaves as an incompatible element in the mantle and lower-crustal mineral species (Selway, 2014). Therefore, it is reasonable to expect that hydrogen proportions will broadly follow patterns of enrichment and depletion of incompatible elements. Regions of the upper mantle which experience repeated melting episodes are likely to become depleted in iron and hydrogen and have high resistivity, while areas effected by subduction or plume activity may be enriched in these elements, and hence have lower resistivity.

In simplistic terms, hydrogen distribution is expected to be correlated to pyroxene in crustal rocks. This is due to a higher hydrogen concentration in pyroxene than other typical deep crustal minerals (Selway, 2014), and relatively high abundance in deep crustal rocks.

1.6 Regional resistivity structures in Queensland

Data collected at the Australia-wide Array of Geomagnetic Stations (AWAGS) (Chamalaun and Barton, 1990), and older arrays (Constable, 1992) have identified several conductivity anomalies across the Australian continent (Constable, 1992; Wang et al., 2014). The deep conductivity structure of Queensland is dominated by the Carpentaria Conductivity Anomaly (CCA; Chamalaun et al., 1999, and referenced therein). This conductive anomaly stretches over 1000 km from the Gulf of Carpentaria in the north, to Birdsville in the south west of Queensland (Figure 1.6). The CCA is primarily identified by long period induction arrows (Chamalaun et al., 1999), and was noted to affect telluric data in southwest Queensland (Woods and Lilley, 1980). More recently, MT inversion has been used to investigate the conductivity structure (Hanekop, 2006; Lilley et al., 2003; Wang et al., 2014).

The CCA broadly corresponds with the eastern edge of the Mount Isa Province, leading Hanekop (2006) and Wang et al. (2014) to speculate that the elevated conductivity may be the result of a collisional event along the margin of the Mount Isa Province. The complexity of the anomaly is acknowledged by other authors (Crowe and Milligan, 2015) as is the need for more work to understand origin and nature of this enigmatic feature.

The CCA is observed to be confined to periods longer than 100 s (Hanekop, 2006; Wang et al., 2014). The range of periods impacted by the CCA has significance for BBMT surveys, which typically have frequency ranges of 250 Hz to 1000 s.

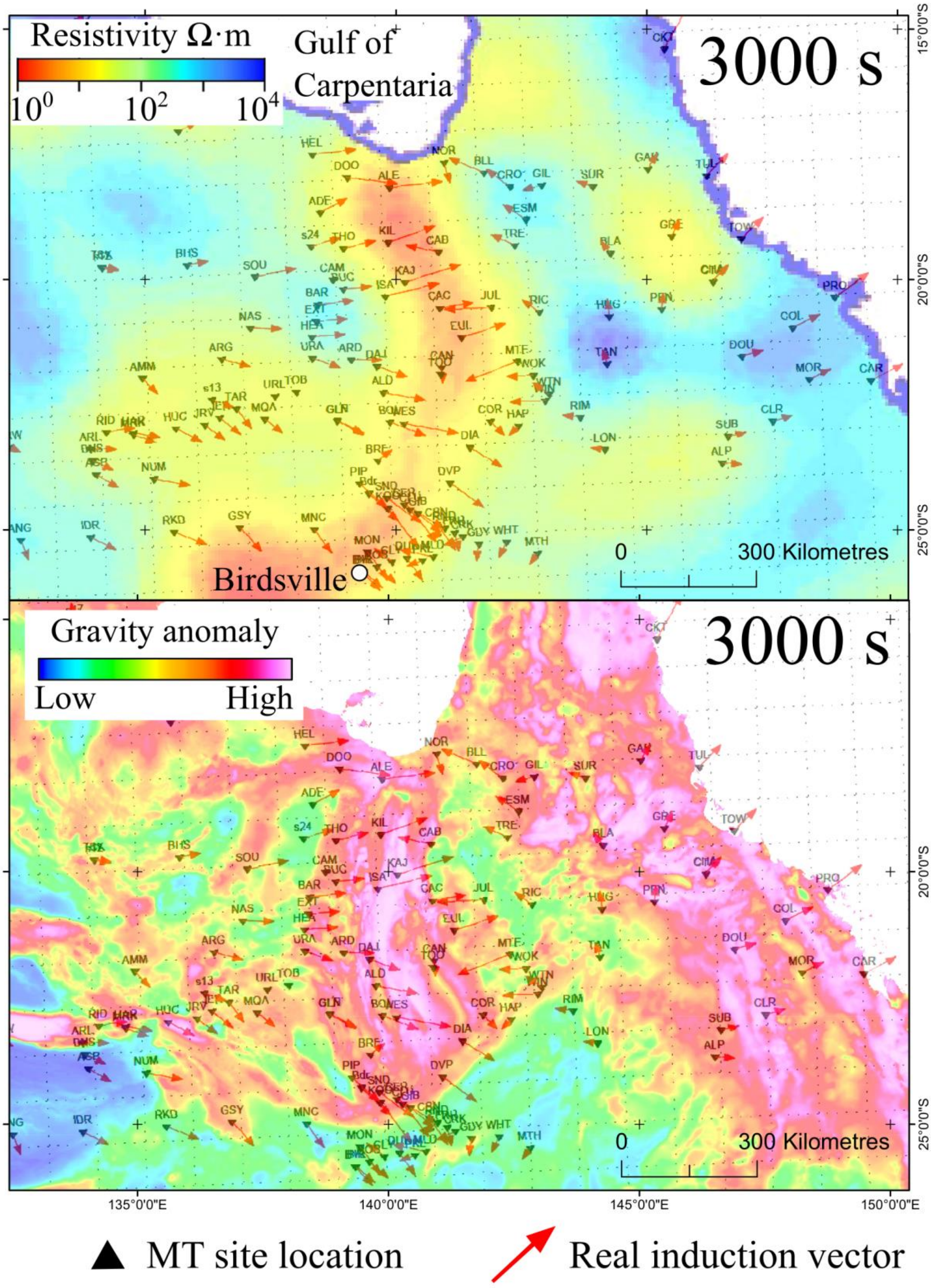

Figure 1.6. Comparison between the regional MT data and the 52 km depth slice from the Wang et al. (2014) conductivity model showing the CCA. Induction vectors (Parkinson (1962) convention) plotted from available historic data at 3000 s. The bottom panel shows a comparison between the regional gravity data and the 3000 s induction arrows.

1.6.1 Implications for modelling the Isa Extension dataset

The Isa Extension Survey is located immediately to the west of the CCA. Phase tensor and induction arrow plots for the dataset are displayed in Figure 1.7; typical apparent resistivity and phase plots, and the location of the CCA compared to the data array are also plotted.

Induction arrows at 1000 s have a consistent south-east orientation (Figure 1.7k). Some scattering of arrows is observed, particularly in the west of the dataset due to increased noise in the data. The phase tensor ellipses at 1000 s also have a consistent orientation across the array (Figure 1.7g). The orientation of both the induction arrows and phase tensor ellipses at 1000 s is consistent with the location of the CCA (compare Figure 1.7k and 1.7n).

At 120 s the induction arrows in the west of the survey have a variety of orientations, while the induction arrows in the central and east parts of the survey area are south oriented, with some minor variation in orientation (Figure 1.7j). The phase tensor ellipses are remarkably homogenous across the data array at 100 s (Figure 1.7f). The south orientation of induction arrows in the east of the Isa Extension survey at 120 s indicates a conductivity structure to the south of the data array (Figure 1.7). This direction is not consistent with the location of the CCA in the Wang et al. (2014) model. However, due to the coarse resolution of the Wang model it is not possible to eliminate the CCA as the cause of the south directed inductions arrows at 120 s; alternatively, there may be an unknown small-scale conductivity feature to the south of the data array

Isa Extension data are sensitive to features within the data array for both the impedance and tipper data to a period of approximately 100 s (Figure 1.7a-e, h and i).

Induction arrows show inductive effects over larger distance-scales than MT impedance data (Chave and Jones, 2012), meaning impedance data will be less affected by regional-scale conductivity features. The effect large-scale conductivity anomalies on inversion of BBMT data depends on the location of the survey relative to the feature. Surveys which only cover one side of a conductivity anomaly will be unable to accurately recover the location of the anomaly, leading to inversion artefacts (Neska, 2016).

Due to its position on the western flank of the CCA the Isa Extension dataset is expected to have significant difficulty producing meaningful inversion results for long period data (periods over 50 s in the east (Figure 1.7m), and 400 s in the west (Figure 1.7m). Data at these longer periods are significantly, or pervasively affected by low-resistivity features outside the data array which are unconstrained by the available data.

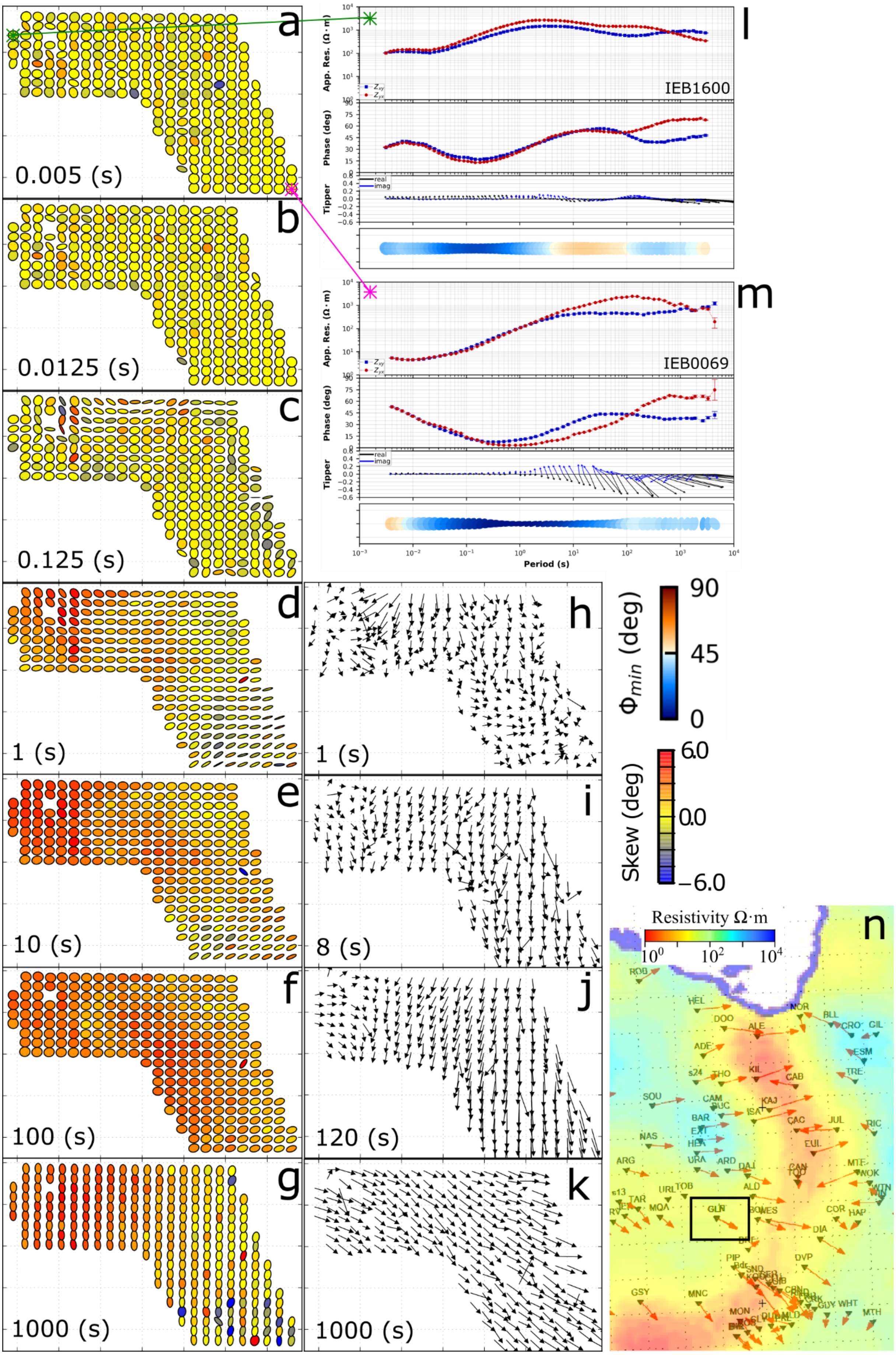
a
0.005 (s)
b
0.0125 (s)
c
0.125 (s)
d
1 (s)
e
10 (s)
f
100 (s)
g
1000 (s)
h
1 (s)
i
8 (s)
j
120 (s)
k
1000 (s)
l
App. Res. (Ω · m)
Phase (deg)
Tipper
IEB1600
Z_{xy}
Z_{yx}
real
imag
m
IEB0069
Period (s)
Φ_{min} (deg)
90
45
0
Skew (deg)
6.0
0.0
−6.0
n
Resistivity Ω·m
10^0
10^2
10^4
ROB
HEL
DOO
ALE
NOR
BLL
CRO
GIL
ESM
ADF
KIL
THO
s24
CAB
TRE
SOU
CAM
BUC
KAJ
ISA
BAR
CAC
JUL
RIC
NAS
EXI
HEA
EUL
ARG
URA
ARD
DAJ
CAN
TOO
MTE
WOK
URL
TOB
ALD
s13
TAR
MOA
GLN
ONES
COR
HAP
DIA
BAE
PIP
DVP
SND
GSY
MNC
WHT
GUY
MTH
MON

Figure 1.7 (left). Phase tensor and induction arrow plots for the Isa Extension BBMT dataset. a-g) phase tensor ellipse coloured by skew; circular ellipses with low skew values are indicative of 1D data, distorted ellipses with low skew values are indicative of 2D data, and ellipses with red or blue colouration indicate 3D subsurface structure. h-k) In-phase induction arrow plots (Parkinson convention) for selected periods and sites. l) Apparent resistivity, phase, tipper and phase ellipses coloured by minimum phase for IEB1600 in the northwest of the data array. m) Apparent resistivity, phase, tipper and phase ellipses coloured by minimum phase for IEB0069 in the southeast of the data array. n) Location of the Isa Extension dataset (black) compared to 1000 s regional in-phase induction arrows in red (Chamalaun and Barton, 1990; Hanekop, 2006) plotted on the 53 km resistivity depth slice (Wang et al. 2014). Displayed ellipses and induction arrows were generated using one third of the total BBMT sites for clarity; plots generated using MTpy (Krieger and Peacock, 2014).

CHAPTER TWO

UNDERSTAING VARIABILITY IN 3D MAGNETOTELLURIC INVERSION

J. Simpson[1,2] and G. Heinson[2]

1 Geological Survey of Queensland, Department of Natural Resources, Mines and Energy, Queensland Government, Brisbane QLD 4000, Australia
2 Department of Earth Sciences, School of Physical Sciences, University of Adelaide, Adelaide SA 5005, Australia

Statement of Authorship

Title of Paper	Understanding variability in 3D magnetotelluric inversion		
Publication Status	☐ Published	☐ Accepted for Publication	
	☑ Submitted for Publication	☐ Unpublished and Unsubmitted work written in manuscript style	
Publication Details	Currently in review in Geophysics (submitted 20 Dec 2018)		

Principal Author

Name of Principal Author (Candidate)	Janelle Simpson		
Contribution to the Paper	Developed workflow, modelled and interpreted data. Wrote manuscript		
Overall percentage (%)	90%		
Certification:	This paper reports on original research I conducted during the period of my Higher Degree by Research candidature and is not subject to any obligations or contractual agreements with a third party that would constrain its inclusion in this thesis. I am the primary author of this paper.		
Signature		Date	27th May 2019

Co-Author Contributions

By signing the Statement of Authorship, each author certifies that:

i. the candidate's stated contribution to the publication is accurate (as detailed above);
ii. permission is granted for the candidate in include the publication in the thesis; and
iii. the sum of all co-author contributions is equal to 100% less the candidate's stated contribution.

Name of Co-Author	Graham Heinson		
Contribution to the Paper	Provided supervision of work, aided in MT data interpretation and manuscript evaluation		
Signature		Date	24th May 2019

Abstract

Inversion variability presents a significant difficulty for interpretation of geology by producing suites of possible models with inconsistent features. This difficulty is exacerbated for 3D MT inversion due to the high computational demand of inversion inhibiting exhaustive model testing, and further compounded by the limited range of 3D inversion algorithms available to the community. Current methodologies for assessing model variability in MT inversion rely heavily on subjective comparison of inversion features and data fits. We present a formalized workflow for objectively assessing model variability based on a sequential inversion method. The workflow is primarily aimed at assessing the variability of individual inversion features and macro-scale model variability. The workflow also enables systematic testing of different inversion parameters and comparison of resulting inversion features. An 800 site gridded dataset from western Queensland, Australia was used to demonstrate the workflow. A high degree of inversion variability is demonstrated to be permissible during inversion of the dataset. This variability is not evenly distributed across the model, and two robustly determined low-resistivity features were identified from inversion of the test dataset. The workflow is viable in areas without independent constraining information and aims to improve quantification of inversion variability to inform interpretation. We also reinforce the clear impact inversion parameterization, particularly the starting model, has on ModEM 3D inversion outcomes and underscore the dangers of using a single inversion model to construct an interpretation.

2.1 Introduction

Model variability is a perennial challenge for producing an interpretation from geophysical inversions. A pragmatic approach to producing better inversions in an unconstrained setting, is to run a variety of starting models before settling on a final favoured model and conducting a series of sensitivity analyses. Sensitivity analysis determines which features are well constrained and those that may be poorly-constrained or simply model artefacts. For a single model, sensitivity analysis is often conducted by a combination of forward and inverse modelling tests of perturbed models or datasets (Becken et al., 2008; Lindsey et al., 2017; Schnaidt and Heinson, 2015; Thiel and Heinson, 2010). Synthetic modelling can also be employed to better understand the range of possible models for a specific dataset (Becken and Ritter, 2012). Analysing a suite of models allows the interpreter to distinguish between features that are consistent in all inversions and features which are inversion specific (Tietze and Ritter, 2013).

Three-dimensional (3D) inversion of MT data is an active area of research with a focus on optimizing both the inversion procedure and outcomes, and reducing computational cost (Siripunvaraporn, 2012). Sensitivity analysis of 3D MT inversion models is more difficult than 2D or 1D models due to the large computational demands and long time-frames. This is further compounded by the reality that the model space of acceptable models for any dataset is large and unknown. Lindsey and Newman (2015) propose a sequential inversion approach to minimize computing resource usage. While this sequential inversion approach allows the user to arrive at a reasonable inversion solution more quickly, it is unable to explore the range of possible models which may account for the data. Indeed, the parameterization of sequential inversion biases the final model from information contained in the prior model.

A number of authors show results of inversion parameter testing and sensitivity analysis to understand 3D MT inversion variability. For example, Özaydın et al. (2018) demonstrate the effect of the initial smoothing regularization parameter, and Fernandes et al. (2018) use a combination of constrained and unconstrained inversion approaches to understand sensitivity of model features to stating model resistivity. Kühn et al. (2018) tested the model covariance to determine combination of parameters to achieve the best fit. Gao et al. (2018) use sensitivity analysis and synthetic modelling to investigate the variability of key conductive features in their inversion models. Meqbel et al. (2014) investigated a number of key attributes, including effect of grid resolution, data component, and presence of conductors outside the modelled area, depth sensitivity and introduction of constraints. Tietze and Ritter (2013) discuss the impact of mesh rotation, inverted data component, error levels and starting resistivity model. A common thread of such analyses is how the variability is assessed. Generally, this involves plotting depth or lateral profiles and conducting a visual comparison in conjunction with analyses of RMS distributions by site, component and frequency. This method allows authors to gain qualitative insights into how specific features in their models vary, but quantitative comparison of variability is difficult.

In this paper we demonstrate how statistical analysis of model variability can provide additional insight. Results of statistical analysis are also used to understand the relative contribution of different model parameters to overall variability and to assist in selection of a preferred model. An approximately 800 site dataset in the Mount Isa region of western Queensland, Australia was used to demonstrate approach and develop a new workflow, based loosely on the sequential inversion workflow presented in Lindsey and Newman (2015).

2.2 Data

The 2014-2015 Mount Isa Extension MT dataset collected in south-west Queensland by the Geological Survey of Queensland was used in this study. The survey of approximately 800 MT sites with a frequency range of 4 x 10^{-3} s to 2000 s was collected on a grid of station spacing 2 km in an east-west direction, along nineteen lines 5 km apart in a north-south direction, as shown in Figure 2.1. The array was collected along strike to the south of a major cluster of world-class mineral deposits of Mesoproterozoic age, where prospective sequences are concealed by younger Neoproterozoic and Mesozoic basin sediments. Thus, a primary aim of the survey was to assist in locating the next generation of concealed mineral deposits.

The phase tensor approach (Bibby et al., 2005; Caldwell et al., 2004), implemented in the MTPy package (Krieger and Peacock, 2014), was used to determine the optimal geoelectric strike and dimension. Figure 2.2 displays the phase tensor ellipses coloured by the skew (β). Skews which deviate significantly from zero (red and blue ellipses) indicate 3D resistivity heterogeneity. We observe that data at periods less than 1 s are indicative of 1D or 2D subsurface structures as indicted by circular tensor plots, or by ellipses with low skews, respectively. At periods 1 – 100 s, a small number of sites in the west have high skew, and at periods >100s, the majority of the project area exhibits 3D induction effects. This trend indicates that geometries are increasingly 3D with depth.

Induction arrows plots for the dataset were generated for periods between 1 – 1000 s, and shown in Figure 2.3. At 1 s, in-phase (or real) induction arrow orientation indicates the presence of resistivity contrasts within the array, but as periods increase, the in-phase arrows are progressively and pervasively affected by resistivity structures well outside the data array. At periods longer than 1000 s, the entire array are effected by a low resistivity feature to the east and south-east (as shown in the inset Figure 2.1 from Wang et al. 2014).

Geoelectric strike analysis indicates a consistent strike direction of N85°E between periods of 10^{-3} s and 100 s, as shown in Figure 2.4. Although there is an ambiguity of 90° in the strike, other geological and geophysical data strongly support the geolelectric strike being in a predominantly north-south orientations (thus approximately N5°W). At periods greater than 100 s, the strike is consistently N10°E in Figure 2.4.

As phase tensor plots and induction arrows are relatively uniform across the array at periods longer than 100 s (Figures 2.2 and 2.3), the data suggest that deep crustal and upper mantle resistivity heterogeneities are small compared to the contrasts outside the array. We note here that the array is located on the western side one of the world's largest crustal resistivity anomalies, known as the Carpentaria Conductivity Anomaly (CCA, Figure 2.3; (Chamalaun et al., 1999; Hanekop, 2006; Wang et al., 2014)).

Overall the data analysis identified three main challenges:

1. All data exhibit 3D induction effects at periods > 100 s, and for sites in the west, the complex dimensionality is evident from 1 s period;
2. Large resistivity contrasts are present outside the survey area which significantly affect all MT responses from 10 s. At periods of about 100 s, resistivity contrasts to the south are evident, but at longer periods more distant contrasts to the east and south east are more dominant;
3. By contrast, deeper resistivity heterogeneities within the lower crust and upper mantle appear to be much more subtle.

Four different sets of MT responses were used for inversion. The first included all 809 stations, but only for bandwidth of 100 Hz - 10 s. The other three subsets (Figures 2.5a, b and c) had reduced lateral sampling, and a bandwidth of 1 s - 2000 s. Such subsets where used to constrain deeper structure of the project area, as suggested by Lindsey and Newman (2015). The first of the coarse datasets had horizontal sub-sampling to a 10 km x 10 km grid with a total of 89 stations. The other two coarse datasets had a random distribution of 99 stations. Each random subset was designed so that no stations were duplicated.

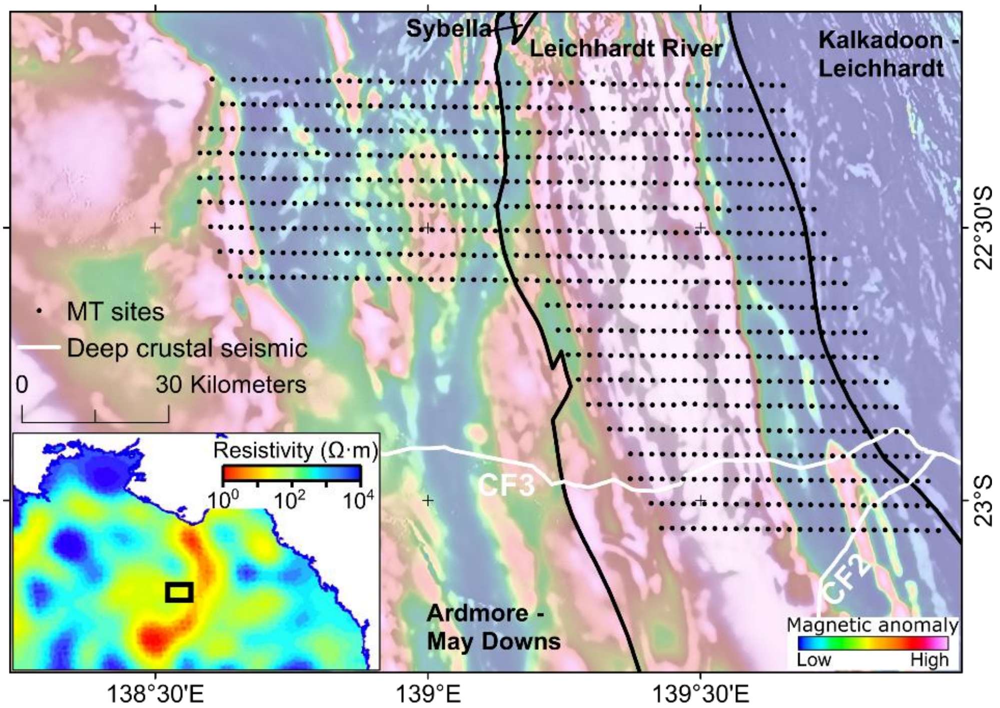

Figure 2.1. Location of the MT array (black dots) shown relative to the Ardmore-May Downs, Leichardt River and Kalkadoon-Leichardt domains (GSQ, 2011) and a composite image of the first vertical derivative of the magnetic data overlain on reduced-to-pole magnetic data. Domain boundaries (solid black lines) are mapped and inferred faults. Inset displays location of the array (black box) against regional resistivity structure at 53 km depth (Wang et al. 2014)).

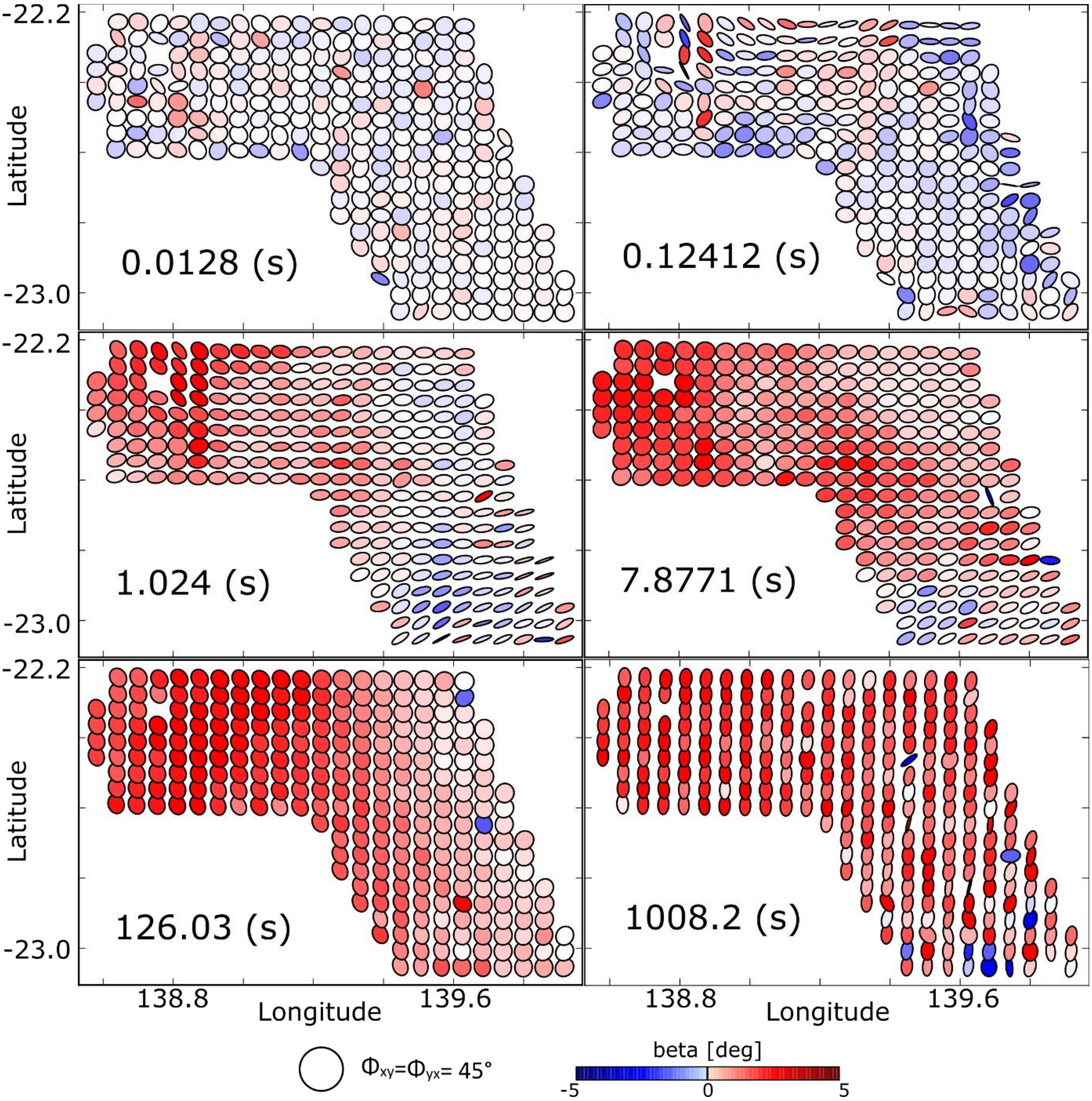

Figure 2.2. Phase tensor ellipses of the test dataset for periods of 0.01, 0.12, 1.02, 7.88, 126.03 and 1008.2 s. Ellipses are coloured by the bata (or skew) value, dark red or blue colorations are indicative of 3D subsurface geoelectric structures. Displayed ellipses were generated using one third of the total sites for clarity.

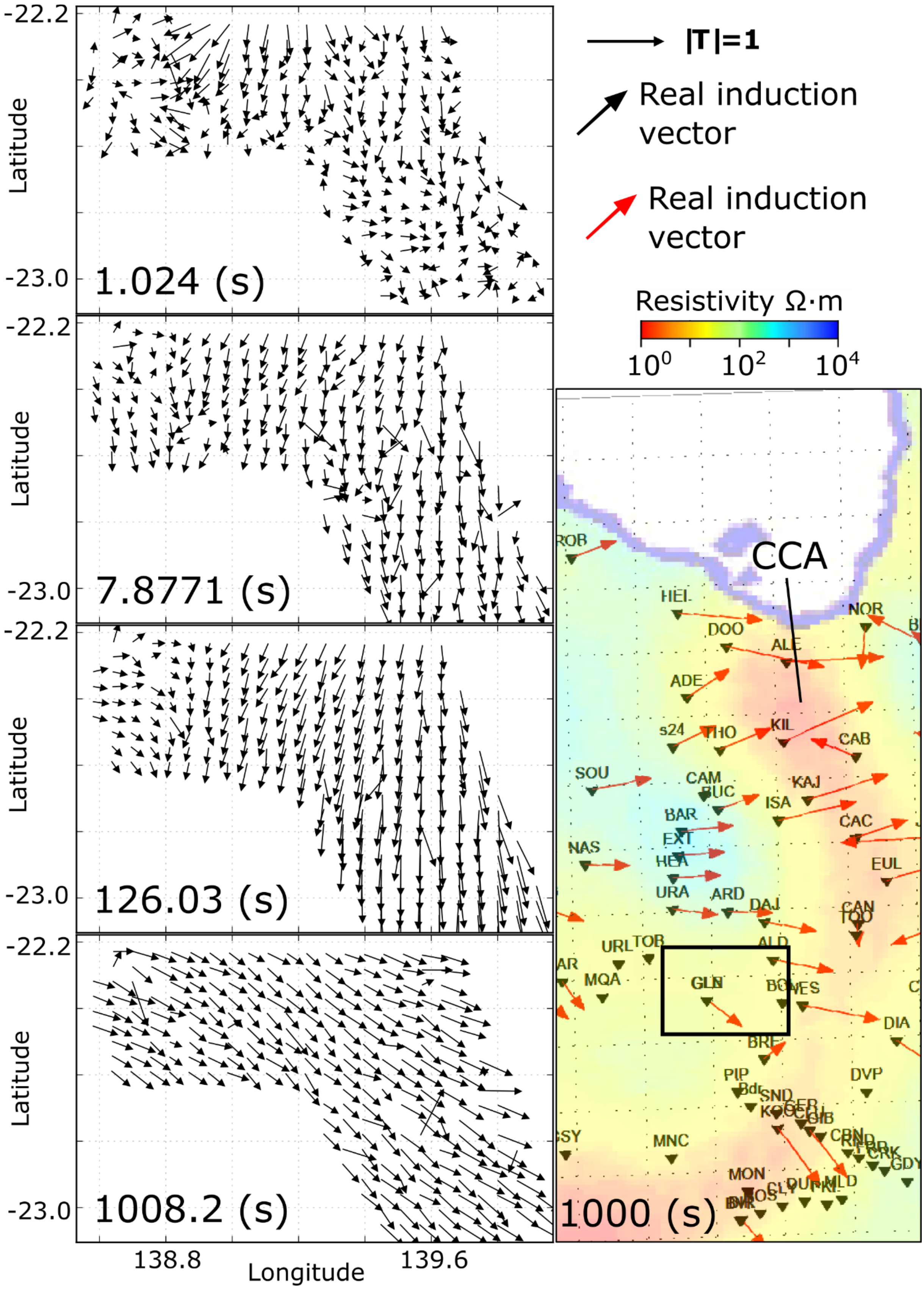

Figure 2.3. Left panels show in-phase induction arrow plots (Parkinson convention) for selected periods and sites; note strong influence of conductive structures outside the data array to both the south and south-east from 7 s. All induction arrows in left panels have same scale. Right panel shows 1000 s regional in-phase induction arrows (Chamalaun and Barton, 1990; Hanekop, 2006) plotted on the 53 km resistivity depth slice (Wang et al. 2014). The approximately north-south low resistivity zone is the Carpentaria Conductivity Anomaly (CCA). The black box on right panel indicates location of array.

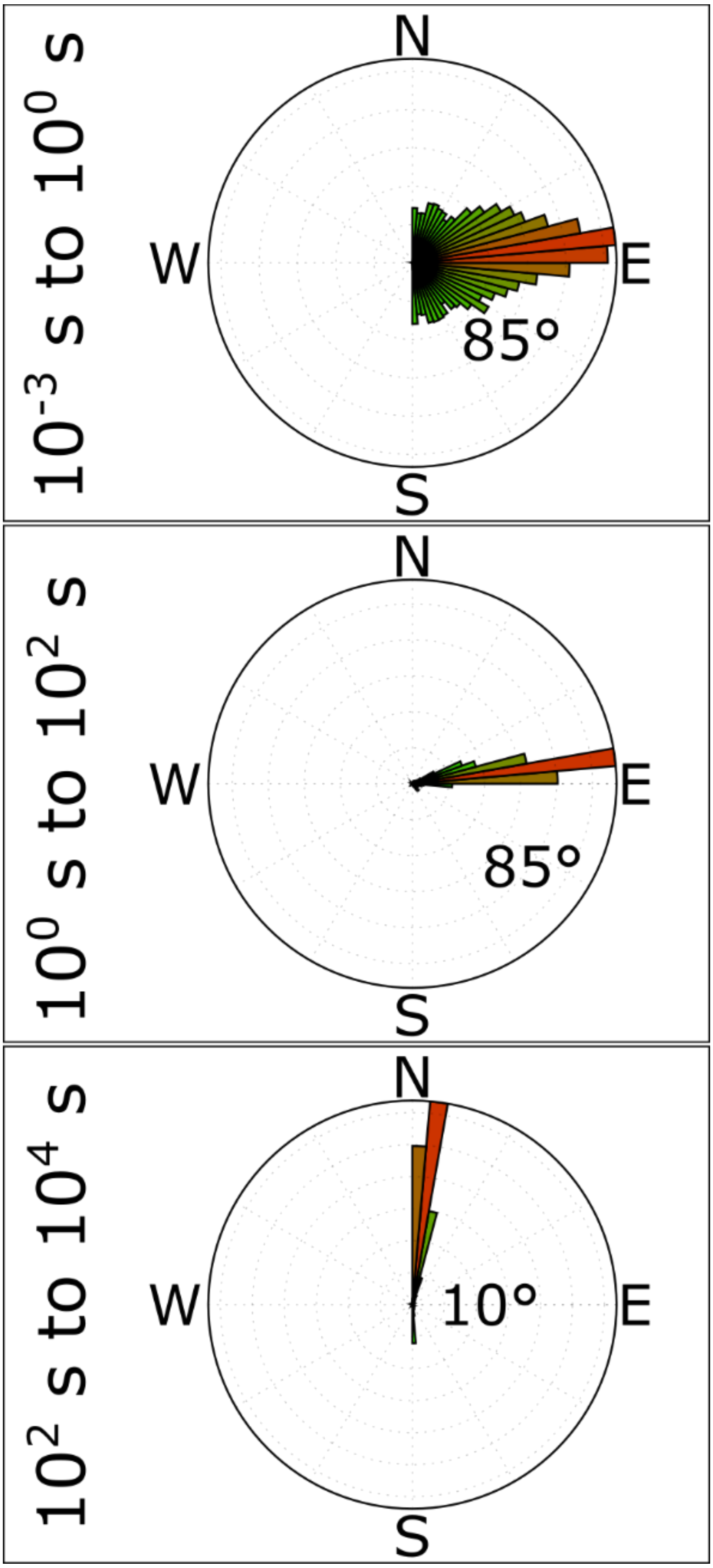

Figure 2.4. Strike analysis using the phase tensor method. Increased orientation scatter at short periods attributed to 1D data.

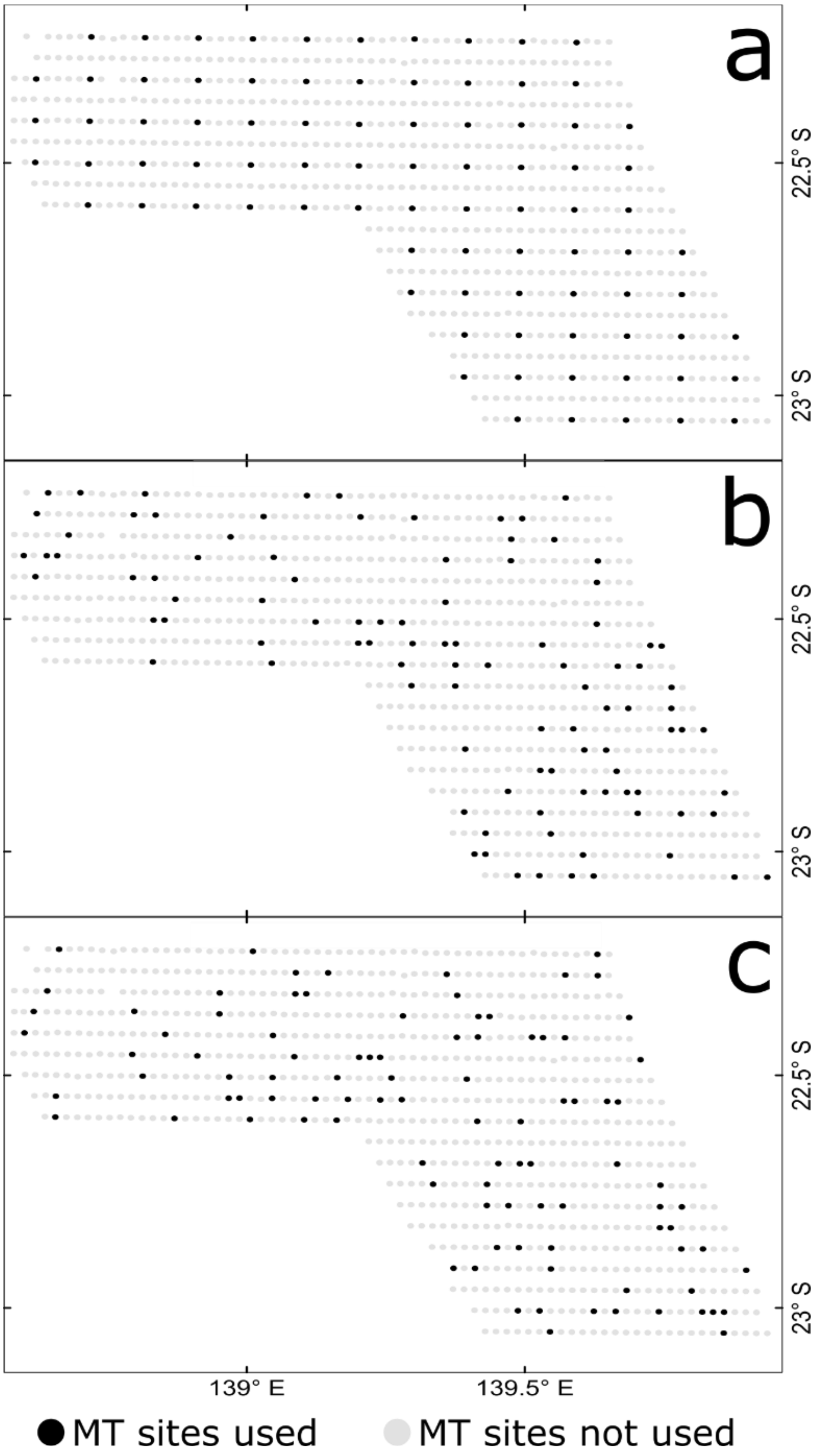

Figure 2.5. (a) Grey dots show the entire set of 809 MT sites. A sub-set sampled at 10 km is shown by the black dots. (b and c) Two random sub-sampled sets of sites, each with 99 sites.

2.3 Workflow

The workflow used in this study is based on the modelling concepts presented in (Lindsey and Newman, 2015; Miensopust, 2017; Tietze and Ritter, 2013), and has five stages which encapsulate data analysis, inversion and model analysis, as shown schematically in Figure 2.6. The two stages of inversion are an initial coarse-inversion of the sub-sampled dataset, followed by inversion of all sites. Coarse-inversions use a subset of the available MT dataset (as shown in Figure 2.5) to establish the large-scale resistivity features. The subsequent fine-inversion uses the coarse-inversion as the starting model to both reduce computational timeframes and improve inversion outcomes (Lindsey and Newman, 2015). The workflow in this paper has two additional steps to include aspects of model assessment and variable testing, as outlined by (Tietze and Ritter, 2013), and recommended by Miensopust (2017).

After data analysis, the second step of the workflow is completion of coarse inversion. For our study we investigated four inversion parameters, namely: smoothing, site distribution; inverted MT components; and influence of the prior model. Four suites of coarse inversions were undertaken which vary from each other in one parameter (Table 1).

The third step of the workflow is analysis of the spatial variability of RMS misfit for each MT function and period. Inversions which fit data poorly are identified, and an understanding of variations in data misfit is established for remaining models to ensure that only model with similar misfits are compared. Additionally, geologically unreasonable models can be identified and removed from further analysis. Optimal 3D model parameters (in the sense that they are consistent between inversions and are geologically feasible) are used as a starting model for fine-inversions.

Analysis of 3D model variability is conducted using the 3D software GoCAD in terms of bulk model variability; variability associated with model parameterization; and variability of specific features. Macro-scale analysis was accomplished through basic statistical comparison of model resistivity populations, spatial plots of average model resistivity and one-dimensional resistivity-depth profiles.

The final step of the analysis is to identify inconsistent resistivity features that are not present in all coarse models. Often such features are small or deep, and have little influence of the broad-scale modelled response. Identification is necessary as their presence in the prior for fine-inversions tends to mean they are preserved as features of the final model.

Fifteen coarse-inversions and one fine-inversion were run using ModEM 3D (Kelbert et al., 2014). Error floors of 5% of $|Zxy\ Zyx|^{1/2}$ for all Z components and 0.1 for the vertical transfer function. Smoothing parameters were established through the a priori model covariance. Static shift was accommodated in thins layers near top of model during inversion. Inversions were started with an initial damping factor (λ) of 30 and a damping factor of 10. Inversion stopped when the iterations reached 150, RMS equalled 1.05 or lambda equalled 10^{-8}. Of the coarse models, seven had different starting models, two had different spatial site distributions, four models inverted either impedance or tipper, and two models varied in smoothing parameterization (through prior model covariance). ModEM 3D uses the stating model as the reference model for inversion.

Of the seven different starting models, three were half-spaces of different resistivity, one was a three-layered model, and three included geological boundaries as priors. The half-space models (UNC10, UNC100 and UNC1000) were of 10, 100 and 1000 Ωm respectively, and the layered model (UNC2) consisted of 100 Ωm to a depth of 100 km, 10 Ωm from 100 to 410 km, and 1 Ωm below 410 km.

Two different geological prior model variants were tested, one developed from the geological domains in Figure 2.1, and the other from interpretation of the 14GA-CF3 and 14GA-CF2 seismic lines displayed in Figure 2.1. The first variant (GEO1) had four resistivity domains: three above 45 km (approximate depth of the Moho), and one for the mantle below 45 km. The three crustal domains were west 50 Ωm, central 1000 Ωm, east 200 Ωm, with a 10 Ωm mantle and smoothing constraint were removed between blocks (see Figure 2.7). These three domains represent interpreted fault bounded blocks of different geological packages. The second geological prior model variant has two subtly different models GEO2 and GEO3. Both models have the same structure below 11 km (west 50 Ωm, east 5000 Ωm, and 100 Ωm below 45km).

Above 11 km GEO3 has a starting resistivity of 500 Ωm, while GEO2 has 10 Ωm to 500m and 1000 Ωm 0.5 – 11km. Resistivity values for the geological starting models were selected after inspection of early results from other coarse models. All other inversion parameters are detailed in Table 2.1.

The coarse mesh had 1790 m cells size in x,y, with an uppermost layer thickness of 50 m, and increasing in thickness by a factor of 1.2 with depth. The array was spanned by 400,200 cells including padding. Total model dimensions are approximately 1000 km in the east-west and north-south directions and 1100 km deep. The fine-mesh sizes was 1790 m and 600 m in the x and y directions respectively, a first z layer thickness of 20 m, increasing in thickness by a factor of 1.2 with depth. The total number of cells was 1,834,300 including padding, with dimensions of 850 km in east-west and north-south directions, and 1100 km deep.

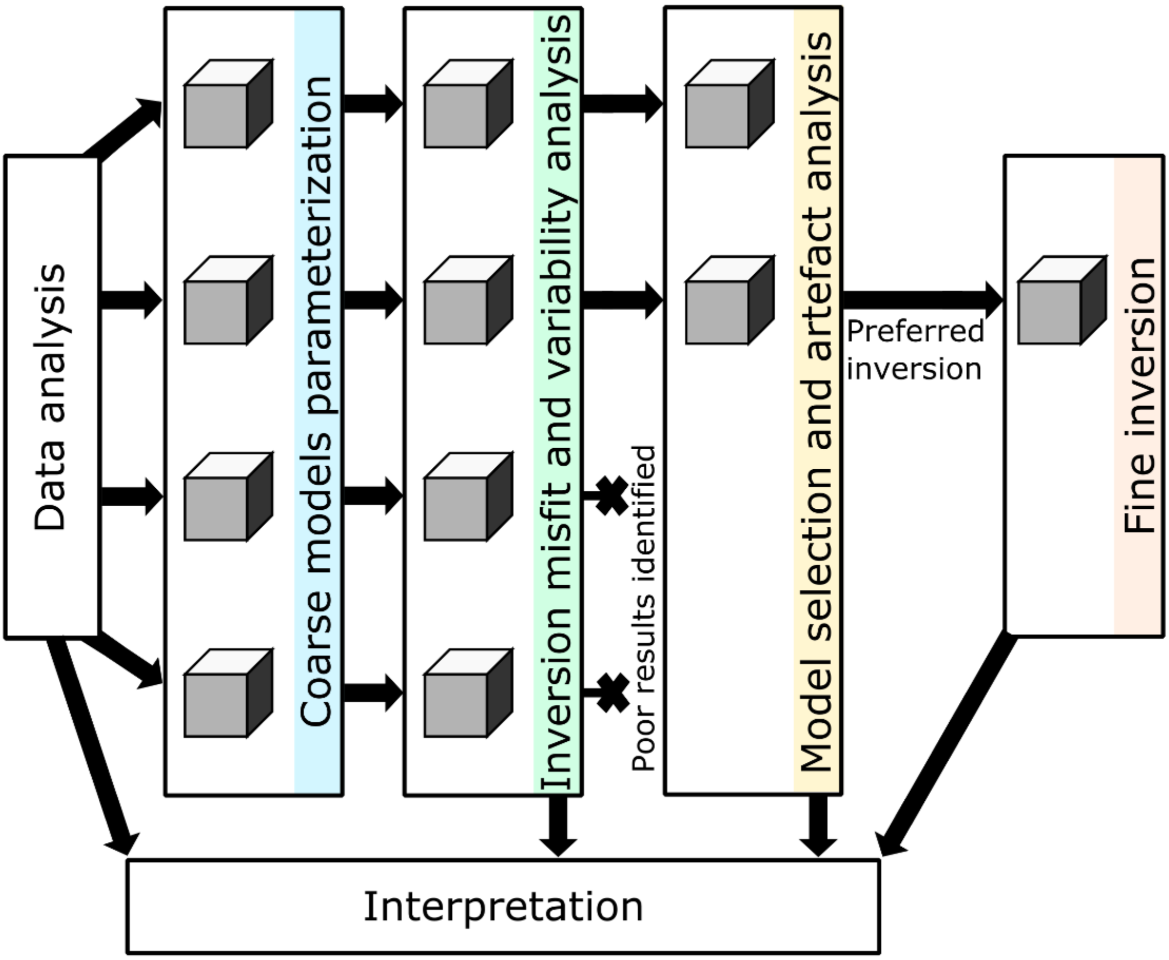

Figure 2.6. Overview of workflow used in this study.

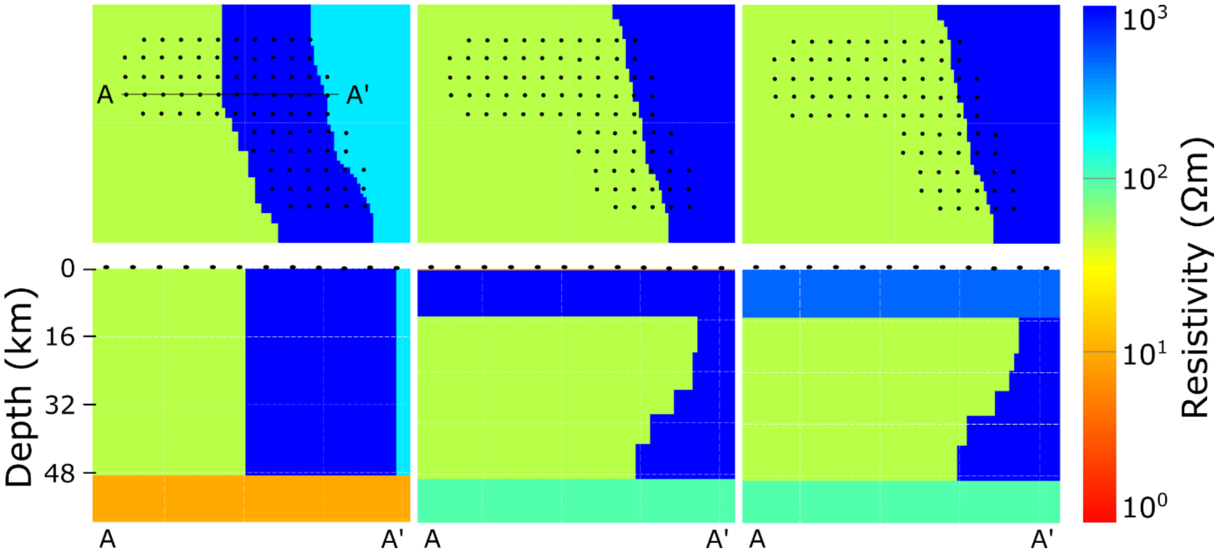

Figure 2.7. Geological starting models in map view at 11 km (top) and profile view (bottom). Black points are MT site locations used for inversions; location of profile indicated on top left panel. Left to right GEO1, GEO2 and GEO3 models. Note the GEO2 model has a 500 m layer of 10 Ω·m at the top of the model.

Table 2.1. Inversion parameters and names for all inversions (see Figure 2.5 for dataset plots and Figure 2.7 for starting models). Models are coloured according to the inversion parameter they were used to investigate: yellow – starting model; green – inverted data component; blue – spatial data distribution; orange – covariance. All coloured models are the result of coarse inversion. Covariance listed in x, y, z directions according to ModEM standard orientations.

Model name	Dataset			Data type		Starting model					Covariance			RMS
	10 km	Rand	Al	Z	T	10	100	1000	Geo	Othe	0.2,0.2,0.2	0.4,0.1,0.2	0.1,0.4,0.2	
UNC10	x			x	x	x					x			1.16
UNC100	x			x	x		x				x			1.13
UNC1000	x			x	x			x			x			1.05
UNC2	x			x	x					x	x			1.04
GEO1	x			x	x				x		x			2.43
GEO2	x			x	x				x		x			1.24
GEO3	x			x	x				x		x			1.05
IMP100	x			x			x				x			1.05
TIPP	x				x		x				x			1.03
IMP10	x			x		x					x			1.08
IMP1000	x			x				x			x			1.06
RAND1		x		x	x		x				x			3.09
RAND2		x		x	x		x				x			3.27
COVX	x			x			x						x	1.04
COVY	x			x			x					x		1.04
FINE			x	x						x	x			1.72

FINE model - started from GEO3 result with top 10 km reset to 500 Ω·m

2.4 Results

All coarse inversions achieved misfits of RMS < 1.5, with the exceptions of RAND1, RAND2 and GEO1 (Table 2.1). Figures 2.8, 2.9 and 2.10 show: the 100 Ωm isosurfaces for all models; variation in RMS misfit with period and component; and spatial distribution of RMS for each coarse model. Spatial misfit distribution for each data component, a 20km depth slice and a model profile are provided in the Appendix B with detailed descriptions of model fit and structures (Figures B.1, B.2 and B.3). Labelling of low-resistivity features (C1, C2, C3, and C4) is consistent for all figures.

As shown in Figure 2.8, a maximum of four low-resistivity features are produced by inversion, but conductor C1 is the only low-resistivity feature present in all. It typically occurs below 20 km and dips to the west. Conductor C1 is broader and deeper than C2, C3 and C4. The conductor C2 is present in seven models and strikes approximately north-northwest and the southern part of the feature extends beyond the data array. Ten of the coarse models have the conductor C3. This feature consistently strikes approximately north-south, but its spatial extents vary considerably between models. Both the C2 and C3 conductors are approximately 10 km wide, which is the site spacing. The conductor C4 feature is only found in models that start from a 10 Ωm half-space.

Spatially, the misfits for the coarse model impedance components are distributed across the array, as shown in Figure 2.10, but tipper misfit data have spatial heterogeneity, with increased misfits in the south and east. Tipper misfits increase markedly to the south-east or east for all coarse inversions with the exception of the GEO3 model. In terms of the period-bandwidth, fits are consistently poorer at periods > 400 s and <4 s for all models, as shown in Figure 2.9. Long-period misfits are predominantly observed in the impedances, but at short-periods the misfit is large in both impedance and tipper. Components Zyx and Zxy accommodate the majority of the short-period misfit. Long-period misfits are likely to be caused by low resistivity regions outside the modelled data array, while at short-periods it is probably associated with insufficient mesh discretization. Overall, tipper component Tzx has the highest misfits; while Zxx and Zyx have higher misfits than Zxy and Zyy (Figure 2.9).

The misfit for the GEO1 model was high across all sites and periods, was excluded from the model variability analysis. The RAND1 and RAND2 models had the highest overall misfits, but most of this misfit is confined to the long-period tipper data (Figures 2.9 and 2.10). Between periods of 5 s and 400 s, the impedance misfits for the RAND2 model in particular was more comparable to other inversions.

Two additional trends are observed across the coarse model suites. Firstly, low-resistivity features (such as conductors C1-C4) are modelled at shallower depths when starting with a low-resistivity half-space (such as UNC10), and deeper in models with high-resistivity half-space (such as UNC1000). Secondly, shallow artefacts (Figure 2.8) occur below 5 km in UNC1000, IMP1000 and GEO1. These features occur between sites, indicative of inversion artefacts. The features are spread across the entire area for UNC1000 and IMP1000 but they are more confined in the GEO1 model, occurring predominantly within the highly resistive unit from the starting model.

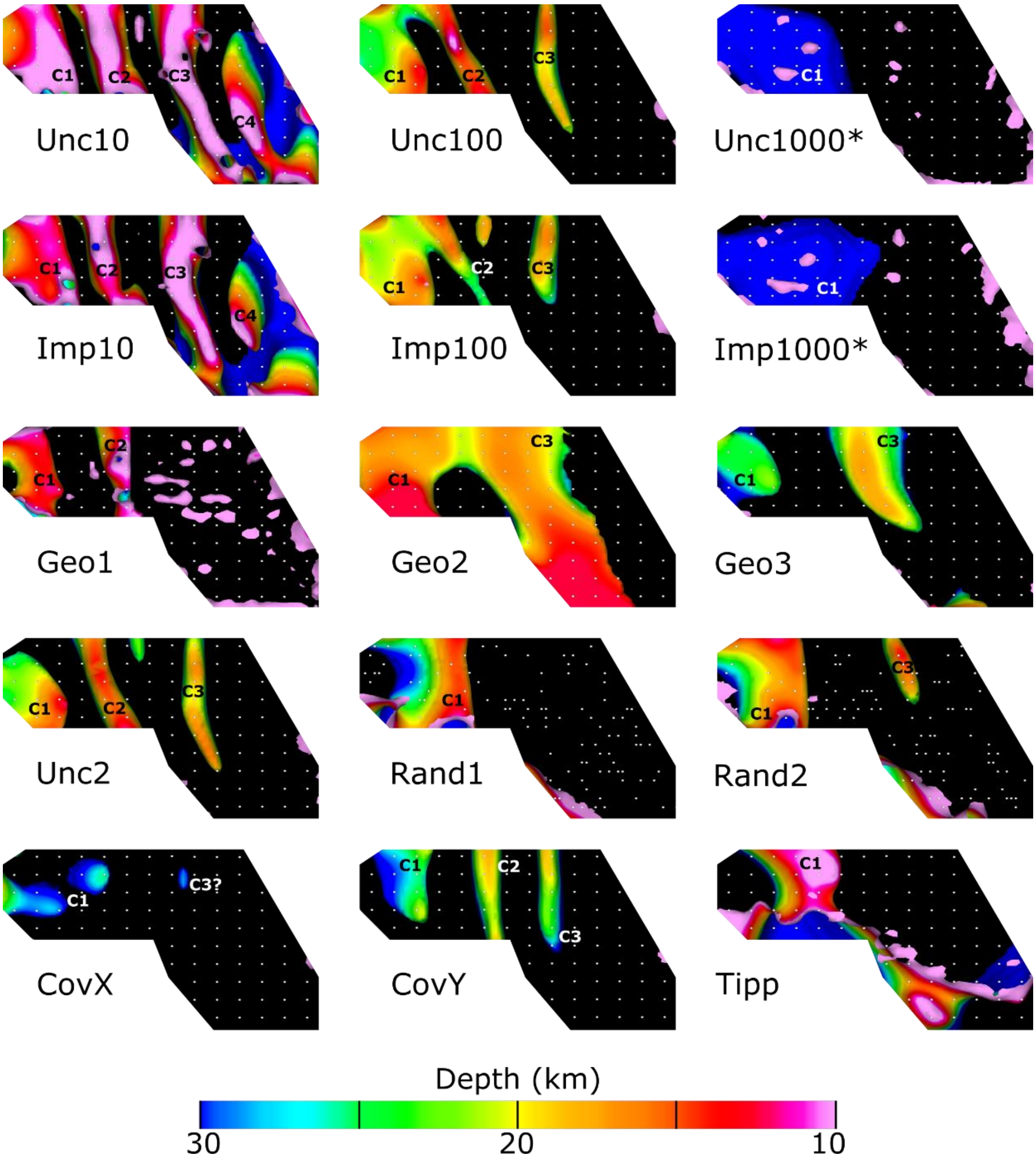

Figure 2.8. 100 Ωm isosurfaces calculated for coarse models; areas within the isosurfaces indicate low-resistivity zones. Isosurfaces are coloured by depth and labelled C1-C4 in each plot, with MT sites as white dots. Black areas indicate an absence of features with a resistivity less than 100 Ωm between 5 km and 50 km. UNC1000 and IMP1000 models display 500 Ωm isosurfaces as there are no features with resistivity less than 100 Ωm within the array.

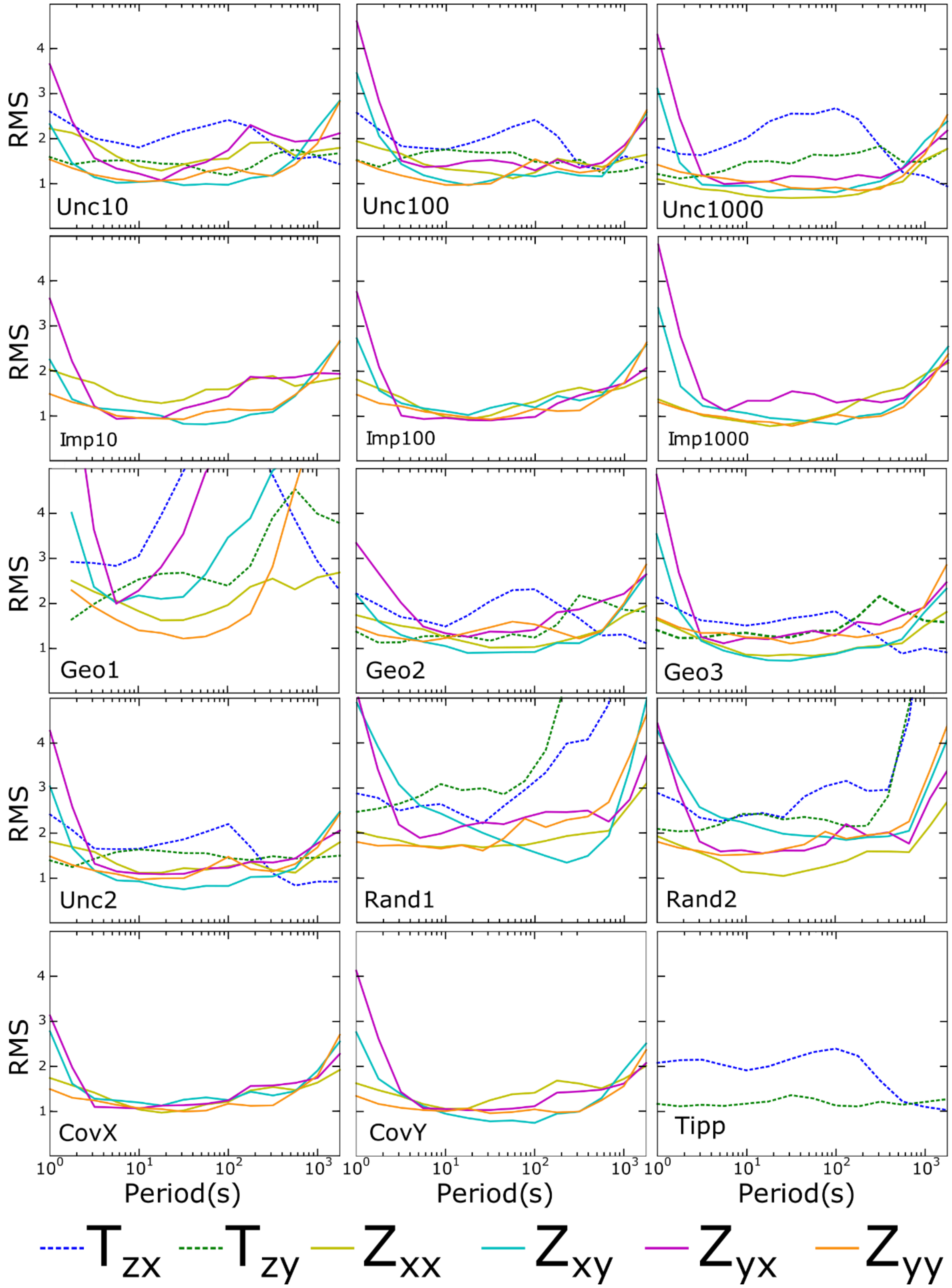

Figure 2.9. RMS distribution for coarse models by period (s) and component.

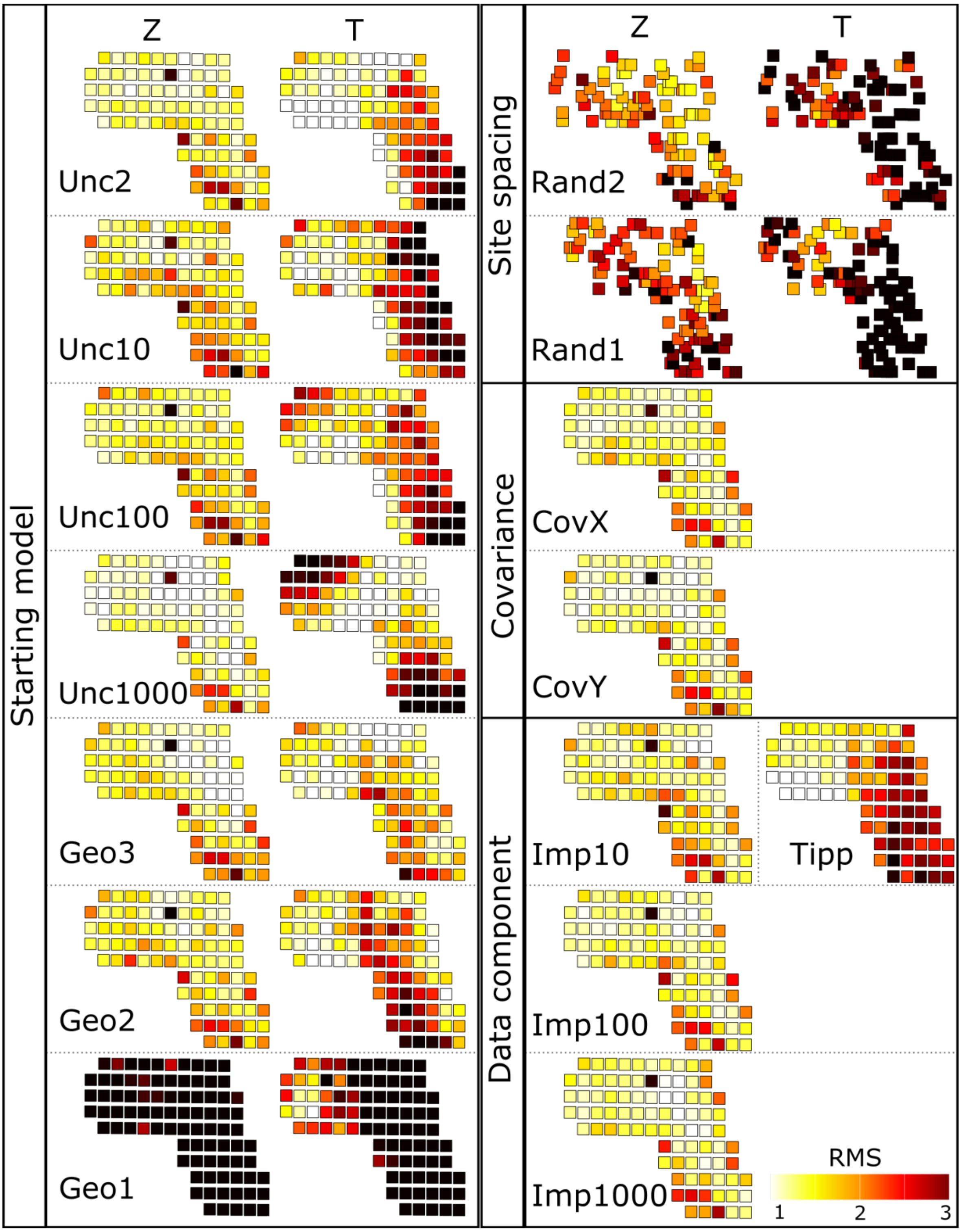

Figure 2.10. Spatial RMS for all coarse models, averaged per site for the impedance (Z) and Tipper (T) data. RMS plots are grouped according to their coarse inversion suites.

2.5 Inversion variability results

Variability was analysed between depths of 5 km and 50 km for mesh cells below the data array. Macro-scale variability of the full set of coarse models was assessed based on bulk resistivity distributions (as shown in Figure 2.11; models averaged as log resistivity), as well as spatial variability (Figure 2.12) and with depth (Figure 2.13). More detailed analysis of variability due to the four different inversion parameter suites is displayed in Figure 2.14, and a spatial variability of individual features in Figure 2.15

2.5.1 Macro-scale variability

The interquartile range for the full suite of coarse models typically plots between 100 and 1000 Ωm (Figure 2.11). There are four notable exceptions to this trend, UNC10, IMP10, UNC1000, and IMP1000. The UNC10 and IMP10 models have a bulk shift to lower resistivity in their overall distribution, while UNC1000 and IMP1000 have a bulk shift to higher resistivity (Figure 2.11).

Despite the similar resistivity distributions identified for models started from a 100 Ωm half-space in Figure 2.11, the same group of models has considerable spatial variation in model resistivity (Figure 2.12; stared models). The top six models in Figure 2.12 have similar misfit and bulk model characteristics but significant variability in spatial resistivity distribution. The resistivity distributions for UNC1000 and IMP1000 are similar to each other, but different to most of the other models. Similarly, UNC10 and IMP10 appear to have resistivity distributions more similar to each other than the rest of the models. The influence of the starting model on spatial resistivity distribution is clearly visible for the three geological models (Figure 2.12). The wide spread of resistivity values for GEO1 indicates that this models may be overfit, possibly the result of an inappropriate reference model.

Three locations were selected to compare resistivity variability with depth, as shown in Figure 2.13. Two of the locations for comparison were near low-resistivity features C1 and C3, and the third was in the high-resistivity southern part of the model. All three have variation of more than two orders of magnitude in resistivity for most depth ranges (Figure 2.13). This is some indication that shallow parts of the model have lower variability, indicating that features within the top 10 km have less variability.

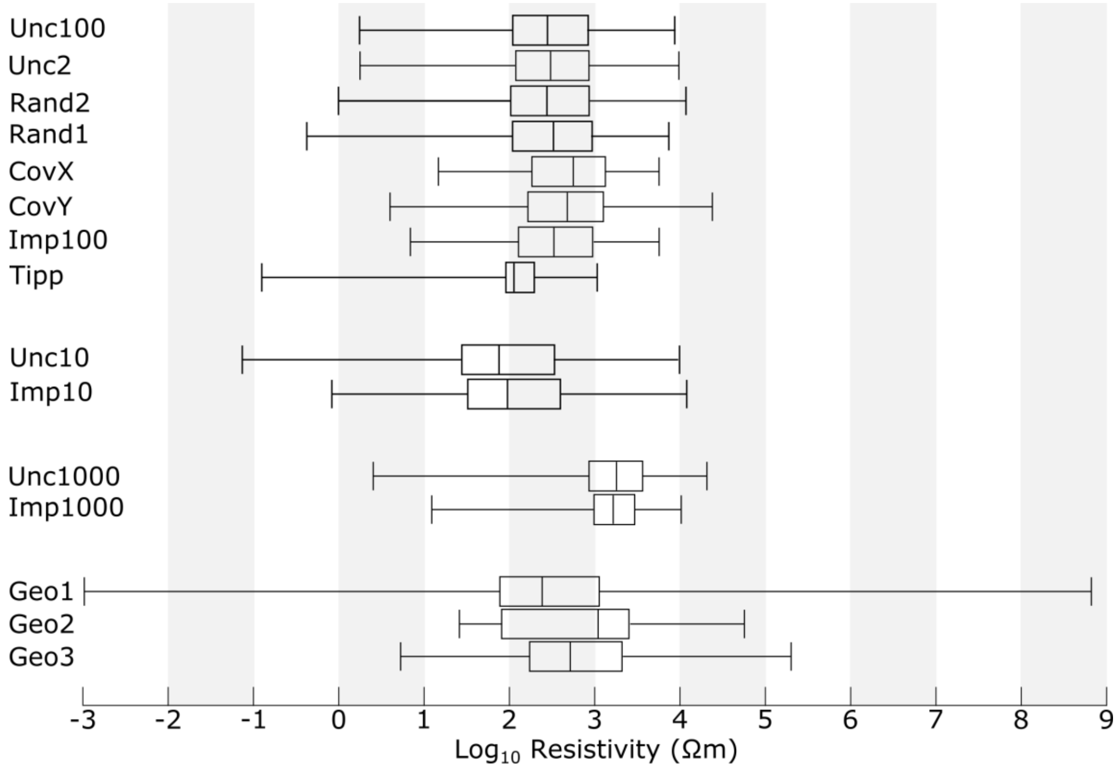

Figure 2.11. Comparison of model resistivity distributions for all coarse models using a box and whisker plot. Resistivity distributions for models with the same starting resistivity display similar characteristics, for example the top seven distributions were from models with a 100 Ωm starting model. The resistivity distribution for models with a starting resistivity of 10 Ωm have lower average resistivity values, while models started from 1000 Ωm have higher average resistivity. Model distributions calculated using data extracted at one point per mesh cell between depths of 5 km and 45 km.

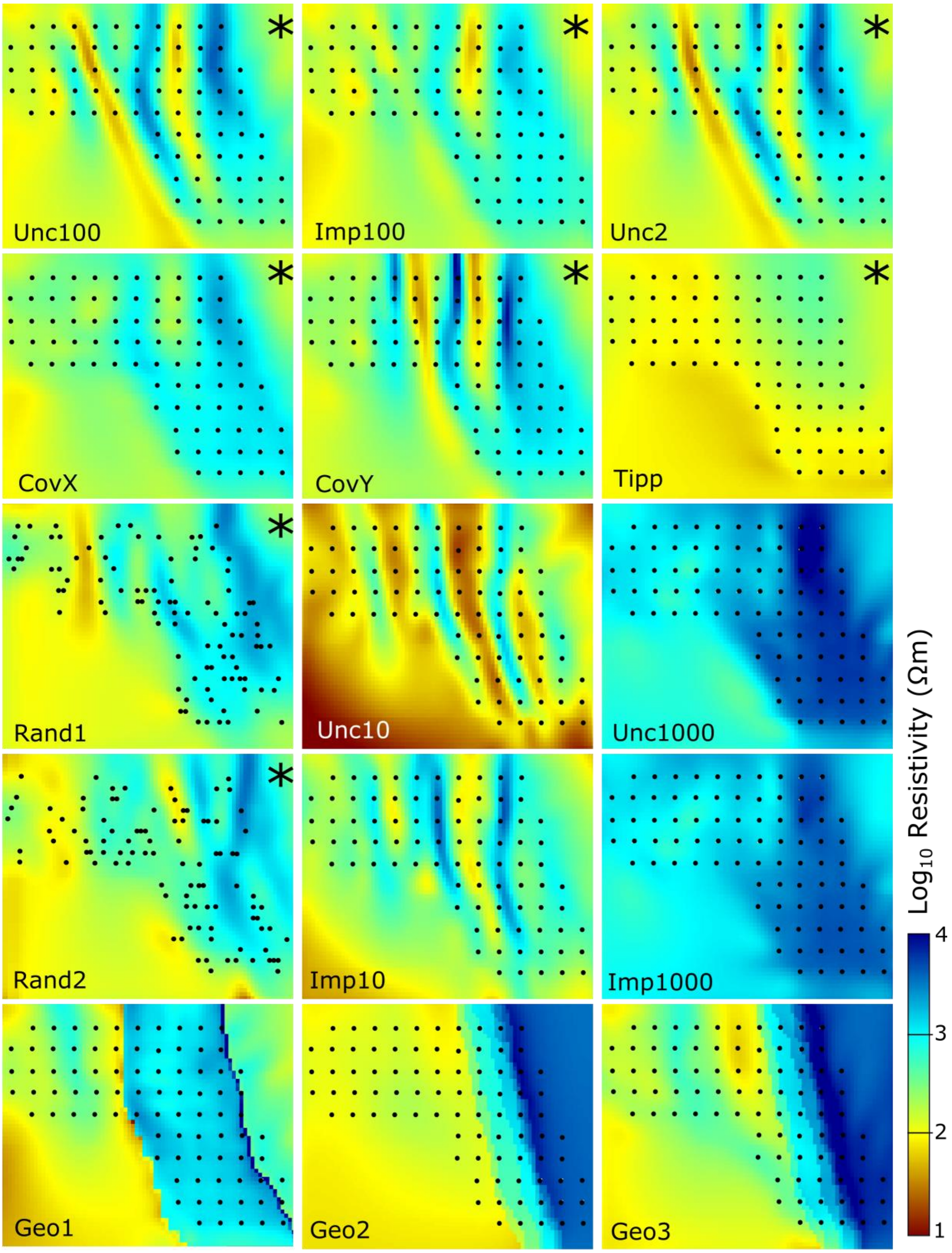

Figure 2.12. Average model resistivity for coarse models calculated between 5 km and 50 km. Averages calculated on Log_{10}Resistivity data. Models marked with a star have 100 Ωm half-space starting models over the analysed interval.

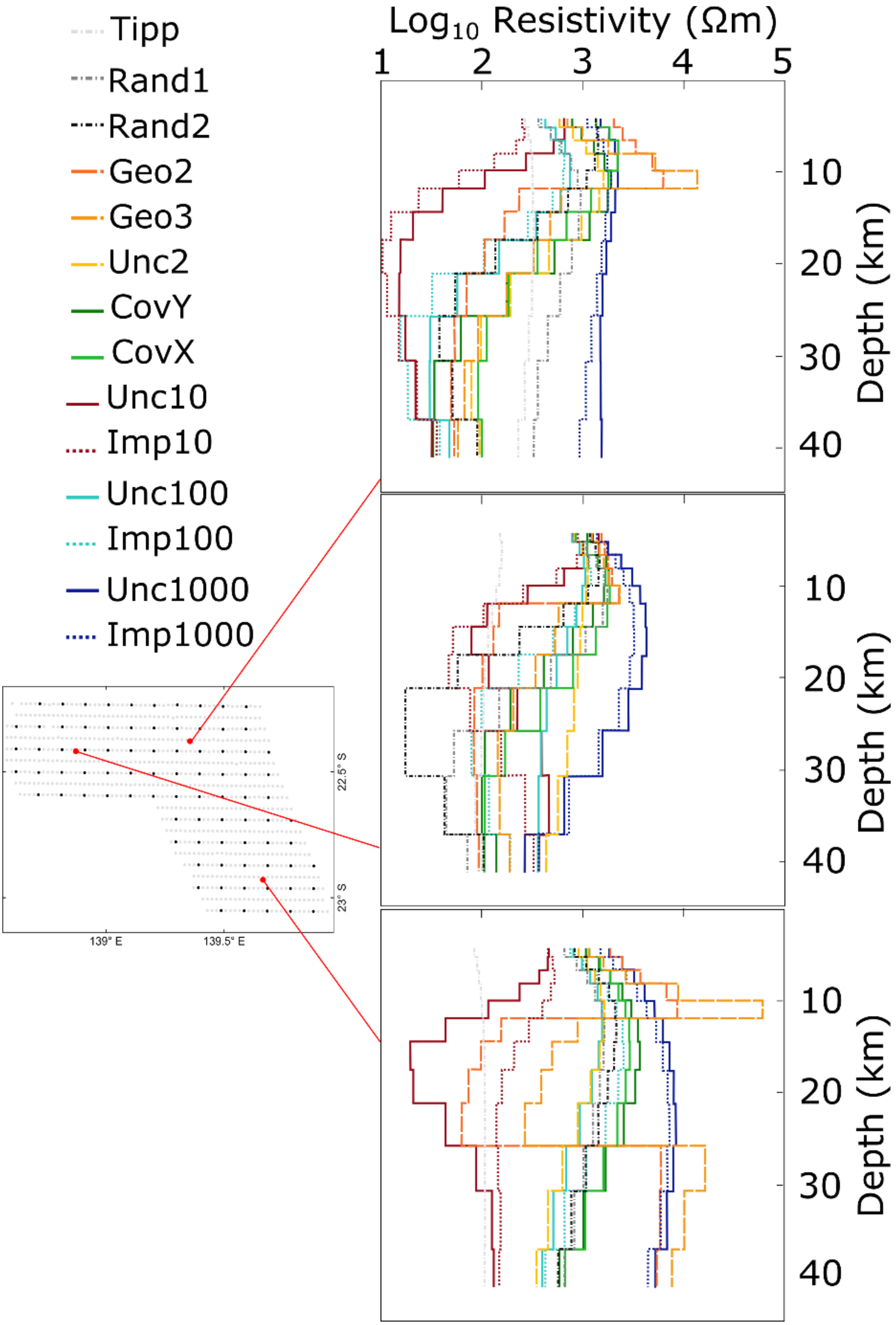

Figure 2.13. 1D model profiles extracted from inversion results for three locations as indicated on the map, top profiles extracted near C3, middle profile plot for near C1 and bottom plot from resistive area in the south of the data array. Plots display variability of resistivity greater than two orders of magnitude for most depths.

2.5.2 Variability linked to inversion parameterisation

Four suites of models were used to investigate the relative contribution to model variability of starting model, site distribution, smoothing, and data type. Variability was calculated by subtracting a selected baseline model from each model in the suite: comparative histograms are shown in Figure 2.14.

The influence of starting model was undertaken with UNC10, UNC100, UNC1000, UNC2, GEO2 and GEO3 (GEO1 was excluded due to high misfit and unrealistic resistivity range). The UNC100 model was selected as the baseline. Model variability of up to three orders of magnitude in resistivity is evident in the starting model suite (Figure 2.14). The UNC10 model is skewed to the left, consistent with lower overall resistivity compared to UNC100; while the UNC1000 model is skewed to the right, and the distributions for GEO2 and GEO3 are very broad.

The impedance-only (IMP100) and tipper-only (TIPP) inversions were compared to with the baseline UNC100 model. The IMP100 histogram has a narrow distribution with a slight skew to the right, indicating that omission of tipper data has minimal impact. Comparisons between UNC10 and IMP10, and UNC1000 and IMP1000 show the same trend. In contrast, omission of impedance data from inversion produces significant variability from the baseline. The variance of the TIPP model is skewed to the left, indicating that the TIPP model has lower resistivity than the UNC100 inversion.

Contribution of smoothing parameters was investigated by comparing COVX and COVY to the selected baseline model, IMP100. Variation in smoothing parameter produced little variability in models.

Inversion variability resulting from changes in spatial site distribution was assessed based on UNC100, RAND1 and RAND2; with UNC100 selected as the baseline. The misfits of RAND1 and RAND2 are not strictly comparable to UNC100. While limiting the analysis depth to 5 – 50 km does eliminate much of misfit difference, overall this comparison is not as robust. Neither RAND1 nor RAND2 plots display any shift from the baseline, but do have broad distributions showing that site location has greater influence than either the tipper data or changes in smoothness.

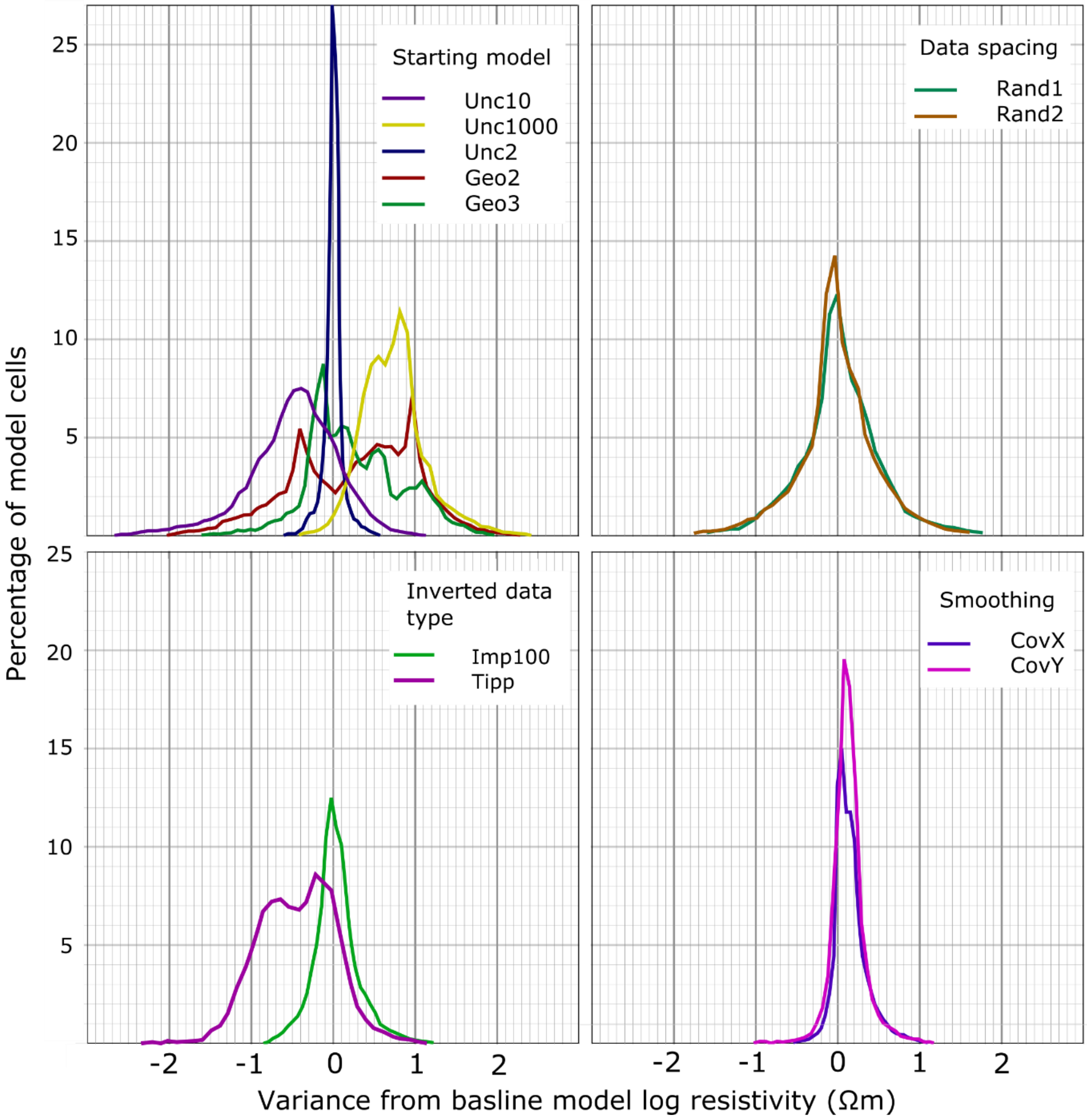

Figure 2.14. Histogram of model variability over depths 5 to 50 km resulting from in changes in stating model, site spacing, data type and smoothing parameters. Population calculated based on one point per mesh cell.

2.5.3 Feature specific variability

More detailed analysis of the variability in the conductive features was achieved though averaging variability of all models, over each model cell (see Appendix B; Figures B.5, B.6 and B.7 for model variability plots for each model). The average was calculated using absolute resistivity values, as shown in Figure 2.15, with the location of low-resistivity features from UNC100 plotted for reference. Each of the three primary conductors (C1, C2, and C3) identified during coarse inversion are associated with different levels of variability. The C1 conductor has low variability at all depths C3 has low variability under the site location with variability present around the peripheries of the feature, indicating its geometry or conductance is more uncertain than C1. C2 has a much higher degree of variability. This pattern is particularly evident on the 18 km and 40 km slices. The split of long period apparent resistivity and phase seen at the two MT responses in Figure B.4 provides direct evidence of strong conductive structure somewhere near each site, supporting the existence of the C3 conductor.

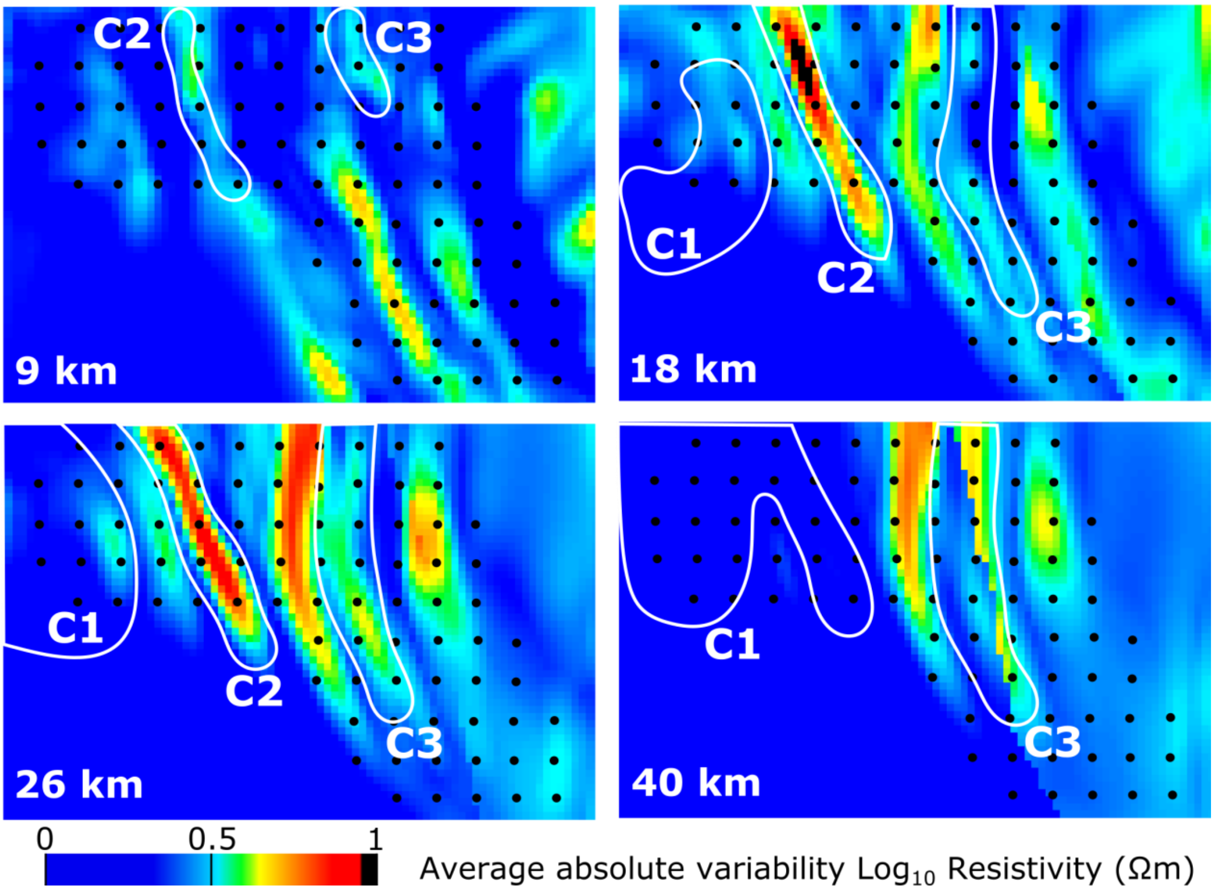

Figure 2.15. Average spatial variability across all coarse inversions compared the location of C1, C2 and C3 from the UNC100 Model. Variability expressed as average resistivity variability from an appropriate baseline model, where a value of 0.5 represents average deviation from a baseline by half an order of magnitude in resistivity. Colour scale chosen to emphasize average variability of greater than half an order of magnitude in resistivity.

2.5.4 Selection of a preferred coarse inversion

Conductors C1 and C3 were the most consistently returned features across all coarse inversions, with C1 being consistent but C3 with significant degree of variability on its southern extent. Of all coarse models that included tipper, only the GEO3 inversion had an even spatial RMS distribution across all data components. Impedance fits across periods for GEO3 was similar to most other models, but tipper fits between 4 s and 400 s were better. Using only RMS analysis would suggest the GEO3 model is the best model to use for initiating a fine inversion.

An alternative approach to selecting a coarse model involves finding an inversion with the most consistent features, which in this case involved a broad deep C1 feature. The model which best displays these characteristics while still having acceptable misfit distribution on the impedance data is the UNC1000 model (Figure 2.8). While the absence of the C3 feature is not entirely consistent with the broader model suite, there is a subtle feature in the resistivity model that is in the approximate location of C3. Additionally because ModEM3D uses the starting model as the reference model for inversion, any reappearance of the C3 in a fine inversion started from UNC1000 would provide further confirmation that it is required by the data.

Macro-scale variability analysis was useful in gaining an understanding of how much variability was permissible during inversion of the dataset. Compared to side by side analysis of inversion models (e.g. Tietze and Ritter, 2013), the dependence on bulk model resistivity values on the starting model was more obvious, particularly in the statistical analysis (Figure 2.11). The depth profiles (Figure 2.13) emphasize the range of resistivity values present at any given depth across the coarse models, with a range of more than two orders of magnitude present in much of the model. Finally, the average resistivity plots (Figure 2.12) offer an easy first glance comparison of the major structures for each model in a single image, but offer the least additional information when compared to more standard comparison techniques. While this macro-scale analysis is interesting and provides large-scale information about the variability of inversion models which may explain the dataset, it does not provide information that assists with selection of a preferred model from which to start a fine inversion.

The variability analysis conducted used inversion parameter suites enabled us to quantify which inversion parameters made the largest contribution to model variability (Figure 2.14). Of the four tested inversion parameters, the starting model made the largest contribution to inversion variability (Figure 2.14). This heavy influence is a consequence of the way ModEM inversions are parameterized, such that the starting model is also the prior model. As deviations from the prior model are minimized during inversion, the final models have a strong dependence on the starting model, regardless of whether it is a half-space or a geological model. This is an obvious advantage in areas where constraining information from independent datasets is available. However, in the absence of robust constraint, this functionality is more problematic and needs to be considered during interpretation. Ideally more variations in parameterization of inversion smoothing would be tested and may offer better insight of any resulting variability introduced.

Of the analysis conducted, the variability of specific features (Figure 2.15) was the most instructive for selecting a model with representative features. While this is not the only criteria used to select a preferred coarse model to use for the second stage of inversion, it is one of the few methods available in areas with limited or no constraining information.

2.6 Fine model results

For demonstration purposes, only one of the two preferred models was selected for fine inversion. The GEO3 model was selected and its mesh refined after removal of structure from the top ten kilometres of the coarse inversion results. These shallow features were under-constrained by the original inversion and consisted of low-resistivity features populated between sites, generally viewed as inversion artefacts. The FINE inversion achieved an RMS of 1.72 and results are displayed in Figure 2.16.

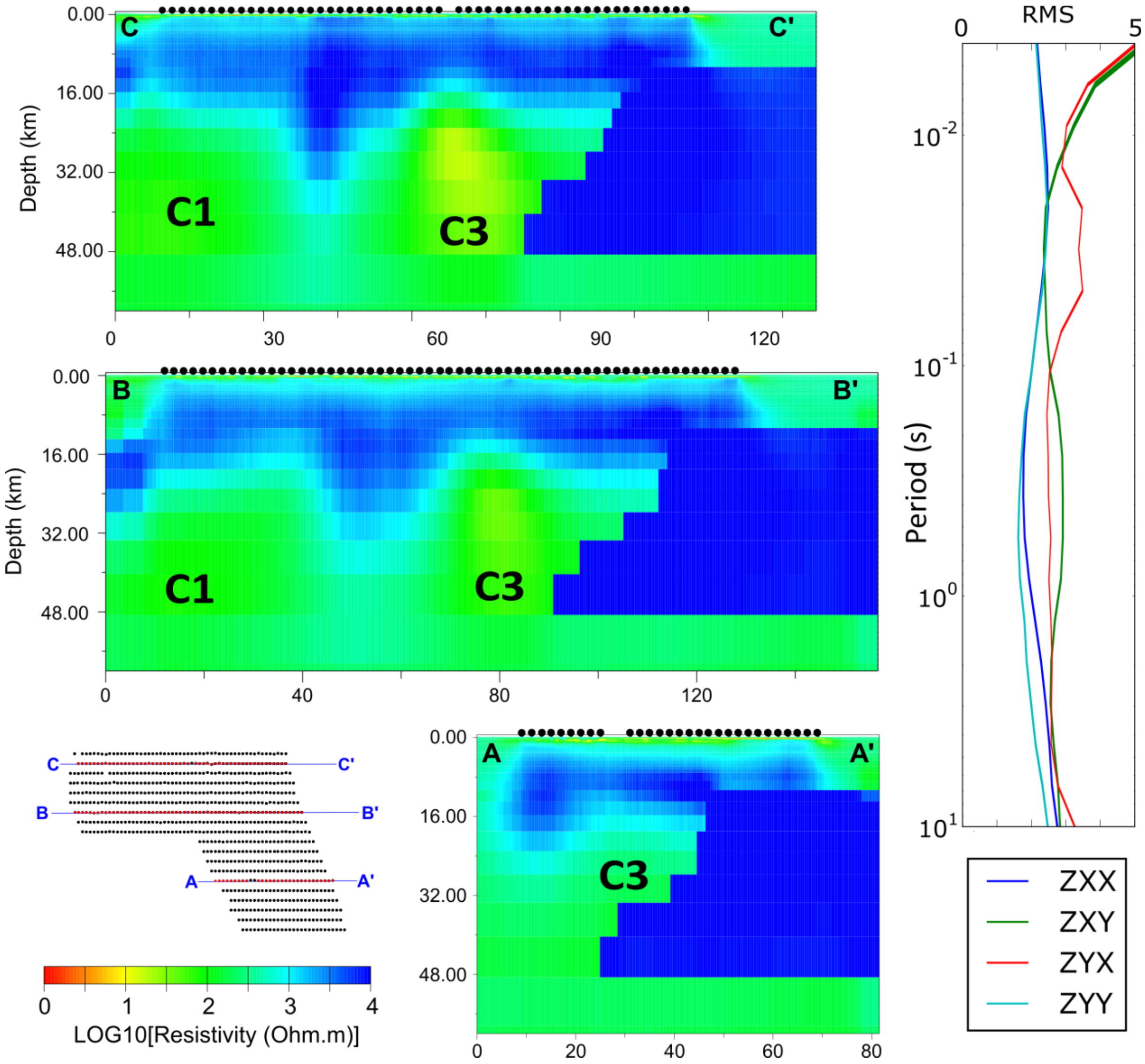

Figure 2.16. FINE inversion results from three selected profiles as indicated. Features C1 and C3 are present below 8 km and the shallow basin sequences deepen to the south, cf. profiles A and C. The RMS distribution by period and component is displayed on the right. Higher RMS misfits are present on the Zxy and Zyx components.

2.7 Conclusions

The highly ambiguous nature of 3D MT inversion is underscored in this paper. The test dataset produced between one and four low-resistivity features with only minor modifications of the inversion parameters.

We present several methods of quantitative analysis of inversion variability with an emphasis on understanding the importance of parameterization. The variability analysis is incorporated into a sequential inversion workflow to leverage the reduced computational timeframe and improved results previously demonstrated to be associated with this style of inversion. Variability was analysed at different scales, from the macroscale resistivity distributions, to analysis of the variability of specific features.

Variability was not evenly distributed across the model for the test dataset, nor did all inversion parameters contribute equally to inversion variability. The starting model parameter greatest impact on model variability, followed by site distribution, while smoothing and inverted data component had a lesser impact. The four low-resistivity features had different levels of variability associated with them, from the highly variable C2 and C4, to the low variability of

C1. Our variability analysis was also able to identify that C3 had higher levels of variability associated with its lateral extents than was present towards its centre.

The macroscale analysis did not provide appreciable benefits when compared to more standard methods of inversion model comparison. Analysis of variability of individual features and variability linked to inversion parameterization did provide additional information to understand the causes of variability and select a preferred model than more standard side-by-side model comparison.

The presented workflow can be implemented for gridded datasets with regular or irregular site spacing. While it is less clear how applicable our workflow is for 3D inversion of 2D profile data, the underlying concept of inversion variability analysis is relevant to all 3D inversions.

CHAPTER THREE

NEW INSIGHTS INTO THE CRUSTAL STRUCUTRE THE SOUTHERN MOUNT ISA PROVINCE FROM JOINT INTERPRETAION OF MAGNETOTELLURIC INVERSION, SEISMIC AND POTENTIAL FIELD DATA

J. Simpson[1, 2] and G. Heinson[2]

1 Geological Survey of Queensland, Department of Natural Resources, Mines and Energy, Queensland Government, Brisbane QLD 4000, Australia

2 Electrical Earth Imaging Group, Department of Earth Sciences, School of Physical Sciences, University of Adeialide, Adelaide SA 5005, Australia

Statement of Authorship

Title of Paper	New insights into the southern Mount Isa Province from integration of magnetotelluric inversion results with seismic and potential field data.
Publication Status	☐ Published ☐ Accepted for Publication ☐ Submitted for Publication ☑ Unpublished and Unsubmitted work written in manuscript style
Publication Details	To be submitted to special edition of Earth Planets and Space by 30th June

Principal Author

Name of Principal Author (Candidate)	Janelle Simpson		
Contribution to the Paper	Performed modelling and interpreted data. Wrote manuscript		
Overall percentage (%)	90%		
Certification:	This paper reports on original research I conducted during the period of my Higher Degree by Research candidature and is not subject to any obligations or contractual agreements with a third party that would constrain its inclusion in this thesis. I am the primary author of this paper.		
Signature		Date	31/05/2019

Co-Author Contributions

By signing the Statement of Authorship, each author certifies that:

i. the candidate's stated contribution to the publication is accurate (as detailed above);

ii. permission is granted for the candidate in include the publication in the thesis; and

iii. the sum of all co-author contributions is equal to 100% less the candidate's stated contribution.

Name of Co-Author	Graham Heinson		
Contribution to the Paper	Provided supervision of work, aided in MT data interpretation and manuscript evaluation		
Signature		Date	3rd June 2019

Abstract

The tectonic architecture of the southern Mount Isa Province in Queensland, Australia has significant implications for understanding the relationship between Mount Isa and the rest of the North Australian Craton (NAC). A suture along the western margin of the Mount Isa Province is invoked as a mechanism for reconciling partly contemporaneous sequences of north-south striking lithology in Queensland and east-west striking lithology in the Northern Territory. There is little direct evidence of this suture and limited agreement about its location and characteristics. We use a multidisciplinary approach, integrating results from 3D MT inversion of an 809 site broadband MT survey with deep crustal seismic reflection profiles and potential field geophysics to investigate the possible suture and provide new insight into the crustal structure of the southern Mount Isa Province.

No compelling evidence was observed in any dataset to suggest the presence of a suture in the project area, although there is some indication that one may exist further east. Instead, a major west-dipping structure that was active pre- and post-Barramundi Orogeny (which produced deformation, metamorphism and cratonisation of the earliest Proterozoic ~2.0−1.9 Ga basins) was identified. This structure is associated with a low-resistivity anomaly and displays evidence of being active during deposition of the Leichhardt Superbasin sediments and is adjacent to a significant change in crustal thickness. Other major features in the project area are a laterally continuous upper-crust and mafic underplating which has undergone significant deformation.

Keywords: Southern Mount Isa Province; magnetotelluric inversion; deep crustal seismic; potential field data; tectonic architecture

3.1 Introduction

The NAC consists of a series of late Archean to Paleoproterozoic cratonic blocks with intervening orogenic belts (Cawood and Korsch, 2008). The relationships between these orogenic belts and cratonic blocks are concealed by sedimentary basins which developed during the late Neoproterozoic to Phanerozoic (Figure 3.1). Outcrop of the NAC Archean basement is limited, but geophysical and isotopic evidence suggests there is widespread Neoarchean to Paleoproterozoic continental crust underlying much of the NAC (Lyons and Huston, 2006).

The NAC has experienced a long and complicated history of deformation both before and after cratonisation at 1640 Ma (Huston, 2006). Despite the impacts of overprinting, several studies have used seismic and potential field data to interpret features attributed to suturing of components of the NAC in the Paleoproterozoic (e.g. the Willowra Suture, Goleby et al., 2009).

MT data have been extensively used to investigate crustal scale features (Becken and Ritter, 2012; Favetto et al., 2008; Gailler et al., 2018; Liang et al., 2018; Logvinov and Tarasov, 2018; Özaydın et al., 2018; Robertson et al., 2015; Selway et al., 2009) and can make a significant contribution to understanding tectonic evolution (Bedrosian, 2016; Dong et al., 2016). MT data are also used to investigate the geometry of cratonic blocks in Archean and Proterozoic terranes (Bologna et al., 2017; Gokarn et al., 2013; Khoza et al., 2013; Thiel et al., 2016) including the orientation of preserved collisional margins (Yin et al., 2017).

Two major sources of resistivity variations in the crust are variation in iron and the presence of hydrogen (Selway, 2014; Yang, 2011; Yang et al., 2012) These properties can be attributed to original rock chemistry or fertilisation of the crust by melt or fluids (Selway, 2014), and have the potential to be preserved over long geological timescales. It is, therefore, possible to use MT to investigate craton amalgamation from the Archean and Proterozoic. Other sources of resistivity variation in crustal rocks include the presence of sulphides or graphite (Selway, 2014), and the effect of high temperature on hydrous minerals (Yang, 2011; Yang et al., 2012).

Identifying suturing structures between amalgamated terranes of Proterozoic age is difficult and best accomplished through a multifaceted approach incorporating a variety of datasets (Bierlein and Betts, 2004). Several tectonic interpretations for the internal structure of the NAC are consistent in defining a boundary on the western edge of the Mount Isa Province (Betts et al., 2016; Korsch and Doublier, 2016; Spampinato et al., 2015), as shown in Figure 3.1. This boundary separates Mount Isa from the rest of the NAC to the west and is defined by a change in the character of potential field data. There is little direct evidence of the exact location and nature of this boundary, particularly its southern extension under the Georgina and Eromanga Basins. In this study, we use new MT and reflection seismic data together with existing potential field data to investigate the existence and nature of the structure in the southern Mount Isa Province. We also consider any implications for the history of the Mount Isa Province and mineral exploration.

3.1.1 Geological background

The Paleoproterozoic was a significant period of crustal amalgamation for Australia, with approximately two-thirds of the continent forming between c. 1860 and 1800 Ma, through the accretion of the West Australian Craton along the southern margin of the NAC (Betts et al., 2002). The late Paleoproterozoic to early Mesoproterozoic is also significant, as it saw the formation of Australia's world-class Proterozoic mineral deposits (Lyons and Huston, 2006).

The Archean basement of the NAC outcrops in the Pine Creek and Tanami regions with ages between 2670 Ma – 2500 Ma (Lyons and Huston, 2006). Outside these areas, the Archean basement is rarely exposed, and relationships between cratonic blocks and orogenic belts are obscured by younger Proterozoic and Phanerozoic cover (Cawood and Korsch, 2008). As a result of the limited outcrop, the exact nature of the basement of much of the NAC remains unclear. Vertical accretion by mafic underplating is thought to be possible across most of the NAC (except the Kimberly Craton) during the Proterozoic (Betts et al., 2002). This underplating occurred either during 2300 – 2100 Ma (Wyborn et al., 1998) or 1800 – 1600 Ma (Giles et al., 2002) and may be partly responsible for the formation of a Neoarchean to Paleoproterozoic basement in the NAC.

Basement for the Mount Isa Province has been dated at between 1880 Ma – 1840 Ma (Page et al., 2000). The western part of the Mount Isa Province may be underlain by an Archean protolith based on the presence of zircons dated to 3300 Ma, however it cannot be ruled out that these zircons have been sourced by melting Paleoproterozoic sedimentary rocks with inherited zircons (Bierlein et al., 2008). The older Archean basement may be present in the Mount Isa Province and simply does not outcrop. Alternatively, Archean basement may be absent under some or all of the Mount Isa Province.

There is some evidence that the Mount Isa Province has a different basement to the other parts of the NAC. A seismic velocity study conducted by Finlayson (1982) reports the P-wave velocity at Mount Isa is significantly lower than at Tennant Creek at depths of 25-40 km. A more recent seismic tomography study by Fishwick et al. (2005) also suggests that there is a difference between most of the NAC, which is underlain by Archean lithosphere, and the Mount Isa Province. Analysis of Archean inheritance from geochronology data across the NAC also suggests a difference in inherited ages between Mount Isa Province and terranes to the west (Scott et al., 2000, Figure 9). Considered together, evidence suggests there may be a difference in the nature of basement between the Mount Isa and Tennant Creek regions. Such a difference could be explained by a suture formed during accretion of the Mount Isa Province onto the proto-NAC.

A number of sutures have been postulated within the NAC. Current tectonic interpretations consistently define a boundary on the western edge of the Mount Isa Province (Betts et al., 2016; Korsch and Doublier, 2016; Spampinato et al., 2015), although not all provide an interpretation of the structure. A change in the character of the potential field data from the dominantly NS-trending in the Mount Isa Province to the WNW- to SE-trending character of the Tennant Creek Province is used to interpret the location of the boundary (Betts et al., 2016; Korsch and Doublier, 2016; Spampinato et al., 2015). Little is known about the boundary other than it is likely to be pre-1870 Ma in age (Betts et al., 2016; Bierlein and Betts, 2004) and may dip to the east (Gessner, 2011; Withnall et al., 2013). Bierlein and Betts (2004) reject the Mount Isa Fault as the location of this crustal suture in the outcropping Mount Isa Province but postulate that one exists further to the west along the May-Downs Fault Zone. Despite this finding, the southern extension of the Mount Isa Fault (also named the Rufus Fault (Withnall et al., 2013)) has been interpreted as the boundary of the Mount Isa Province (Spampinato et al., 2015).

Three other sutures of relevance to the Mount Isa Province are the Willowra Suture (Betts et al., 2016; Goleby et al., 2009), the Final Nuna Suture (Nordsvan et al., 2018; Pourteau et al., 2018) and the Gidyea Suture (Betts et al., 2016; Blaikie et al., 2017; Korsch et al., 2012). These structures (Figure 3.2) do not have direct bearing on the study area, but do offer insight into characteristics used to infer Proterozoic sutures (Figure 3.2). The Willowra Suture was identified through deep crustal seismic as a reversal of the dip in major reflective packages and a significant thickening of the crust (Goleby et al., 2009). It is a south-dipping feature which bounds the northern extent of the Arunta Province and represents its contact with the proto-NAC (Betts et al., 2016). The Willowra Suture is interpreted to be approximately 1865 Ma (Goleby et al., 2009). The eastern extent of this structure is interpreted from regional magnetic and gravity coverage but has low reliability (Korsch and Doublier, 2016).

The Gidyea suture zone has been interpreted from deep crustal seismic along the eastern margin of the Mount Isa Province and is characterised by a bland region of reduced seismic reflection, a Moho offset, and an MT resistivity anomaly (Korsch et al., 2012). It is a west-dipping feature interpreted to record the collision between the Numil Terrane and the basement rocks of the Mount Isa Province however its age is unresolved (Betts et al., 2016). The combined work of several recent studies suggest that it may have been active between 1740 – 1710 Ma (Blaikie et al., 2017; Nordsvan et al., 2018; Pourteau et al., 2018). The Carpentaria Conductivity Anomaly is postulated to be related to the Gidyea suture (Wang et al., 2014)

Finally, the Nuna Suture is a west-dipping feature that has been identified based on Lu-Hf geochronology and P-T history estimation, comparison of detrital zircon spectra, and paleo current analysis, supplemented with seismic interpretation (Nordsvan et al., 2018; Pourteau et al., 2018). The seismic displays a reversal in dip of major packages across the suture and has an age of approximately 1600 Ma.

The large number of tectonic events the NAC has been subject to post-cratonisation further complicate identification of structures formed during amalgamation. A possible plume track has been identified in the Eastern Succession of the Mount Isa Province at approximately 1500 Ma (Betts et al., 2009), but no plume-related volcanism or intrusive units are recognised in the project area. Crustal thickness is approximately 45 km across of the project area, and deepens to over 50 km to the east of the project area (Kennett et al., 2018).

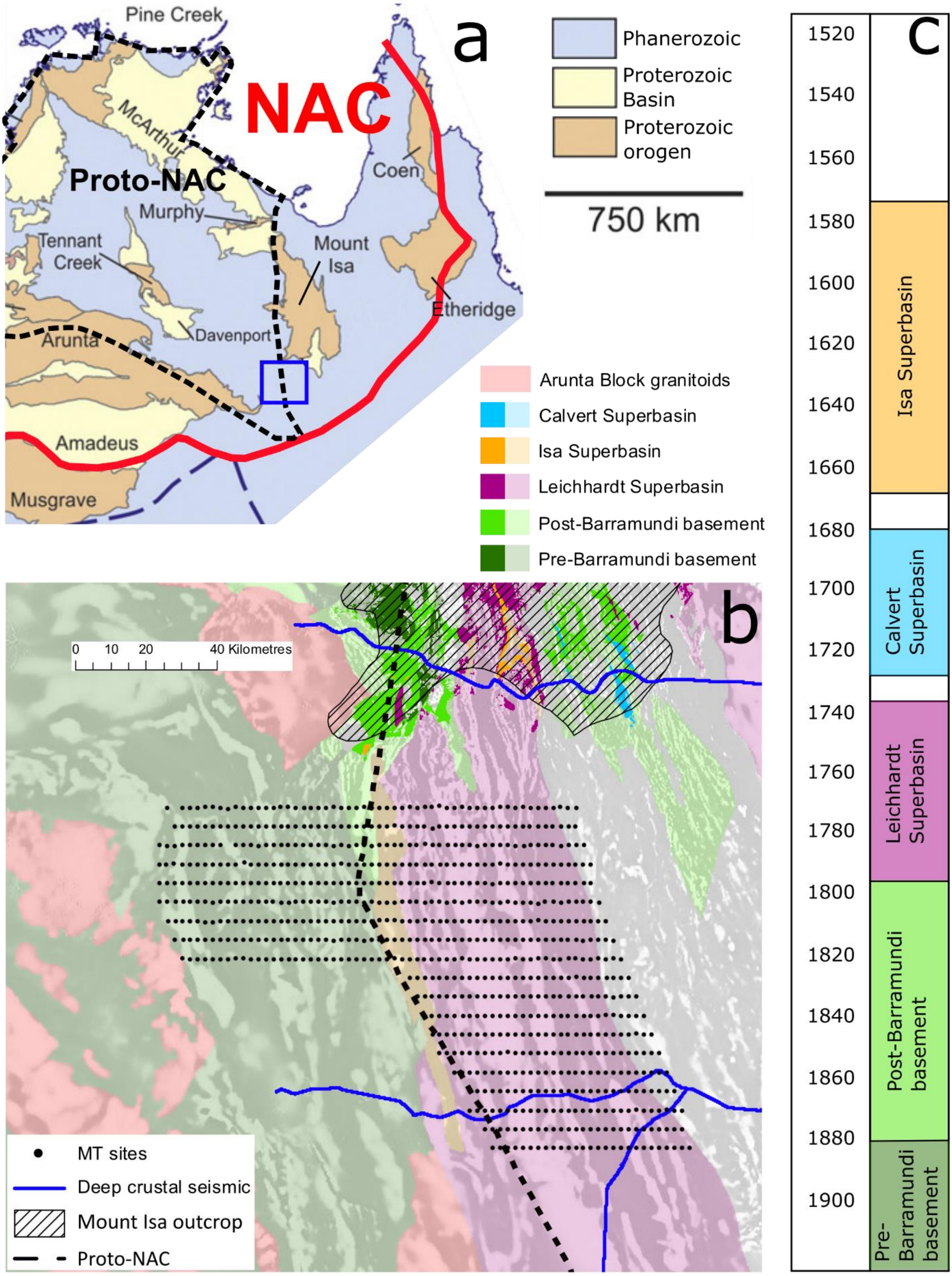

Figure 3.1. Project location and solid geology of the Mount Isa region. a) Major elements of the North Australian Craton, interpreted margin of the NAC marked in red; project area in blue (modified after Korsch and Doublier, 2016; proto-NAC outline after Betts et al., 2016). The proto-NAC boundary is interpreted as the western extent of the Mount Isa Province. b) Location of project MT dataset compared to the proto-NAC boundary, and outcropping and interpreted extents of the Mount Isa superbasins and other significant sequences, overlain on the first vertical derivative of the TMI data (solid geology modified after GSQ, 2011). Outcropping sections indicated by solid colours, solid geology interpretation indicated by transparent colour. Location of deep crustal seismic lines also indicated in blue. c) Timing of major Mount Isa Province packages (modified after Withnall et al., 2013). Colour scale applies for b and c.

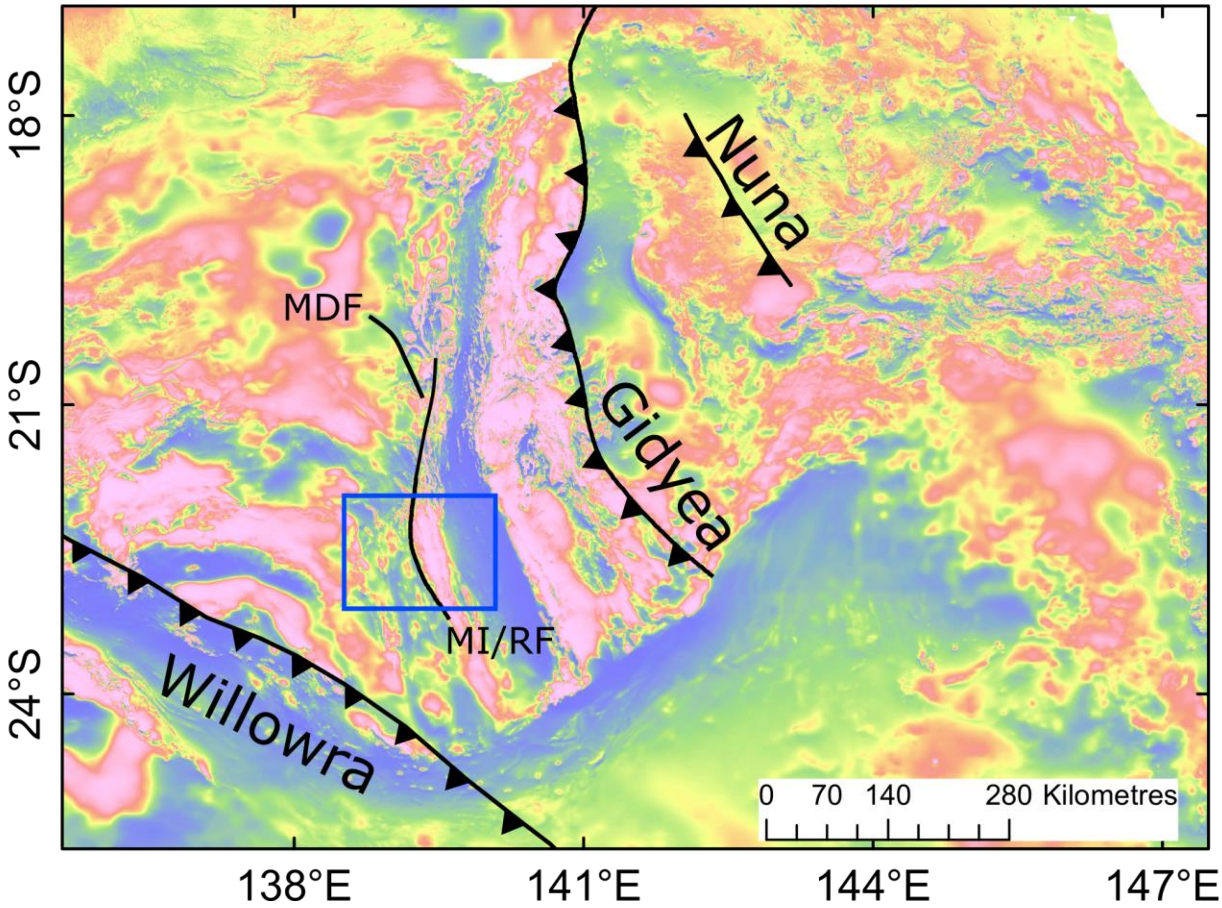

Figure 3.2. Suture locations from literature overlain on the TMI data. The project area is indicated in blue with potential suture investigated by this study marked. Willowra location after Betts et al., (2016) and Goleby et al., (2009); Gidyea location after Korsch et al., (2012); and Nuna Suture after Nordsvan et al., (2018) and Pourteau et al., (2018). MDF – May Downs Fault; MI/RF – Mount Isa/Rufus Fault

3.1.2 Sources of resistivity anomalies in the crust

Crystalline crust with low porosity will have a high electrical resistivity (Evans, 2012). Where low-resistivity features are present, an understanding of potential sources of reduced resistivity is vital to interpreting specific features and general trends. Sources of electrical resistivity vary with depth in the crust and are reliant on four primary mechanisms: ionic conduction in fluids, compositional differences (e.g. elevated iron and sulphur concentrations), silica semi-conduction aided by elevated hydrogen and hydros mineral concentrations and the presence of graphite (Selway, 2014; Yang, 2011; Yang et al., 2012). Silica semi-conduction and formation of graphite are dependent on temperature, with reduced resistivity associated with higher temperatures (Selway, 2014). Graphite can produce large reductions in electrical resistivity when it is present as interconnected sheets or films, such as grain-boundary graphite (Mathez, 1987), however these structure are thought to be unstable outside the temperature range of 600–900 °C (Selway, 2014). Despite this limitation of grain boundary graphite films as a source of conductivity, graphite bearing rocks are known present in the broader Mount Isa Province (Withnall et al., 2013) and may make a significant contribution to low-resistivity anomalies.

Recent work suggests that other compositional variations may contribute to low-resistivity features in crustal settings. Total alkaline ion concentration has been demonstrated to produce lowered resistivity in gneissic and granitic rocks; an effect which increases with temperature, i.e. at higher temperatures the same composition rocks had lower resistivity (Dai et al., 2018).

Based on the current geotherm for the Mount Isa Province (Gessner, 2011), the contribution of hydrogen content to lowered resistivity will be significant at depths greater than approximately 10–15 km (at temperatures above 200–300 °C (Selway, 2014)). Ionic conduction is expected to make a significant contribution to crustal resistivity in the upper 12 km, above the brittle ductile transition where fluids can be hosted in pore spaces and fractures. Compositional differences are expected to be a primary source of variability in resistivity for much of the project area. In addition to variation in hydrogen, iron and alkaline ion concentrations previously discussed, consideration must be given to the presence of sulphide bearing deposits and graphitic shales which are present across the broader Mount Isa Province (Withnall et al., 2013) and would cause localised low-resistivity anomalies in MT data. The temperature (Kennett et al., 2018) and stress fields (Rajabi et al., 2017) for the project area are consistent, eliminating these factors as contributors to lateral variations in resistivity, although the impact of high-heat producing elements cannot be ruled out.

3.2 MT dataset

The MT dataset used for this study was collected in 2014 in a collaboration between the Geological Survey of Queensland and Geoscience Australia. A total of 809 stations with a frequency range of 3 x 10^{-3} to 3000 s were collected at 2 km stations spacing in an east-west orientation, separated by 5 km in a north-south direction (Figure 3.1b).

Understanding the dimensionality and strike of an MT dataset is vital in properly parameterising inversion, especially in the case of 2D inversion (Chave, 2014; Simpson and Bahr, 2005). Data were assessed for geoelectric strike and dimensionality with the MTpy implementation (Krieger and Peacock, 2014) of the phase tensor method (Figure 3.3; Bibby et al., 2005; Caldwell et al., 2004). Induction arrows are also plotted using the tipper data in the Parkinson convention (Parkinson, 1959) such that in-phase (or real) arrows point towards low-resistivity features (Figure 3.4).

Data with periods less than 1 s are predominantly 1D or 2D, except in the west (Figure 3.3). The data have a consistent strike of N85°E for periods between 0.1 s and 100 s. At periods longer than 100 s, data are significantly 3D (Figure 3.3) and have a strike of N5°E. The induction arrows at periods above 1000 s also indicate that the data are sensitive to a low-resistivity feature outside the bounds of the survey to the southeast, and data between 8 and 120 s are sensitive to a low resistivity feature to the south (Figure 3.4). The feature to the south is currently unknown, but may be related to thickening of conductive Eromanga Basin sediments to south of the project area (Cook et al., 2013; Spence and Finlayson, 1983). The feature to the southeast is likely to be the Carpentaria Conductivity Anomaly (Chamalaun et al., 1999; Crowe and Milligan, 2015; Lilley et al., 2003). The dataset has a high degree of homogeneity at most periods with structures indicated within the data array only at periods less than approximately 120 s (Figures 3.3 and 3.4). Based on the outcomes of the preliminary data analysis, 3D inversion is required to adequately model data with periods longer than 1 s, particularly in the west of the project area. The longer period data is also expected to be difficult to model due to features outside the data array (Figure 3.4).

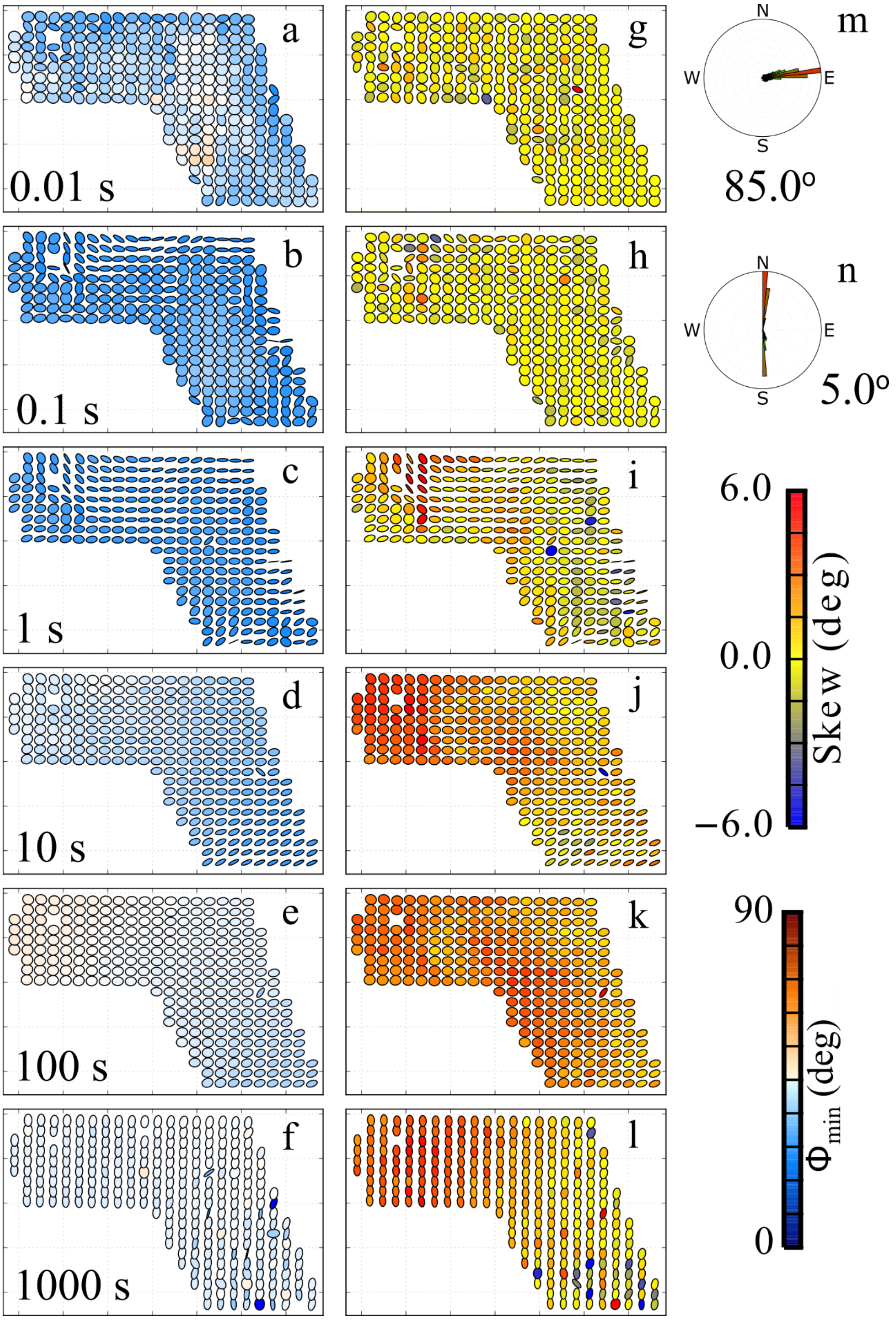

Figure 3.3. Summary of phase tensor plots for MT dataset. All plots generated with MTpy (Krieger and Peacock, 2014). a-f) phase tensor ellipses coloured by minimum phase. Minimum phase values less than 45° indicate resistivity increasing with depth, while minimum phase values greater than 45° are indicative of resistivity decreasing with depth. g-l) phase tensor ellipse coloured by skew; Circular ellipses with low skew values are indicative of 1D data, distorted ellipses with low skew values are indicative of 2D data, and ellipses with red or blue colouration indicate 3D subsurface structure. m) Strike analysis for periods between 0.1 and 10 s. n) Strike analysis for periods between 10 and 1000 s. Displayed ellipses were generated using one third of the total BBMT sites for clarity.

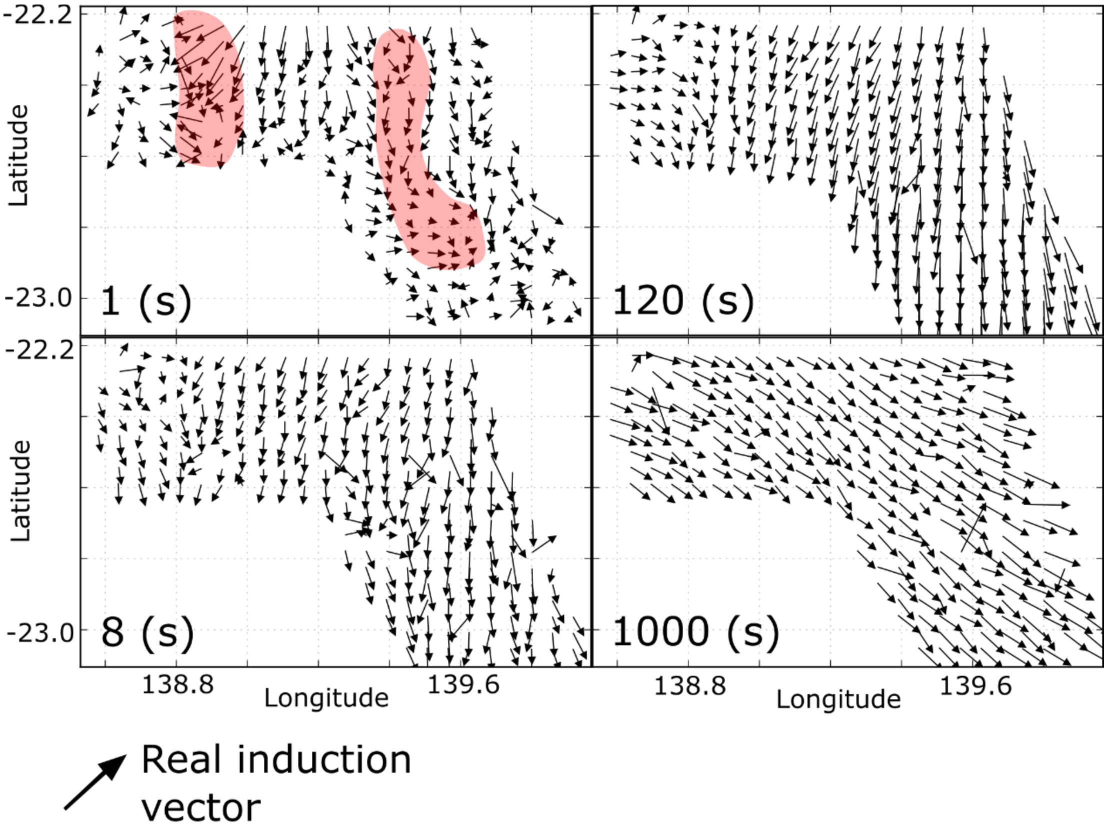

Figure 3.4. Induction arrows for periods between 1 and 1000 s. Variations in resistivity inside the project area are present to 120 s; represented by reversals in induction arrow direction within the data array. Induction arrows at between periods of 8 s and 120 s are sensitive to a low-resistivity feature to the south of the data array for sites in the east. Data at 1000 s are sensitive to a feature the southeast outside the project area for the entire array. Red shaded areas indicate induction arrow reversals consistent with location of low-resistivity inversion in the 3D inversion (C1 and C3). Displayed induction arrows were generated using one third of the total BBMT sites for clarity.

3.3 Inversion parameterisation

ModEM3D (Kelbert et al., 2014) was used to generate all inversions. Initial inversion testing was conducted on a sub-sampled dataset with 10 km station spacing and a reduced bandwidth of 1 – 1000 s (see Figure 3.5). Error floors for 3D inversion were 5% of $|Zxy\ Zyx|^{1/2}$ for all Z components and 0.03 for the vertical transfer function. A minimum of 100 km of padding was added around the margins of the area of interest in the x and y directions to limit the presence of edge effects; the total depth of the models was 1100 km, with the vertical mesh size increasing by a factor of 1.2 with depth. The top of the mesh was finely discretised to account for near-surface distortion, as suggested in Meqbel et al. (2014). Final mesh size was 82 x 106 x 46 for a total of approximately 400,000 cells. Variations in starting model, smoothing covariant and inverted data component were tested (see Table 3.1 for additional inversion parameters). A total of 15 different parameters setups were tested (see inversion parameter table in Appendix 1 and inverted model nRMS).

A preferred model was selected from the initial inversion testing suite and used as a starting model for a subsequent higher resolution inversion (FINE inversion). The FINE mesh size was 1790 m and 600 m in the x and y directions respectively, a first z layer thickness of 20 m, increasing in thickness by a factor of 1.2 with depth. The FINE inversion was run using the result of the GEO3 model as the staring model. Shallow features identified as inversion artefacts were present in the top 10 km of the GEO3 model (see shallow heterogeneous features in Figure 3.6 which plot between MT sites). To avoid these feature becoming embedded in the FINE inversion, the top 10 km of the GEO3 model was replaced with a 500 Ωm layer before mesh refinement.

All data sites were used for inversion, but the bandwidth was reduced to 0.004 – 10 s with the same error floors as the original inversion. The total number of cells was 1,834,300 including padding, with dimensions of 850 km in east-west and north-south directions, and 1100 km deep.

Table 3.1. Inversion parameters for five inversion presented in this manuscript. Starting model of 100 or 1000 indicates the respective resistivity half space as a starting model. See Figure 3.5 for GEO3 starting model plot. Data type indicates whether impedance data (Z) and/or indicates tipper data (T) were used for the inversion. Covariance is a smoothing parameter and is listed in x, y, z directions according to ModEM standard orientations (Kelbert et al., 2014).

Model name	Dataset		Data type		Starting model				Covariance		RMS
	10 km	All	Z	T	100	1000	Geo	Other	0.2,0.2,0.2	0.1,0.4,0.2	
UNC100	x		x	x	x				x		1.13
UNC1000	x		x	x		x			x		1.05
GEO3	x		x	x			x		x		1.05
COVX	x		x		x					x	1.04
FINE		x	x					x	x		1.46

FINE model - started from GEO3 result with top 10 km reset to 500 Ω·m

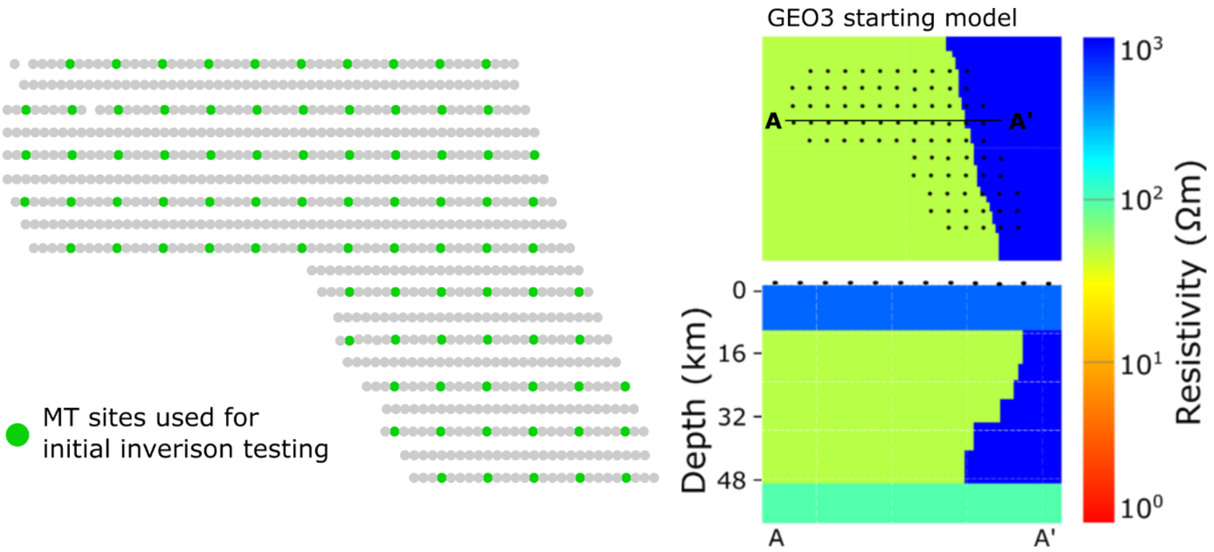

Figure 3.5. Sites used for initial inversion testing and GEO3 starting model. GEO3 starting model map view at 11 km (top) and profile view (bottom). The GEO3 model was created from information available in the deep crustal seismic line GA14-CF3 and potential field data. The laterally extensive upper crust, west-dipping lower crustal feature and the thickness of the crust were taken from the seismic, while the absolute resistivity values were estimated using results from other initial inversions. Absolute resistivity values for GEO3: above 11 km resistivity of 500 Ωm; lower crust west 50 Ω·m; lower crust east 5000 Ω·m; and 100 Ω·m below 48km. Block resistivity values were assigned based on early unconstrained inversion results.

3.4 Results

3.4.1 Initial MT inversion testing

The 3D models obtained from a variety of parameters have a high degree of variability (Figures 3.6 and 3.7). Only four of the total fifteen models tested are presented here, chosen to represent the diversity of inverted features returned across the full suite of models. Between one and three low-resistivity features where produced (C1, C2 and C3). A fourth low-resistivity feature (C4) was present in only two models, and appears to dependant on 10 Ωm stating half space, and for these reasons are not discussed further. Of the three main low-resistivity features, only C1 was present in all inversions. The C3 feature was present in most models, while the C2 feature was more variable, only present in UNC100 for the presented subset and less than half of all models (Figure 3.6c). A single high resistivity feature (R1) was returned by all inversions, however the size, location and absolute resistivity value of the feature is variable (c.f. Figure 3.6c and d).

The overall nRMS misfit for all models was low (Table 3.1). Inspection of nRMS distribution across periods and data components for all models suggests that the tipper data is poorly fit compared to the impedance data, and that the fit for both impedance and tipper data deteriorates at short (<5 s) and long (>400 s) periods (Figure 3.6). The inability of these initial testing inversions to fit data shorter than 4 s is interpreted to be near-surface heterogeneities that are not captured by the mesh spacing. On the other hand, at long periods the misfits are high due to the low-resistivity features outside the gridded area. The top 10 km of these initial models is considered to be unreliable due to the station spacing and the character of inversion features returned across the suite of models; namely low-resistivity features populated between sites at shallow depths, generally viewed as inversion artefacts.

The COVX inversion achieved an nRMS misfit of 1.04. All components fit the data well between periods of 3 s and 500 s with misfits increasing outside this range (Figure 3.6a). C1 and C3 are both present in the COVX model (Figure 3.6a), however the resistivity of these features is higher than other models, leading to the features being largely absent from the isosurface (Figure 3.7). C3 is present from approximately 10 km depth and C1 present from 20 km.

UNC100 has three low-resistivity features at approximately 15 km depth which have variable intensities (C1, C2, C3; Figure 3.6c). C3 is an elongate feature with an approximate north-south strike direction while C2 has the highest conductivity of the three features and has a slightly more westerly strike than C3 (Figure 3.7). C1 is a broad area of moderately high conductivity which deepens to the north-west (Figure 3.7). C1 and C2 become a single feature in the north-west of the survey area (Figure 3.7). The fit of the tipper data for this inversion is very poor, particularly in the southeast. The Tx component also has higher misfit with the period range of 10 – 200 s.

The overall nRMS misfit for UNC1000 was 1.05, with a tipper nRMS of 0.99 and an impedance nRMS of 1.15. A single, broad lower crustal conductor is present in the UNC1000 model (Figure 3.6d). This feature is in approximately the location of C1 in the other models but may be an amalgamation of C1 and C2. The cross section plots of the UNC1000 model have subtle features in the middle of the survey area which may be C2 and C3. They are not well developed and it is unclear what, if any, impact they have on overall model nRMS. In addition to these conductors a number of very small, shallow conductors are evident in the isosurface (Figure 3.7). Some of these features coincide with the location of C3 in other models but they generally occur between MT sites, consistent with the behaviour of inversion artefacts.

The GEO3 inversion achieved a total nRMS of 1.05. The C1 and C3 features are both present in the final model for GEO3 (Figure 3.6b). C3 in this model has the largest expression of any of the coarse models, while the C1 extent is among the smallest of any model (Figure 3.7). The influence of the starting model is clearly evident in the final inversion features for GEO3 (compare Figure 3.5 and 3.6b). The tipper and impedance nRMS is low for this model and is generally evenly distributed across the array, with a slight increase in the south. The long period misfit for this model is also relatively low (Figure 3.6).

From the suite of initial inversion models the GEO3 model was selected for use as the staring model for the FINE inversions. This model was selected on two primary criteria:

1. Even distribution of nRMS misfit across sites, data components and periods compared to other inversion results
2. Presence of C1 and C2 low-resistivity features, consistent with the data (Figure 3.4).

The GEO3 starting model features were also developed with consideration of the features present in the 14GA-CF3 seismic line, meaning they have independent constraint on inversion features lacking from other models.

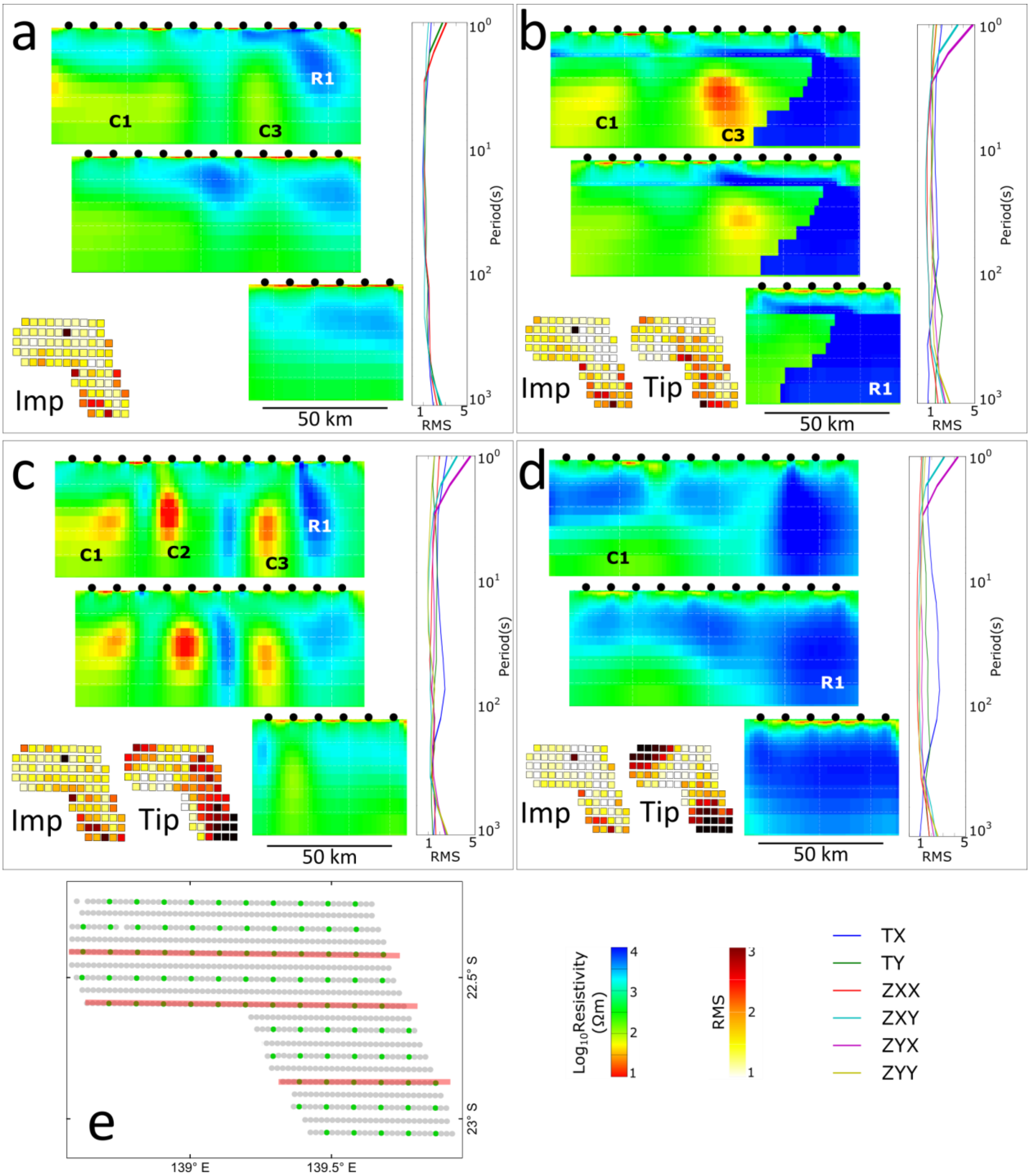

Figure 3.6. Four representative inversion results from initial inversion testing. Sections for each model extracted along red lines in e; all profiles plotted from 0 km to 50 km depth. Each panel has RMS per site for impedance (Imp) and tipper (Tip) data components and RMS vs period for each data component. a) COVX inversion b) GEO3 inversion c) UNC100 inversion d) UNC1000 inversion e) location of displayed profiles, green sites are the 10 km site spacing dataset, and grey sites are the full dataset.

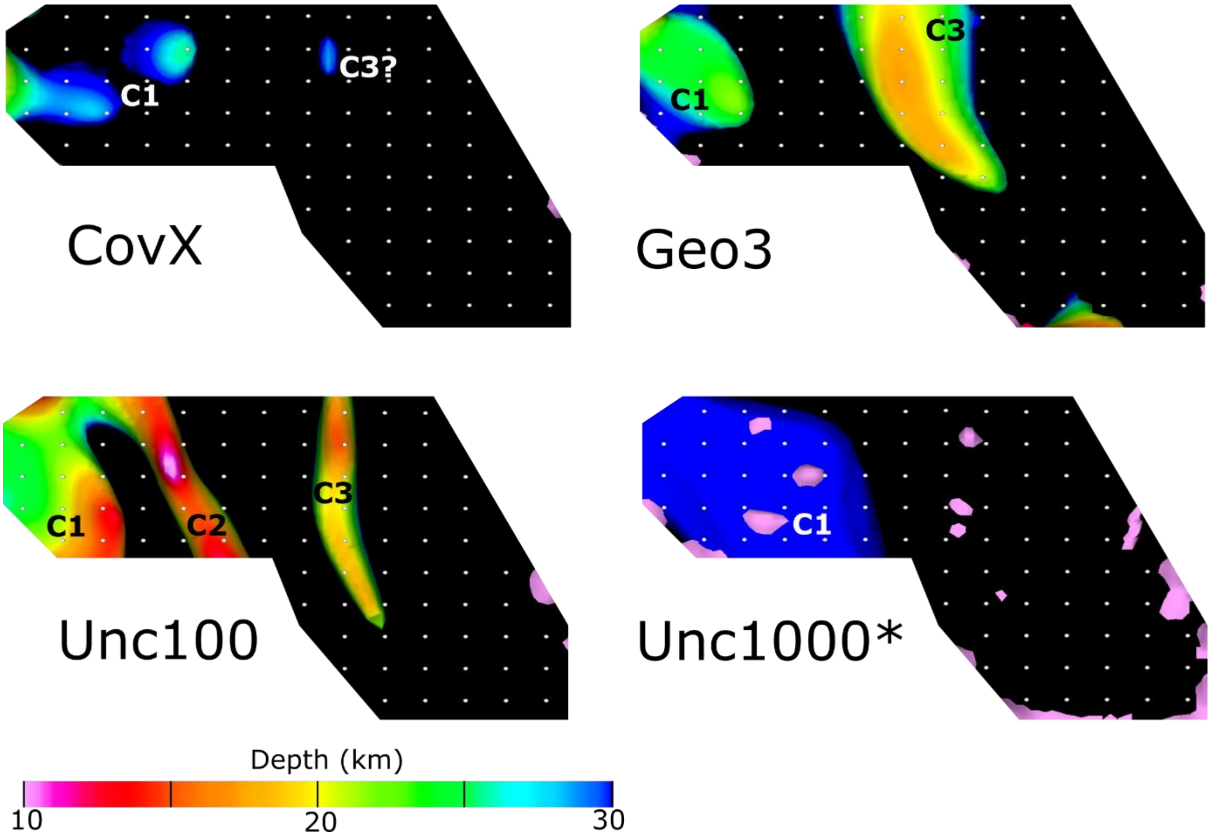

Figure 3.7. 100 Ωm isosurfaces calculated for initial inversion testing models. Areas within the isosurfaces indicate low-resistivity zones. Isosurfaces are coloured by depth and labelled C1-C3 in each plot, with MT sites as white dots. Black areas indicate an absence of features with a resistivity less than 100 Ωm between 5 km and 50 km. UNC1000 model display 500 Ωm isosurfaces as there are no features with resistivity less than 100 Ωm within the array.

3.4.2 High resolution MT inversion

The GEO3 model was selected and its mesh refined after removal of structure from the top ten kilometres of the coarse inversion results. These shallow features were under-constrained by the original inversion and consisted of low-resistivity features populated between sites, generally viewed as inversion artefacts. The FINE inversion achieved an nRMS of 1.46 and results are displayed in Figure 3.8. The nRMS increases at short periods, likely due to insufficient mesh discretisation. Other than an increased nRMS at short periods the misfit evenly distributed across data components, sites and periods, indicating that the model is a reasonable fit to the observed data (Figure 3.8).

The C1, C3 and R1 features from the starting model are all still present, although absolute resistivity and size of C1 and C3 has been modified (c.f. Figure 3.8 and 3.6b). R1 is unchanged from the GEO3 model. Two new resistive features are present in the FINE model, a high-resistivity trough between C1 and C3, labelled R2; and a laterally continuous moderate-high resistivity feature between 2 km and 12 km present across much of the project area (R3). The R2 feature trends north-south and is present to approximately 40 km depth. R3 is less pronounced in the northwest and southeast of the project area. Above 2 km a shallow moderate- to low-resistivity feature (C5) is present across the entire project area, thickening to the south.

Comparison of the resistivity distribution of the FINE and GEO3 inversion results indicates that the deeper parts of the model were largely unchanged by the FINE inversion (Figure 3.9). This is consistent with the use of GEO3 as a prior model and exclusion of the longer period data from inversion parameterisation. The notable exception is insertion of the R2 feature in the mid to lower crust which has a clear impact on the scatter plot distribution (Figure 3.9a). Two other features of note are present in Figure 3.9a, labelled i and ii. Feature i corresponds to part of the model that was overfit in the GEO3 inversion but not the FINE inversion. The very high resistivity present in the ii box in Figure 3.9a indicate that part of the model is overfit in both the GEO3 and FINE inversion. These overfit areas of the model are contained within the R1 feature, suggesting that the a priori dipping fault may be leading to overestimation of the resistivity of R1 in the FINE model.

The histogram distribution of the difference between the models has a significant right skew indicating the resistivity of the FINE inversion is higher overall than the GEO3 result (Figure 3.9b); consistent with presence of R2 and R3 in the FINE model. The shallow parts of the two models display large variability, consistent with the poorly constrained nature of the shallow GEO3 features (Figure 3.9a).

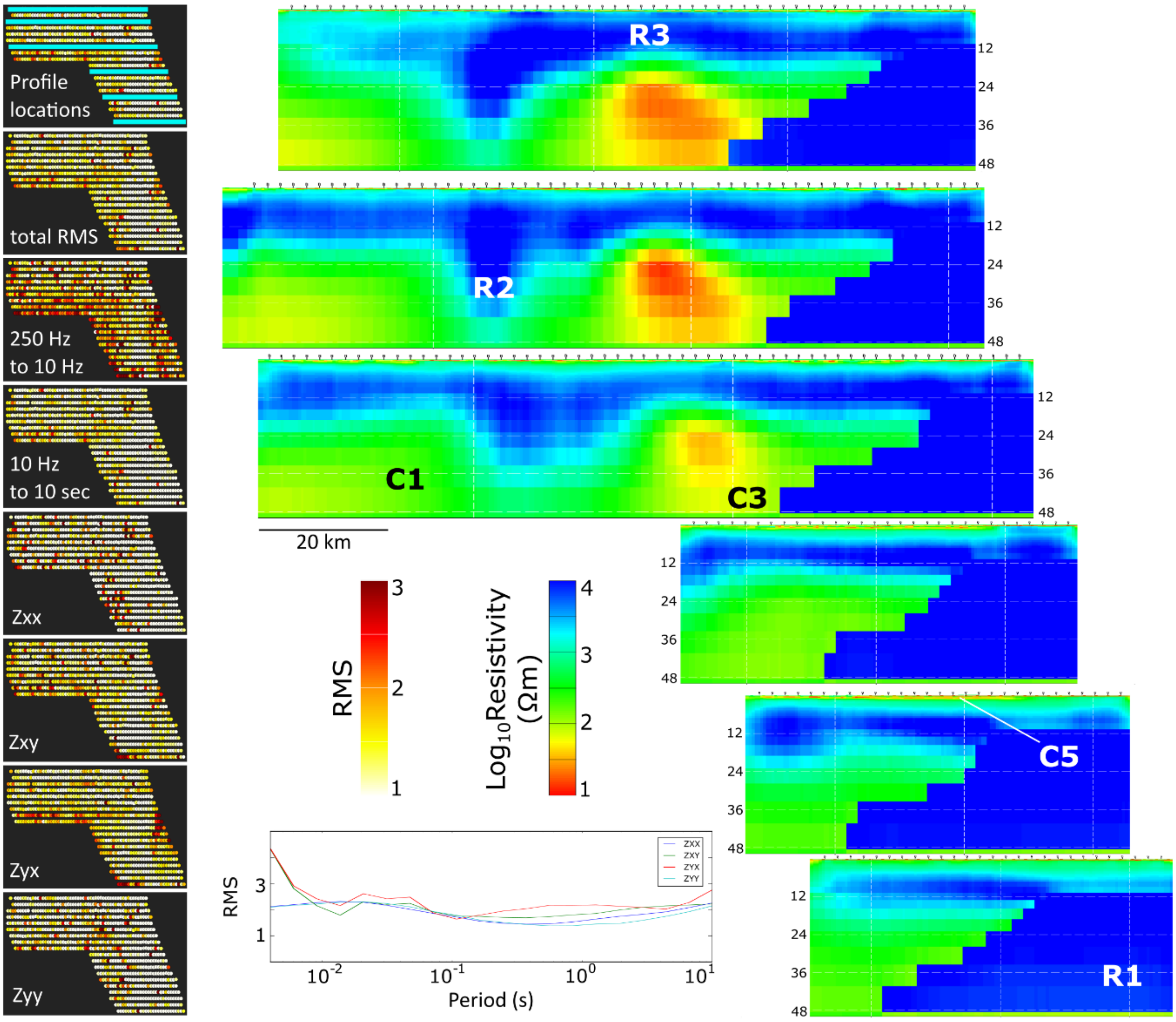

Figure 3.8. Model profiles and RMS plots for the FINE inversion. The profiles are extracted to a depth of 50 km and the same colour stretch applies to all RMS plots.

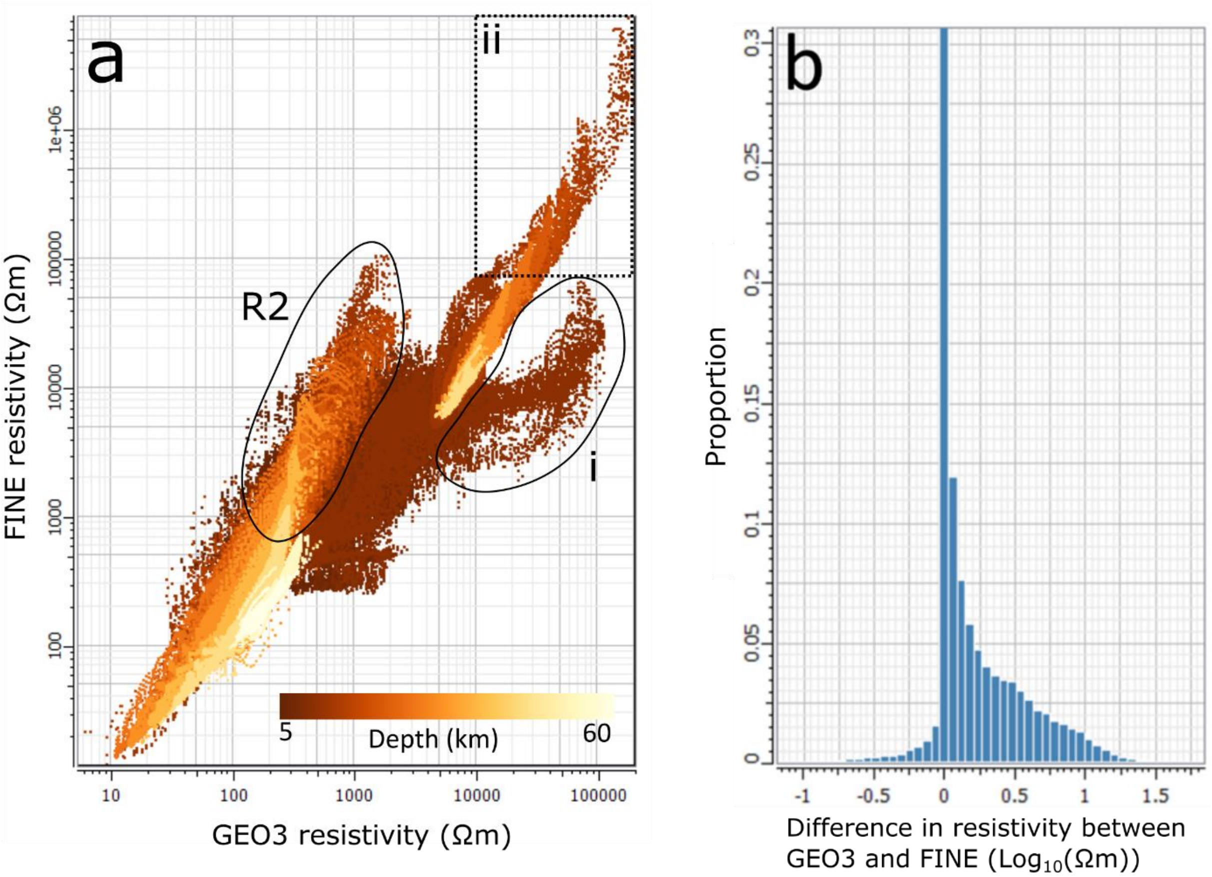

Figure 3.9. Cross plot and histogram distribution comparing resistivity distributions for the GEO3 and FINE inversions. a) Cross plot of resistivity values for GEO3 and FINE inversions coloured by depth. Deeper parts of the model, indicated by lighter colours, are similar between the two inversions. Resistivity values in the shallow parts of the model display greater scatter, signifying differences between the two models. Features R2, i and ii discussed in text b) Histogram distribution of difference in resistivity between GEO3 and FINE inversion. Resistivity extracted per mesh cell of the FINE inversion.

3.4.3 Seismic interpretation

There are no published interpretations available for 14GA-CF3, so a basic interpretation was constructed for the section of the line which is coincident with the MT model (Figure 3.10).

A number of features are present in the seismic data. The west dipping lower crustal feature used in generating the GEO3 starting model is present in the central part of Figure 3.10 b. The upper extent of this feature is not clearly defined in the seismic data and is marked with a dashed line. The Palaeozoic sedimentary basin cover is visible at the top of the section, marked in pink. Under this is a discontinuous, sub-horizontal layer; comparison to the solid geology interpretation (GSQ, 2011) suggests this may be part of the Leichhardt Superbasin, although it extends further west than the previously interpreted extent (Figure 3.1b). Beneath that feature there are very few seismic reflectors until the mid-deep crust. The Moho deepens to the east, a trend also present in the interpretation by Kennett et al. (2018). On the western end of the profile, an area of high reflectivity is present along the Moho with complex internal structure; truncated by the west dipping structure. The lower crust reflector reappears at the eastern end of the profile, where it displays significant uplift and faulting, and is no longer at the base of the crust (Figure 3.10b). Mafic underplating has been invoked as a mechanism for generating high seismic reflectivity in the lower-crust elsewhere in the NAC (Cawood and Korsch, 2008), and represents a possible interpretation for this feature.

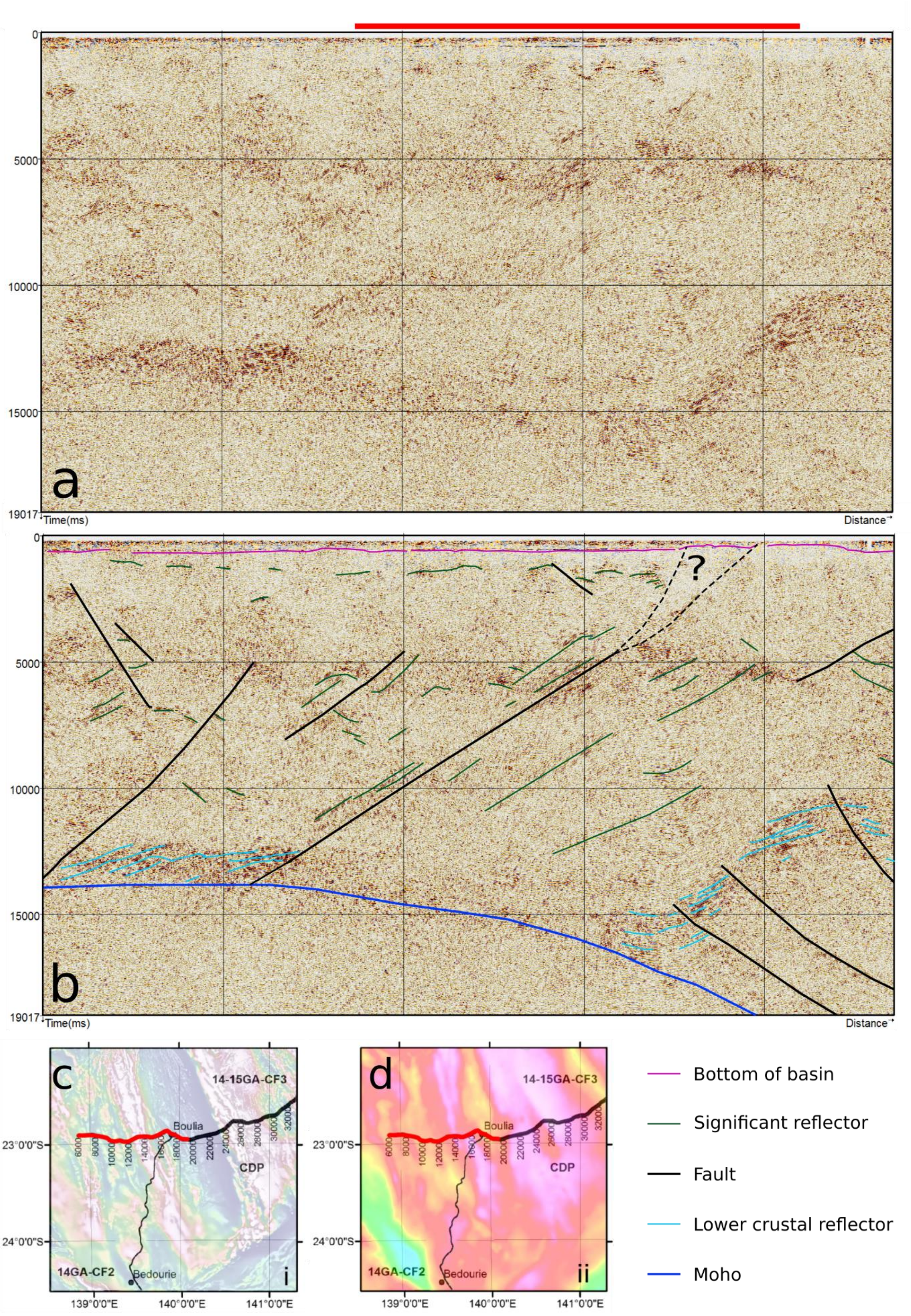

Figure 3.10. Interpretation of 14GA-CF3 deep crustal seismic. a) Un-interpreted seismic data to 20 seconds two way travel time; spatial extent of MT array indicated in red; see Figure 3.1b for MT and seismic location map view comparison. b) Interpreted seismic line with major west dipping fault and lower crustal reflective packages. Uncertain upper extension of the west dipping fault is indicated as a dashed line. Post stack migration seismic data displayed, section represents a cropped extent, highlighted in red on location maps c and d. c) Location map over TMI data. d) Location map over isostatically corrected Bouguer gravity.

Additional deep crustal seismic data is available to the north of the project area (07GA-M6; Figures 3.1b and 3.12c). Recent interpretations of this data have not included the lower crust (Gibson et al., 2016). The lower 10 seconds of this seismic profile does not display any significant structure and the Moho is not visible. It is difficult to determine if the lack of reflectors in the lower 10 seconds of the M6 line is due to geological factors or a result of poor data quality. Comparison of seismic acquisition parameters suggest there is likely to be poorer resolution in the deep section of the M6 line than the CF3 line due to a smaller Vibroseis, lower fold and shorter array offsets (Table 3.2), but it is unclear whether this difference is enough to account for the lack of reflectors in M6.

Table 3.2. Comparison of survey parameters from CF3 and M6 deep crustal seismic lines.

Parameter	CF3	M6
Source weight	60,000 lbs	50,000 lbs
Nominal fold	75	60
Distance between VPs	80 m	80 m
Distance between recording sites	20 m	40 m
Base frequency	6-64 Hz	6-64 Hz
Spread offset	6 km	4.7 km

3.5 Discussion

3.5.1 Inversion features

A limitation of any multiphase inversion approach, is that artefacts produced in the first phase of inversion will be embedded in the final inversion, through the prior model. Model artefacts are not limited to a multiphase inversion, as standard unconstrained inversions can also produce artefacts in areas where there is limited data sensitivity (Rodi and Mackie, 2012). By considering the results of the initial testing inversions and the final FINE inversion together, we differentiate between the features which are robustly determined by the data and those which are artefacts or under-constrained during the inversion process. Model artefacts are defined as any features which are produced in a single inversion with no corresponding structure in other inversion results, or independent datasets. Under-constrained features appear in more than one inversion but have different geometries or extents, or are well supported by independent data, e.g. seismic data.

The initial inversion testing performed on the MT dataset used in this project indicate a wide variety of inversion models are compatible with the data. The preferred FINE model has three low-resistivity features (C1, C3 and C5) and three high-resistivity features (R1, R2 and R3). The shallow low-resistivity feature above 2km (C5 in Figure 3.8) is due to the presence of the Eromanga and Georgina Basins which overly the crystalline basement in the project area (Ambrose et al., 2001; Cook et al., 2013; Kruse et al., 2013). These basins thicken to the south and west and are visible in the FINE inversion results (Figure 3.8). Examined in detail, C5 has poor lateral continuity. While the data contains frequencies high enough to provide information about the shallow feature, the site spacing pf 2 km is too coarse to appropriately model the subtleties of the feature. It is possible that increasing the lateral smoothing constraints or other inversion parameters would improve the continuity of C5. Additional inversions would be required to better capture this feature but because it is not of central importance to the aims of this study no additional work was undertaken to optimise C5.

Beneath the low-resistivity basin feature the project area is almost uniformly resistive (values over 5000 Ωm) to a depth of approximately 10 km (R3 feature in Figure 3.8). The exception to this trend is in the northwest and the southeast, where the resistivity between 2 km and 10 km is closer to 1000 Ωm (Figure 3.8). While both trends may reflect actual changes in crustal resistivity, in the southeast the lower resistivity of the crust between 2 km and 10 km is suspicious as it directly overlies the resistive lower crustal block present in the starting model (R1). It is not possible to eliminate the possibility that lower resistivity in the upper 10 km of the model in this area is compensating for an inappropriately high resistivity below 10 km introduced in the starting model. Subsequently low confidence is attributed to this feature.

The low resistivity of this part of the crust implies that large sulphide or graphite bodies have not been imaged by the MT dataset between 2 km and 10 km in the project area. The overlying C5 feature would provide some shielding, so smaller scale anomalies cannot be ruled out, especially as the site spacing in between 2 km and 5 km. Smaller bodies may be present between sites in the shallow basement which would not be imaged by the current dataset. Subtle variations in resistivity, such as those associated with disseminated sulphide are also potentially undetected by the dataset. A comparison of the conductance of C5 and R3 also provides evidence that R3 is likely poorly resolved. For C3 the conductance is around 2000 m/100 Ωm or 20 S whereas for R5 it is around 10000 m/5000 Ωm or 2 S. It will be difficult to resolve parameters of a 2 S layer beneath a 20 S layer.

The R1 feature is present in the lower crust for the eastern part of the model, however it is largely unchanged from the starting model and thus its reliability warrants further investigation. The R1 feature is also present in all models across the initial inversion suite but its extent varies considerably (Figure 3.6). Comparison of the R1 feature between the UNC100, COVX and UNC1000 models suggests it is not present at depth in the south of the project area, where all three models trend towards the resistivity values of their starting half spaces (100 Ωm for COVX and UNC100; 1000 Ωm for UNC1000). Due to its presence in all models R1 is interpreted to be required by the data, however it is likely that the spatial extent is overestimated in the FINE inversion, particularly at depth in the south. Resistive features are conducive to deep investigation depths, so the poorly constrained nature of the bottom of R1 is surprising. A possible explanation for this lack of resolution is the highly conductive Eromanga Basin units (C5), which thicken to the south in the project area (Cook et al., 2013). The presence of the highly resistive R1 feature to a depth of at least 20 km suggests that the crust in this area has low concentrations of hydrous minerals, iron and other elements which would reduce the crustal resistivity.

C1 and C3 are two broad areas of reduced resistivity present below depths of approximately 12 km, which form part of a single broad anomaly in the deep crust. The C3 feature forms a more discrete anomaly and exhibits the lowest resistivity in the project area. The C1 feature is a broad moderate- to low-resistivity feature, whose resistivity decreases with depth in the FINE model (Figure 3.8). The C3 feature is proximal to the R1 feature discussed previously. While we are confident that the feature is required by the data, absolute resistivity maybe be too low in an effort to compensate for the too-large extent of R1 previously discussed. Inspection of the C3 feature in the initial inversion models (Figure 3.6a and d) suggests that it is likely to be a more subtle feature than the one present in the FINE model.

The resistivity of C1 decreases with depth suggesting that there may be a temperature control on the resistivity response for this body. Consequently, the presence of elevated hydrogen or hydros mineral phases are good candidates for the source of the anomaly due to their dependence on temperature. The top of the body is also located at approximately 15 km, consistent with the minimum depths at which hydrogen diffusion is expected to influence resistivity. The top of the C3 feature is also located at approximately 15 km depth, suggesting hydrogen diffusion as a mechanism for this anomaly too. In contrast to C1, C3 is smaller and has a lower absolute resistivity value. Because of the smaller nature of this anomaly, approximately 12-15 km across, a more localised source of low-resistivity is considered possible for this C3 feature. Additionally, the low spatial resolution at depth of the MT technique may cause the inversion feature to appear larger than the actual source of the anomaly. It is possible that the C3 feature is caused by a large heat-producing or hydrous intrusion or alteration associated with large-scale faults.

The final feature from the FINE model is R2, situated between C1 and C3. R2 is essentially a localised thickening of the C3 feature present in the central west of the project area. It is present in UNC100 and COVX models of the initial inversion suite, although less well defined. The feature is only 8 km wide in the north and broadens to nearly 20 km in the south. The likely reason for the poorly resolved nature of R2 in the initial inversion suite is that the subsampled dataset was too coarse to define such a narrow feature. Similar to R1, the low resistivity of R2 suggests a lack of and compositional variations which reduce resistivity in this area. There no correlated thickening of shallow low-resistivity features (C5) and the location of R2, so the variation cannot simply be explained by additional shielding from overlying sediments.

The starting model has significant control on the resistivity features produced during inversion; however the insertion of the R2 feature in the FINE model provides reassurance that new features can still be produced. In contrast to the insertion of R2, the boundary between the C3 and R1 features was unchanged throughout the inversion of both GEO3 and FINE models. This suggests the boundary is permissible by the MT data, but does not imply it is well constrained. While preliminary interpretations based on the MT inversion results alone in possible; comparison of the MT inversion features to other datasets was undertaken to better interpret the structure of the project area.

3.5.2 Comparison to other MT inversions

Data from another MT survey is available in the broader Mount Isa Province (Figure 3.8). These data were collected in 2009 by the Geological Survey of Queensland and have a bandwidth of 0.01 to 1000 s. Two-dimensional inversions are available for the survey to a depth of 20 km (Figure 3.11). Subsequently the reliability of individual features is unknown, but broad trends from this earlier work are likely to be more robust.

Comparison of our new inversion results to the inversion results for the earlier survey indicate resistive feature identified in our study (R1) is part of a broader trend across the central part of Mount Isa to the north (Figure 3.11). There is a tantalising hint that the western end of the MT line immediately to the north of the study area has a low-resistivity feature at the western end which may correspond to the C3 anomaly in our survey. More work would be required to establish the reliability of this features as we are unable to eliminate the possibility that it is simply an edge effect in the other inversion. Unfortunately the spatial distribution of the previous MT sites does not extend to the west of the potential suture boundary in any meaningful way, and thus offers no insight into the extent of the moderate- top low-resistivity features in the western side of our models.

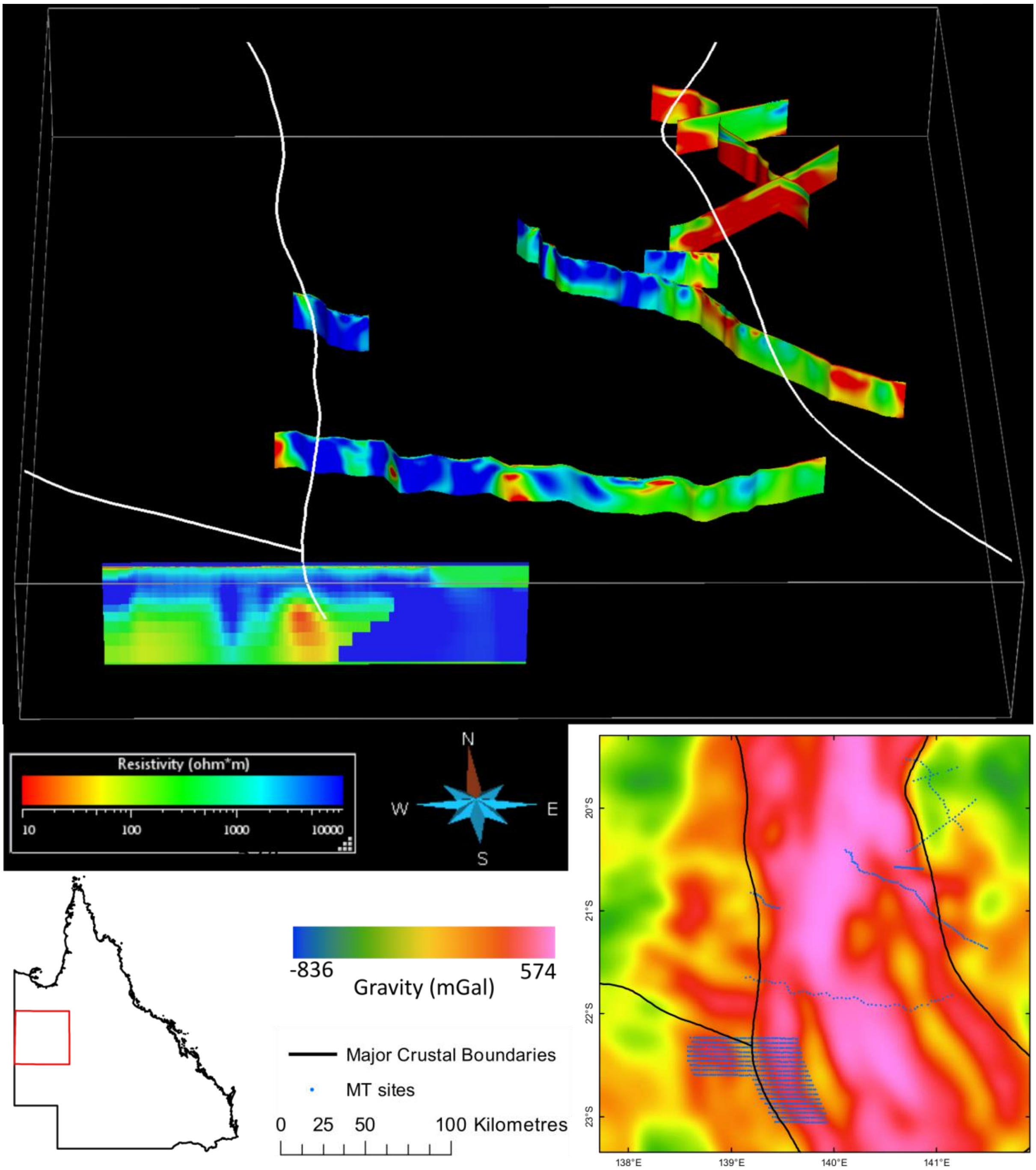

Figure 3.11. Comparison of a section from the new MT model with existing MT models across the Mount Isa region. Section from new 3D model displayed to 50 km depth, other models displayed to 20 km depth. Same colour stretch applies to all sections. The location inset displays MT site location for all sections against low pass filter (wavelength cut-off 50 km) of the isostatically corrected Bouguer gravity, which emphasised deep structure.

3.5.3 Comparison to seismic data

Comparison of the seismic interpretation and two profiles selected from the FINE inversion is provided in Figure 3.12. Figure 3.12a has a MT profile extracted from the FINE model roughly coincident with the seismic traverse, while Figure 3.12b has a section from the middle of the model projected along the geoelectric strike (Figure 3.3m) onto the seismic profile. The comparison is only approximate as the seismic data is presented in time while the resistivity features are plotted in depth. Comparison between the seismic data and coincident part of the resistivity model suggests a laterally continuous upper crust underlain by a mid- to lower-crust which has a of a broad-scale change in resistivity character across the west dipping feature in the seismic (Figure 3.12a). There is a reduction of resistivity to the east of the uncertain upper extent to the west dipping feature, however as discussed previously, the uncertainty associated with this resistivity feature is high.

Analysis of the relationship between seismic and resistivity features in Figure 3.12b suggests a more nuanced interpretation is required. As observed in Figure 3.12a, the R3 feature correlates with a bland section of the seismic profile without significant reflectors, extending across the project area to the west. The broad-scale change in resistivity character across major west dipping structure is more discontinuous in Figure 3.12b. C3 is located between the major west dipping structure and a smaller west dipping feature in the mid-crust (Figure 3.12b). The spatial association between faults and C3 suggests that it may be the results of fluid pathways or alteration rather than primary composition variation. C1 is primarily located off the western end of the seismic profile based on our translation of resistivity features. The eastern extent of C1 is confined by the west dipping fault on the western end of the seismic profile. The lower crustal reflective package in the seismic is associated with the low resistivity feature between the C1 and C3 features. These interpreted correlations between MT and seismic features based on Figure 3.12b require validation with additional MT data acquisition coincident with the seismic profile as it is not possible to determine if translation of resistivity features along geoelectric strike is a reliable method of comparison.

3.5.4 Comparison to potential field data

Gravity and magnetic data are also available across the project area; Figure 3.13 displays the comparison between features from the FINE inversion and seismic interpretation with the potential field data. Filtering of the gravity and magnetic data was used to emphasize shallow or deep features, Figure 3.13a and b, and Figure 3.13c and d respectively.

The fault location plotted in Figure 3.13a and b is the location of the lower crustal west dipping feature at approximately 10 km (the approximate top of the certain part of the interpretation from Figure 3.10b). The fault trace is clearly correlated with features in the shallow potential field data (Figure 3.13a and b), supporting the existence of the dashed extent of the feature. Unsurprisingly there is no clear correlation between the shallow potential field data and the locations of the deep low-resistivity features C1 and C3, indicated as hatched areas on Figure 3.13a and b.

The low-resistivity features from the FINE inversion do correlate more strongly with deep potential field data, particularly the magnetic data (Figure 3.13d). The C3 features is co-located with a magnetic high, as is the C1 feature. The location of R2 is a significant magnetic low in the magnetic data filtered to emphasize deep features. The gravity data in Figure 3.13c does not display clear correlations between resistivity features and density anomalies. There is an interesting correlation between the location of the deep crustal high reflectivity zones from the seismic and the gravity data filtered to emphasise deep features (Figure 3.13c). Additional forward gravity modelling would be needed to assess whether the gravity response is related to the location of the high-reflectivity packages in the seismic.

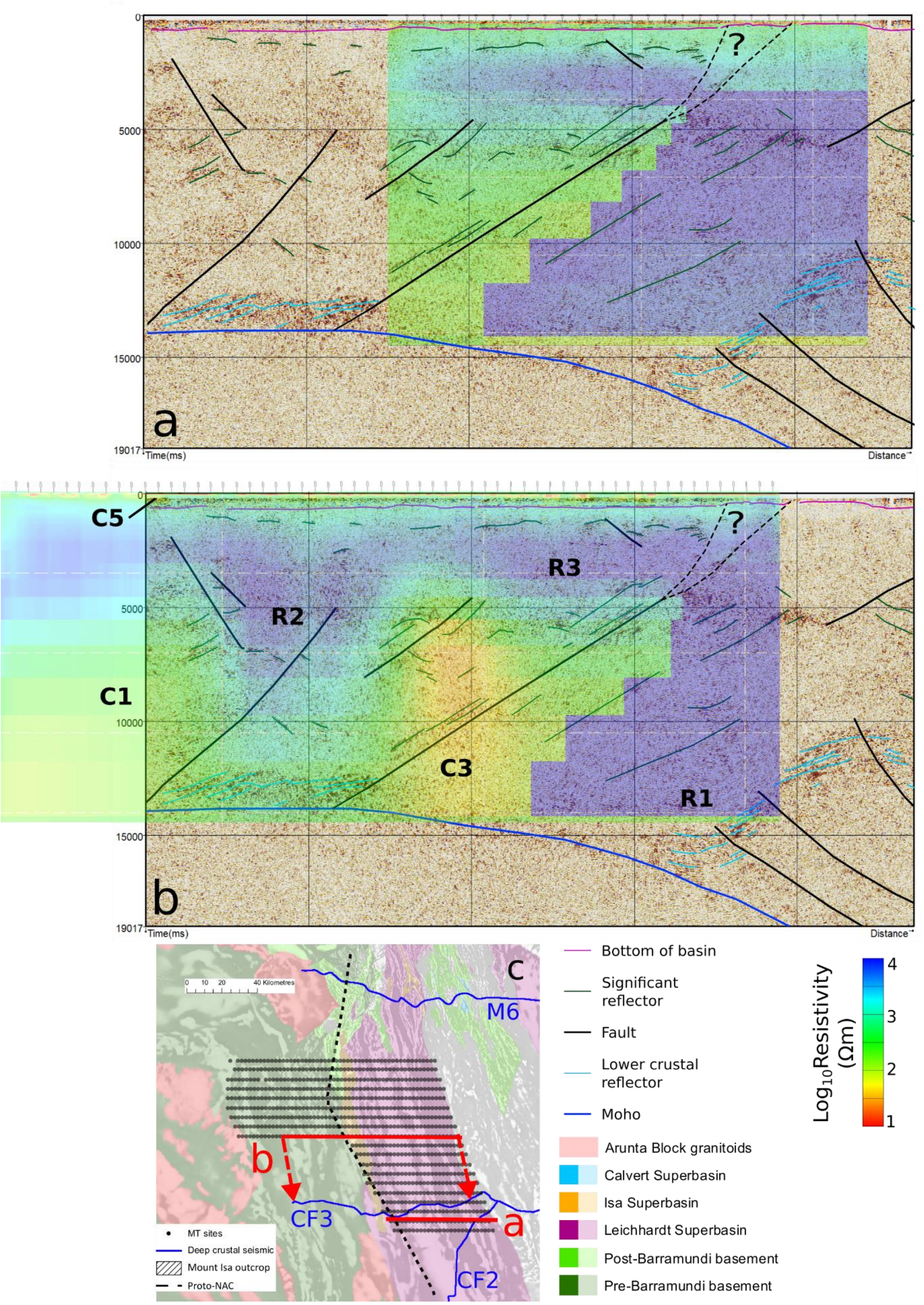

Figure 3.12. Comparison between seismic interpretation and FINE inversion features. a) Comparison between the parts of the resistivity model coincident with the seismic line. b) Comparison between a midpoint section from the resistivity model and the seismic interpretation. To create this comparison the resistivity profile was translated along the red dashed arrows in part c); orientation of translation based on strike of MT data (Figure 3.3m with 90° strike orientation resolved using potential field data strike). c) Current solid geology interpretation over 1VD of TMI data. Location of the two resistivity profiles is indicated as is the location of the seismic and potential suture boundary.

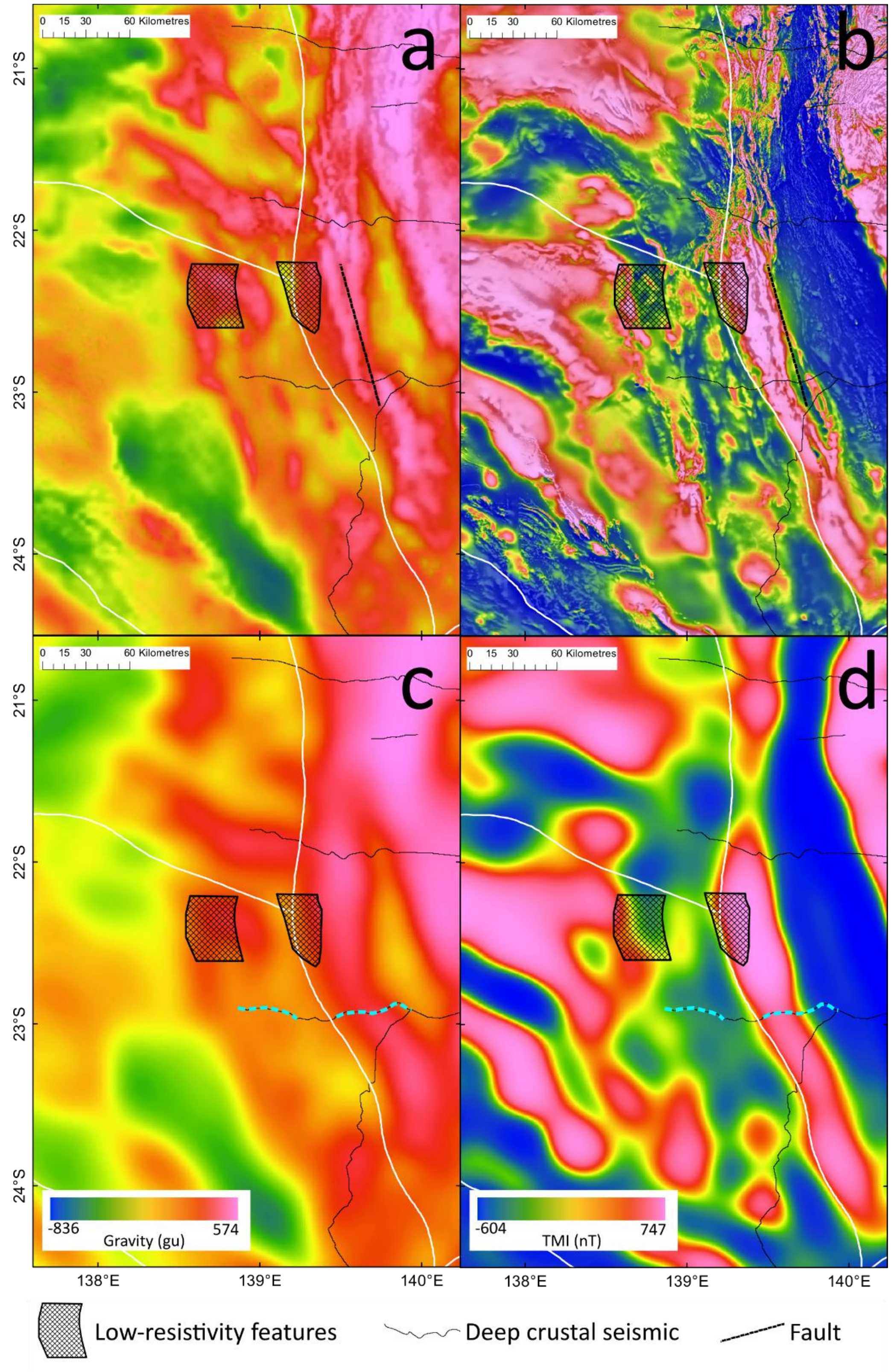

Figure 3.13. Comparison between inversions and potential field data. Data in top two panels filtered to emphasise shallower features and bottom two panels emphasise deep features. The location of low-resistivity features and fault from the FINE model are plotted on each subplot. White lines indicate the location of the crustal boundaries in Korsch and Doublier (2016). a) Partially transparent overlay of first vertical derivative of isostatically corrected gravity over isostatically corrected Bouguer gravity data. b) Partially transparent overlay of first vertical derivative of TMI over TMI data. Figures 3.13 a) and b) both contain an indication of the location of the west dipping fault at approximately 5 s; the reliable top extent of the feature. c) Low pass filter of the isostatically corrected gravity data with wavelengths shorter than 40 km removed. d) Low pass filter of the TMI data with wavelengths shorter than 40 km removed. Figures 3.13 c) and d) both contain an indication of the location of the lower crustal high reflectivity zones identified in Figure 3.10b as cyan dashed lines.

3.5.5 Integrated interpretation

Integration of MT, seismic and potential field geophysical data has defined a new crustal scale west dipping feature associated with a major change in crustal thickness. The feature is also associated with a major change in crustal resistivity, marking a boundary between high-resistivity crust in the east from lower-resistivity crust in the west. A thick extent of Leichhardt-Isa Superbasin sediments is interpreted on the west of the feature, suggesting it was active during deposition of these sediment after 1780 Ma. A conductor (C3) is located on or just above this interface and spatially associated with faults. This association has implications for exploration as it is suggestive of alteration or fluid flow on a structure which is also present in the shallow crust, and could represent an exploration target.

The major structure in the project area dips the west rather than east as previously proposed (Gessner, 2011; Withnall et al., 2013). There are no obvious indications in the seismic data that the west dipping feature represents a crustal suture. There is no reversal of the dip of reflectors across the feature, used by Goleby et al. (2009) and Pourteau et al. (2018) to interpret a suture; nor is there wholesale destruction of seismic reflectors as used by Korsch et al. (2012). The MT and potential field data also do not provides compelling evidence that the west dipping structure is a suture. The interpretation of Betts et al., (2016) that it is a major crustal discontinuity active during the Barramundi Orogeny is consistent with the features present in the data; however the extension into the shallow crust indicated by potential field data implies that the features has also been active post-Barramundi Orogeny. The discontinuous horizontal reflector interpreted to be part of the Leichhardt Superbasin is not present to the east of the structure (Figure 3.10b), allowing the possibility it was a controlling feature during deposition of this package.

Other features identified include a laterally extensive high resistivity (R3) layer present across the majority of the project area between 2 km and 10 km associated with low seismic reflectivity; and a highly seismic reflectivity package in the lower crust associated with moderate resistivity and high gravity. This lower crustal package is located at the base of the crust in the west, but is deformed and uplift into the mid crust in the east.

The Mount Isa Province has been adjacent to the proto-NAC since at least 1880 Ma (Betts et al., 2016; Evans and Mitchell, 2011; Zhang et al., 2012). The laterally continuous resistivity and seismic character of the top 10 km of crust (Figure 3.12) in the project area is suggestive of a continuous unit which is consistent with this interpretation. Forward gravity modelling by Betts et al. (2016) suggests that a mafic underplate and transitional lower crust is continuous from the proto-NAC to the eastern limit of the Mount Isa Province. While our study is supportive that a mafic underplate is present in the project area, it is not a continuous feature and has been subject to significant deformation. The thickened, deformed lower crust in the east of the profile (Figure 3.10b) may indicate that a suture is present further to the east.

High-resistivity crust was also identified from inversion of MT data in the east of the project area and is present to depths of at least 20 km. This feature is part of a broader trend of high-resistivity crust across much of the central Mount Isa Province, and potentially extends over 400 km to the north.

Comparison of the results from our modelling to other MT data across the Mount Isa Province (Figure 3.11) provide some evidence that the central part of the Mount Isa Province is highly resistive while the eastern and western parts of the Province have low-resistivity signatures. The trend we see in our study is superficially similar to the South Australian case. Results from modelling long period MT AusLAMP data in South Australia identified a macro-scale difference in the resistivity of the Archean craton and surrounding Proterozoic belts. The craton was highly resistive, while the surrounding Proterozoic belts had a low-resistivity signature

(Thiel et al., 2016). Juxtapositions of resistive and more conductive crust have also been attributed to margins of Archean and Proterozoic crust globally; at margins of the Archean Slave Craton and Wopmay Orogen (Wu et al., 2005), the Archean Superior Craton and the Grenville Province (Adetunji et al., 2014), and the Archean Superior Province and the Proterozoic Trans Hudson Orogen (Jones et al., 2005). Current MT data coverage across the Mount Isa Province is not sufficient to understand the lateral extent of this trend or its implications. Further MT data acquisition is warranted to better understand the resistivity character of the Mount Isa Province.

3.6 Conclusion

The geophysical data sets define a crustal-scale west-dipping feature that is adjacent to a major change in crustal thickness and associated with a major change in crustal resistivity (that extends at least 400 km to the north). There is additionally a conductor located on or just above the interface and significant changes in the potential field response corresponding to both upper crustal and lower crustal depths. This major crustal boundary identified in the project area is unlikely to represent a crustal suture between the Mount Isa Province and the NAC terrane but is interpreted to have been active during both the Barramundi Orogeny and deposition of the Leichhardt Superbasin sediments. The west dipping feature is spatially associated with a low-resistivity response (interpreted to be due to fluid movement or alteration), extends into the shallow crust and represents a possible exploration target. Other feature of note identified include a discontinuous mafic underplate which has undergone significant defamation, and consistent upper-crustal characteristics which are laterally extensive to the west.

A resistive block of crust identified in the east of the project area is part of a broader trend through the central part of the Mount Isa Province. This trend is under-constrained by the current data coverage but could potentially indicate a difference between Archean and Proterozoic crustal packages.

Acknowledgements

This work was completed as part of a PhD at the University of Adelaide. The work was conducted with the support of supercomputing resources provided by the Phoenix HPC service at the University of Adelaide. This research did not receive any specific grant from funding agencies in the public, commercial, or not-for-profit sectors. Naser Meqbel is thanked for the use of his 3D Grid software. The authors thank the Geological Survey of Queensland and Geoscience Australia for access to state and federal geophysical and geological databases.

CHAPTER FOUR

SYNTHETIC MODELLING OF DOWNHOLE RESISTIVITY DATA TO IMPROVE INTERPRETATION OF BASIN MORPHOLOGY FROM MAGNETOTELLURIC INVERSION

J. Simpson[1,2] and G. Heinson[2]

1 Geological Survey of Queensland, Department of Natural Resources, Mines and Energy, Queensland Government, Brisbane QLD 4000, Australia
2 Electrical Earth Imaging Group, Department of Earth Sciences, School of Physical Sciences, University of Adeialide, Adelaide SA 5005, Australia

Statement of Authorship

Title of Paper	Synthetic modelling of downhole resistivity data to improve interpretation of basin morphology from magnetotelluric inversion	
Publication Status	☐ Published ☑ Submitted for Publication	☐ Accepted for Publication ☐ Unpublished and Unsubmitted work written in manuscript style
Publication Details	In review with special edition of Earth Planets and Space (Submitted May 7 2019)	

Principal Author

Name of Principal Author (Candidate)	Janelle Simpson		
Contribution to the Paper	Modelled and interpreted data, wrote manuscript		
Overall percentage (%)	90 %		
Certification:	This paper reports on original research I conducted during the period of my Higher Degree by Research candidature and is not subject to any obligations or contractual agreements with a third party that would constrain its inclusion in this thesis. I am the primary author of this paper.		
Signature		Date	27th May 2019

Co-Author Contributions

By signing the Statement of Authorship, each author certifies that:

i. the candidate's stated contribution to the publication is accurate (as detailed above);

ii. permission is granted for the candidate in include the publication in the thesis; and

iii. the sum of all co-author contributions is equal to 100% less the candidate's stated contribution.

Name of Co-Author	Graham Heinson		
Contribution to the Paper	Provided supervision of work, aided in MT data interpretation and manuscript evaluation		
Signature		Date	24th May 2019

Abstract

Geophysical inversion models are inherently non-unique, requiring independent geophysical and geological constraint to reducing model uncertainty. Where data are not available to constrain inversion, alternative approaches to dealing in inversion variability are required. This study uses synthetic data based on downhole resistivity to select ideal magnetotelluric (MT) inversion parameters and guide interpretation of basin morphology.

The area selected for this study contains 809 broadband MT (BBMT) and 855 audiomagnetotelluric (AMT) stations, collected in 2014-2015, covering the Eromanga and Georgina Basins in Queensland, Australia. Downhole resistivity logs were obtained from three drill holes adjacent to the study area, and 1D resistivity models were generated from the downhole data. A suite of 1D and 2D MT inversion codes were tested to determine their ability to resolve basin layering and the basement interface.

Shallow basin layers were well resolved by all inversion codes but the basement interface was poorly resolved due to resistive (low-porosity) basin sediments towards the bottom of the Georgina Basin having only small contrast with the crystalline basement. A combination of Occam2D and rjMcMC inversions were used to produce interpretation of the base of the Eromanga Basin, and intra-Georgina Basin low-resistivity layer and depth to basement, all of which have associated error estimates. This study provides new interpretations of the morphology of the Georgina and Eromanga Basins but also serves as a cautionary example of the difficulties in using MT inversion to estimate basement depths where unfavourable petrophysical structures exist in the overlying basin.

Keywords: Basin interpretation, magnetotelluric inversion, synthetic modelling, Georgina Basin, Eromanga Basin

4.1 Introduction

Basin morphology, and more specifically depth to basement is a key consideration for mineral exploration. Many methodologies exist for deriving basement depth directly from potential field data, based primarily on automatic depth to magnetic source calculation (Moreau et al., 1999; Naudy, 1971; Reid et al., 1990; Thurston and Smith, 1997; Werner, 1953). Inversion of potential field data can also be used to estimate the thickness of sedimentary cover (Barbosa et al., 1997; Gallardo-Delgado et al., 2003), however such studies typically do not resolve internal basin structures. While a simple interpretation of depth to basement may be sufficient for de-risking mineral exploration, additional information about the character of the cover sequences contributes to improving the geological understanding of an area.

Electrical methods have the ability to resolve internal basin morphology and have been used to estimate basement depths (Cai and Zhdanov, 2015; Carreira et al., 2018; Majcin et al., 2018; Roach et al., 2018; Zevallos et al., 2009). The distinction between the lower resistivity of the basin sediments and the higher resistivity of the underlying basement rocks is key to using electrical data for depth to basement studies (Cai and Zhdanov, 2015). Decreased resistivity in basin units is primarily attributed to the presence of fluids in pore spaces (Evans, 2012; Selway, 2014). Magnetotelluric data are more typically used for crustal-scale tectonic studies, but depending on the range of frequencies collected and site spacing, can also provide information about shallow features.

Magnetotelluric data are inverted to produce resistivity depth models prior to interpretation. As with all geophysical inversion, MT inversion suffers from being inherently non-unique (Parker, 1994). Incorporating independent information during inversion or interpretation can produce models consistent with a variety of datasets, thereby reducing the uncertainty in interpreting the inversion models (Carreira et al., 2018; Le et al., 2016; Roach et al., 2018). Some MT studies have successfully used seismic data as an additional constraint, either during inversion (Yan et al., 2017) or the interpretation process (Ogaya et al., 2016). Downhole resistivity log data have also been used either as a constraint during inversion (Yan, 2016) or as a qualitative validation of inversion accuracy (Moorkamp et al., 2013). Another approach is the joint inversion of MT with potential field or seismic data to better constrain the outputs (Cai and Zhdanov, 2017; Le et al., 2016; Moorkamp et al., 2013). These approaches all require coincident constraining information, limiting their application in data-poor areas.

The project area for this study does not contain sufficient independent data, coincident with the MT data to constrain the inversion or interpretation. Instead, we use synthetic modelling of downhole resistivity data adjacent to the area of interest to assist with selection of the most appropriate inversion codes and inversion parameters. The synthetic modelling results are also used to guide interpretation. The study provides new information about the depth and character of the Eromanga and Georgina Basins in southwest Queensland. °

4.1.1 Geological background

Prospective Mount Isa Province units in the study area are entirely covered by the Georgina and Eromanga Basins (Figure 4.1; Walter et al. 1995; Greene 2010; Cook et al. 2013; Kruse et al. 2013). Previous drilling results (Figure 4.1c) indicate that basement depths range from less than 100 m in the north (where the Georgina Basin thins onto the outcropping Mount Isa sequences) to over one kilometre in the south-west (where the Georgina Basin thickens into the Toko Syncline). The Georgina Basin is a Neoproterozoic to early Palaeozoic epicratonic basin (Walter et al., 1995) present across the entire study area. The Eromanga Basin is an Early Jurassic to Cretaceous cratonic sag basin (Cook et al., 2013) and overlays parts of the Georgina Basin in the east of the study area. Neoproterozoic rift packages underlying the Georgina Basin also occur in the broader region (Greene, 2010), but have not been identified in the project area.

The Toko, Cockroach and Narpa Groups are the outcropping Georgina Basin units (Figures 4.1 and 4.2). These units broadly date from the Cambrian to Ordovician and are carbonate dominated (Withnall et al., 2013). Drilling indicates that the older Morpunga and Shadow Groups are also present in the study area, though not exposed at the surface (Green et al., 1963; Kress, 1989; Kress and Simeone, 1993). The Eromanga Basin is comprised of the Wilgunya Subgroup and the Longsight Sandstone in the study area (Figure 4.1 and 4.2). These units are Upper Jurassic to Lower Cretaceous siliclastic sediments and are dominantly mud-rich (Cook et al., 2013).

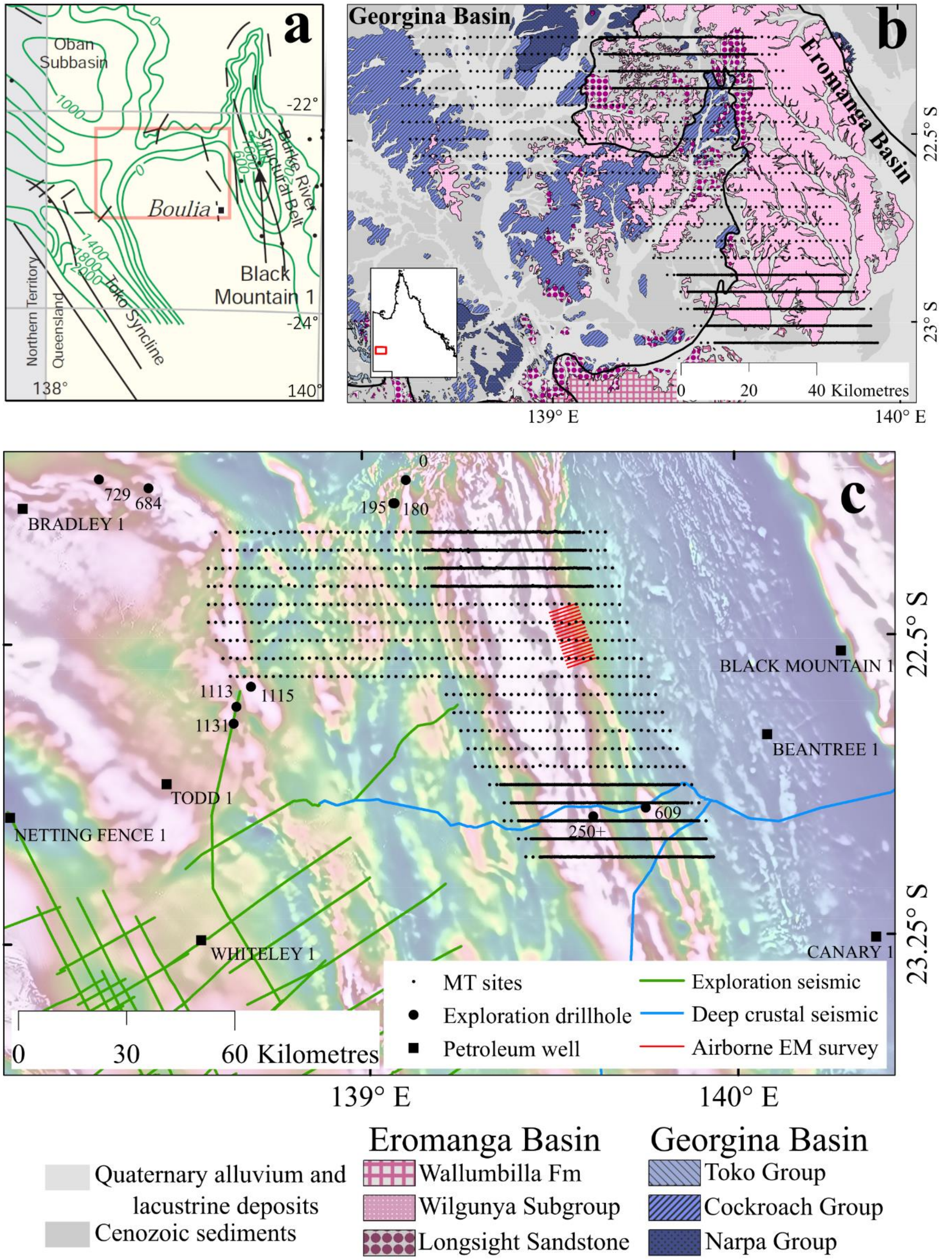

Figure 4.1. Summary of mapped surface geology and available constraining information. a) Location of the project area in red compared to Georgina Basin subbasins with project area indicated in red (modified after Withnall et al. (2013)). b) Mapped surface geology, thick black line denotes margin of the Eromanga Basin, points are the MT sites used for the study. c) Composite first vertical derivative and total magnetic intensity map of the study area showing a north-south strike for the magnetic basement units. Available exploration data for study area also shown, exploration drill holes annotated with intersected basement depths or maximum hole depth where basement was not intersected (indicated by + after depth).

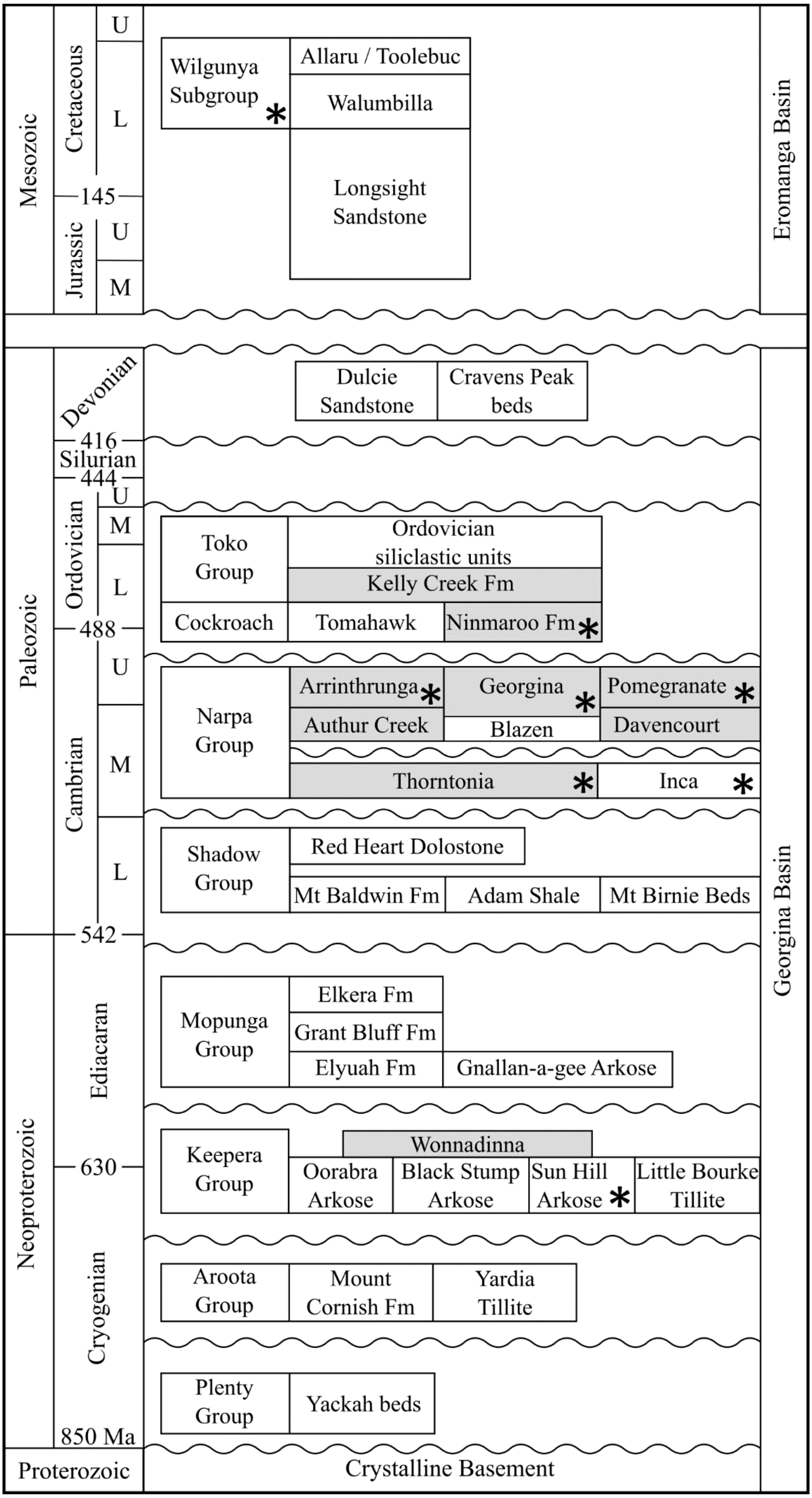

Figure 4.2. Simplified stratigraphy for relevant units of the Georgina and Eromanga Basins. Modified after Greene (2010) with data from Ambrose et al. (2001), Draper (2007) and Kruse et al. (2013). Grey units are predominantly limestone, and white units are siliciclastic. Starred units intersected by Todd 1, Bradley 1 or Beantree 1 (location of wells shown on Figure 4.1).

4.1.2 Independent data

A variety of geophysical and geological datasets are present in or near the project area (Figure 4.1c). The MT dataset which is the primary focus for this study contains over 1600 sites of either BBMT (2.2×10^{-4} Hz to 3×10^{2} Hz) or AMT (0.5 Hz to 10^{4} Hz) frequency ranges. Several exploration drillholes are present near the project area which intersect basement, however only one with present within the MT data array. None of these exploration drillholes have associated resistivity logs, and the geological logging of basin sequences is generally poor. A small number of petroleum wells are available slightly further away from the main project area. These wells do have downhole resistivity logs and have detailed geological descriptions for the basin sequences.

A small airborne EM survey was conducted in the survey area, along with regional magnetic and gravity coverage. The airborne EM survey does not penetrate the conductive Eromanga Basin units and therefore cannot assist with basin modelling or depth to basement estimation. The gravity data has a station spacing of 4 km, making it too coarse to constrain the MT inversion. Seismic data along 2D profiles is present near, but not within the study area. Data from a deep crustal seismic line is available, but the acquisition parameters and processing are poorly optimised to resolve shallow features.

The magnetic data is high resolution with a line spacing of 400 m and forms the basis of two depth to basement interpretations in the area (Frogtech Geoscience, 2018; GSQ, 2011). Both are primarily based on depth to magnetic source estimation and are broadly comparable, although the Frogtech Geoscience (2018) interpretation is newer and higher resolution. Comparison of the Frogtech Geoscience (2018) interpretation to known basement depths from drilling suggests that the basement interface is poorly resolved in this area by depth to magnetic source (Figure 4.3).

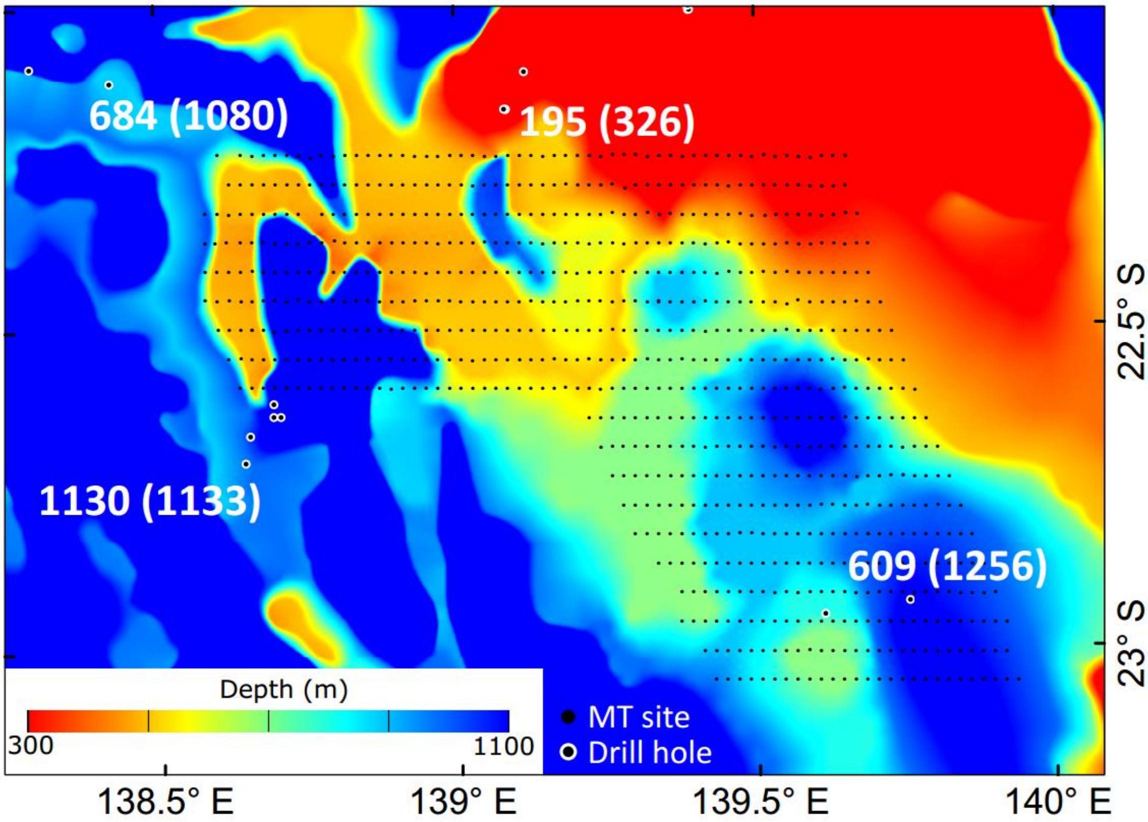

Figure 4.3. Frogtech Geoscience (2018) depth to basement interpretation for the study area. Selected drillholes annotated with actual basement depth, predicted Frogtech basement depth in brackets.

4.2 Synthetic Modelling

Three petroleum wells with downhole resistivity logs are available near the study area (Figure 4.1c). These wells are not inside the study area and therefore cannot be used to directly constrain the inversion, as suggested in (Yan, 2016). Instead, they have been used to understand the expected resistivity of the basin sequences and basement. The airborne electromagnetic survey was used to supplement the petroleum wells to characterise the resistivity for the shallow Eromanga Basin units (Figure 4.1c). Another MT study of the Eromanga Basin has been conducted several hundred kilometres to the south but also suggests the Eromanga Basin sequences are exceptionally conductive (Spence and Finlayson, 1983)

Downhole resistivity data were extracted from well completion reports (Green et al., 1963; Kress, 1989; Kress and Simeone, 1993). The downhole resistivity data were averaged over areas of consistent resistivity response in Log_{10} (ResistivityΩm) and each model named after their respective source wells, Todd1, Bradley1 and Beantree1 (Figure 4.4). Synthetic data were generated for the three models using ModEM 3D (Egbert and Kelbert, 2012; Kelbert et al., 2014). Synthetic data had a frequency range of 0.1 Hz to 10^4 Hz, with five points per decade to represent the attributes of actual AMT data in the study area. A 2% error was used for the generated data, and 2.5% Gaussian noise was added to the data and error. These data were used to produce inversions with a variety of inversion codes to assess which methods provided the best recovery of the original structure (Figure 4.4).

4.2.1 1D inversion

Three 1D inversion codes were chosen for testing: Occam; SimPEG; and rj-McMC (Brodie and Jiang, 2018; Cockett et al., 2015; Constable et al., 1987). These codes were chosen as they are all open source and have different methodologies; smooth inversion, standard inversion and probabilistic inversion.

The ModEM generated synthetic data were inverted using Occam 1D (Constable et al., 1987). Data with frequencies higher than 6 Hz were used for inversion. The models had a maximum depth of 7.5 km with a target depth of 2 km. Two inversions were run for each model, one with the minimum number of layers (n) required for the inversion to achieve an RMS of 1 and converge appropriately (n=8 for Bradley1 and Beantree1; n=9 for Todd1). The second inversion used an arbitrarily large number of layers (n=100) to investigate a smooth inversion result for the same data (Figure 4.4).

Figure 4.4 (right). Summary of synthetic modelling conducted using downhole resistivity from petroleum wells. a) Todd 1 (Kress and Simeone, 1993), b) Bradley 1 (Kress 1989), and c) Beantree 1 (Green et al. 1963). From left to right for : downhole logged geology, limestone units in grey, siliclastic units in white and basement in red; measured downhole resistivity, black logarithmic scale, blue linear scale; 1D synthetic model created from downhole resistivity data, annotated with resistivity (Ωm), basement interface indicated with black dashed line; results from Occam1D inversion, model in thick dashed line, minimum layer model green, n = 100 model blue; 1D MT SimPEG inversion, model in dashed line, inverted response in blue; Occam 2D inversion results for BBMT and AMT frequency ranges; rj-McMC MT inversion with automatically generated changepoint probability. rj-McMC MT inversion plot displays mean model (blue), mode model (green), median model (red) and the 10th and 90th percentile models (red dashed); synthetic model resistivity in dashed blue. Colour scale applies to all plots, including models. Gl, Georgina Limestone; Bm, basement; Ar, Arrinthrunga Formation; Nm, Nimaroo Formation; Sh, Sun Hill Arkose, Pl, Pomegranate Limestone; Ud, Undifferentiated; Ar, Arrinthrunga Formation; Wl, Willgunya Subgroup; Nm, Nimaroo Formation; Th, Thorntonia Limestone.

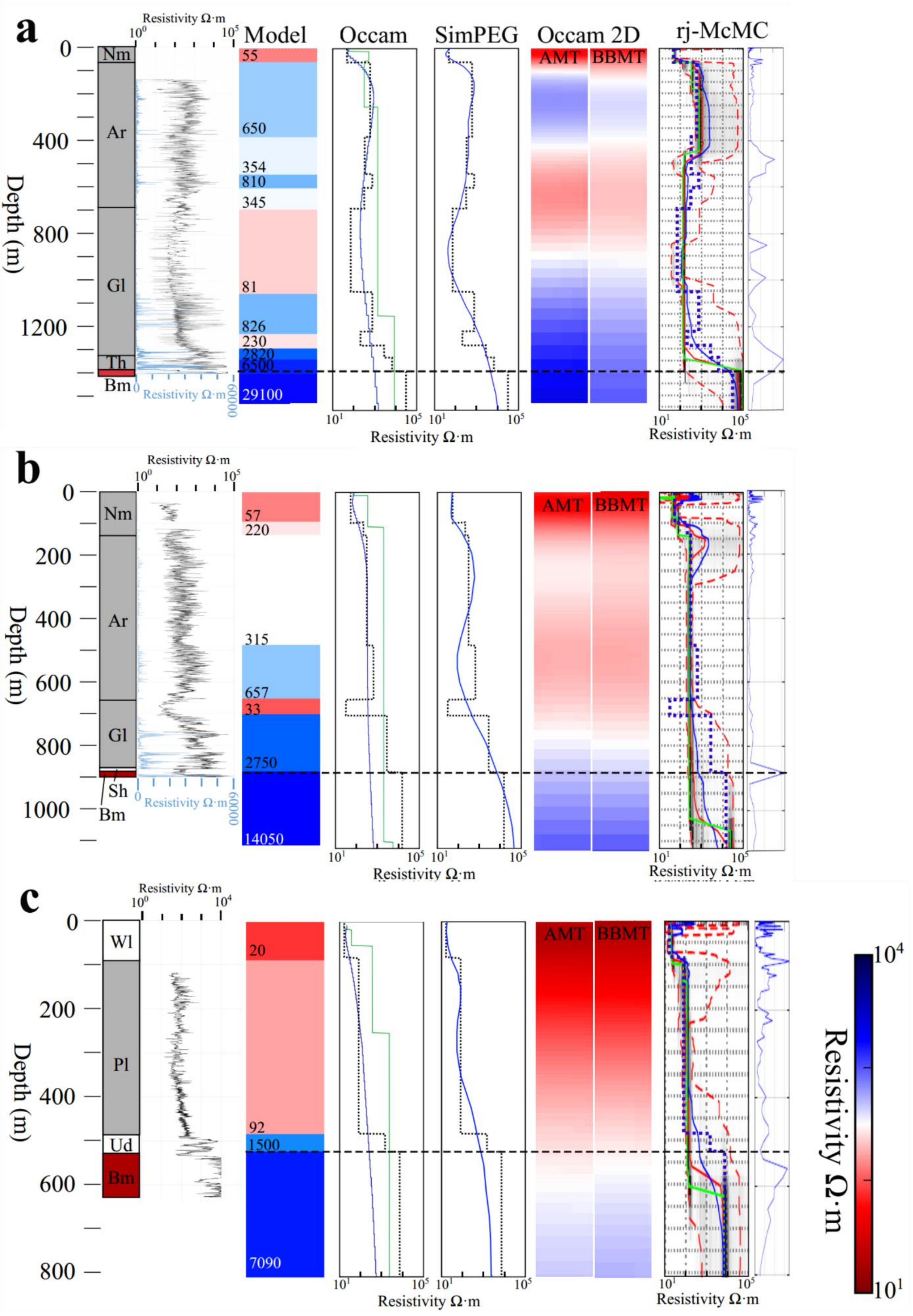
a
Resistivity Ω·m
10^0
10^5
Model
Occam
SimPEG
Occam 2D
rj-McMC
AMT
BBMT
Depth (m)
0
400
800
1200
Nm
Ar
Gl
Th
Bm
Resistivity Ω·m
0
60000
55
650
354
810
345
81
826
230
2820
6500
29100
10^1
10^5
Resistivity Ω·m
b
Resistivity Ω·m
10^0
10^5
Depth (m)
0
200
400
600
800
1000
Nm
Ar
Gl
Sh
Bm
Resistivity Ω·m
0
60000
57
220
315
657
33
2750
14050
AMT
BBMT
10^1
10^5
Resistivity Ω·m
c
Resistivity Ω·m
10^0
10^4
Depth (m)
0
200
400
600
800
Wl
Pl
Ud
Bm
20
92
1500
7090
AMT
BBMT
10^1
10^5
Resistivity Ω·m
10^4
Resistivity Ω·m
10^1

ModEM synthetic data were also used for 1D inversion with the rj-McMC 1DMT code (Brodie and Jiang, 2018). Inversions were parameterised to have a maximum number of layers of 20 and maximum layer depth of 2000 m. Selection of these parameters was informed by the complexity of the available downhole resistivity data and maximum expected basement depths from drilling. The frequency range was limited to 10 – 10^4 Hz, and permissible resistivity values limited between 10^{-1} and 10^5 Ωm. Inversions were run for 10^4 burn-in samples and 10^5 total samples.

The synthetic models were also inverted using MT1D from the SimPEG suite of codes (Cockett et al., 2015). SimPEG's inbuilt capability to generate data from synthetic models was used rather than the ModEM synthetic data. The data error was set to 3% for this modelling. Optimised values for key inversion parameters for each synthetic model were established through a series of inversion tests. The αs, cooling factor, cooling rate, α_z and B_0 where all varied in an effort to produce an inversion model which closely resembled the synthetic model (Figure 4.4). For all three models the $\alpha_s = 0.001$, cooling factor = 2 and cooling rate = 1. Beantree1 and Bradley1 had $\alpha_z = 1$, while Todd1 had $\alpha_z = 2$. The B_0 ratio was 6 for Bradley1 and Todd1, and 8 for Beantree1.

4.2.2 2D inversion

Occam 2D was selected for testing 2D inversion of the synthetic models, primarily as it is open source. Occam 2D inversion (deGroot-Hedlin and Constable, 1990) was conducted using the ModEM generated synthetic data, with all inversion files prepared using MT-py codes (Krieger and Peacock, 2014). Inversion mesh was parameterised to 3 km depth, with a first layer thickness of 5 m. Only data with frequencies above 6 Hz were used. All inversions used both the TE and TM components and were started from a 100 Ωm half space. A series of inversions were run for each synthetic dataset to test the effect of the number of layers and error floors on inversion products. The number of layers tested was n= 20, 40, 60, 80 and 100. Error floors tested range between 2% and 10%. Models achieved an RMS of 1 and ran to convergence. The preferred inversion parameters were selected based on the agreement between the synthetic and inversion models. The final inversions (Figure 4.4) were run with n = 60, rho error floor = 5% and phase error floor = 0.2°.

The effect of input frequency range was also tested for these 2D inversions. The synthetic data were subset to frequencies between 1 Hz and 300 Hz to represent BBMT data collected in the study area. These data were inverted using the same parameters as the AMT frequency inversions and outputs compared (Figure 4.4).

4.3 Synthetic modelling results

The inversion codes tested recovered varying levels of the original structure (Figure 4.4). No models were run using a priori information as this information is not reliably available for inversion of real data. Importantly, no code was able to recover the full original structure from a half space starting model. A combination of noise levels and difficulties resolving thin layers at depth are primarily responsible for the poor recovery of the original models. The smoothing algorithms used to stabilise the inversions also contribute to the inversions being unable to determine the original basin layering.

Shallow layering was reliably returned by all inversions while the basement interface was not sharply determined from any inversion. The inability to resolve the basement contact may be entirely due to the known difficulty in delineating conductor bottoms (Bedrosian 2007).

Synthetic modelling suggested that the more limited high-frequency component for BBMT data, when compared to AMT data, reduces the ability of inversions using the BBMT data to resolve shallow features (Figure 4.4). Despite this limitation, it possible to produce recognisable basin features from inversion of the BBMT data.

4.3.1 1D results

All inversion codes tested were able to produce inversion models which fit the data to an RMS of 1. The minimum layer Occam 1D models do not reproduce features from the synthetic models (Figure 4.4). The smooth (n = 100 layer) Occam inversion models are similar to the synthetic models for the shallow section, however the basement resistivity is poorly reproduced by these inversions (Figure 4.4).

Inversion of data from the Todd1 and Beantree1 models using the SimPEG 1DMT code produced models which closely resemble the synthetic models (Figures 4.4a and c). Inversion results of the Bradley1 synthetic data using the SimPEG code are broadly similar to the original synthetic modelling layers (Figure 4.4b), however the narrow low-resistivity unit at approximately 600 m is poorly resolved.

The rj-McMC inversion results also generally reproduced the synthetic model features (Figure 4.4). The true model is contained within the p10 to p90 bounds and typically resembles the mode model. The low-resistivity feature at approximately 600 m depth in the Bradley1 model is the only part of any model which does not plot within the p10 to p90 bounds (Figure 4.4b). This feature is also not resolved by the SimPEG modelling and Occam results, suggesting it is not resolvable from the data. The basement interface all three models has a change point peak in close proximity and is associated with a broad region, defined by p10 to p90 bounds, which represents a step change in the resistivity (Figure 4.4).

4.3.2 2D results

Occam 2D inversions for the Beantree1 dataset produced a model which resembles the synthetic model (Figure 4.4c). 2D Occam inversion results from Todd1 and Bradley1 are broadly similar to the synthetic model (Figure 4.4a and b), however conductive units occur at shallower depths, and the basement interface is not recognisable. A comparison between inversions of BBMT and AMT frequency ranges was conducted using the Occam 2D code. Inversion of synthetic data with only BBMT frequency ranges produced similar results to the AMT frequency ranges for all three synthetic models. The BBMT inversion tests generally had more smooth results compared to the AMT inversions.

4.4 Basement resolvability testing

Additional testing of basement interface resolvability was conducted, prompted by concerns regarding the sensitivity of MT data to the top of the resistive basement surface (Bedrosian, 2007). The 1D and 2D inversion testing results suggest it is possible to reproduce the synthetic models to a reasonable degree of accuracy (see especially SimPEG results in Figure 4.4a and c), but it is unclear whether the basement interface is well determined but the data. The large spread in p10 to p90 bounds of results around the basement interface for rj-McMC inversions suggest that the interface is not well resolved. However the changepoint peak predicts basement at approximately the correct depth in the tested models. The ability of rj-McMC inversion to discern the upper resistive layer comes from the fact that there is sufficient information in the data to resolve both the conductivity and conductance of the overlying conductive layer permitting a good estimate of the thickness. This is also likely to be the reason why the method provides a reasonably high probability changepoint near the correct depth in Figures 4.4a and 4.4b. The result in Figure 4.4a is more complicated but the changepoint occurs at around the correct depth because the data can resolve the averaged conductivity for the lower conductive and moderately resistive layers as well as the integrated conductance of the layers providing information on the thickness. Alternatively it is also possible that the infinite thickness of the basement unit used to generate synthetic data, and absence of any structure within the synthetic basement, may spuriously increase the resolvability of basement in the testing.

To further examine the ability of the rj-McMC inversion to resolve basement, a simple test case of two models (Model1 and Model2) was created with basin layering similar to Beantree1. The models have a basement depth difference of 250 m, meaning basement was located at 600 m in Model1 and 850 m in Model2. A moderately resistive layer was inserted directly above the basement contact for Model2 and the forward responses for the two models calculated and compared. This kind of moderately resistive basin package is evident in the lower part of the Georgina Basin in Todd 1 and Bradley 1.

The rj-McMC MT inversion routine was used to invert synthetic data for both models using the same parameters as the synthetic modelling exercise. This code was selected to provide an estimate of the range of possible inversion results for Model1 and Model2.

Finally, ModEM 3D (Egbert and Kelbert, 2012; Kelbert et al., 2014) was used to test whether a pre-existing depth-to-basement surface could be used in the starting and prior models to assist in resolving the basement depth. Four two-layer starting models were generated to test the effect of an a priori basement surface. One model had a surface at approximately the correct depth (1390 m), two models had shallower basement surfaces (710 m and 1130 m) and one model had a deeper basement surface (1770 m; Figure 4.7). The stating models had a resistivity of 353 Ωm above the basement surface, and 10,000 Ωm below the basement surface. The top layer resistivity value was an average of the basin resistivity values from the Todd1 model, and the inversion was run using synthetic data generated from Todd1.

Figures 4.5, 4.6 and 4.7 show results from additional testing of the resolvability of the basement interface. The forward calculated data in Figure 4.5 is noise free and displays only a very minor variation in overall response. In the presence of noise it would be very difficult to differentiate between the two responses despite an increase in basement depth of approximately thirty percent.

Inversions of synthetic data produced from Model1 and Model2 with the rj-McMC code are almost indistinguishable in their predicted structure, especially the mean, mode and median models (Figure 4.6). The number of layers differs, with a strong peak of three layers for Model 1 and a more distributed range of layers for Model 2. Both inversions have broad range of permissible basement depths, as indicated by the broad changepoint peaks. This testing demonstrates resistivity structure of the basins in the project area will impede the use of MT data to resolve the basement.

Results from testing the effect of a starting model with an a priori basement interface inserted are shown in Figure 4.7. The four tested models had a basement surface approximately 50% too shallow, approximately 20 % too shallow, approximately 30 % too deep and one at the correct depth (Figure 4.7b - e). Where the a priori basement surface was 50 % too shallow there is a noticeable impact on the returned inversion features, with a low-resistivity layer placed directly adjacent to the basement interface (Figure 4.7b). For the other scenarios there is minimal impact on the returned inversion features, compare Figure 4.7c – e to the 2D Occam inversion in Figure 4.7f. A subjective determination of where basement is too deep may be possible due to the presence of a thickened higher resistivity package beneath the low-resistivity feature at 800 m, but the value of such a result is questionable.

Comparison between the current depth to basement surface and drilling suggests that basement depths are overestimated (Figure 4.3) so using this surface to create a starting model for inversion testing is unlikely to provide additional information.

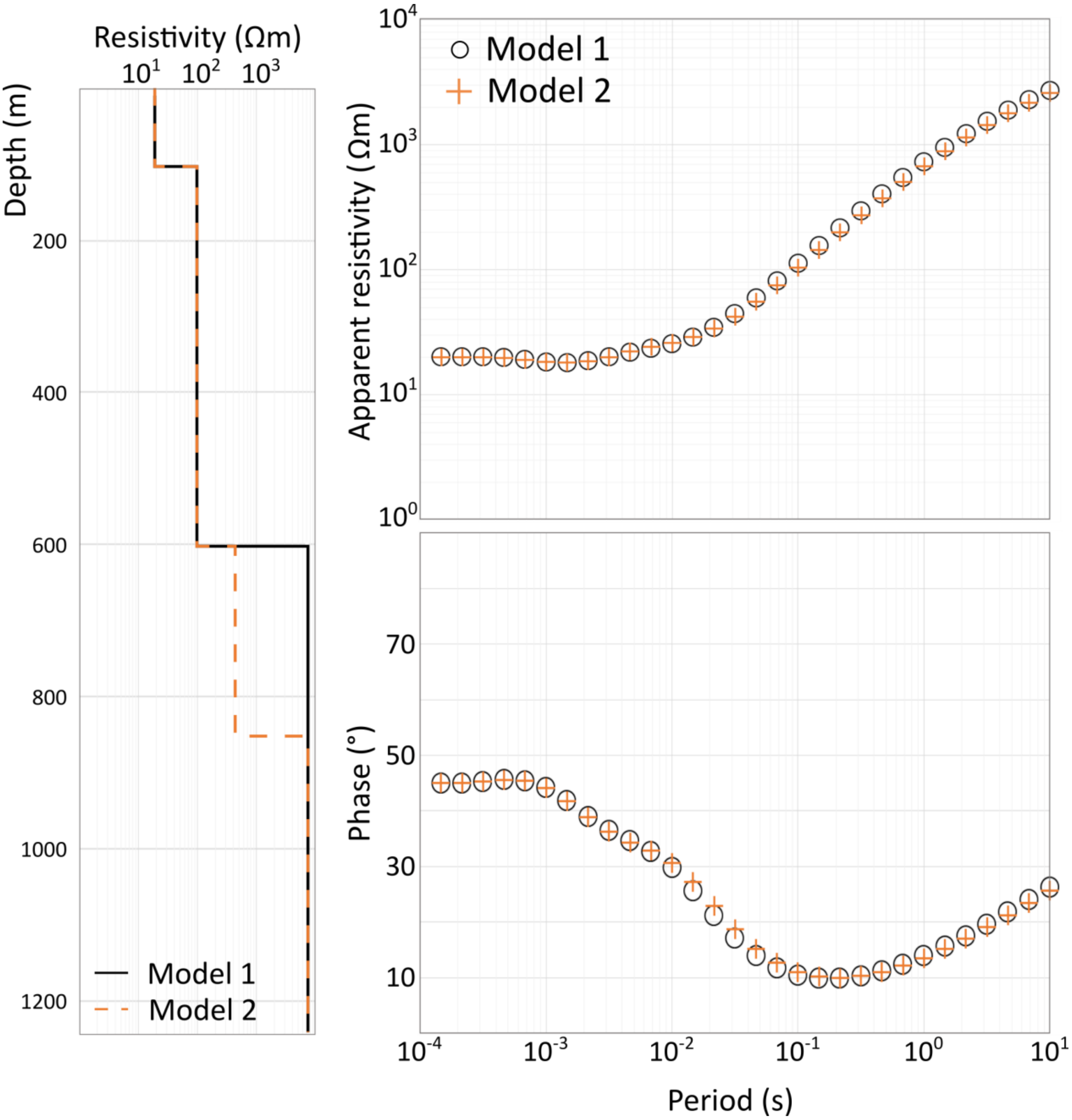

Figure 4.5. Apparent resistivity and phase plots for Model1 and Model2, used to assess basement resolvability. Model1 is a simple three-layer model with a basement interface at 600 m. Model2 has the same structure above 600 m but has an additional 250 m thick, moderately resistive layer with basement at 850 m.

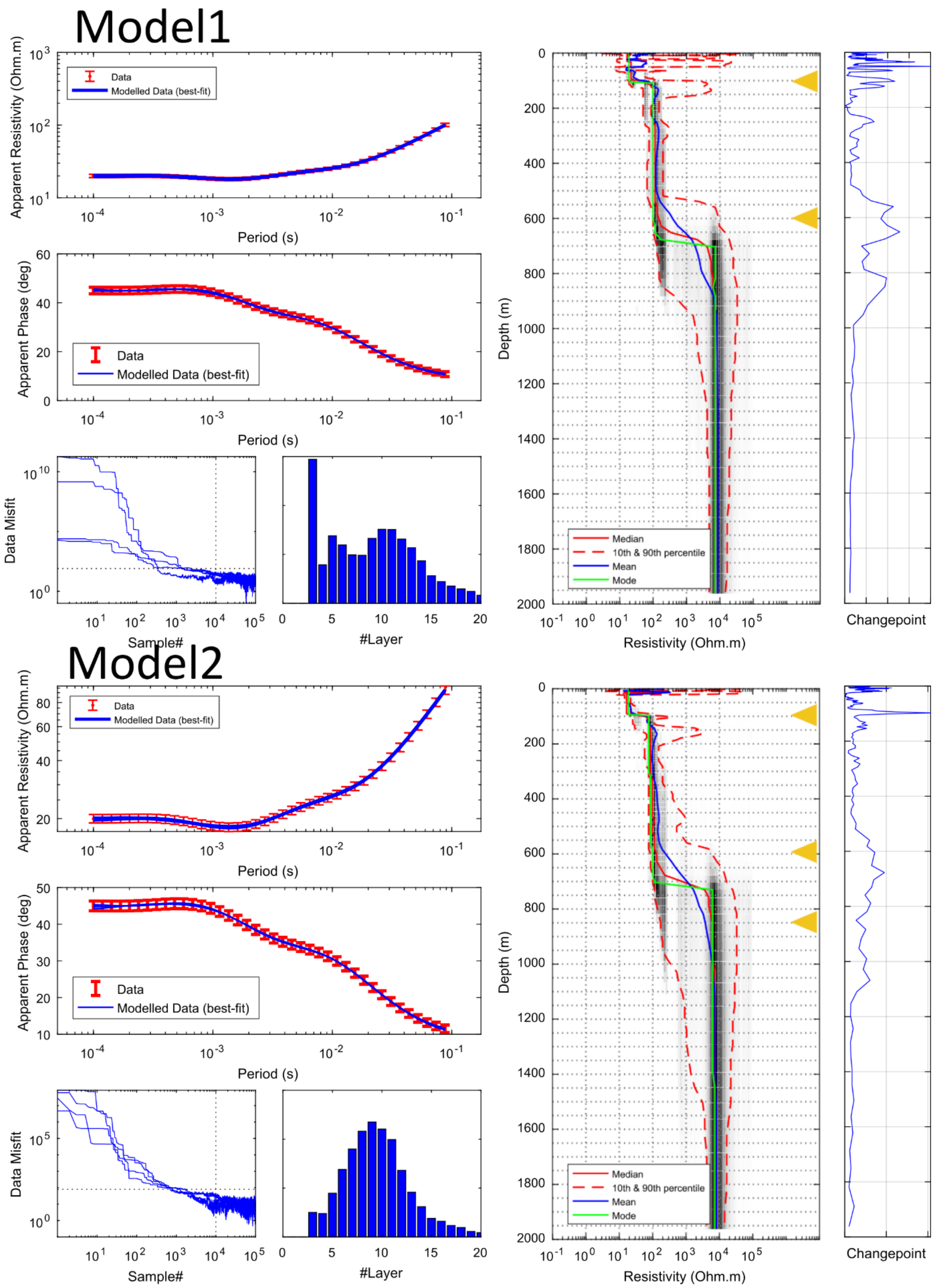

Figure 4.6. Results from rj-McMC 1DMT inversion of Model1 and Model2 (Figure 4.5). Inversion structure displays a high degree of similarity for the two models, however the Model1 result has a significant peak in the number of layers which is absent from the Model2 result. Location of model layers indicated by yellow arrows.

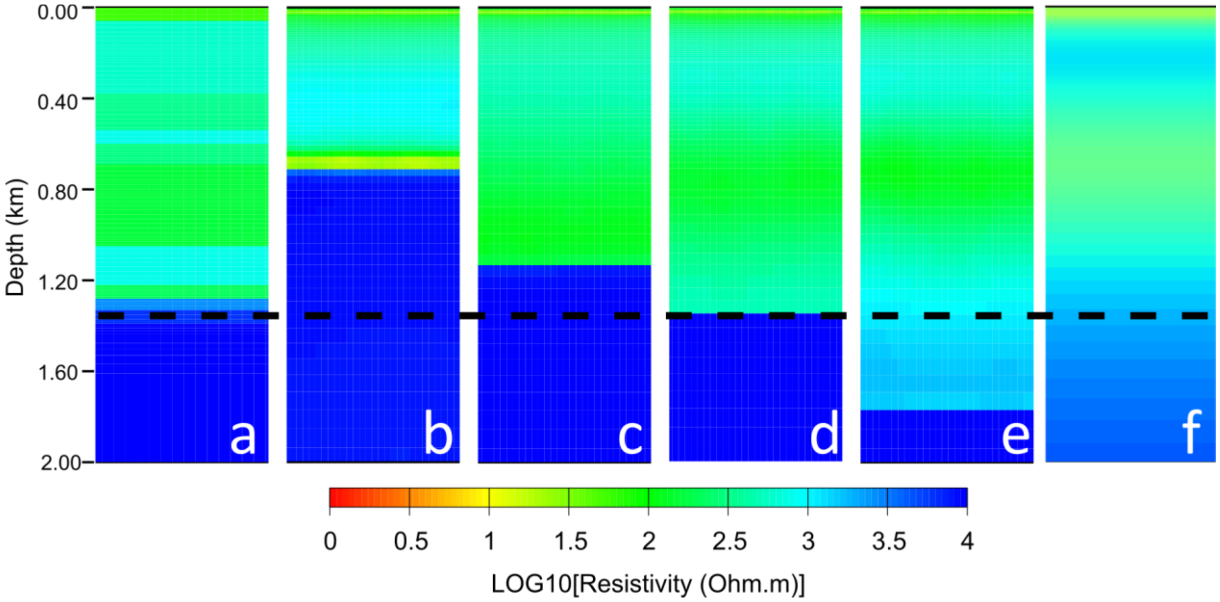

Figure 4.7. Results from inversion testing with pre-exiting basement surface incorporated into the starting and prior models. a) Todd1 model, true basement depth 1390 m b) inversion result from staring model with basement at 710 m c) inversion result from staring model with basement at 1130 m d) inversion result from staring model with basement at 1350 m e) inversion result from staring model with basement at 1770 m f) Occam 2D inversion result from inverting Todd1 synthetic data for comparison (see also Figure 4.4).

4.5 Application to real data

A collaboration between the Geological Survey of Queensland and Geoscience Australia produced BBMT and AMT data collected on a regional grid in the Boulia region of western Queensland (Figure 4.1b). A total of 809 BBMT stations were collected at 2 km station spacing (E-W) along 5 km spaced profiles (N-S). The BBMT dataset was complemented by the collection of 855 AMT stations at 500 m spacing, co-located along nine of the BBMT profiles (Figure 4.1). The higher resolution AMT collected information from approximately 0.5 Hz to 10^4 Hz and the BBMT stations collected data from 2.2 x 10^{-4} Hz to 3 x 10^2 Hz.

MT-py (Krieger and Peacock, 2014) was used to determine dimensionality, geoelectric strike and the presence of galvanic distortion (Simpson and Bahr, 2005). Phase tensor (Bibby et al., 2005; Caldwell et al., 2004) pseudosections and maps were produced to assess the character of the data and noise distribution. Geoelectric dimensionality was assessed through both the phase tensor method (Bibby et al., 2005; Caldwell et al., 2004) and WALDIM analysis (Martí et al., 2009). Results from two methods are broadly similar, but the phase tensor method showed a more consistent dimensionality pattern and was thus the preferred method of analysis. The data were determined to be predominantly 1D at high frequencies (>100 Hz) and became 2D with decreasing frequency (Figure 4.8). A small subset of stations in the west and north of the study area have 3D characteristics at frequencies lower than 10 Hz.

The geoelectric strike for the 2D data was determined using MT-Py (Krieger and Peacock, 2014). The geoelectric strike is calculated based on the phase tensor (Bibby et al., 2005; Caldwell et al., 2004) and impedance tensor invariant (Weaver et al., 2000; Weaver and Lilley, 2004) methods. The strike analysis has a 90° ambiguity (Thiel, 2008)), but the geological trends show that the strike is N15°W. Static shift was accounted for during inversion (e.g. Ogawa 2002).

The northern block of AMT stations was significantly affected by low signal to noise ratio in the deadband while the southern AMT block was relatively unaffected (Figure 4.8). This effect is confined to frequencies between 3000 – 5000 Hz or below 1 Hz due to low-signal due to

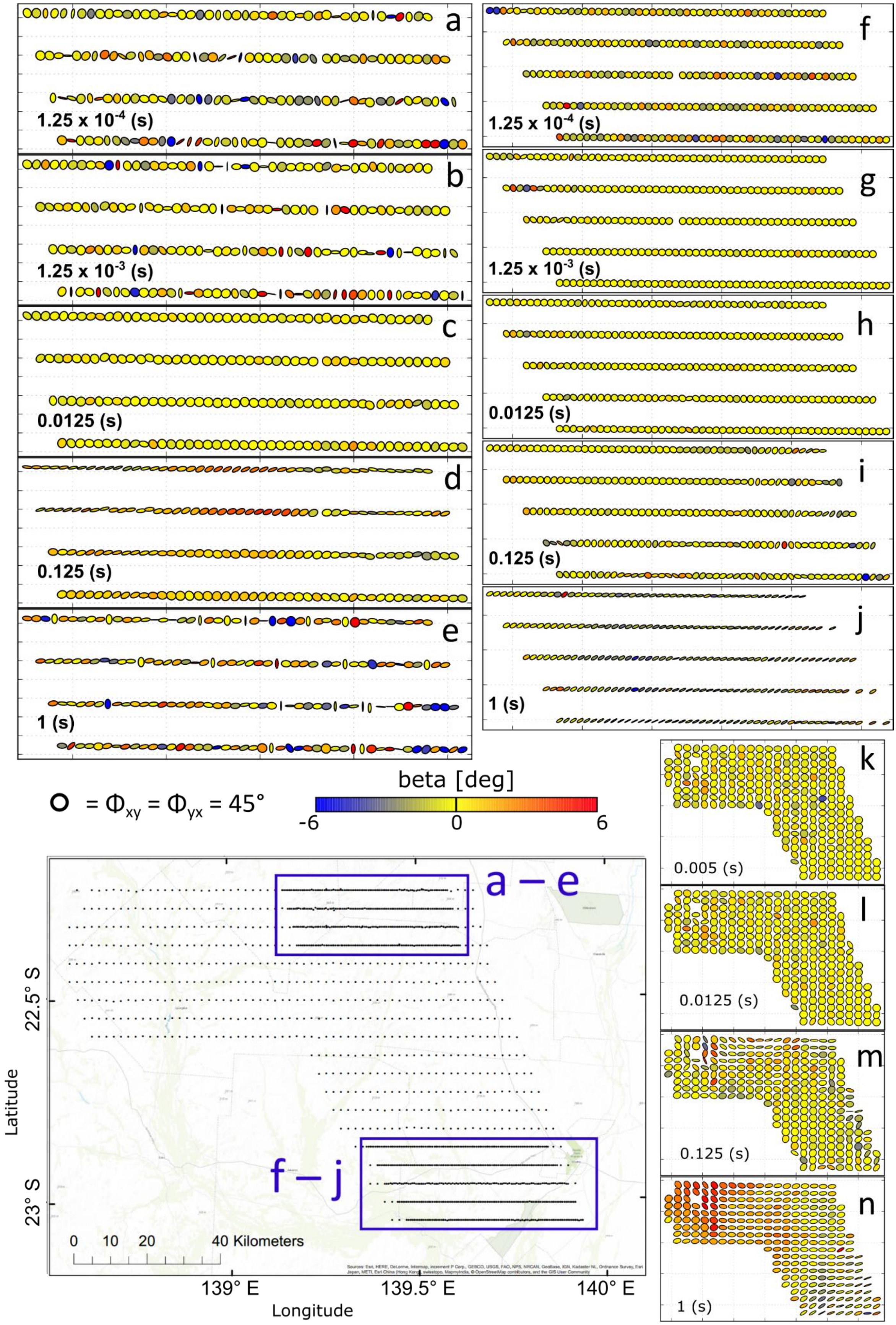

Figure 4.8. Phase tensor plots coloured by skew for AMT and BBMT datasets (annotated with period). Data unaffected by noise are predominantly 1D at short periods, as indicated by yellow circular ellipses. Distorted ellipses with low skew values are indicative of 2D data, while ellipses with red or blue colouration indicate 3D subsurface structure. a – e) north block AMT data, increased data noise responsible for scattering at 1 s, 1.25 x 10^{-3} s and 1.25 x 10^{-4} s. f – j) southern block AMT data. k – n) data for BBMT sites, western sites are 3D at 1 s. Displayed ellipses were generated using one third of the total BBMT sites and half of all AMT sites for clarity.

daytime acquisition (Garcia and Jones, 2008), and data were masked to minimise its effect during inversion. The AMT and BBMT data were truncated to frequencies above 10 Hz to remove 3D data. The AMT and BBMT data were inverted using rj-McMC and Occam 2D with the inversion parameters identified during synthetic modelling. The rj-McMC inversion code was selected because it is a probabilistic inversion code which offers an estimate of uncertainty (Brodie and Jiang, 2018). Occam2D was selected to ensure the 2D data in the project area were adequately modelled and provide results for interpretation with a high degree of lateral continuity.

The rj-McMC inversions were parameterised to have a maximum number of layers of 20 and maximum layer depth of 2000 m. Permissible resistivity values limited between 10^{-1} and 10^5 Ωm and inversions were run for 10^4 burn-in samples and 10^5 total samples. Three sets of inversion were conducted with rj-McMC; BBMT sites were run with an input frequency range of 10 – 3 x 10^2 Hz, full frequency (FF) AMT with a frequency range of 10 – 10^4 Hz, and reduced frequency (RF) AMT with a range of 10 – 10^3 Hz.

Occam 2D inversion files were created with MTpy with mesh parameterised to 3 km depth and a first layer thickness of 5 m. All inversions used both the TE and TM components, were started from a 100 Ωm half space and were parameterised to invert for static shift. Inversions were run with n = 60, rho error floor = 5% and phase error floor = 0.2°. Occam inversions ran to an average RMS of 1.2.

4.6 Real data results

Typical results for the rj-McMC and Occam 2D inversions, including data fits are presented in Figure 4.9 and 4.10 respectively. Results for all Occam 2D inversion profiles are displayed in Figure 4.11 and results from all rj-McMC inversions are available in Appendix D.1 and D.2.

The rj-McMC inversions commonly displayed structures similar to those in Figure 4.9a, with a low-resistivity top layer (C1), a moderate-resistivity layer with high uncertainty (R1), a low/moderate-resistivity layer with low uncertainty (C2), and a high-resistivity basement layer (R2). Some inversions were missing the C1 features, consistent with the uneven distribution of the Eromanga Basin sediments across the study area. The R1 layer is also either missing from some of the 1D inversions, or not interpretable due to poor inversion results (see Figure 4.9b). The RF AMT and BBMT inversions were able to produce similar features to the FF AMT inversions despite the reduced frequency range of the input data (Figure 4.9). Figure 4.12a has a side by side comparison of a RF AMT and FF AMT inversions for three sites and the associated change point curves and interpretation picks. Sites with poorer results for the FF AMT inversion can generally be attributed to the presence of deadband noise (see Appendix D.2 to compare RF AMT and FF AMT inversions).

The same four-layer resistivity structure seen in the 1D inversions is evident in both the AMT and BBMT 2D Occam inversion results (Figure 4.10 and 4.11) for the majority of the study area. Inversion results for the BBMT data typically have higher roughness and poorer lateral continuity of structures than the AMT inversions, due primarily to increased station spacing. This difference aside, similar features are evident in the AMT and BBMT data (Figure 4.10 and 4.11). A small area in the east of the study area displays a two-layer resistivity signature (Figure 4.11). This area corresponds to a thickening of Eromagna Basin sediments (C1), and it is not obvious whether the moderately conductive C2 feature is absent or being shielded by the overlying sediments. The C2 feature is present on the two southern-most profiles which also have a thick extent for C1, suggesting that C2 may be absent on the eastern margin of the survey.

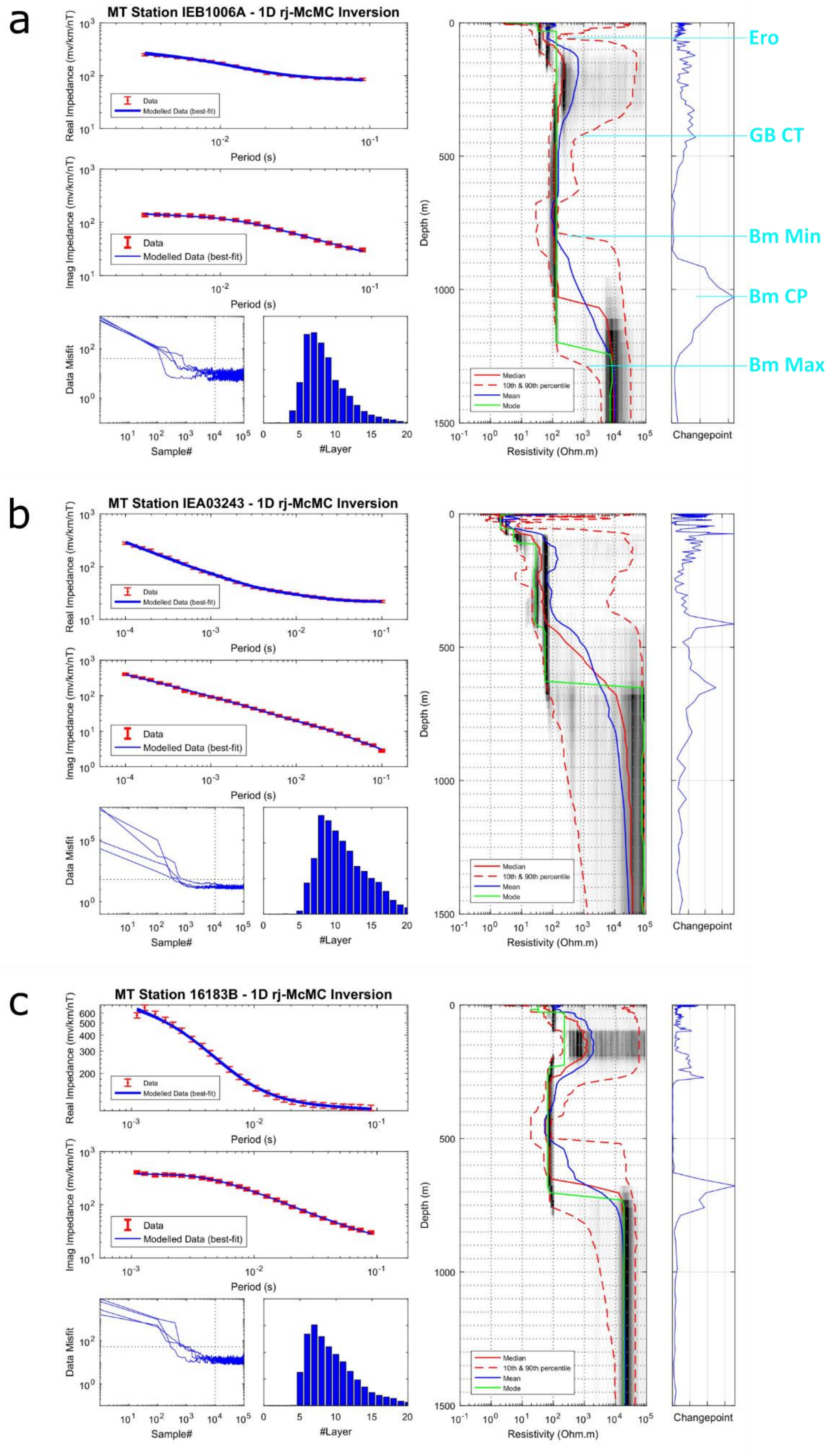

Figure 4.9. Typical rj-McMC 1D MT inversion results. a) a BBMT site with interpretation picks indicated in cyan, b) a full frequency AMT site and c) reduced frequency AMT site. The data fit, misfit convergence, predicted number of layers and change point prediction curve for each site are displayed alongside the inversion model. The black-white colouration on the 1D model indicates model probability, with black areas indicating high probability structure. Inversion result plots for all MT sites can be found in Appendix D.2.

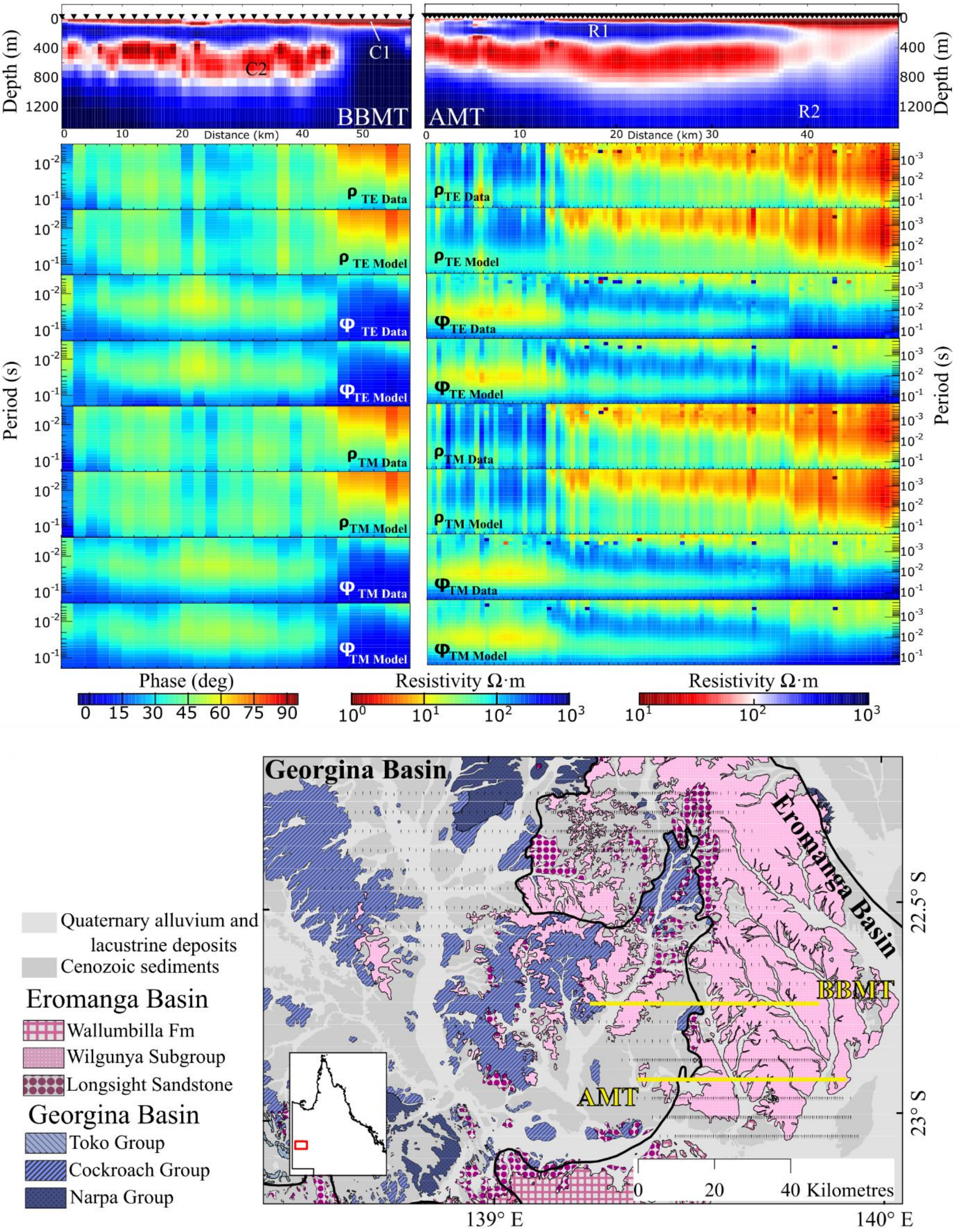

Figure 4.10. Typical Occam 2D inversion results and data fit for BBMT (left) and AMT (right). Apparent resistivity (ρ) and phase (ϕ) pseudosections for the observed data compared to the calculated response (model) are displayed below the inversion section (top). Transverse electric (TE) and transverse magnetic (TM) modes both displayed. R1, R2, C1 and C2 features referred to in text are indicated. Location of two inversions indicated in yellow in bottom panel.

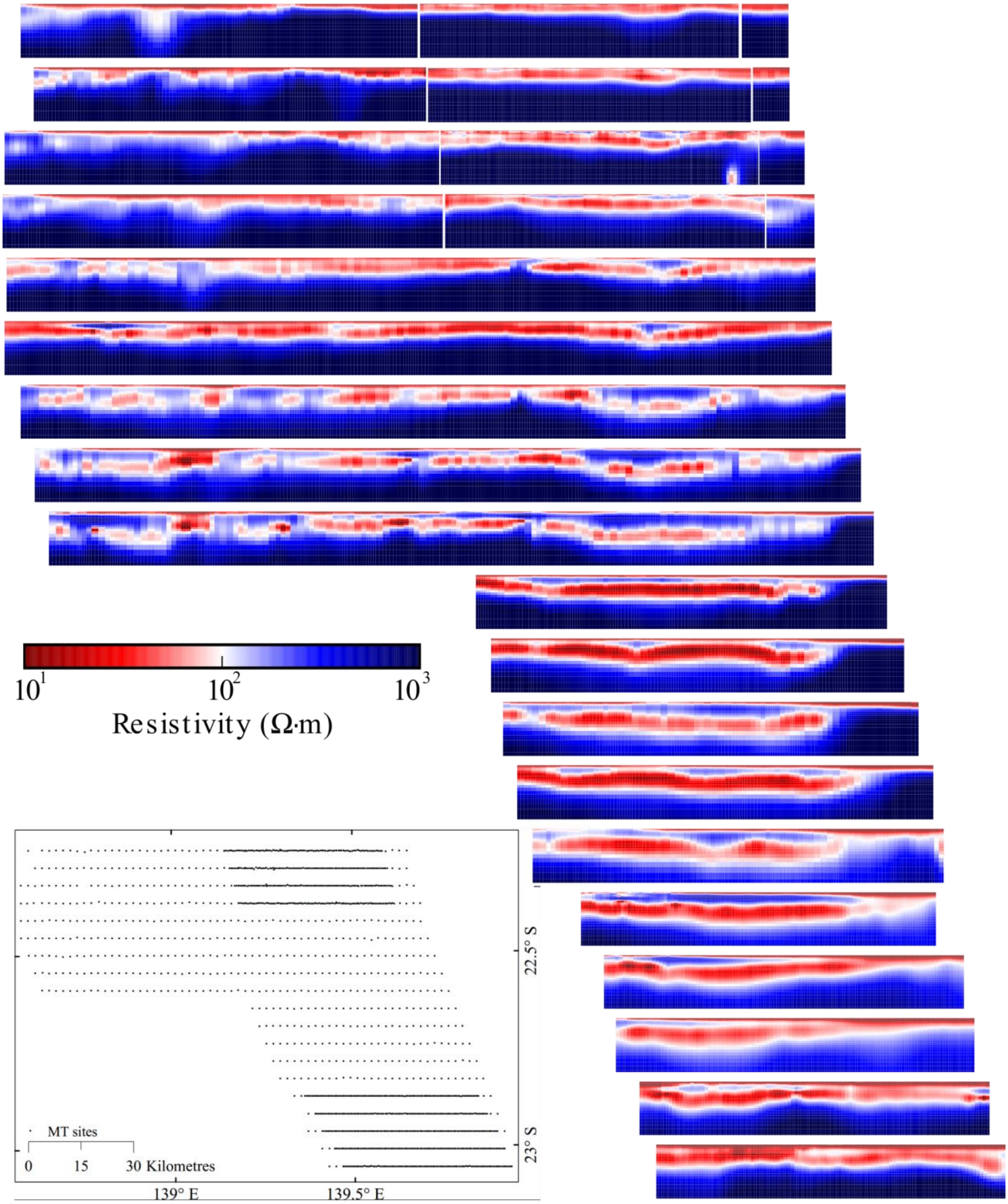

Figure 4.11. Occam 2D inversion results for all profiles in study area. Where BBMT and AMT data are both present, only AMT inversion results are displayed. Location of all stations used for modelling shown in inset. Sections have a depth extent of 1500 m.

4.6.1 Interpretation workflow and criteria

Interpretation of the 1D inversion results was conducted in Geolog®, then integrated with the 2D inversion results in GoCAD® (Figure 4.12) to produce the final interpretation (Figure 4.13). The mean, mode, median, p10 and p90 curves from each rj-McMC inversion were imported into Geolog® alongside the change point curves for interpretation. The RF and FF AMT results were plotted side-by-side for comparison (Figure 4.12; see Appendix C.1 for a record of which frequency range inversion was used for the interpretation at each site). Some of the 1D inversion results were not used due to poor data fit (also indicated in Appendix C.1).

Five interpretation ‘picks’ were generated in Geolog® based on the following criteria for the 1D inversions (see also Figure 4.9a for these picks applied to real data):

1. Ero (base Eromanga Basin). Identifiable as the first significant increase in the mean/mode/median resistivity. Where possible, the Ero pick is interpreted using the change point peak. Resistivity of the first layer typically between 1 Ωm and 10 Ωm, where the surface resistivity is greater than 10 Ωm and there is no significant step in resistivity no Ero unit is picked. Final Ero picks refined based on mapped surface geology (Figure 4.1a).
2. GB CT (Georgina Basin conductor top). Top of the section where the p10-p90 bounds are very narrow (< 1 order of magnitude).
3. Bm Min (basement minimum). Defined as the depth at which the p90 curve diverges from the mean, mode and medina curves below the GB CT pick.
4. Bm Max (basement maximum). The depth at which the p10 curve is greater than 1000 Ωm.
5. Bm CP (basement change point). Defined at the highest probability change point contained between the Bm Min and Bm Max picks.

GoCAD® was used to compare the 1D and 2D results, and create the final interpretation surfaces (Figure 4.12 and 4.13). The 1D inversion picks displayed a large amount of scatter but by combining them with the 2D inversions is was possible to generate a cohesive interpretation (Figure 4.13). A schematic representation of how the labelled resistivity features from the 2D inversion, related to the picked interfaces from 1D inversions and the macroscale geology is found in Figure 4.14.

4.6.2 Interpretation and estimation of uncertainty

Three surfaces make up the final interpretation derived from integration of the 1D and 2D inversion results: base of Eromanga; top of Georgina Basin conductor; and basement (Figure 4.13). The final extents of the base of Eromanga Basin interpretation (Figure 4.13a) were constrained by the limits of outcropping Eromanga Basin sediments (Figure 4.1). The interpretation of the depth to the top of the Georgina Basin conductor (C2) covers the entire area but there are two parts of the interpretation, indicated as hatched areas in Figure 4.13c where it is uncertain whether that unit is present. The third interpretation surface is the base Georgina/basement interface (Figure 4.13e).

Each interpreted interface has an uncertainty due to the scattering of 1D interpretation picks as shown in Figure 4.12b. Some of the scatter in 1D inversion results is due to the presence of static shift at some sites, identified during data analysis. The presence of multi-dimensionality (i.e. 2D data) identified during data analysis also contributes to differences between the 2-D and 1-D inversion results and to some of the local variation in interface depth. Because of these two factors, the error estimation based on the 1D inversion results may be higher than necessary. The difference between the final interpretation surface (e.g. Base Eromanga) and the 1D inversion pick at each site was calculated and is displayed in Figure 4.13b, d and f. Figure 4.13g has a corresponding histogram plot for the uncertainty for each layer. The Base Eromanga and top Georgina conductor layers have an approximately normal distribution, indicating that the final interpretations surfaces are a fair representation of the 1D inversion results. The error for each surface is randomly distributed across the project area, indicating there are no spatial biases in the interpreted surfaces. The histogram for the base Georgina surface is slightly left skewed indicating that the final interpretation surface is shallower on average than the 1D inversions suggest. Based on the histograms an error of ±20 m is assigned to the base Eromanga surface, ±75 m to the top Georgina conductor and ±200 m to the basement surface.

Due to the poorly constrained nature of the basement interface an additional estimate of uncertainty was calculated based on comparison between the Bm Min and Bm Max picks from 1D inversion, and the final base Georgina (basement) surface interpretation (Figure 4.15).

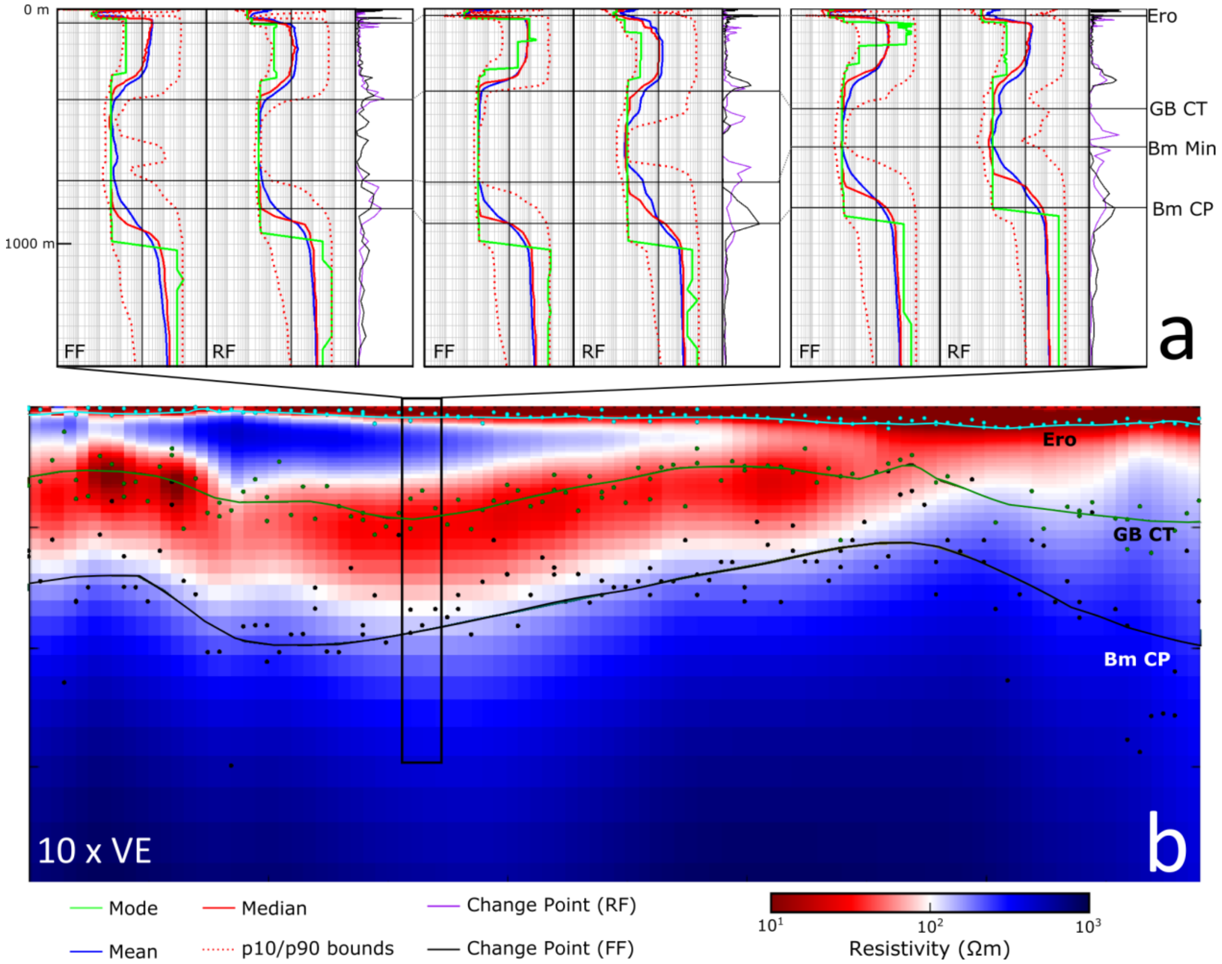

Figure 4.12. Integrated 1D and 2D inversion interpretation summary. a) RF and FF inversion for three sites as displayed in Geolog® with associated picks. b) Picks from 1D inversions (see Figure 4.14) shown as points for Bm CP, Ero and GB CT layers with associated interpretation surfaces.

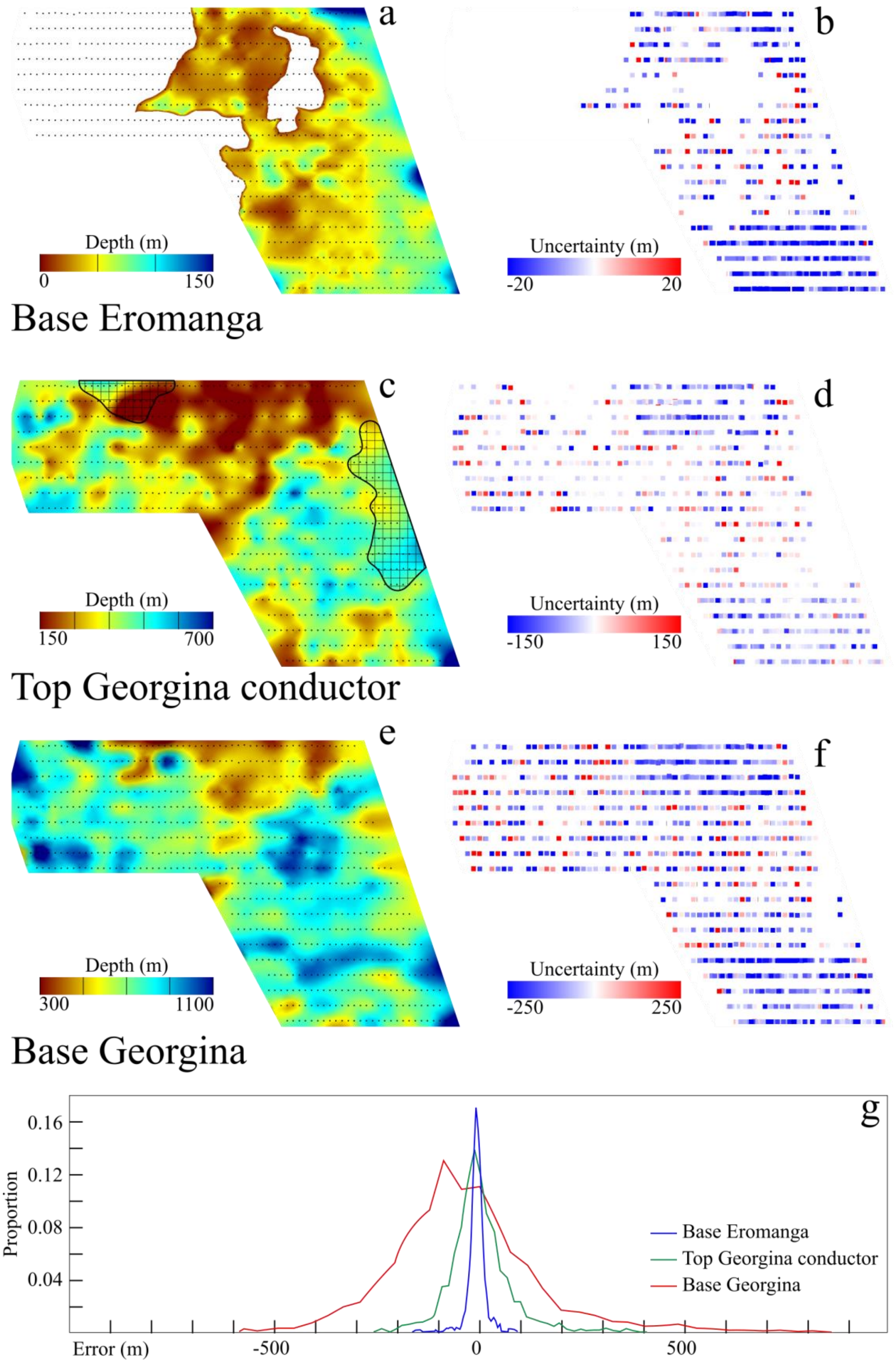

Figure 4.13. Interpreted geological layers and associated uncertainty. a) Interpreted base of Eromanga Basin, extents limited to location of Eromanga Basin sediments (Figure 4.1b). b) Uncertainty of base of Eromanga at each MT site, where a negative value indicates the final interpretation surface is shallower than the 1D inversion result, and a positive value indicates the interpretation is deeper than the 1D inversion result at that site. c) Interpreted top of Georgina conductor (C2), black hatched areas indicate areas where the unit may be missing. d) Uncertainty of the top of Georgina conductor layer based on difference between interpretation surface and 1D inversion pick. e) Interpreted base Georgina (basement). f) Uncertainty of the base Georgina interface based on difference between interpretation surface and 1D inversion pick. g) histogram distribution of errors for each interpretation layer.

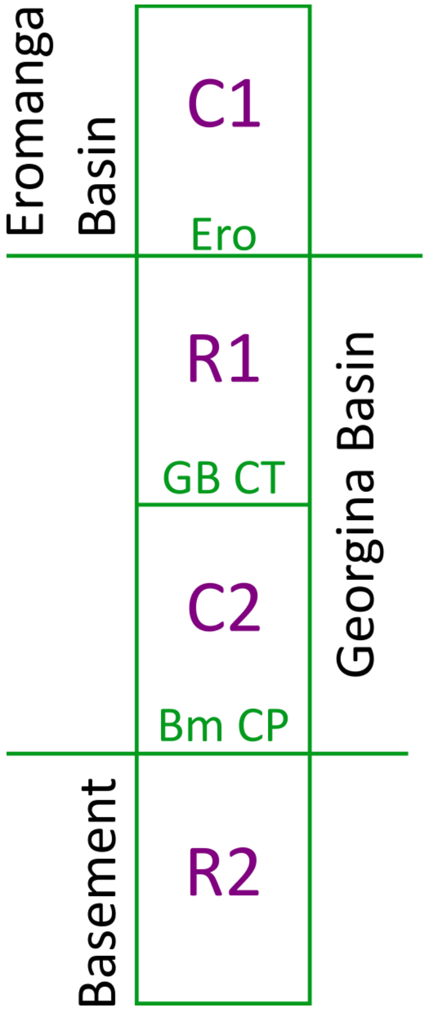

Figure 4.14. Schematic summary of interpretation. Labelled features from 2D inversion are indicated in purple and picked interfaces based on 1D inversions are indicated in green. Macroscale geological subdivisions are indicated in black.

Synthetic testing suggests that the true basement interface will lie between the Bm Min and Bm Max, so the difference between these values and the base Georgina (basement) surface should provide a better estimate of the uncertainty than the scatter in 1D inversion results (Figure 4.13f). The median difference between the Bm Min pick and the interpretation surface is 200 m, while the median difference for the Bm Max pick is 446 m. The percentage difference between the Bm Min / Bm Max and the base Georgina surface was also calculated (Figure 4.15d). The uncertainty analysis suggests that the true basement surface may lie between 30% shallower and 60% deeper than the final interpretation.

The new basement interpretation is broadly similar to the Frogtech Geoscience (2018) result (Figure 4.16). The Frogtech (2018) interpretation contains more detailed basement geometry, however it fails to accurately predict known basement intersects. Consequently, it is difficult understand the reliability of the interpretation. Our new interpretation of basement depth underestimates true basement depth when compared to drilling (Figure 4.16b), but if used together with the uncertainty estimates is within error of true depths. Figure 4.16i and ii show a comparison of our interpretation’s basement depth predictions, the Frogtech (2018) interpretation and the true basement depth from drilling. While the large magnitude of the uncertainty associated with the basement interface in our interpretation is not ideal for de-risking mineral exploration, it does represent an improvement in accuracy on the Frogtech (2018) interpretation.

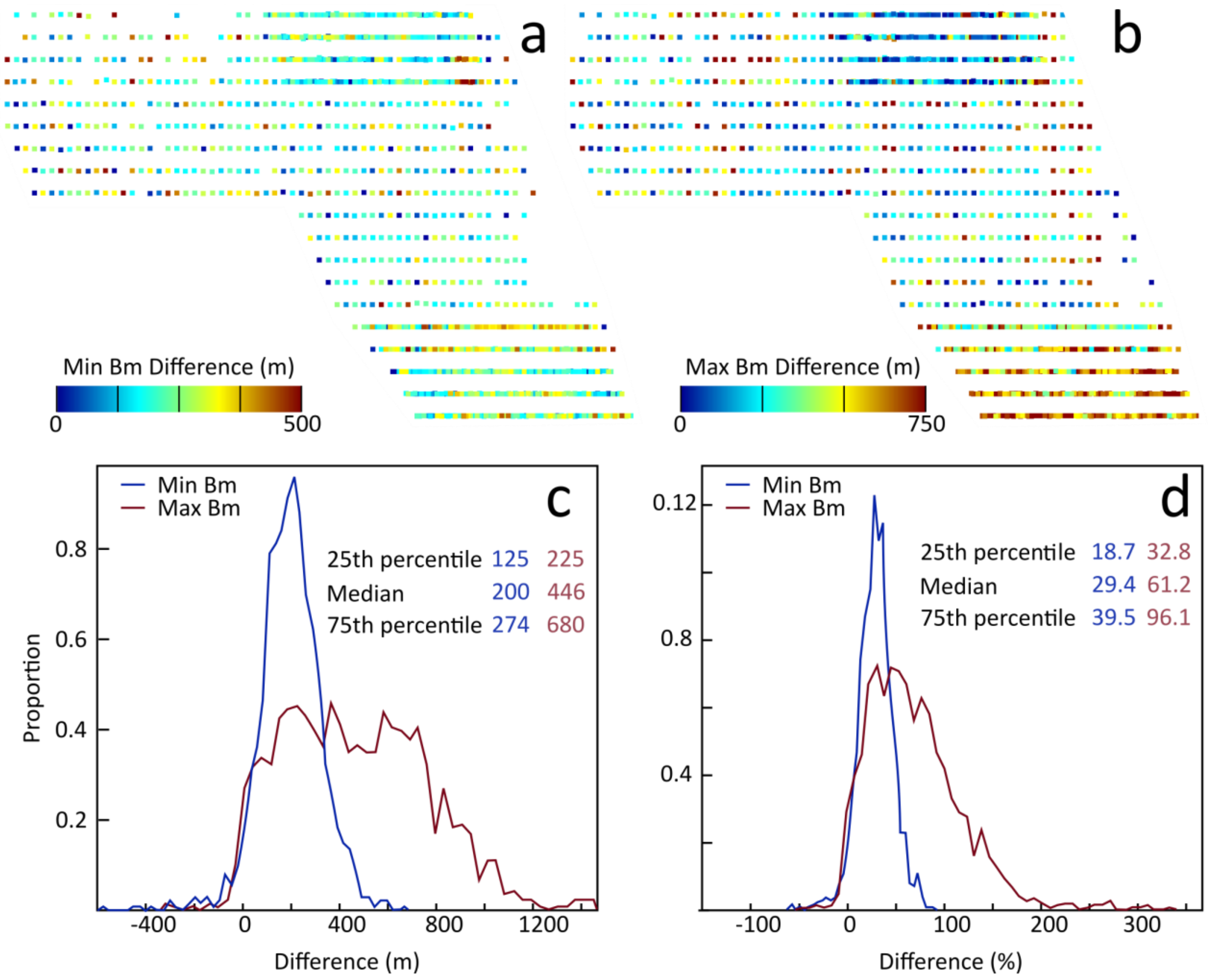

Figure 4.15. Uncertainty of basement interface. a) Calculated difference between the base Georgina (basement) surface at the Bm Min at each site. b) Calculated difference between the base Georgina (basement) surface at the Bm Max at each site. c) Histogram distribution of the difference (m) between the Bm Min and Bm Max and the final interpretation at each MT site. d) Histogram distribution of the difference (%) between the Bm Min and Bm Max and the final interpretation at each MT site.

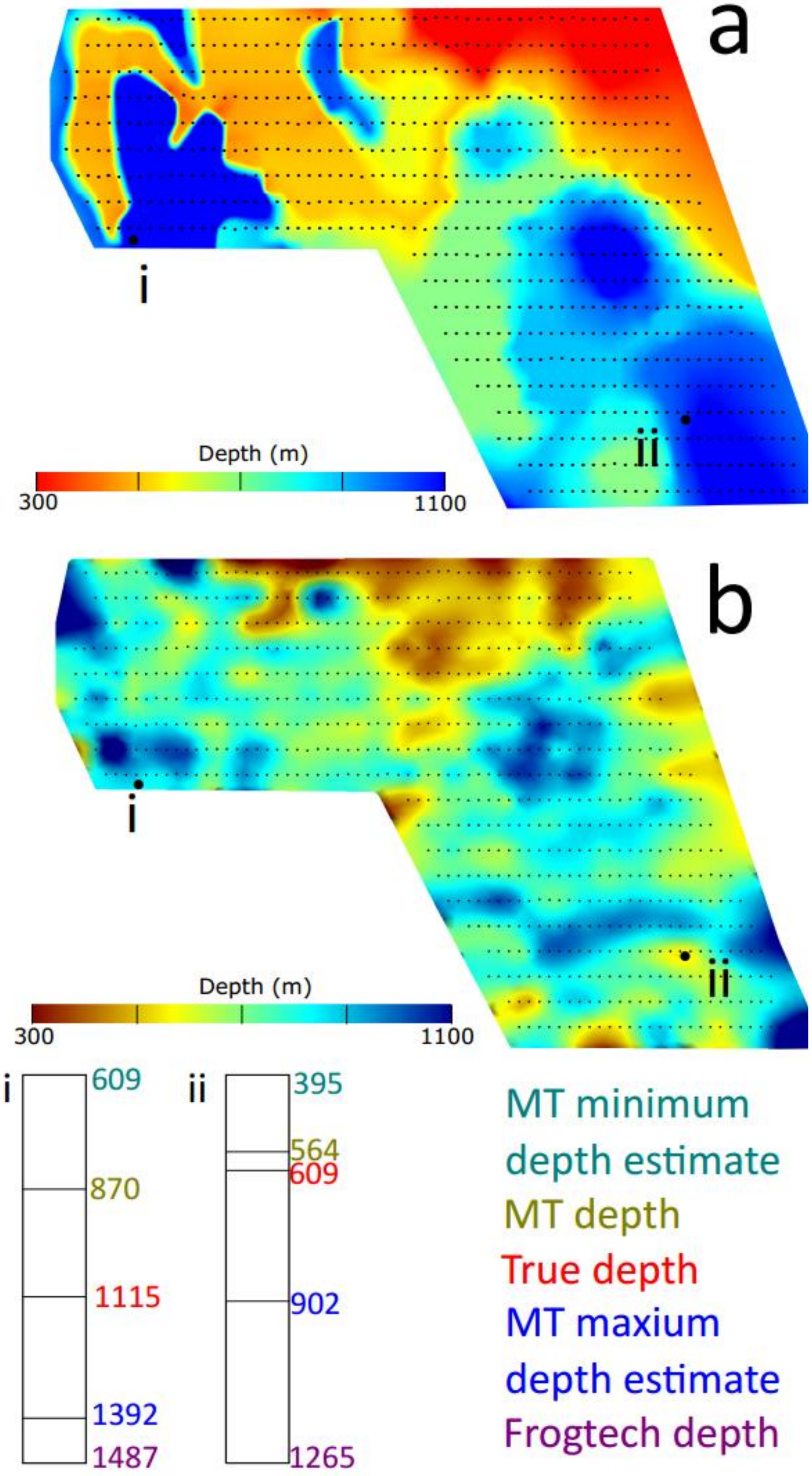

Figure 4.16. Comparison of new and existing basement interpretations to known drilling intercepts. a) the Frogtech Geoscience (2018) interpretation overestimates the true basement depths. b) New interpretation of basement underestimate the true depth of basement, but when used in association with error estimates is consistent with the known depths.

4.7 Discussion

The presented methodology uses synthetic modelling based on downhole resistivity data to select inversion parameters and guide interpretation. The resulting interpretation provides an updated depth to basement surface for the study area, with definition of additional intra-basin layers unavailable in previous interpretations. Importantly, all interpretation surfaces have error estimates, ensuring that results are used in accordance with their reliability.

The final interpretation uses the 2D inversion results to guide interpretation of the scattered 1D inversion results, with the 1D and 2D inversions generally producing comparable results. A notable exception to this generalisation is the disparity between 1D and 2D inversion in the east and north (see Figure 4.12b; hatched areas on Figure 4.13c). These areas correspond to increased skew values and ellipticity (Figure 4.8m), suggesting they have a 2D electrical character. Consequently, the difference between the 1D and 2D inversions may be entirely due to the 1D inversion being inappropriately applied to 2D data. The interpretation in these two areas should be treated with additional caution.

The new basement interpretation is broadly similar to the Frogtech Geoscience (2018) result (Figure 4.16). The Frogtech (2018) interpretation contains more detailed basement geometry, however it fails to accurately predict known basement intersects. Consequently, it is difficult understand the reliability of the interpretation. Our new interpretation of basement depth underestimates true basement depth when compared to drilling (Figure 4.16b), but if used together with the uncertainty estimates is within error of true depths. It is possible that the interpretation surface underestimates the true basement depth due to the slightly biased nature of the basement interpretation identified in Figure 4.13g. Figure 4.16i and ii show a comparison of our interpretation’s basement depth predictions, the Frogtech (2018) interpretation and the true basement depth from drilling. While the large magnitude of the uncertainty associated with the basement interface in our interpretation is not ideal for de-risking mineral exploration, it does represent an improvement in accuracy on the Frogtech (2018) interpretation. Validation of our interpretation is based on available drilling, limited to only two holes. Ideally, additional drilling is required to better validate the accuracy of the interpretation.

Two methods for estimating interpretation uncertainty were undertaken. Both methods of estimating interpretation uncertainty are objectively derived, rather than being subjectively determined, limiting the influence of interpreter bias. The first method of uncertainty estimation uses the scattering of interpretation picks generated from the 1D inversion results as a proxy inversion uncertainty (Figure 4.13). Because the 1D and 2D inversions were parameterised differently and use different inversion methodologies - deterministic vs. probabilistic - the difference in inversion results is likely due to the inherently non-unique nature of inversion modelling. The additional uncertainty estimation for the basement surface was derived from the 1D probabilistic inversion results. Synthetic modelling suggested that the basement interface will be between the Bm Min and Bm Max picks (Figure 4.4; see Figure 4.9a for selection criteria for Bm Min and Bm Max. The median distance between the interpreted basement surface and these two picks at each site as a percentage was used as the final estimate of uncertainty. Use of the median value means the uncertainty of the basement surface may be underestimated in some areas, however comparison to the available drilling supports the selected error margins.

The intra-basin layers defined in our interpretation provide clues that there may be a difference between the resistivity structure of the Toko Syncline and Bourke River Structural Belt (Figure 5.1a). A macro-scale change in resistivity character for the eastern vs. western parts of the survey was evident in the synthetic modelling. Bradley1 and Todd1 in the west both have a generalised three-layer basin response while Beantree1 has a simple two-layer basin response. The moderate-high resistivity Georgina Basin unit (R1) was not present in Beantree1. This trend also appears in the 2D inversion results and may represent a difference in sub-basin geology from the Toko Syncline in the west to the Bourke River Structural Belt in the east. Additional investigation would be required to determine if this is a real trend or simply variability in a small dataset. More broadly, the new interpretation of basin units from this study extends the location of the Georgina Basin sequences further to the south east than previous interpretations (Figure 4.1a), suggesting the basin is larger than previously thought.

There are a number of advantages and limitations associated with the presented approach for characterizing basin morphology from MT data. The primary advantage is that the synthetic modelling allows insight gained from a small amount of non-coincident constraining information to be used to better understand inversion results. Synthetic modelling was useful to determine which inversion features were well constrained by the data and select inversion parameters. The additional hypothesis testing style of synthetic modelling conducted to determine the resolvability of the basement interface was vital to understanding the true degree to which the MT data were insensitive to the basement interface. The method is especially applicable to data poor areas. As MT gains increased acceptance in the mineral exploration industry, more data will be collected in greenfields areas with limited amount of constraining information.

The presented method allows a large number of inversion results to be integrated into a single, cohesive interpretation. Our study utilises over 2000 1D inversion results and 22 2D inversion profiles. By generating 1D interpretation picks in a software designed to handle drilling logs, and integrating these picks with the 2D inversion results in a 3D modelling software, we made the task of interpreting such a number of inversion results manageable.

A significant limitation of the presented methodology for using synthetic modelling to inform MT interpretation is that it assumes lateral consistency in resistivity signatures. Extrapolating the results of the current study to the broader Georgina Basin is problematic due to the known presence of thick Neoproterozoic sediments which would be difficult to distinguish from basement. More complex geological settings also present a challenge to the presented method however they do not preclude the use of this method. Additional synthetic modelling would need to be conducted to cover the range of possible geological models in such environments. Practically this work is most applicable to sedimentary basins where lateral continuity of resistivity character and geological units is a reasonable assumption. A sedimentary basin environment, such as the one in this study, allows conclusions from fewer synthetic models to be more broadly applied than would be possible in complex crystalline basement terranes.

4.8 Conclusions

This study explores the use of synthetic modelling of downhole resistivity data to aid in construction a geological interpretation of MT inversions in the context of basin morphology. The particular challenge addressed in this study was how to make use of sparse or non-coincident constraining information in a way that improves interpretation outcomes.

Downhole resistivity data from petroleum wells were used to generate 1D resistivity models of the Eromanga and Georgina Basins in the study area. Synthetic MT data were generated from the models and used to demonstrate the suitability of various MT inversion codes for resolving the expected electrical structure. Shallow basin units could be adequately interpreted from any of the codes tested. While the basement interface was poorly constrained. We chose a combination of Occam2D and rj-McMC 1DMT to provide surety that the 2D data was being adequately modelled and provide uncertainty estimates in interface depths.

A depth to basement surface which accurately reproduces known drilling intersects was produced with an associated error estimate. It was also possible to create new interpretations for the base of the Eromanga Basin and the top of a conductive package in the Georgina Basin. Importantly the combination of probabilistic inversion and synthetic modelling enabled creation of uncertainty estimates for each of the interpreted surfaces. This work highlights the difficulty in interpreting the resistive basement interface, especially where independent constraint is sparse and knowledge of the petrophysical character of cover is unavailable.

Acknowledgements

Published with the permission of the Chief Government Geologist of the Geological Survey of Queensland. This work was completed as part of a PhD at the University of Adelaide. The work was conducted with the support of supercomputing resources provided by the Phoenix HPC service at the University of Adelaide. Naser Meqbel is thanked for the use of his 3D Grid software, and Alison Kirkby and Kate Robertson for MTpy support. The authors thank SC Constable and colleagues for the Occam1D and 2D codes, R. Brodie et.al for rj-McMC codes, and R Cockett et al. for SimPEG codes; all of which are made freely available to the academic community. We also thank the Geological Survey of Queensland for access to state geophysical and geological databases.

CHAPTER
FIVE

SUMMARY AND CONCLUSIONS

5.1 Summary

This thesis explores methods for dealing with the inherently non-unique nature of MT inversion, with the goal of producing better geological interpretations. The study was focused on the undercover, southern extension of the Mount Isa Province, which is poorly understood at all geological scales. This limited understanding has led to reduced exploration success, despite the high density of mineral occurrences in the adjacent outcropping portion of the Mount Isa Province (Figure 1.2). The poor historical exploration success prompted acquisition of a 1600 site MT survey which is the primary dataset used for this thesis. A complementary deep crustal seismic survey was also undertaken. Both surveys were acquired through a partnership between the Geological Survey of Queensland and Geoscience Australia and all data are freely available.

The MT dataset used for this thesis is a superficially un-complex dataset with minimal internal structures, and which is largely affected by out of area conductors on a regional scale. Despite the apparent simplicity, considered use of a range of inversion techniques, quantification of inversion uncertainty and integration with other datasets allowed a range of geological conclusions to be drawn from the data.

The fundamental research question posed in this thesis is given the inherently non-unique nature of MT inversion products, what methods can be employed in poorly understood, data-poor greenfields terranes to create geological interpretations commensurate with data limitations? Three studies aimed at addressing different aspects of this question were undertaken, presented in Chapters 2 – 4.

Chapter 2 presents methods of objectively assessing the variability of models produced during 3D MT inversion. The presented workflow leverages a sequential inversion methodology to test model variability, while minimising the computational demand of 3D inversion. The workflow is applicable to areas without independent constraining information and aims to improve quantification of inversion variability to inform interpretation. We also reinforce the clear impact inversion parameterisation in ModEM 3D has on inversion outcomes, and underscore the dangers of using a single inversion model to construct an interpretation.

Chapter 3 integrates the results of 3D MT inversion with new deep crustal seismic interpretation and potential field data to refine our understanding to the southern Mount Isa Province. A primary aim of this study was to determine if there evidence of a suture in the project area. The inversion variability from Chapter 2 is considered together with independent data to produce an interpretation that would not be possible from consideration of the MT inversion results alone. No suture is present in the study area from the data examined, however there was an indication that one may exist to the east. The study area contains a major west-dipping crustal feature which was active pre- and post-Barramundi Orogeny. The feature is also spatially associated with a low-resistivity anomaly and represents a potential exploration target. A regional high-resistivity trend was identified through the central part of the Mount Isa Province, but additional data acquisition would be required to verify and interpret this feature. The work presented in this chapter is an example of integration of uncertainty and independent constraint to improve geological interpretation.

Chapter 4 is focused on resolving the depth to basement and basin morphology of the Neoproterozoic-Mesozoic cover basins in the project area. Resolving the depth to basement from MT data is inherently difficult due to the data's insensitivity to the top of a resistive package (in this case the top of basement). A typical approach is to constrain the inversion with other data such as gravity data. We did not have any such data at sufficient resolution available to constrain our inversion. Instead, we used a combination of 1D probabilistic inversion, 2D deterministic inversion and synthetic modelling of downhole resistivity data to inform inversion, interpretation and estimate the uncertainty of the final interpretation. This chapter addresses the case where independent constraining information is not coincident with the project dataset and offers an approach to make use of such information.

5.2 Conclusions and future directions

The works presented in this thesis represent multi-scale, multi-method analysis of the Isa Extension MT dataset along with the derivation of associated geological results. The variability of modelling results presented serve as a cautionary example of relying on a single inversion model. The strong dependency between inversion parameterisation and model features is clearly demonstrated in Chapter 2, as is the high degree of variability present in MT inversion features. It is possible that the inversion variability present in our study is linked to the low data variability of the Isa Extension dataset, but that does not imply that datasets with more prominent resistivity features are immune to similar limitations.

There were two primary geological aims for the thesis: better define the depth to Proterozoic basement to de-risk mineral exploration; and improve the understanding of the deep structure of the project area, and any implications for mineral exploration.

Despite the limitations of MT as a method for determining basement depths, we demonstrate that it can provide meaningful improvement in the accuracy of the basement interpretation if analysis of inversion variability is used to determine the resolution limitations. Our basement interpretation is more accurate than the existing interpretation and assists in de-risking mineral exploration.

Integration of MT inversion results with potential field and seismic data was used in Chapter 3 to provide new insight into the deep structure of the southern Mount Isa Province. Consideration was given to inversion variability to ensure resistivity structures were not over interpreted. The presence of a suture in the project area was dismissed and a major west-dipping feature was imaged which represents a new exploration target in the area.

More broadly, we demonstrate that an understanding of data resolution and model uncertainty does enable production of new, worthwhile interpretations even in difficult circumstances. These findings support the use of MT as a regional exploration tool that can be used in greenfield terranes; although independent constraint in the form of complementary geophysical, geological or petrophysical datasets assists in constructing a quality interpretation.

A number of avenues for further research were highlighted during this project:

1. Application of the workflow presented in Chapter 2 to other datasets is required to better understand its broad-scale applicability.
2. More extensive seismic interpretation with associated gravity modelling, particularly to the east of the project area.
3. Testing of the depth to basement/basin interpretation with drilling.

4. More study into potential sub basin differences between the Toko Syncline and Bourke River Structural Belt.
5. Additional work to discern what scale of anomaly could be shielded in the shallow basement by the basin sequences would provide valuable additional information to assist explorers in the use of the MT dataset.
6. A study to characterise the influence of the Carpentaria Conductivity Anomaly on the impedance and tipper MT data across Queensland, with a particular aim to characterising the length-scale of any impact on BBMT data.
7. Further MT data acquisition and modelling to understand the resistivity structure of the Mount Isa Province and implications for its evolution

BIBLIOGRAPHY

Adetunji, A.Q., Ferguson, I.J., Jones, A.G., 2014. Crustal and lithospheric scale structures of the Precambrian Superior–Grenville margin. Tectonophysics 614, 146–169. https://doi.org/10.1016/j.tecto.2013.12.008

Allègre, C.J., Poirier, J.-P., Humler, E., Hofmann, A.W., 1995. The chemical composition of the Earth. Earth and Planetary Science Letters 134, 515–526. https://doi.org/10.1016/0012-821X(95)00123-T

Ambrose, G.J., Kruse, P.D., Putnam, P.E., 2001. Geology and hydrocarbon potential of the southern Georgina Basin, Australia. Appea Journal 41, 139–163.

Barbosa, V.C.F., Silva, J.B.C., Medeiros, W.E., 1997. Gravity inversion of basement relief using approximate equality constraints on depths. Geophysics 62, 1745–1757. https://doi.org/10.1190/1.1444275

Becken, M., Ritter, O., 2012. Magnetotelluric studies at the San Andreas Fault Zone: implications for the role of fluids. Surveys in Geophysics 33, 65–105. https://doi.org/10.1007/s10712-011-9144-0

Becken, M., Ritter, O., Park, S.K., Bedrosian, P.A., Weckmann, U., Weber, M., 2008. A deep crustal fluid channel into the San Andreas Fault system near Parkfield, California. Geophysical Journal International 173, 718–732. https://doi.org/10.1111/j.1365-246X.2008.03754.x

Bedrosian, P.A., 2016. Making it and breaking it in the Midwest: Continental assembly and rifting from modeling of EarthScope magnetotelluric data. Precambrian Research 278, 337–361. https://doi.org/10.1016/j.precamres.2016.03.009

Bedrosian, P.A., 2007. MT+, Integrating Magnetotellurics to Determine Earth Structure, Physical State, and Processes. Surveys in Geophysics 28, 121–167. https://doi.org/10.1007/s10712-007-9019-6

Betts, P.G., Armit, R.J., Stewart, J., Aitken, A.R.A., Ailleres, L., Donchak, P., Hutton, L., Withnall, I., Giles, D., 2016. Australia and Nuna. Geological Society, London, Special Publications 424, 47–81. https://doi.org/10.1144/SP424.2

Betts, P.G., Giles, D., Foden, J., Schaefer, B.F., Mark, G., Pankhurst, M.J., Forbes, C.J., Williams, H.A., Chalmers, N.C., Hills, Q., 2009. Mesoproterozoic plume-modified orogenesis in eastern Precambrian Australia: Proterozoic plume modified orogensis. Tectonics 28. https://doi.org/10.1029/2008TC002325

Betts, P.G., Giles, D., Lister, G.S., Frick, L.R., 2002. Evolution of the Australian lithosphere. Australian Journal of Earth Sciences 49, 661–695. https://doi.org/10.1046/j.1440-0952.2002.00948.x

Bibby, H.M., Caldwell, T.G., Brown, C., 2005. Determinable and non-determinable parameters of galvanic distortion in magnetotellurics. Geophysical Journal International 163, 915–930. https://doi.org/10.1111/j.1365-246X.2005.02779.x

Bierlein, F., Betts, P., 2004. The Proterozoic Mount Isa Fault Zone, northeastern Australia: is it really a ca. 1.9 Ga terrane-bounding suture? Earth and Planetary Science Letters 225, 279–294. https://doi.org/10.1016/j.epsl.2004.06.022

Bierlein, F., Black, L., Hergt, J., Mark, G., 2008. Evolution of Pre-1.8Ga basement rocks in the western Mt Isa Inlier, northeastern Australia—Insights from SHRIMP U–Pb dating and in-situ Lu–Hf analysis of zircons. Precambrian Research 163, 159–173. https://doi.org/10.1016/j.precamres.2007.08.017

Blaikie, T.N., Betts, P.G., Armit, R.J., Ailleres, L., 2017. The ca. 1740-1710 Ma Leichhardt Event: Inversion of a continental rift and revision of the tectonic evolution of the North Australian Craton. Precambrian Research. https://doi.org/10.1016/j.precamres.2017.02.003

Boerner, D.E., Kurtz, R.D., Craven, J.A., 1996. Electrical conductivity and Paleo-Proterozoic foredeeps. Journal of Geophysical Research: Solid Earth 101, 13775–13791. https://doi.org/10.1029/96JB00171

Bologna, M.S., Egbert, G.D., Padilha, A.L., Pádua, M.B., Vitorello, Í., 2017. 3-D inversion of complex magnetotelluric data from an Archean-Proterozoic terrain in northeastern São Francisco Craton, Brazil. Geophysical Journal International 210, 1545–1559. https://doi.org/10.1093/gji/ggx261

Booker, J.R., 2014. The magnetotelluric phase tensor: a critical review. Surveys in Geophysics 35, 7–40. https://doi.org/10.1007/s10712-013-9234-2

Brasse, H., 2002. The Bolivian Altiplano conductivity anomaly. Journal of Geophysical Research 107. https://doi.org/10.1029/2001JB000391

Brodie, R., Jiang, W., 2018. Trans-dimensional Monte Carlo inversion of short period magnetotelluric data for cover thickness estimation. Australian Exploration Geoscience Conference, Sydney.

Cai, H., Zhdanov, M.S., 2017. Joint inversion of gravity and magnetotelluric data for the depth-to-basement estimation. IEEE Geoscience and Remote Sensing Letters 14, 1228–1232. https://doi.org/10.1109/LGRS.2017.2703845

Cai, H., Zhdanov, M.S., 2015. Magnetotelluric inversion for depth-to-basement estimation. Presented at the SEG New Orleans Annual Meeting, Society of Exploration Geophysicists, SEG New Orleans Annual Meeting, pp. 874–878. https://doi.org/10.1190/segam2015-5880335.1

Caldwell, T.G., Bibby, H.M., Brown, C., 2004. The magnetotelluric phase tensor. Geophysical Journal International 158, 457–469. https://doi.org/10.1111/j.1365-246X.2004.02281.x

Carreira, V.R., La Terra, E.F., Fontes, S.L., 2018. Density model for the central part of Parana Basin, using magnetotellurics as basement constraint, southern portion of Brazil. Revista Brasileira de Geofísica 36, 59. https://doi.org/10.22564/rbgf.v36i1.893

Cawood, P.A., Korsch, R.J., 2008. Assembling Australia: Proterozoic building of a continent. Precambrian Research 166, 1–35. https://doi.org/10.1016/j.precamres.2008.08.006

Chamalaun, F., Barton, C., 1990. Comprehensive mapping of Australia’s geomagnetic variations. Eos, Transactions American Geophysical Union 71, 1867. https://doi.org/10.1029/90EO00376

Chamalaun, F.H., Lilley, F.E.M., Wang, L.J., 1999. Mapping the Carpentaria conductivity anomaly in northern Australia. Physics of the Earth and Planetary Interiors 116, 105–115. https://doi.org/10.1016/S0031-9201(99)00126-0

Chave, A.D., 2014. Magnetotelluric data, stable distributions and impropriety: an existential combination. Geophysical Journal International 198, 622–636. https://doi.org/10.1093/gji/ggu121

Chave, A.D., Jones, A.G. (Eds.), 2012. The magnetotelluric method: theory and practice. Cambridge University Press, New York.

Chave, A.D., Smith, J.T., 1994. On electric and magnetic galvanic distortion tensor decompositions. Journal of Geophysical Research: Solid Earth 99, 4669–4682. https://doi.org/10.1029/93JB03368

Chen, J., Hoversten, G.M., Key, K., Nordquist, G., Cumming, W., 2012. Stochastic inversion of magnetotelluric data using a sharp boundary parameterization and application to a geothermal site. Geophysics 77, E265–E279. https://doi.org/10.1190/geo2011-0430.1

Choo, H., Song, J., Lee, W., Lee, C., 2016. Impact of pore water conductivity and porosity on the electrical conductivity of kaolinite. Acta Geotechnica 11, 1419–1429. https://doi.org/10.1007/s11440-016-0490-4

Cockett, R., Kang, S., Heagy, L.J., Pidlisecky, A., Oldenburg, D.W., 2015. SimPEG: An open source framework for simulation and gradient based parameter estimation in geophysical applications. Computers & Geosciences 85, 142–154. https://doi.org/10.1016/j.cageo.2015.09.015

Constable, S.C., 1992. Electrical studies of the Australian lithosphere. Geological Society of Australia, Special Publication 17, 121–140.

Constable, S.C., Parker, R.L., Constable, C.G., 1987. Occam’s inversion: A practical algorithm for generating smooth models from electromagnetic sounding data. Geophysics 52, 289–300. https://doi.org/10.1190/1.1442303

Conway, D., Simpson, J., Didana, Y., Rugari, J., Heinson, G., 2018. Probabilistic Magnetotelluric Inversion with Adaptive Regularisation Using the No-U-Turns Sampler. Pure and Applied Geophysics. https://doi.org/10.1007/s00024-018-1870-5

Cook, A.G., Bryan, S.E., Draper, J.J., Boltitude, R.J., Champion, D.C., Cross, A.J., Jell, J.S., Jell, P.A., McKellar, J.L., Purdy, D.J., 2013. Post-orogenic Mesozoic basins and magmatism, in: Jell, Peter A (Ed.), Geology of Queensland. Queensland Government, pp. 515–576.

Crowe, M.C.A., Milligan, P.R., 2015. Carpentaria conductivity anomaly revisited with preliminary magnetotelluric results from the SE Mt Isa Survey 2014. Presented at the ASEG-PESA 2015 - 24th international geophysical conference and exhibition, Perth.

Dai, L., Sun, W., Li, H., Hu, H., Wu, L., Jiang, J., 2018. Effect of chemical composition on the electrical conductivity of gneiss at high temperatures and pressures. Solid Earth 9, 233–245. https://doi.org/10.5194/se-9-233-2018

de Groot-Hedlin, C., Constable, S., 2004. Inversion of magnetotelluric data for 2D structure with sharp resistivity contrasts. Geophysics 69, 78–86. https://doi.org/10.1190/1.1649377

de Vries, S.T., Fry, N., Pryer, L., 2006. OZ SEEBASE Proterozoic basins study. FrOG Tech.

deGroot-Hedlin, C., Constable, S., 1990. Occam's inversion to generate smooth, two-dimensional models from magnetotelluric data. Geophysics 55, 1613–1624. https://doi.org/10.1190/1.1442813

deGroot-Hedlin, C., 1991. Removal of static shift in two dimensions by regularized inversion. GEOPHYSICS 56, 2102–2106. https://doi.org/10.1190/1.1443022

Dong, H., Wei, W., Jin, S., Ye, G., Zhang, L., Jing, J., Yin, Y., Xie, C., Jones, A.G., 2016. Extensional extrusion: insights into south-eastward expansion of Tibetan Plateau from magnetotelluric array data. Earth and Planetary Science Letters 454, 78–85. https://doi.org/10.1016/j.epsl.2016.07.043

Draper, J., 2007. Georgina Basin – an early Palaeozoic carbonate petroleum system in Queensland. APPEA Journal 47, 105–124.

Duba, A.G., Shankland, T.J., 1982. Free carbon & electrical conductivity in the Earth's mantle. Geophysical Research Letters 9, 1271–1274. https://doi.org/10.1029/GL009i011p01271

Egbert, G.D., Kelbert, A., 2012. Computational recipes for electromagnetic inverse problems. Geophysical Journal International 189, 251–267. https://doi.org/10.1111/j.1365-246X.2011.05347.x

Evans, D.A.D., Mitchell, R.N., 2011. Assembly and breakup of the core of Paleoproterozoic-Mesoproterozoic supercontinent Nuna. Geology 39, 443–446. https://doi.org/10.1130/G31654.1

Evans, R.L., 2012. Conductivity of Earth materials, in: Chave, A.D., Jones, A.G. (Eds.), The Magnetotelluric Method Theory and Practice. Cambridge University Press, pp. 50–95.

Favetto, A., Pomposiello, C., López de Luchi, M.G., Booker, J., 2008. 2D Magnetotelluric interpretation of the crust electrical resistivity across the Pampean terrane–Río de la Plata suture, in central Argentina. Tectonophysics 459, 54–65. https://doi.org/10.1016/j.tecto.2007.11.071

Fernandes, C.M., Fontes, S.L., La Terra, E.F., Miquelutti, L.G., Maurya, V.P., 2018. Electrical crustal structure of Alta Floresta Gold Province eastern sector, SW Amazon Craton, Brazil. Journal of South American Earth Sciences 86, 244–258. https://doi.org/10.1016/j.jsames.2018.06.022

Finlayson, D.M., 1982. Seismic crustal structure of the Proterozoic North Australian Craton between Tennant Creek and Mount Isa. Journal of Geophysical Research: Solid Earth 87, 10569–10578. https://doi.org/10.1029/JB087iB13p10569

Fishwick, S., Kennett, B.L.N., Reading, A.M., 2005. Contrasts in lithospheric structure within the Australian craton—insights from surface wave tomography. Earth and Planetary Science Letters 231, 163–176. https://doi.org/10.1016/j.epsl.2005.01.009

Frogtech Geoscience, 2018. North West Queensland SEEBASE® Study and GIS (Queensland Geological Record No. 2018/03). Brisbane Australia.

Gailler, L.-S., Martí, A., Lénat, J.-F., 2018. Complex structure of Piton de la Fournaise and its underlying lithosphere revealed by magnetotelluric 3D inversion. Journal of Volcanology and Geothermal Research. https://doi.org/10.1016/j.jvolgeores.2018.03.006

Gallardo-Delgado, L.A., Pérez-Flores, M.A., Gómez-Treviño, E., 2003. A versatile algorithm for joint 3D inversion of gravity and magnetic data. Geophysics 68, 949–959. https://doi.org/10.1190/1.1581067

Gao, J., Zhang, H., Zhang, S., Chen, X., Cheng, Z., Jia, X., Li, S., Fu, L., Gao, L., Xin, H., 2018. Three-dimensional magnetotelluric imaging of the geothermal system beneath the Gonghe Basin, Northeast Tibetan Plateau. Geothermics 76, 15–25. https://doi.org/10.1016/j.geothermics.2018.06.009

Garcia, X., Jones, A.G., 2008. Robust processing of magnetotelluric data in the AMT dead band using the continuous wavelet transform. Geophysics 73, F223–F234. https://doi.org/10.1190/1.2987375

Gessner, K., 2011. Hot lithosphere at Mount Isa: implications for Proterozoic tectonics and mineralisation. Australian Journal of Earth Sciences 58, 875–886. https://doi.org/10.1080/08120099.2011.571284

Gibson, G.M., Meixner, A.J., Withnall, I.W., Korsch, R.J., Hutton, L.J., Jones, L.E.A., Holzschuh, J., Costelloe, R.D., Henson, P.A., Saygin, E., 2016. Basin architecture and evolution in the Mount Isa mineral province, northern Australia: Constraints from deep seismic reflection profiling and implications for ore genesis. Ore Geology Reviews 76, 414–441. https://doi.org/10.1016/j.oregeorev.2015.07.013

Giles, D., Betts, P.G., Lister, G.S., 2002. Far-field continental backarc setting for the 1.80-1.67 Ga basins of northeastern Australia. Geology 30, 823.

Gokarn, S.G., Rao, C.K., Selvaraj, C., Gupta, G., Singh, B.P., 2013. Crustal evolution and tectonics of the Archean Bundelkhand craton, Central India. Journal of the Geological Society of India 82, 455–460. https://doi.org/10.1007/s12594-013-0176-6

Goleby, B.R., Huston, D.L., Lyons, P., Vandenberg, L., Bagas, L., Davies, B.M., Jones, L.E.A., Gebre-Mariam, M., Johnson, W., Smith, T., English, L., 2009. The Tanami deep seismic reflection experiment: An insight into gold mineralization and Paleoproterozoic collision in the North Australian Craton. Tectonophysics 472, 169–182. https://doi.org/10.1016/j.tecto.2008.05.031

Gough, D.I., 1986. Seismic reflectors, conductivity, water and stress in the continental crust. Nature 323, 143–144. https://doi.org/10.1038/323143a0

Grandis, H., Menvielle, M., Roussignol, M., 1999. Bayesian inversion with Markov chains-I. The magnetotelluricone-dimensional case. Geophysical Journal International 138, 757–768. https://doi.org/10.1046/j.1365-246x.1999.00904.x

Green, D.C., Hamling, D.D., Kyranis, N., 1963. CR1065: A-P 54P, PPC Elizabeth Springs 1, PPC Beantree 1, PPC Canary 1, PPC Black Mountain 1, stratigraphic drilling, Boulia area, well completion report (No. CR1065), QDEX report. Department of Natural Resources, Mines and Energy, QLD.

Greene, D.C., 2010. Neoproterozoic rifting in the southern Georgina Basin, central Australia: implications for reconstructing Australia in Rodinia. Tectonics 29, n/a-n/a. https://doi.org/10.1029/2009TC002543

GSQ, 2011. North-west Queensland Mineral and Energy Province report. Geological Survey of Queensland, Brisbane.

Hanekop, O., 2006. Large scale resistivity surveys combining magnetic and magnetotelluric observations - Examples from central Australia -. University of Göttingen, Germany.

Hill, G.J., Caldwell, T.G., Heise, W., Chertkoff, D.G., Bibby, H.M., Burgess, M.K., Cull, J.P., Cas, R.A.F., 2009. Distribution of melt beneath Mount St Helens and Mount Adams inferred from magnetotelluric data. Nature Geoscience 2, 785–789. https://doi.org/10.1038/ngeo661

Huston, D.L., 2006. Mineral systems and tectonic evolution of the North Australian Craton. Presented at the Evolution and Metallogenesis of the Northern Australian Craton Conference, Geoscience Australia, Alice Springs, pp. 64–70.

Jessell, M.W., Ailleres, L., de Kemp, E.A., 2010. Towards an integrated inversion of geoscientific data: what price of geology? Tectonophysics 490, 294–306. https://doi.org/10.1016/j.tecto.2010.05.020

Jones, A.G., 2012. Distortion of magnetotelluric data: its identification and removal, in: Chave, A.D., Jones, A.G. (Eds.), The Magnetotelluric Method Theory and Practice. Cambridge University Press, pp. 219–302.

Jones, A.G., 1988. Static shift of magnetotelluric data and its removal in a sedimentary basin environment. Geophysics 53, 967–978. https://doi.org/10.1190/1.1442533

Jones, A.G., Garcia, X., 2003. Okak Bay AMT data-set case study: lessons in dimensionality and scale. Geophysics 68, 70–91. https://doi.org/10.1190/1.1543195

Jones, A.G., Ledo, J., Ferguson, I.J., 2005. Electromagnetic images of the Trans-Hudson orogen: the North American Central Plains anomaly revealed. Canadian Journal of Earth Sciences 42, 457–478. https://doi.org/10.1139/e05-018

Kelbert, A., Meqbel, N., Egbert, G.D., Tandon, K., 2014. ModEM: a modular system for inversion of electromagnetic geophysical data. Computers & Geosciences 66, 40–53. https://doi.org/10.1016/j.cageo.2014.01.010

Kennett, B., Chopping, R., Blewett, R., 2018. The Australian Continent: A Geophysical Synthesis, 1st ed. ANU Press. https://doi.org/10.22459/AC.08.2018

Khoza, T.D., Jones, A.G., Muller, M.R., Evans, R.L., Miensopust, M.P., Webb, S.J., 2013. Lithospheric structure of an Archean craton and adjacent mobile belt revealed from 2-D and 3-D inversion of magnetotelluric data: example from southern Congo craton in northern Namibia. Journal of Geophysical Research: Solid Earth 118, 4378–4397. https://doi.org/10.1002/jgrb.50258

Korja, T., 2007. How is the European Lithosphere Imaged by Magnetotellurics? Surveys in Geophysics 28, 239–272. https://doi.org/10.1007/s10712-007-9024-9

Korsch, R.J., Doublier, M.P., 2016. Major crustal boundaries of Australia, and their significance in mineral systems targeting. Ore Geology Reviews 76, 211–228. https://doi.org/10.1016/j.oregeorev.2015.05.010

Korsch, R.J., Huston, D.L., Henderson, R.A., Blewett, R.S., Withnall, I.W., Fergusson, C.L., Collins, W.J., Saygin, E., Kositcin, N., Meixner, A.J., Chopping, R., Henson, P.A., Champion, D.C., Hutton, L.J., Wormald, R., Holzschuh, J., Costelloe, R.D., 2012. Crustal architecture and geodynamics of North Queensland, Australia: insights from deep seismic reflection profiling. Tectonophysics 572–573, 76–99. https://doi.org/10.1016/j.tecto.2012.02.022

Kress, A.G., 1989. CR20150: PGA Bradley NO. 1, A-P 380P, well completion report (No. CR20150), QDEX report. Department of Natural Resources, Mines and Energy.

Kress, A.G., Simeone, S.F., 1993. CR24824: A-P 380P, PGA Todd 1, well completion report (No. CR24824), QDEX report. Department of Natural Resources, Mines and Energy.

Kriaa, A., Hajji, M., Jamoussi, F., Hamzaoui, A.H., 2014. Electrical conductivity of 1 : 1 and 2 : 1 clay minerals. Surface Engineering and Applied Electrochemistry 50, 84–94. https://doi.org/10.3103/S1068375514010104

Krieger, L., Peacock, J.R., 2014. MTpy: A Python toolbox for magnetotellurics. Computers & Geosciences 72, 167–175. https://doi.org/10.1016/j.cageo.2014.07.013

Kruse, P.D., Dunster, J.N., Munson, T.J., 2013. Georgina Basin, in: Ahmad, M., Munson, T.J. (Eds.), Geology and Mineral Resources of the Northern Territory. Northern Territory Government Printing Office, Darwin, pp. 28:1-28:56.

Kühn, C., Brasse, H., Schwarz, G., 2018. Three-Dimensional Electrical Resistivity Image of the Volcanic Arc in Northern Chile—An Appraisal of Early Magnetotelluric Data. Pure and Applied Geophysics 175, 2153–2165. https://doi.org/10.1007/s00024-017-1764-y

Le, C.V.A., Harris, B.D., Pethick, A.M., Takam Takougang, E.M., Howe, B., 2016. Semiautomatic and Automatic Cooperative Inversion of Seismic and Magnetotelluric Data. Surveys in Geophysics 37, 845–896. https://doi.org/10.1007/s10712-016-9377-z

Ledo, J., 2006. 2-D Versus 3-D Magnetotelluric Data Interpretation. Surveys in Geophysics 27, 111–148. https://doi.org/10.1007/s10712-006-0002-4

Ledo, J., Queralt, P., Martí, A., Jones, A.G., 2002. Two-dimensional interpretation of three-dimensional magnetotelluric data: an example of limitations and resolution. Geophysical Journal International 150, 127–139. https://doi.org/10.1046/j.1365-246X.2002.01705.x

Liang, H., Jin, S., Wei, W., Gao, R., Ye, G., Zhang, L., Yin, Y., Lu, Z., 2018. Lithospheric electrical structure of the middle Lhasa terrane in the south Tibetan plateau. Tectonophysics 731–732, 95–103. https://doi.org/10.1016/j.tecto.2018.01.020

Lilley, F.E.M., Wang, L.J., Chamalaun, F.H., Ferguson, I.J., 2003. Carpentaria Electrical Conductivity Anomaly, Queensland, as a major structure in the Australian Plate, in: Special Paper 372: Evolution and Dynamics of the Australian Plate. Geological Society of America, pp. 141–156. https://doi.org/10.1130/0-8137-2372-8.141

Lindsay, M., Perrouty, S., Jessell, M., Ailleres, L., 2014. Inversion and geodiversity: searching model space for the answers. Mathematical Geosciences 46, 971–1010. https://doi.org/10.1007/s11004-014-9538-x

Lindsey, N.J., Kaven, J.O., Davatzes, N., Newman, G.A., 2017. Compartmentalization of the Coso East Flank geothermal field imaged by 3-D full-tensor MT inversion. Geophysical Journal International 208, 652–662. https://doi.org/10.1093/gji/ggw408

Lindsey, N.J., Newman, G.A., 2015. Improved workflow for 3D inverse modeling of magnetotelluric data: Examples from five geothermal systems. Geothermics 53, 527–532. https://doi.org/10.1016/j.geothermics.2014.09.004

Logvinov, I.M., Tarasov, V.N., 2018. Electric resistivity distribution in the Earth's crust and upper mantle for the southern East European Platform and Crimea from area-wide 2D models. Acta Geophysica. https://doi.org/10.1007/s11600-018-0125-2

Lyons, P., Huston, D.L. (Eds.), 2006. Evolution and metallogenesis of the North Australian Craton: conference abstracts. Geoscience Australia, Canberra.

Majcin, D., Bezák, V., Klanica, R., Vozár, J., Pek, J., Bilčík, D., Telecký, J., 2018. Klippen Belt, Flysch Belt and Inner Western Carpathian Paleogene Basin Relations in the Northern Slovakia by Magnetotelluric Imaging. Pure and Applied Geophysics 175, 3555–3568. https://doi.org/10.1007/s00024-018-1891-0

Mareschal, M., Fyfe, W.S., Percival, J., Chan, T., 1992. Grain-boundary graphite in Kapuskasing gneisses and implications for lower-crustal conductivity. Nature 357, 674–676. https://doi.org/10.1038/357674a0

Martí, A., Queralt, P., Ledo, J., 2009. WALDIM: A code for the dimensionality analysis of magnetotelluric data using the rotational invariants of the magnetotelluric tensor. Computers & Geosciences 35, 2295–2303. https://doi.org/10.1016/j.cageo.2009.03.004

Mathez, E.A., 1987. Carbonaceous matter in mantle xenoliths: composition and relevance to the isotopes. Geochimica et Cosmochimica Acta 51, 2339–2347. https://doi.org/10.1016/0016-7037(87)90288-2

McCuaig, T.C., Hronsky, J., 2014. The mineral systems concept: the key to exploration targeting. The Society of Economic Geology Special Publication 18, 153–175.

McDonough, W.F., Sun, S. -s., 1995. The composition of the Earth. Chemical Geology 120, 223–253. https://doi.org/10.1016/0009-2541(94)00140-4

Meqbel, N., Egbert, G.D., Wannamaker, P.E., Kelbert, A., Schultz, A., 2014. Deep electrical resistivity structure of the northwestern U.S. derived from 3-D inversion of USArray magnetotelluric data. Earth and Planetary Science Letters 402, 290–304. https://doi.org/10.1016/j.epsl.2013.12.026

Meqbel, N., Ritter, O., 2015. Joint 3D inversion of multiple electromagnetic datasets. Geophysical Prospecting 63, 1450–1467. https://doi.org/10.1111/1365-2478.12334

Miensopust, M.P., 2017. Application of 3-D Electromagnetic Inversion in Practice: Challenges, Pitfalls and Solution Approaches. Surveys in Geophysics 38, 869–933. https://doi.org/10.1007/s10712-017-9435-1

Moorkamp, M., Roberts, A.W., Jegen, M., Heincke, B., Hobbs, R.W., 2013. Verification of velocity-resistivity relationships derived from structural joint inversion with borehole data. Geophysical Research Letters 40, 3596–3601. https://doi.org/10.1002/grl.50696

Moreau, F., Gibert, D., Holschneider, M., Saracco, G., 1999. Identification of sources of potential fields with the continuous wavelet transform: basic theory. Journal of Geophysical Research: Solid Earth 104, 5003–5013. https://doi.org/10.1029/1998JB900106

Naudy, H., 1971. Automatic determination of depth on aeromagnetic profiles. Geophysics 36, 717–722. https://doi.org/10.1190/1.1440207

Neska, A., 2016. Conductivity anomalies in Central Europe. Surveys in Geophysics 37, 5–26. https://doi.org/10.1007/s10712-015-9349-8

Nordsvan, A.R., Collins, W.J., Li, Z.-X., Spencer, C.J., Pourteau, A., Withnall, I.W., Betts, P.G., Volante, S., 2018. Laurentian crust in northeast Australia: Implications for the assembly of the supercontinent Nuna. Geology 46, 251–254. https://doi.org/10.1130/G39980.1

Ogawa, Y., 2002. On Two-Dimensional Modeling Of Magnetotelluric Field Data. Surveys in Geophysics 23, 251–273. https://doi.org/10.1023/A:1015021006018

Ogawa, Y., Uchida, T., 1996. A two-dimensional magnetotelluric inversion assuming Gaussian static shift. Geophysical Journal International 126, 69–76. https://doi.org/10.1111/j.1365-246X.1996.tb05267.x

Ogaya, X., Alcalde, J., Marzán, I., Ledo, J., Queralt, P., Marcuello, A., Martí, D., Saura, E., Carbonell, R., Benjumea, B., 2016. Joint interpretation of magnetotelluric, seismic, and well-log data in Hontomín (Spain). Solid Earth 7, 943–958. https://doi.org/10.5194/se-7-943-2016

Özaydın, S., Tank, S.B., Karaş, M., 2018. Electrical resistivity structure at the North-Central Turkey inferred from three-dimensional magnetotellurics. Earth, Planets and Space 70. https://doi.org/10.1186/s40623-018-0818-4

Page, R.W., Jackson, M.J., Krassay, A.A., 2000. Constraining sequence stratigraphy in north Australian basins: SHRIMP U–Pb zircon geochronology between Mt Isa and McArthur River. Australian Journal of Earth Sciences 47, 431–459. https://doi.org/10.1046/j.1440-0952.2000.00797.x

Parker, R.L., 1994. Geophysical inverse theory. Princeton University Press, Princeton, N.J.

Parkinson, W.D., 1962. The influence of continents and oceans on geomagnetic variations. Geophysical Journal International 6, 441–449. https://doi.org/10.1111/j.1365-246X.1962.tb02992.x

Parkinson, W.D., 1959. Directions of rapid geomagnetic fluctuations. Geophysical Journal International 2, 1–14. https://doi.org/10.1111/j.1365-246X.1959.tb05776.x

Pourteau, A., Smit, M.A., Li, Z.-X., Collins, W.J., Nordsvan, A.R., Volante, S., Li, J., 2018. 1.6 Ga crustal thickening along the final Nuna suture. Geology. https://doi.org/10.1130/G45198.1

Pous, J., Muñoz, G., Heise, W., Melgarejo, J.C., Quesada, C., 2004. Electromagnetic imaging of Variscan crustal structures in SW Iberia: the role of interconnected graphite. Earth and Planetary Science Letters 217, 435–450. https://doi.org/10.1016/S0012-821X(03)00612-5

Rajabi, M., Tingay, M., Heidbach, O., Hillis, R., Reynolds, S., 2017. The present-day stress field of Australia. Earth-Science Reviews 168, 165–189. https://doi.org/10.1016/j.earscirev.2017.04.003

Reid, A.B., Allsop, J.M., Granser, H., Millett, A.J., Somerton, I.W., 1990. Magnetic interpretation in three dimensions using Euler deconvolution. Geophysics 55, 80–91. https://doi.org/10.1190/1.1442774

Roach, I.C., Folkes, C.B., Goodwin, J., Holzschuh, J., Jiang, W., McPherson, A.A., Meixner, A.J., 2018. Applied geophysics for cover thickness mapping in the southern Thomson Orogen. Australian Journal of Earth Sciences 1–25. https://doi.org/10.1080/08120099.2018.1452295

Robertson, K., Taylor, D., Thiel, S., Heinson, G., 2015. Magnetotelluric evidence for serpentinisation in a Cambrian subduction zone beneath the Delamerian Orogen, southeast Australia. Gondwana Research 28, 601–611. https://doi.org/10.1016/j.gr.2014.07.013

Rodi, W., Mackie, R.L., 2001. Nonlinear conjugate gradients algorithm for 2-D magnetotelluric inversion. Geophysics 66, 174–187. https://doi.org/10.1190/1.1444893

Rodi, W.L., Mackie, R.L., 2012. The inverse problem, in: Chave, A.D., Jones, A.G. (Eds.), The Magnetotelluric Method Theory and Practice. Cambridge University Press, pp. 347–420.

Rosas-Carbajal, M., Linde, N., Peacock, J., Zyserman, F.I., Kalscheuer, T., Thiel, S., 2015. Probabilistic 3-D time-lapse inversion of magnetotelluric data: application to an enhanced geothermal system. Geophysical Journal International 203, 1946–1960. https://doi.org/10.1093/gji/ggv406

Schäfer, A., Houpt, L., Brasse, H., Hoffmann, N., EMTESZ Working Group, 2011. The North German Conductivity Anomaly revisited. Geophysical Journal International 187, 85–98. https://doi.org/10.1111/j.1365-246X.2011.05145.x

Schnaidt, S., Heinson, G., 2015. Bootstrap resampling as a tool for uncertainty analysis in 2-D magnetotelluric inversion modelling. Geophysical Journal International 203, 92–106. https://doi.org/10.1093/gji/ggv264

Scott, D.L., Rawlings, D.J., Page, R.W., Tarlowski, C.Z., Idnurm, M., Jackson, M.J., Southgate, P.N., 2000. Basement framework and geodynamic evolution of the Palaeoproterozoic superbasins of north-central Australia: an integrated review of geochemical, geochronological and geophysical data. Australian Journal of Earth Sciences 47, 341–380. https://doi.org/10.1046/j.1440-0952.2000.00793.x

Selway, K., 2014. On the causes of electrical conductivity anomalies in tectonically stable lithosphere. Surveys in Geophysics 35, 219–257. https://doi.org/10.1007/s10712-013-9235-1

Selway, K., Sheppard, S., Thorne, A., Johnson, S., Groenewald, P., 2009. Identifying the lithospheric structure of a Precambrian orogen using magnetotellurics: the Capricorn Orogen, Western Australia. Precambrian Research 168, 185–196. https://doi.org/10.1016/j.precamres.2008.09.010

Simpson, F., Bahr, K., 2005. Practical magnetotellurics. Cambridge University Press, Cambridge, UK ; New York.

Siripunvaraporn, W., 2012. Three-dimensional magnetotelluric inversion: an introductory guide for developers and users. Surveys in Geophysics 33, 5–27. https://doi.org/10.1007/s10712-011-9122-6

Smith, T., Hoversten, M., Gasperikova, E., Morrison, F., 1999. Sharp boundary inversion of 2D magnetotelluric data. Geophysical Prospecting 47, 469–486. https://doi.org/10.1046/j.1365-2478.1999.00145.x

Spampinato, G.P.T., Betts, P.G., Ailleres, L., Armit, R.J., 2015. Structural architecture of the southern Mount Isa terrane in Queensland inferred from magnetic and gravity data. Precambrian Research 269, 261–280. https://doi.org/10.1016/j.precamres.2015.08.017

Spence, A.G., Finlayson, D.M., 1983. The resistivity structure of the crust and upper mantle in the central Eromanga Basin, Queensland, using magnetotelluric techniques. Journal of the Geological Society of Australia 30, 1–16. https://doi.org/10.1080/00167618308729232

Takeuchi, A., Nagao, T., 2013. Activation of hole charge carriers and generation of electromotive force in gabbro blocks subjected to nonuniform loading. Journal of Geophysical Research: Solid Earth 118, 915–925. https://doi.org/10.1002/jgrb.50111

Thiel, S., 2008. Modelling and inversion of magnetotelluric data for 2-D and 3-D lithospheric structure, with application to obducted and subducted terranes. (PhD). The University of Adelaide.

Thiel, S., Heinson, G., 2010. Crustal imaging of a mobile belt using magnetotellurics: an example of the Fowler Domain in South Australia. Journal of Geophysical Research 115. https://doi.org/10.1029/2009JB006698

Thiel, S., Heinson, G., Reid, A., Robertson, K., 2016. Insights into lithospheric architecture, fertilisation and fluid pathways from AusLAMP MT. ASEG Extended Abstracts 2016, 1. https://doi.org/10.1071/ASEG2016ab261

Thurston, J.B., Smith, R.S., 1997. Automatic conversion of magnetic data to depth, dip, and susceptibility contrast using the SPI (TM) method. Geophysics 62, 807–813. https://doi.org/10.1190/1.1444190

Tietze, K., Ritter, O., 2013. Three-dimensional magnetotelluric inversion in practice--the electrical conductivity structure of the San Andreas Fault in Central California. Geophysical Journal International 195, 130–147. https://doi.org/10.1093/gji/ggt234

Tournerie, B., Chouteau, M., 2005. Three-dimensional magnetotelluric survey to image structure and stratigraphy of a sedimentary basin in Hungary. Physics of the Earth and Planetary Interiors 150, 197–212. https://doi.org/10.1016/j.pepi.2004.08.028

Walter, M.R., Veevers, J.J., Calver, C.R., Grey, K., 1995. Neoproterozoic stratigraphy of the Centralian Superbasin, Australia. Precambrian Research 73, 173–195. https://doi.org/10.1016/0301-9268(94)00077-5

Wang, L., Hitchman, A.P., Ogawa, Y., Siripunvaraporn, W., Ichiki, M., Fuji-ta, K., 2014. A 3-D conductivity model of the Australian continent using observatory and magnetometer array data. Geophysical Journal International 198, 1171–1186. https://doi.org/10.1093/gji/ggu188

Watson, H.C., Roberts, J.J., Tyburczy, J.A., 2010. Effect of conductive impurities on electrical conductivity in polycrystalline olivine. Geophysical Research Letters 37. https://doi.org/10.1029/2009GL041566

Weaver, J.T., Agarwal, A.K., Lilley, F.E.M., 2000. Characterization of the magnetotelluric tensor in terms of its invariants. Geophysical Journal International 141, 321–336. https://doi.org/10.1046/j.1365-246x.2000.00089.x

Weaver, J.T., Lilley, F.E.M., 2004. Using Mohr circles to identify regional dimensionality and strike angle from distorted magnetotelluric data. Exploration Geophysics 35, 251. https://doi.org/10.1071/EG04251

Wellmann, J.F., Horowitz, F.G., Schill, E., Regenauer-Lieb, K., 2010. Towards incorporating uncertainty of structural data in 3D geological inversion. Tectonophysics 490, 141–151. https://doi.org/10.1016/j.tecto.2010.04.022

Werner, S., 1953. Interpretation of magnetic anomalies of sheet-like bodies. Sveriges Geologiska Undersökning, Årsbok 43, 1–130.

Wiese, H., 1962. Geomagnetische tiefentellurik teil II: die streichrichtung der untergrundstrukturen des elektrischen widerstandes erschlossen aus geomagnetischen variationen [Strike direction of underground strucutres of electric resistivity, inferred from geomagnetic variations]. Pure and Applied Geophysics 52, 83–103.

Withnall, I.W., Hutton, L.J., Armit, R.J., Betts, P.G., Blewett, R.S., Champion, D.C., 2013. North Australian Craton, in: Jell, P.A. (Ed.), Geology of Queensland. Queensland Government, pp. 23–112.

Woods, D.V., Lilley, F.E.M., 1980. Anomalous geomagnetic variations and the concentration of telluric currents in south-west Queensland, Australia. Geophysical Journal International 62, 675–689. https://doi.org/10.1111/j.1365-246X.1980.tb02599.x

Wu, X., Ferguson, I.J., Jones, A.G., 2005. Geoelectric structure of the Proterozoic Wopmay Orogen and adjacent terranes, Northwest Territories, Canada. Can. J. Earth Sci. 42, 955–981. https://doi.org/10.1139/e05-042

Wyborn, L., Hazell, M., Page, R., Idnurm, M., Sun, S., 1998. A newly discovered major Proterozoic granite-alteration system in the Mount Webb region, central Australia, and implications for Cu-Au mineralisation, AGSO Research Newsletter.

Xiang, E., Guo, R., Dosso, S.E., Liu, J., Dong, H., Ren, Z., 2018. Efficient hierarchical trans-dimensional Bayesian inversion of magnetotelluric data. Geophysical Journal International 213, 1751–1767. https://doi.org/10.1093/gji/ggy071

Yan, P., 2016. Inversion of magnetotelluric data constrained by borehole logs and reflection seismic sections. Acta Universitatis Upsaliensis, Uppsala.

Yan, P., Kalscheuer, T., Hedin, P., Garcia Juanatey, M.A., 2017. Two-dimensional magnetotelluric inversion using reflection seismic data as constraints and application in the COSC project. Geophysical Research Letters 44, 3554–3563. https://doi.org/10.1002/2017GL072953

Yang, X., 2011. Origin of high electrical conductivity in the lower continental crust: a review. Surveys in Geophysics 32, 875–903. https://doi.org/10.1007/s10712-011-9145-z

Yang, X., Keppler, H., McCammon, C., Ni, H., 2012. Electrical conductivity of orthopyroxene and plagioclase in the lower crust. Contributions to Mineralogy and Petrology 163, 33–48. https://doi.org/10.1007/s00410-011-0657-9

Yin, Y., Wei, W., Jin, S., Santosh, M., 2017. Fossil oceanic subduction zone beneath the western margin of the Trans-North China Orogen: Magnetotelluric evidence from the Lüliang Complex. Precambrian Research. https://doi.org/10.1016/j.precamres.2017.01.012

Zevallos, I., Assumpção, M., Padilha, A.L., 2009. Inversion of teleseismic receiver function and magnetotelluric sounding to determine basement depth in the Paraná Basin, SE Brazil. Journal of Applied Geophysics 68, 231–242. https://doi.org/10.1016/j.jappgeo.2008.11.002

Zhang, P., Pedersen, L.B., Mareschal, M., Chouteau, M., 1993. Channelling contribution to tipper vectors: a magnetic equivalent to electrical distortion. Geophysical Journal International 113, 693–700. https://doi.org/10.1111/j.1365-246X.1993.tb04661.x

Zhang, S., Li, Z.-X., Evans, D.A.D., Wu, H., Li, H., Dong, J., 2012. Pre-Rodinia supercontinent Nuna shaping up: a global synthesis with new paleomagnetic results from North China. Earth and Planetary Science Letters 353–354, 145–155. https://doi.org/10.1016/j.epsl.2012.07.034

APPENDICES

APPENDIX A

A.1 MT station locations

Table A.1. Location of BBMT and AMT stations used in thesis. Locations are in GDA94 Geodetic coordinates.

Station number	Latitude	Longitude	Elevation (m)	Data type
15125A	-22.370806	139.188639	200	AMT
15126A	-22.370639	139.1935	200	AMT
15127A	-22.371028	139.198417	201	AMT
15128A	-22.370861	139.203306	200	AMT
15129A	-22.371083	139.208083	202	AMT
15130A	-22.371222	139.212972	201	AMT
15131A	-22.371139	139.217833	208	AMT
15132A	-22.371417	139.222639	208	AMT
15133A	-22.3715	139.227528	206	AMT
15134A	-22.371444	139.232639	215	AMT
15135A	-22.371056	139.236806	218	AMT
15136A	-22.37125	139.241528	220	AMT
15137A	-22.371222	139.246806	222	AMT
15138A	-22.371028	139.251361	215	AMT
15139A	-22.371778	139.256222	227	AMT
15140A	-22.371528	139.262111	226	AMT
15141A	-22.371472	139.266556	225	AMT
15142A	-22.371889	139.2715	231	AMT
15143A	-22.371861	139.275972	224	AMT
15144A	-22.372278	139.280667	225	AMT
15145A	-22.372056	139.285778	231	AMT
15146A	-22.371722	139.291194	234	AMT
15147A	-22.371833	139.295444	239	AMT
15148A	-22.372083	139.300972	235	AMT
15149A	-22.372167	139.305194	227	AMT
15150A	-22.372306	139.31	221	AMT
15151A	-22.372306	139.314917	231	AMT
15152A	-22.372278	139.319806	236	AMT
15153A	-22.372278	139.324556	237	AMT
15154A	-22.372306	139.329333	237	AMT
15155A	-22.372417	139.334361	240	AMT
15156A	-22.372528	139.339083	246	AMT
15157A	-22.372528	139.344056	238	AMT
15158A	-22.372611	139.348889	236	AMT
15159A	-22.372611	139.353722	231	AMT
15160A	-22.372694	139.358583	230	AMT
15161A	-22.372722	139.3635	231	AMT

15162A	-22.372722	139.368278	237	AMT
15163A	-22.372833	139.373194	232	AMT
15164A	-22.372889	139.377972	231	AMT
15165B	-22.373	139.383056	236	AMT
15166A	-22.373028	139.387722	236	AMT
15167A	-22.373083	139.392611	233	AMT
15168A	-22.372694	139.397306	227	AMT
15169B	-22.373222	139.402278	223	AMT
15170A	-22.373111	139.407361	223	AMT
15171A	-22.373222	139.412028	216	AMT
15172A	-22.373278	139.416889	215	AMT
15173A	-22.373306	139.421778	213	AMT
15174A	-22.373389	139.426528	211	AMT
15175A	-22.373361	139.431472	212	AMT
15176A	-22.373444	139.436278	206	AMT
15177B	-22.373472	139.441167	206	AMT
15178A	-22.373472	139.446	206	AMT
15179A	-22.373583	139.450833	203	AMT
15180B	-22.373556	139.455111	212	AMT
15181B	-22.373639	139.460556	215	AMT
15182A	-22.373639	139.465361	212	AMT
15183A	-22.373778	139.470278	209	AMT
15184A	-22.373778	139.475056	206	AMT
15185B	-22.373861	139.479944	211	AMT
15186A	-22.373944	139.484861	209	AMT
15187B	-22.373972	139.489694	211	AMT
15188A	-22.375722	139.494472	211	AMT
15189A	-22.374111	139.499361	212	AMT
15190A	-22.374111	139.504139	210	AMT
15191A	-22.374139	139.508806	210	AMT
15192A	-22.374139	139.513944	213	AMT
15193B	-22.374222	139.518806	215	AMT
15194A	-22.374222	139.523611	212	AMT
15195A	-22.374306	139.528611	216	AMT
15196A	-22.374722	139.533139	219	AMT
15197A	-22.374389	139.538194	230	AMT
15198A	-22.374472	139.543111	227	AMT
15199A	-22.374472	139.548	225	AMT
15200A	-22.374583	139.552778	222	AMT
15201A	-22.374611	139.557611	225	AMT
15202A	-22.374639	139.5625	227	AMT
15203A	-22.374694	139.567333	230	AMT
15204A	-22.375444	139.572667	234	AMT
15205A	-22.374778	139.577056	236	AMT
15206A	-22.374833	139.581917	241	AMT
15207A	-22.374861	139.586806	252	AMT
15208C	-22.376028	139.592056	252	AMT
15209A	-22.374944	139.596472	249	AMT
15210A	-22.374917	139.601389	249	AMT
15211A	-22.375028	139.606278	246	AMT
15212A	-22.374889	139.610972	241	AMT
15213A	-22.375111	139.615861	243	AMT

16122A	-22.325611	139.174361	210	AMT
16123A	-22.325556	139.179056	213	AMT
16124A	-22.325694	139.184472	212	AMT
16125A	-22.32575	139.189306	219	AMT
16126A	-22.325806	139.194	214	AMT
16127A	-22.325889	139.198861	220	AMT
16128A	-22.325389	139.203139	227	AMT
16129A	-22.326583	139.208861	227	AMT
16130A	-22.326083	139.213389	228	AMT
16131A	-22.326028	139.218611	231	AMT
16132A	-22.326167	139.223139	232	AMT
16133A	-22.326417	139.22825	240	AMT
16134A	-22.326056	139.233028	228	AMT
16135A	-22.326222	139.2375	234	AMT
16136A	-22.326417	139.241806	230	AMT
16137A	-22.326222	139.247389	231	AMT
16138A	-22.326528	139.252944	230	AMT
16139A	-22.326611	139.257139	230	AMT
16140A	-22.327111	139.262528	232	AMT
16141A	-22.32625	139.266694	234	AMT
16142A	-22.326889	139.271611	237	AMT
16143A	-22.326639	139.276389	242	AMT
16144A	-22.326611	139.281778	253	AMT
16145A	-22.326472	139.286167	246	AMT
16146A	-22.326694	139.290889	246	AMT
16147A	-22.326917	139.295833	245	AMT
16148A	-22.327056	139.300944	240	AMT
16149A	-22.326806	139.305389	245	AMT
16150A	-22.326694	139.310417	240	AMT
16151A	-22.326944	139.315444	246	AMT
16152A	-22.324972	139.320639	250	AMT
16153A	-22.327139	139.325528	248	AMT
16154A	-22.327083	139.33	250	AMT
16155B	-22.326972	139.335	257	AMT
16156A	-22.327417	139.340389	265	AMT
16157A	-22.327306	139.344778	258	AMT
16158A	-22.327667	139.349611	253	AMT
16159A	-22.327972	139.354667	253	AMT
16160A	-22.326444	139.358389	265	AMT
16161A	-22.327611	139.363972	250	AMT
16162A	-22.3275	139.368944	238	AMT
16163A	-22.328194	139.373556	233	AMT
16164A	-22.328	139.378417	234	AMT
16165A	-22.327	139.383694	232	AMT
16166A	-22.327972	139.388278	229	AMT
16167A	-22.327972	139.393361	224	AMT
16168A	-22.328333	139.397806	222	AMT
16169A	-22.328028	139.403	219	AMT
16170A	-22.327944	139.407611	216	AMT
16171A	-22.328139	139.412361	218	AMT
16172A	-22.328278	139.417278	217	AMT
16173A	-22.328222	139.422306	215	AMT

16174A	-22.328306	139.427278	211	AMT
16175A	-22.328222	139.431889	212	AMT
16176A	-22.328139	139.436639	213	AMT
16177A	-22.328389	139.441639	215	AMT
16178A	-22.328389	139.446361	215	AMT
16179A	-22.328417	139.451167	215	AMT
16180A	-22.328472	139.456417	218	AMT
16181A	-22.328667	139.461222	216	AMT
16182A	-22.328667	139.465722	221	AMT
16183B	-22.328639	139.470778	227	AMT
16184A	-22.328028	139.475556	230	AMT
16185A	-22.328722	139.480194	234	AMT
16186B	-22.328694	139.485278	238	AMT
16187A	-22.328778	139.490028	234	AMT
16188A	-22.33025	139.494889	228	AMT
16189A	-22.328722	139.499944	235	AMT
16190A	-22.329083	139.505	227	AMT
16191A	-22.329056	139.509528	222	AMT
16192A	-22.328972	139.514361	224	AMT
16193B	-22.330389	139.516944	222	AMT
16194A	-22.329361	139.524167	228	AMT
16195A	-22.329222	139.528806	237	AMT
16196A	-22.329444	139.535083	236	AMT
16197A	-22.328972	139.538944	235	AMT
16198A	-22.329028	139.543806	230	AMT
16199A	-22.329444	139.548444	232	AMT
16200a	-22.329194	139.553028	236	AMT
16201B	-22.328722	139.558111	245	AMT
16202A	-22.329472	139.563472	246	AMT
16203A	-22.328028	139.567556	247	AMT
16204A	-22.329	139.572778	249	AMT
16205A	-22.329889	139.577806	260	AMT
16206A	-22.329222	139.582056	252	AMT
16207A	-22.329472	139.587028	257	AMT
16208A	-22.329583	139.591583	257	AMT
16209A	-22.329722	139.597028	251	AMT
16210A	-22.329444	139.601861	251	AMT
16211A	-22.329861	139.606639	249	AMT
17119A	-22.280194	139.160639	211	AMT
17120A	-22.280361	139.165611	214	AMT
17121A	-22.280389	139.170361	218	AMT
17122A	-22.280472	139.175306	219	AMT
17123A	-22.280556	139.180417	222	AMT
17124A	-22.280528	139.185083	226	AMT
17125A	-22.280056	139.189833	236	AMT
17126A	-22.280611	139.194528	226	AMT
17127A	-22.281028	139.200444	243	AMT
17128A	-22.280556	139.204306	243	AMT
17129A	-22.280861	139.209139	236	AMT
17130A	-22.280806	139.214139	241	AMT
17131A	-22.280917	139.219056	245	AMT
17132A	-22.280889	139.223556	251	AMT

17133A	-22.283667	139.228194	256	AMT
17134A	-22.279389	139.234111	260	AMT
17135A	-22.281139	139.239306	268	AMT
17136A	-22.280889	139.243667	259	AMT
17137A	-22.281361	139.248222	255	AMT
17138A	-22.281222	139.252889	252	AMT
17139A	-22.281361	139.257667	252	AMT
17140A	-22.280556	139.261972	252	AMT
17141A	-22.282444	139.267472	262	AMT
17142A	-22.281556	139.273056	255	AMT
17143A	-22.2815	139.277278	257	AMT
17144A	-22.280028	139.281944	267	AMT
17145A	-22.281639	139.286722	278	AMT
17146A	-22.281972	139.291361	284	AMT
17147A	-22.281583	139.296833	267	AMT
17148A	-22.281917	139.301111	271	AMT
17149A	-22.281861	139.30625	271	AMT
17150A	-22.281861	139.311083	265	AMT
17151A	-22.281917	139.316028	266	AMT
17152A	-22.281389	139.320833	263	AMT
17153A	-22.282111	139.325778	266	AMT
17154A	-22.282139	139.330583	254	AMT
17155A	-22.282167	139.335389	253	AMT
17156A	-22.282139	139.34025	250	AMT
17157A	-22.282306	139.345278	252	AMT
17158A	-22.282222	139.349556	251	AMT
17159A	-22.282361	139.354611	252	AMT
17160A	-22.282722	139.359389	255	AMT
17161A	-22.281806	139.364889	261	AMT
17162A	-22.282306	139.369722	260	AMT
17163A	-22.282389	139.374278	247	AMT
17164A	-22.282361	139.378944	237	AMT
17165B	-22.282639	139.383889	232	AMT
17166A	-22.282694	139.388833	229	AMT
17167A	-22.282861	139.393833	222	AMT
17168A	-22.282667	139.398611	220	AMT
17169B	-22.282806	139.403306	225	AMT
17170A	-22.282861	139.408056	221	AMT
17171A	-22.282944	139.413056	220	AMT
17172A	-22.283139	139.417833	222	AMT
17173A	-22.283028	139.422806	220	AMT
17174A	-22.283278	139.427694	218	AMT
17175A	-22.283056	139.432361	217	AMT
17176A	-22.283389	139.437556	224	AMT
17177A	-22.283056	139.441694	232	AMT
17178A	-22.283361	139.446611	236	AMT
17179A	-22.283361	139.451917	225	AMT
17180A	-22.283917	139.456694	235	AMT
17181A	-22.283333	139.461556	232	AMT
17182A	-22.283528	139.466333	230	AMT
17183A	-22.283583	139.471278	230	AMT
17184A	-22.283444	139.475972	228	AMT

17185A	-22.283528	139.480944	232	AMT
17186A	-22.283722	139.485694	235	AMT
17187A	-22.283639	139.490639	235	AMT
17188B	-22.283694	139.495417	242	AMT
17189A	-22.283778	139.500333	249	AMT
17190A	-22.283833	139.505167	247	AMT
17191A	-22.283861	139.510028	254	AMT
17192A	-22.283778	139.514972	247	AMT
17193B	-22.283861	139.519722	246	AMT
17194A	-22.284	139.524556	240	AMT
17195A	-22.284	139.529444	239	AMT
17196A	-22.284306	139.533361	236	AMT
17197A	-22.284111	139.539139	248	AMT
17198A	-22.284056	139.544028	253	AMT
17199A	-22.284056	139.548861	250	AMT
17200A	-22.284306	139.553694	256	AMT
17201A	-22.284306	139.558611	254	AMT
17202A	-22.284333	139.563333	259	AMT
17203A	-22.284306	139.567861	274	AMT
17204A	-22.284194	139.572694	272	AMT
17205A	-22.284389	139.577972	273	AMT
17206A	-22.284611	139.582889	265	AMT
17207A	-22.284472	139.587639	266	AMT
17208A	-22.285056	139.592	259	AMT
17209A	-22.284639	139.597333	268	AMT
18116A	-22.235361	139.146694	206	AMT
18117A	-22.234972	139.151528	202	AMT
18118A	-22.235111	139.156389	209	AMT
18119A	-22.235111	139.161306	213	AMT
18120A	-22.235083	139.166222	217	AMT
18121A	-22.23525	139.170972	218	AMT
18122A	-22.235333	139.175889	226	AMT
18123A	-22.235306	139.180694	228	AMT
18124A	-22.235139	139.185472	230	AMT
18125A	-22.235361	139.190389	231	AMT
18126A	-22.235472	139.19525	232	AMT
18127A	-22.235611	139.200222	234	AMT
18128A	-22.235611	139.205028	234	AMT
18129A	-22.235667	139.209806	231	AMT
18130A	-22.235694	139.214639	232	AMT
18131A	-22.235722	139.219556	233	AMT
18132A	-22.234611	139.224583	248	AMT
18133A	-22.235944	139.229306	245	AMT
18134A	-22.235778	139.234556	255	AMT
18135A	-22.235944	139.238917	248	AMT
18136A	-22.236444	139.243694	254	AMT
18137A	-22.235694	139.24825	258	AMT
18138A	-22.236111	139.253472	260	AMT
18139A	-22.236472	139.258361	277	AMT
18140A	-22.236194	139.263139	269	AMT
18141A	-22.236278	139.268	265	AMT
18142A	-22.236333	139.272861	261	AMT

18143A	-22.236389	139.277722	258	AMT
18144A	-22.234583	139.282556	260	AMT
18145A	-22.236444	139.287417	263	AMT
18146A	-22.236528	139.292278	278	AMT
18147A	-22.236722	139.296778	271	AMT
18148A	-22.236639	139.301944	279	AMT
18149A	-22.236611	139.306639	259	AMT
18150A	-22.23675	139.311611	277	AMT
18151A	-22.236806	139.316528	256	AMT
18152A	-22.237111	139.321222	249	AMT
18153A	-22.236889	139.326139	243	AMT
18154A	-22.236917	139.331056	241	AMT
18155A	-22.236972	139.335889	239	AMT
18156A	-22.237028	139.340694	238	AMT
18157A	-22.237028	139.345694	242	AMT
18158A	-22.23725	139.350528	241	AMT
18159A	-22.237139	139.355278	239	AMT
18160A	-22.237222	139.360139	235	AMT
18161A	-22.237278	139.364972	230	AMT
18162A	-22.237278	139.369694	228	AMT
18163A	-22.237389	139.374778	226	AMT
18164A	-22.23775	139.379667	224	AMT
18165A	-22.237389	139.384444	236	AMT
18166A	-22.237528	139.389222	233	AMT
18167A	-22.237778	139.393972	229	AMT
18168A	-22.237639	139.399056	227	AMT
18169A	-22.237444	139.40375	235	AMT
18170A	-22.237778	139.408444	232	AMT
18171A	-22.237694	139.413306	231	AMT
18172A	-22.237694	139.418361	227	AMT
18173A	-22.237667	139.423306	228	AMT
18174A	-22.238028	139.427667	238	AMT
18175A	-22.237972	139.432917	240	AMT
18176A	-22.237861	139.437306	242	AMT
18177A	-22.237694	139.442806	244	AMT
18178A	-22.238194	139.447583	246	AMT
18179A	-22.237889	139.451306	253	AMT
18180A	-22.237194	139.457139	254	AMT
18181A	-22.238056	139.462722	267	AMT
18182A	-22.237694	139.467028	260	AMT
18183A	-22.237028	139.470861	256	AMT
18184A	-22.237556	139.476639	267	AMT
18185A	-22.238944	139.481278	265	AMT
18186A	-22.238278	139.48625	257	AMT
18187A	-22.238611	139.490944	253	AMT
18188A	-22.239611	139.495444	260	AMT
18189A	-22.239056	139.501306	265	AMT
18190A	-22.238639	139.50575	265	AMT
18191A	-22.238472	139.510667	272	AMT
18192A	-22.236583	139.516028	272	AMT
18193A	-22.2375	139.520444	266	AMT
18194A	-22.239056	139.525083	260	AMT

18195A	-22.238444	139.529694	255	AMT
18196A	-22.239611	139.534472	251	AMT
18197A	-22.238833	139.539639	249	AMT
18198A	-22.239028	139.543778	255	AMT
18199A	-22.239111	139.549028	253	AMT
18200A	-22.239111	139.554139	259	AMT
18201A	-22.239194	139.558944	256	AMT
18202A	-22.239389	139.563833	263	AMT
18203A	-22.238556	139.569056	278	AMT
18204A	-22.239361	139.573556	276	AMT
18205A	-22.239361	139.578722	276	AMT
18206A	-22.239611	139.583222	274	AMT
IEA00184	-23.05113333	139.4675333	122	AMT
IEA00185	-23.05118333	139.47245	121	AMT
IEA00186	-23.05113333	139.47725	120	AMT
IEA00187	-23.05118333	139.4820667	121	AMT
IEA00188	-23.05128333	139.48705	121	AMT
IEA00189	-23.05128333	139.4920333	120	AMT
IEA00190	-23.05145	139.4968667	132	AMT
IEA00191	-23.0514	139.5017	117	AMT
IEA00192	-23.05143333	139.5065833	121	AMT
IEA00193	-23.05151667	139.5114833	120	AMT
IEA00194	-23.0515	139.5163333	117	AMT
IEA00195	-23.0517	139.5212333	118	AMT
IEA00196	-23.05143333	139.5261	122	AMT
IEA00197	-23.05171667	139.5310833	121	AMT
IEA00198	-23.0518	139.5358833	119	AMT
IEA00199	-23.05178333	139.5407333	122	AMT
IEA00200	-23.05158333	139.5452	120	AMT
IEA00201	-23.05198333	139.5506833	119	AMT
IEA00202	-23.05181667	139.55535	120	AMT
IEA00203	-23.05195	139.5602	122	AMT
IEA00204	-23.05183333	139.5651333	118	AMT
IEA00205	-23.0521	139.5700167	117	AMT
IEA00206	-23.05223333	139.57495	123	AMT
IEA00207	-23.05211667	139.5797167	121	AMT
IEA00208	-23.05215	139.5846667	124	AMT
IEA00209	-23.05225	139.5895667	123	AMT
IEA00210	-23.05226667	139.5943667	120	AMT
IEA00211	-23.05226667	139.5992667	126	AMT
IEA00212	-23.05236667	139.6041	124	AMT
IEA00213	-23.05241667	139.6089667	123	AMT
IEA00214	-23.05251667	139.6140167	129	AMT
IEA00215	-23.05243333	139.6188833	125	AMT
IEA00216	-23.0524	139.6238167	123	AMT
IEA00217	-23.0525	139.6286	126	AMT
IEA00218	-23.05266667	139.6335167	133	AMT
IEA00219	-23.05265	139.63835	126	AMT
IEA00220	-23.05268333	139.6431833	131	AMT
IEA00221	-23.05271667	139.6480167	129	AMT
IEA00222	-23.05278333	139.6529333	131	AMT
IEA00223	-23.05281667	139.65795	135	AMT

IEA00224	-23.0528	139.6627667	135	AMT
IEA00225	-23.05291667	139.6676167	132	AMT
IEA00226	-23.05293333	139.6723333	136	AMT
IEA00227	-23.05308333	139.6770833	136	AMT
IEA00228	-23.05303333	139.6821167	132	AMT
IEA00229	-23.05308333	139.6870833	133	AMT
IEA00230	-23.05318333	139.69195	138	AMT
IEA00231	-23.05305	139.6967833	132	AMT
IEA00232	-23.05315	139.7015833	134	AMT
IEA00233	-23.0533	139.70665	133	AMT
IEA00234	-23.0532	139.7115	134	AMT
IEA00235	-23.05333333	139.7163833	136	AMT
IEA00236	-23.05335	139.7211333	134	AMT
IEA00237	-23.05341667	139.7261667	136	AMT
IEA00238	-23.05338333	139.7309833	136	AMT
IEA00239	-23.05338333	139.7359167	137	AMT
IEA00240	-23.05346667	139.7406833	134	AMT
IEA00241	-23.05351667	139.7457333	138	AMT
IEA00242	-23.05355	139.7506	138	AMT
IEA00243	-23.05373333	139.75545	139	AMT
IEA00244	-23.05365	139.76035	148	AMT
IEA00245	-23.05365	139.7651667	137	AMT
IEA00246	-23.05393333	139.7702833	135	AMT
IEA00247	-23.05375	139.77495	140	AMT
IEA00248	-23.054	139.7799667	137	AMT
IEA00249	-23.0538	139.7842667	131	AMT
IEA00250	-23.05395	139.7896667	137	AMT
IEA00251	-23.05405	139.7947167	133	AMT
IEA00252	-23.05393333	139.7996333	141	AMT
IEA00253	-23.054	139.8042667	135	AMT
IEA00254	-23.05385	139.8091167	137	AMT
IEA00255	-23.05423333	139.8139667	136	AMT
IEA00256	-23.05376667	139.8185	141	AMT
IEA00257	-23.05406667	139.8238333	131	AMT
IEA00258	-23.05416667	139.8285833	132	AMT
IEA00259	-23.05415	139.83345	131	AMT
IEA00260	-23.05416667	139.8384	137	AMT
IEA00261	-23.05423333	139.8432167	140	AMT
IEA00262	-23.05426667	139.8481833	135	AMT
IEA00263	-23.0543	139.8529333	146	AMT
IEA00264	-23.05435	139.8577	143	AMT
IEA00265	-23.05443333	139.8628333	143	AMT
IEA00266	-23.05445	139.8679	142	AMT
IEA00267	-23.0545	139.8725167	127	AMT
IEA00268	-23.05451667	139.8773667	133	AMT
IEA00269	-23.05461667	139.8822	136	AMT
IEA00270	-23.0545	139.88705	135	AMT
IEA00271	-23.05456667	139.8920333	138	AMT
IEA00272	-23.05468333	139.8968833	131	AMT
IEA00273	-23.05475	139.90165	139	AMT
IEA00274	-23.05476667	139.9067167	140	AMT
IEA00275	-23.05478333	139.9115833	136	AMT

IEA00276	-23.0548	139.9164667	135	AMT
IEA00277	-23.0548	139.9213167	139	AMT
IEA00278	-23.05501667	139.9263167	137	AMT
IEA00279	-23.05486667	139.93105	131	AMT
IEA00280	-23.05493333	139.9360333	134	AMT
IEA01179	-23.00563333	139.4436667	124	AMT
IEA01180	-23.00576667	139.4483667	125	AMT
IEA01181	-23.00581667	139.4534167	127	AMT
IEA01182	-23.00591667	139.45835	131	AMT
IEA01183	-23.00583333	139.4632	128	AMT
IEA01184	-23.00593333	139.4679833	129	AMT
IEA01185	-23.006	139.47295	131	AMT
IEA01186	-23.00606667	139.4777833	131	AMT
IEA01187	-23.0061	139.4827167	129	AMT
IEA01188	-23.00613333	139.4876	132	AMT
IEA01189	-23.0062	139.49245	135	AMT
IEA01190	-23.00628333	139.4973833	127	AMT
IEA01191	-23.00625	139.5022167	131	AMT
IEA01192	-23.00621667	139.5070667	137	AMT
IEA01193	-23.00633333	139.51185	129	AMT
IEA01194	-23.00641667	139.51685	133	AMT
IEA01195	-23.00653333	139.5217333	132	AMT
IEA01196	-23.00646667	139.5265833	134	AMT
IEA01197	-23.00648333	139.53145	140	AMT
IEA01198	-23.0066	139.5363167	130	AMT
IEA01199	-23.00658333	139.5412167	133	AMT
IEA01200	-23.00666667	139.54615	130	AMT
IEA01201	-23.00666667	139.5509	134	AMT
IEA01202	-23.00676667	139.5558833	131	AMT
IEA01203	-23.00685	139.56075	127	AMT
IEA01204	-23.00683333	139.5656333	128	AMT
IEA01205	-23.0069	139.5705333	134	AMT
IEA01206	-23.00693333	139.5753833	133	AMT
IEA01207	-23.00703333	139.5802	133	AMT
IEA01208R	-23.00681667	139.5851167	139	AMT
IEA01209	-23.00711667	139.59	135	AMT
IEA01210	-23.00711667	139.59485	130	AMT
IEA01211	-23.00713333	139.5997833	128	AMT
IEA01212	-23.00715	139.60455	127	AMT
IEA01213	-23.00723333	139.60955	131	AMT
IEA01214	-23.00726667	139.6144333	135	AMT
IEA01215	-23.00733333	139.6192833	132	AMT
IEA01216	-23.00728333	139.6241333	130	AMT
IEA01217	-23.0074	139.62905	129	AMT
IEA01218	-23.00745	139.6338833	131	AMT
IEA01219	-23.00748333	139.6388333	135	AMT
IEA01220	-23.0075	139.6436667	132	AMT
IEA01221	-23.00798333	139.6483667	134	AMT
IEA01222	-23.00766667	139.6534	133	AMT
IEA01223	-23.00768333	139.6582667	129	AMT
IEA01224	-23.00768333	139.6631333	134	AMT
IEA01225	-23.00753333	139.6684333	137	AMT

IEA01226	-23.00781667	139.6729167	139	AMT
IEA01227	-23.00793333	139.6774167	143	AMT
IEA01228	-23.00783333	139.68265	139	AMT
IEA01229	-23.00788333	139.6876167	145	AMT
IEA01230	-23.00795	139.69245	146	AMT
IEA01231	-23.00801667	139.69715	159	AMT
IEA01232	-23.00805	139.70215	153	AMT
IEA01233R	-23.00801667	139.7069833	152	AMT
IEA01234R	-23.00805	139.71185	156	AMT
IEA01235	-23.00813333	139.7168333	173	AMT
IEA01236	-23.00835	139.7214	159	AMT
IEA01237	-23.00818333	139.7266167	168	AMT
IEA01238	-23.00825	139.7315	166	AMT
IEA01239	-23.00828333	139.7363333	164	AMT
IEA01240	-23.00828333	139.7411833	160	AMT
IEA01241	-23.00833333	139.7460833	149	AMT
IEA01242	-23.00841667	139.7509667	150	AMT
IEA01243	-23.00865	139.7556	148	AMT
IEA01244	-23.00851667	139.7607667	147	AMT
IEA01245	-23.0086	139.76565	141	AMT
IEA01246	-23.00858333	139.77045	143	AMT
IEA01247	-23.00865	139.77525	143	AMT
IEA01248	-23.0088	139.7799167	134	AMT
IEA01249	-23.00868333	139.7851	136	AMT
IEA01250	-23.00878333	139.7899833	133	AMT
IEA01251	-23.00833333	139.7949667	136	AMT
IEA01252	-23.00873333	139.79975	139	AMT
IEA01253	-23.00885	139.8046167	139	AMT
IEA01254	-23.00891667	139.80955	135	AMT
IEA01255	-23.00875	139.8139167	134	AMT
IEA01256	-23.00893333	139.8192833	136	AMT
IEA01257	-23.00901667	139.8241333	133	AMT
IEA01258	-23.009	139.8296	125	AMT
IEA01259	-23.00898333	139.8339	132	AMT
IEA01260	-23.00908333	139.8387667	134	AMT
IEA01261	-23.00913333	139.84365	139	AMT
IEA01262	-23.00918333	139.8485667	140	AMT
IEA01263	-23.0092	139.85345	142	AMT
IEA01264	-23.00923333	139.8583333	137	AMT
IEA01265	-23.0092	139.8632167	143	AMT
IEA01266	-23.0093	139.8680833	136	AMT
IEA01267	-23.00933333	139.8729667	135	AMT
IEA01268R	-23.00936667	139.87775	143	AMT
IEA01269	-23.00938333	139.8825667	141	AMT
IEA01270	-23.0094	139.8875167	140	AMT
IEA01271	-23.0095	139.8924333	137	AMT
IEA01272	-23.00948333	139.8972833	134	AMT
IEA01273	-23.00958333	139.90225	139	AMT
IEA01274	-23.00955	139.9070333	141	AMT
IEA01275	-23.00956667	139.9119167	137	AMT
IEA01276	-23.0097	139.9168667	141	AMT
IEA02173	-22.96035	139.4149333	127	AMT

IEA02174	-22.96035	139.41985	129	AMT
IEA02175	-22.96026667	139.4247167	141	AMT
IEA02176	-22.96046667	139.4295	132	AMT
IEA02177	-22.9604	139.4346333	135	AMT
IEA02178	-22.96048333	139.4393833	138	AMT
IEA02179	-22.9606	139.4442333	131	AMT
IEA02180	-22.96056667	139.4491	132	AMT
IEA02181	-22.96071667	139.4539833	127	AMT
IEA02182	-22.96083333	139.4589333	138	AMT
IEA02183	-22.96075	139.4637167	127	AMT
IEA02184	-22.96076667	139.4685833	131	AMT
IEA02185	-22.96086667	139.4734833	135	AMT
IEA02186	-22.96091667	139.4783167	140	AMT
IEA02187	-22.96093333	139.4831667	150	AMT
IEA02188	-22.96095	139.4881	149	AMT
IEA02189	-22.96103333	139.493	142	AMT
IEA02190	-22.96111667	139.4984	142	AMT
IEA02191	-22.96116667	139.5027333	146	AMT
IEA02192	-22.9612	139.5075833	148	AMT
IEA02193	-22.96121667	139.5124333	149	AMT
IEA02194	-22.96141667	139.5174833	144	AMT
IEA02195	-22.9613	139.5222	141	AMT
IEA02196	-22.96135	139.5271	153	AMT
IEA02197	-22.96166667	139.5320333	139	AMT
IEA02198	-22.9614	139.53685	147	AMT
IEA02199	-22.9615	139.5417333	142	AMT
IEA02200	-22.96153333	139.5466333	152	AMT
IEA02201	-22.9616	139.5514167	145	AMT
IEA02202	-22.96156667	139.5563	143	AMT
IEA02203	-22.96165	139.56125	136	AMT
IEA02204	-22.96171667	139.56605	138	AMT
IEA02205	-22.96146667	139.5712333	134	AMT
IEA02206	-22.96183333	139.57585	130	AMT
IEA02207	-22.96183333	139.5807	131	AMT
IEA02208	-22.96193333	139.5855833	132	AMT
IEA02209	-22.96185	139.5904667	125	AMT
IEA02210R	-22.962	139.5953333	137	AMT
IEA02211	-22.96186667	139.6002833	133	AMT
IEA02212	-22.96206667	139.60505	134	AMT
IEA02213	-22.96201667	139.6101	136	AMT
IEA02214	-22.96218333	139.6149	136	AMT
IEA02215	-22.96218333	139.6196833	138	AMT
IEA02216	-22.96228333	139.62455	138	AMT
IEA02217	-22.96193333	139.6295833	134	AMT
IEA02218R	-22.96233333	139.6343333	136	AMT
IEA02219	-22.96233333	139.6392333	130	AMT
IEA02220	-22.96235	139.6440333	138	AMT
IEA02221	-22.96243333	139.64895	134	AMT
IEA02222	-22.96248333	139.65385	137	AMT
IEA02223	-22.9625	139.6586667	140	AMT
IEA02224	-22.96255	139.6636167	145	AMT
IEA02225	-22.96261667	139.6684833	131	AMT

IEA02226	-22.96261667	139.6733333	141	AMT
IEA02227	-22.96273333	139.6782333	136	AMT
IEA02228	-22.96265	139.68315	139	AMT
IEA02229	-22.96276667	139.6880333	133	AMT
IEA02230	-22.96285	139.6929167	144	AMT
IEA02231	-22.96283333	139.6978833	141	AMT
IEA02232	-22.96286667	139.7026167	145	AMT
IEA02233	-22.96286667	139.7075833	145	AMT
IEA02234	-22.96298333	139.7124333	143	AMT
IEA02235	-22.9631	139.7179	150	AMT
IEA02236	-22.96305	139.7221167	151	AMT
IEA02237	-22.96305	139.727	152	AMT
IEA02238	-22.96305	139.7319167	171	AMT
IEA02239	-22.96318333	139.7368	161	AMT
IEA02240	-22.96316667	139.74155	149	AMT
IEA02241	-22.96328333	139.7465667	167	AMT
IEA02242	-22.9633	139.7513	159	AMT
IEA02243	-22.96338333	139.7563167	161	AMT
IEA02244	-22.96335	139.76115	157	AMT
IEA02245	-22.96361667	139.7662667	167	AMT
IEA02246	-22.96346667	139.7709833	150	AMT
IEA02247	-22.96343333	139.7758	156	AMT
IEA02248	-22.96343333	139.7802833	150	AMT
IEA02249	-22.9636	139.78565	149	AMT
IEA02250	-22.96363333	139.7904333	145	AMT
IEA02251	-22.96365	139.7953333	143	AMT
IEA02252	-22.9635	139.8001	139	AMT
IEA02253	-22.96355	139.8051667	142	AMT
IEA02254	-22.96373333	139.8097167	143	AMT
IEA02255	-22.9638	139.81475	146	AMT
IEA02256	-22.96385	139.8194667	142	AMT
IEA02257	-22.96386667	139.8245667	144	AMT
IEA02258	-22.96378333	139.8295	146	AMT
IEA02259	-22.96378333	139.8342833	144	AMT
IEA02260	-22.96393333	139.8391833	144	AMT
IEA02261	-22.96398333	139.8442	159	AMT
IEA02262	-22.96405	139.849	144	AMT
IEA02263	-22.964	139.8538167	142	AMT
IEA02264	-22.96405	139.8586	144	AMT
IEA02265	-22.96406667	139.8635667	138	AMT
IEA02266	-22.9643	139.8686667	142	AMT
IEA02267	-22.96403333	139.8736667	156	AMT
IEA02268	-22.96391667	139.8780833	141	AMT
IEA02269	-22.96401667	139.8829333	161	AMT
IEA02270	-22.96428333	139.8879833	141	AMT
IEA02271	-22.96436667	139.8928667	144	AMT
IEA03168	-22.91483333	139.3911	143	AMT
IEA03169	-22.9149	139.3959333	142	AMT
IEA03170R	-22.915	139.40085	139	AMT
IEA03171	-22.91503333	139.4057	143	AMT
IEA03172	-22.91503333	139.4105167	138	AMT
IEA03173R	-22.91513333	139.4154667	134	AMT

IEA03174R	-22.91521667	139.4203	134	AMT
IEA03175	-22.9152	139.4251333	139	AMT
IEA03176	-22.91521667	139.4300833	147	AMT
IEA03177	-22.91531667	139.4349	140	AMT
IEA03178	-22.9154	139.4397833	152	AMT
IEA03179	-22.91545	139.4447	140	AMT
IEA03180	-22.91543333	139.4496333	139	AMT
IEA03181	-22.91553333	139.4544167	143	AMT
IEA03182	-22.91551667	139.4593	139	AMT
IEA03183	-22.91556667	139.4642167	153	AMT
IEA03184	-22.91563333	139.4690167	139	AMT
IEA03185	-22.91568333	139.4738833	136	AMT
IEA03186	-22.9157	139.4788	150	AMT
IEA03187	-22.91581667	139.4836667	138	AMT
IEA03188	-22.91583333	139.4884833	140	AMT
IEA03189	-22.91595	139.4934333	139	AMT
IEA03190	-22.91595	139.4982833	138	AMT
IEA03191	-22.91596667	139.50315	132	AMT
IEA03192	-22.91598333	139.50805	139	AMT
IEA03193	-22.91608333	139.5128833	131	AMT
IEA03194	-22.9161	139.5178	137	AMT
IEA03195	-22.91616667	139.5226833	140	AMT
IEA03196	-22.91623333	139.5275833	141	AMT
IEA03197	-22.91621667	139.53245	153	AMT
IEA03198	-22.91641667	139.53695	151	AMT
IEA03199	-22.9163	139.5422333	146	AMT
IEA03200	-22.91635	139.5469833	149	AMT
IEA03201R	-22.91655	139.5518	147	AMT
IEA03202	-22.9163	139.5571167	142	AMT
IEA03203	-22.9166	139.5620167	139	AMT
IEA03204	-22.91661667	139.5664833	150	AMT
IEA03205	-22.91666667	139.5718	164	AMT
IEA03206	-22.91658333	139.57645	147	AMT
IEA03207	-22.9167	139.581	144	AMT
IEA03208	-22.9167	139.5864667	146	AMT
IEA03209	-22.91685	139.5908833	143	AMT
IEA03210	-22.9164	139.5959833	161	AMT
IEA03211	-22.91686667	139.6008	142	AMT
IEA03212	-22.91681667	139.6056333	140	AMT
IEA03213	-22.91695	139.61035	137	AMT
IEA03214	-22.91698333	139.6154333	136	AMT
IEA03215	-22.91691667	139.6201667	145	AMT
IEA03216	-22.91708333	139.6250667	143	AMT
IEA03217	-22.91715	139.6299667	136	AMT
IEA03218	-22.91716667	139.6347833	139	AMT
IEA03219	-22.91691667	139.64	146	AMT
IEA03220	-22.91716667	139.64475	148	AMT
IEA03221	-22.91738333	139.6493333	151	AMT
IEA03222	-22.91728333	139.65425	147	AMT
IEA03223	-22.91743333	139.6591667	147	AMT
IEA03224	-22.91748333	139.664	150	AMT
IEA03225	-22.91755	139.6689333	151	AMT

IEA03226	-22.9175	139.6737667	154	AMT
IEA03227	-22.91743333	139.6783167	159	AMT
IEA03228	-22.91763333	139.6833333	158	AMT
IEA03229	-22.91755	139.6884333	159	AMT
IEA03230	-22.9176	139.6928	163	AMT
IEA03231	-22.91785	139.6981667	156	AMT
IEA03232	-22.91761667	139.7030167	152	AMT
IEA03233	-22.91765	139.70805	158	AMT
IEA03234	-22.91813333	139.7128167	157	AMT
IEA03235	-22.91785	139.7177167	173	AMT
IEA03236R	-22.91788333	139.72255	170	AMT
IEA03237	-22.9179	139.7274333	160	AMT
IEA03238R	-22.9181	139.7322667	157	AMT
IEA03239	-22.91801667	139.7371333	157	AMT
IEA03240	-22.91805	139.74205	155	AMT
IEA03241	-22.91798333	139.7469333	160	AMT
IEA03242	-22.91815	139.7516667	153	AMT
IEA03243	-22.91811667	139.7567333	147	AMT
IEA03244	-22.9186	139.7615	148	AMT
IEA03245	-22.91821667	139.7662167	161	AMT
IEA03246	-22.9184	139.77135	167	AMT
IEA03247	-22.91826667	139.7761833	149	AMT
IEA03248	-22.91835	139.7810333	146	AMT
IEA03249R	-22.91835	139.7858	148	AMT
IEA03250	-22.91848333	139.7906833	167	AMT
IEA03251	-22.91821667	139.7956667	162	AMT
IEA03252R	-22.91851667	139.8006	169	AMT
IEA03253R	-22.91851667	139.80545	160	AMT
IEA03254	-22.9187	139.8101167	149	AMT
IEA03255R	-22.91868333	139.8150667	152	AMT
IEA03256R	-22.91865	139.8200333	154	AMT
IEA03257	-22.91863333	139.8252167	160	AMT
IEA03258	-22.91893333	139.8298167	144	AMT
IEA03259	-22.91856667	139.83475	113	AMT
IEA03260	-22.91883333	139.83955	135	AMT
IEA03261	-22.91888333	139.8446833	136	AMT
IEA03262	-22.91886667	139.8493833	140	AMT
IEA03263	-22.9189	139.8542167	185	AMT
IEA03264	-22.91896667	139.8589333	139	AMT
IEA03265	-22.91891667	139.8639	140	AMT
IEA03266	-22.91896667	139.8688333	151	AMT
IEA04162	-22.8694	139.3624333	144	AMT
IEA04163	-22.86943333	139.36725	138	AMT
IEA04164	-22.86951667	139.3721333	144	AMT
IEA04165	-22.86955	139.377	139	AMT
IEA04166	-22.86958333	139.38185	143	AMT
IEA04167	-22.8697	139.3867167	146	AMT
IEA04168	-22.86971667	139.3916167	149	AMT
IEA04169	-22.86975	139.3964833	149	AMT
IEA04170	-22.8698	139.4013333	147	AMT
IEA04171	-22.86988333	139.4062333	146	AMT
IEA04172	-22.8699	139.4110667	146	AMT

IEA04173	-22.86991667	139.4159833	145	AMT
IEA04174	-22.87001667	139.4208833	138	AMT
IEA04175	-22.8701	139.4257333	137	AMT
IEA04176	-22.87008333	139.4305833	141	AMT
IEA04177	-22.87018333	139.43545	144	AMT
IEA04178	-22.87021667	139.44035	139	AMT
IEA04179	-22.87016667	139.4451667	149	AMT
IEA04180	-22.87025	139.4500667	144	AMT
IEA04181RR	-22.87033333	139.45495	144	AMT
IEA04182	-22.87038333	139.4598333	142	AMT
IEA04183	-22.87046667	139.46465	135	AMT
IEA04184	-22.87043333	139.46955	140	AMT
IEA04185R	-22.87056667	139.4744667	147	AMT
IEA04186	-22.87061667	139.4793667	144	AMT
IEA04187	-22.87065	139.4842333	147	AMT
IEA04188	-22.87071667	139.48905	145	AMT
IEA04189R	-22.87076667	139.4939167	139	AMT
IEA04190	-22.87078333	139.4988333	152	AMT
IEA04191	-22.8708	139.50365	145	AMT
IEA04192R	-22.87088333	139.50855	151	AMT
IEA04193	-22.87088333	139.51345	147	AMT
IEA04194	-22.87098333	139.5183	148	AMT
IEA04195	-22.87098333	139.5231833	154	AMT
IEA04196	-22.87103333	139.5280667	148	AMT
IEA04197	-22.8711	139.5329333	148	AMT
IEA04198	-22.87113333	139.5377667	155	AMT
IEA04199	-22.8712	139.5427167	152	AMT
IEA04200	-22.8712	139.5475167	152	AMT
IEA04201	-22.87126667	139.5524167	157	AMT
IEA04202	-22.87136667	139.5573	156	AMT
IEA04203	-22.87125	139.5622167	153	AMT
IEA04204	-22.87131667	139.5671167	150	AMT
IEA04205	-22.87148333	139.5719833	151	AMT
IEA04206	-22.87145	139.5767833	146	AMT
IEA04207	-22.87158333	139.5816167	149	AMT
IEA04208	-22.87143333	139.5863833	147	AMT
IEA04209	-22.87161667	139.59125	149	AMT
IEA04210	-22.8716	139.5966	145	AMT
IEA04211	-22.87178333	139.6012	150	AMT
IEA04212	-22.87175	139.60595	150	AMT
IEA04213	-22.87181667	139.6110167	155	AMT
IEA04214	-22.87185	139.6157333	148	AMT
IEA04215	-22.8719	139.6207	155	AMT
IEA04216	-22.87181667	139.6255167	150	AMT
IEA04217	-22.87195	139.6304333	152	AMT
IEA04218	-22.87208333	139.6353333	155	AMT
IEA04219	-22.87216667	139.6400833	158	AMT
IEA04220	-22.87196667	139.64495	163	AMT
IEA04221	-22.87218333	139.6498667	160	AMT
IEA04222	-22.87225	139.6546667	166	AMT
IEA04223	-22.87223333	139.6595833	164	AMT
IEA04224	-22.87216667	139.6644833	159	AMT

IEA04225	-22.87228333	139.66905	173	AMT
IEA04226	-22.87226667	139.6743333	169	AMT
IEA04227	-22.87245	139.67915	159	AMT
IEA04228	-22.87235	139.68395	160	AMT
IEA04229	-22.8724	139.6888667	164	AMT
IEA04230	-22.87245	139.6937833	162	AMT
IEA04231	-22.8724	139.6985167	171	AMT
IEA04232	-22.87256667	139.7033667	176	AMT
IEA04233	-22.87258333	139.7083667	167	AMT
IEA04234	-22.87265	139.7131833	170	AMT
IEA04235	-22.87266667	139.7180667	173	AMT
IEA04236	-22.87271667	139.7229	169	AMT
IEA04237	-22.87273333	139.7278167	163	AMT
IEA04238	-22.8728	139.7326667	161	AMT
IEA04239	-22.87285	139.7375833	158	AMT
IEA04240	-22.87285	139.7424333	160	AMT
IEA04241R	-22.87288333	139.7474	160	AMT
IEA04242	-22.87291667	139.7522	157	AMT
IEA04243R	-22.87306667	139.7570667	159	AMT
IEA04244	-22.87303333	139.7619167	155	AMT
IEA04245	-22.873	139.7666167	180	AMT
IEA04246	-22.87308333	139.7717833	161	AMT
IEA04247	-22.87315	139.7765	160	AMT
IEA04248	-22.87326667	139.7815	173	AMT
IEA04249	-22.87315	139.7863833	170	AMT
IEA04250	-22.87316667	139.79125	164	AMT
IEA04251	-22.87343333	139.79595	191	AMT
IEA04252R	-22.87336667	139.8009333	165	AMT
IEA04253	-22.87338333	139.8059167	162	AMT
IEA04254	-22.8734	139.8107667	161	AMT
IEA04255	-22.8734	139.8156333	154	AMT
IEA04256	-22.8734	139.8204667	154	AMT
IEA04257	-22.8735	139.8254	153	AMT
IEA04258	-22.87355	139.8302667	148	AMT
IEA04259	-22.87355	139.83505	148	AMT
IEA04260	-22.87361667	139.8399333	146	AMT
IEA04261	-22.87361667	139.84485	145	AMT
IEB0044	-23.050717	139.4285	121	BBMT
IEB0045	-23.050933	139.447983	120	BBMT
IEB0046	-23.051133	139.467533	122	BBMT
IEB0047	-23.051283	139.48705	121	BBMT
IEB0048	-23.051433	139.506583	121	BBMT
IEB0049	-23.051433	139.5261	122	BBMT
IEB0050	-23.051583	139.5452	120	BBMT
IEB0051	-23.051833	139.565133	118	BBMT
IEB0052	-23.05215	139.584667	124	BBMT
IEB0053	-23.052367	139.6041	124	BBMT
IEB0054	-23.0524	139.623817	123	BBMT
IEB0055	-23.052683	139.643183	131	BBMT
IEB0056	-23.0528	139.662767	135	BBMT
IEB0057	-23.053033	139.682117	132	BBMT
IEB0058	-23.05315	139.701583	134	BBMT

IEB0059	-23.05335	139.721133	134	BBMT
IEB0060	-23.053467	139.740683	134	BBMT
IEB0061	-23.05365	139.76035	148	BBMT
IEB0062	-23.054	139.779967	137	BBMT
IEB0063	-23.053933	139.799633	141	BBMT
IEB0064	-23.053767	139.8185	141	BBMT
IEB0065	-23.054167	139.8384	137	BBMT
IEB0066	-23.05435	139.8577	143	BBMT
IEB0067	-23.054517	139.877367	133	BBMT
IEB0068	-23.054683	139.896883	131	BBMT
IEB0069	-23.0548	139.916467	135	BBMT
IEB0070	-23.054933	139.936033	134	BBMT
IEB0143	-23.005317	139.409517	109	BBMT
IEB0144	-23.005583	139.4291	116	BBMT
IEB0145	-23.005767	139.448367	125	BBMT
IEB0146	-23.005933	139.467983	129	BBMT
IEB0147	-23.006133	139.4876	132	BBMT
IEB0148	-23.006217	139.507067	137	BBMT
IEB0149	-23.006467	139.526583	134	BBMT
IEB0150	-23.006667	139.54615	130	BBMT
IEB0151	-23.006833	139.565633	128	BBMT
IEB0152R	-23.006817	139.585117	139	BBMT
IEB0153	-23.00715	139.60455	127	BBMT
IEB0154	-23.007283	139.624133	130	BBMT
IEB0155	-23.0075	139.643667	132	BBMT
IEB0156	-23.007683	139.663133	134	BBMT
IEB0157	-23.007833	139.68265	139	BBMT
IEB0158	-23.00805	139.70215	153	BBMT
IEB0159	-23.00835	139.7214	159	BBMT
IEB0160	-23.008283	139.741183	160	BBMT
IEB0161	-23.008517	139.760767	147	BBMT
IEB0162	-23.0088	139.779917	134	BBMT
IEB0163	-23.008733	139.79975	139	BBMT
IEB0164	-23.008933	139.819283	136	BBMT
IEB0165	-23.009083	139.838767	134	BBMT
IEB0166	-23.009233	139.858333	137	BBMT
IEB0167R	-23.009367	139.87775	143	BBMT
IEB0168	-23.009483	139.897283	134	BBMT
IEB0169	-23.0097	139.916867	141	BBMT
IEB0241	-22.959867	139.371017	125	BBMT
IEB0242	-22.960033	139.3906	114	BBMT
IEB0243	-22.96025	139.41005	128	BBMT
IEB0244	-22.960467	139.4295	132	BBMT
IEB0245	-22.960567	139.4491	132	BBMT
IEB0246	-22.960767	139.468583	131	BBMT
IEB0247	-22.96095	139.4881	149	BBMT
IEB0248	-22.9612	139.507583	148	BBMT
IEB0249	-22.96135	139.5271	153	BBMT
IEB0250	-22.961533	139.546633	152	BBMT
IEB0251	-22.961717	139.56605	138	BBMT
IEB0252	-22.961933	139.585583	132	BBMT
IEB0253	-22.962067	139.60505	134	BBMT

IEB0254	-22.962283	139.62455	138	BBMT
IEB0255	-22.96235	139.644033	138	BBMT
IEB0256	-22.96255	139.663617	145	BBMT
IEB0257	-22.96265	139.68315	139	BBMT
IEB0258	-22.962867	139.702617	145	BBMT
IEB0259	-22.96305	139.722117	151	BBMT
IEB0260	-22.963167	139.74155	149	BBMT
IEB0261	-22.96335	139.76115	157	BBMT
IEB0262	-22.963433	139.780283	150	BBMT
IEB0263	-22.9635	139.8001	139	BBMT
IEB0264	-22.96385	139.819467	142	BBMT
IEB0265	-22.963933	139.839183	144	BBMT
IEB0266	-22.96405	139.8586	144	BBMT
IEB0267	-22.963917	139.878083	141	BBMT
IEB0268	-22.964383	139.8976	130	BBMT
IEB0269	-22.96445	139.917233	139	BBMT
IEB0341	-22.9147	139.371683	128	BBMT
IEB0342	-22.914833	139.3911	143	BBMT
IEB0343	-22.915033	139.410517	138	BBMT
IEB0344	-22.915217	139.430083	147	BBMT
IEB0345	-22.915433	139.449633	139	BBMT
IEB0346	-22.915633	139.469017	139	BBMT
IEB0347	-22.915833	139.488483	140	BBMT
IEB0348	-22.915983	139.50805	139	BBMT
IEB0349	-22.916233	139.527583	141	BBMT
IEB0350	-22.91635	139.546983	149	BBMT
IEB0351	-22.916617	139.566483	150	BBMT
IEB0352	-22.9167	139.586467	146	BBMT
IEB0353	-22.916817	139.605633	140	BBMT
IEB0354	-22.917083	139.625067	143	BBMT
IEB0355	-22.917167	139.64475	148	BBMT
IEB0356	-22.917483	139.664	150	BBMT
IEB0357	-22.917633	139.683333	158	BBMT
IEB0358	-22.917617	139.703017	152	BBMT
IEB0359R	-22.917883	139.72255	170	BBMT
IEB0360	-22.91805	139.74205	155	BBMT
IEB0361	-22.9186	139.7615	148	BBMT
IEB0362	-22.91835	139.781033	146	BBMT
IEB0363R	-22.918517	139.8006	169	BBMT
IEB0364R	-22.91865	139.820033	154	BBMT
IEB0365	-22.918833	139.83955	135	BBMT
IEB0366	-22.918967	139.858933	139	BBMT
IEB0367	-22.919117	139.878583	155	BBMT
IEB0368	-22.9191	139.898067	152	BBMT
IEB0439	-22.869167	139.333133	145	BBMT
IEB0440	-22.86935	139.35265	137	BBMT
IEB0441	-22.869517	139.372133	144	BBMT
IEB0442	-22.869717	139.391617	149	BBMT
IEB0443	-22.8699	139.411067	146	BBMT
IEB0444	-22.870083	139.430583	141	BBMT
IEB0445	-22.87025	139.450067	144	BBMT
IEB0446	-22.870433	139.46955	140	BBMT

IEB0447	-22.870717	139.48905	145	BBMT
IEB0448R	-22.870883	139.50855	151	BBMT
IEB0449	-22.871033	139.528067	148	BBMT
IEB0450	-22.8712	139.547517	152	BBMT
IEB0451	-22.871317	139.567117	150	BBMT
IEB0452	-22.871433	139.586383	147	BBMT
IEB0453	-22.87175	139.60595	150	BBMT
IEB0454	-22.871817	139.625517	150	BBMT
IEB0455	-22.871967	139.64495	163	BBMT
IEB0456	-22.872167	139.664483	159	BBMT
IEB0457	-22.87235	139.68395	160	BBMT
IEB0458	-22.872567	139.703367	176	BBMT
IEB0459	-22.872717	139.7229	169	BBMT
IEB0460	-22.87285	139.742433	160	BBMT
IEB0461	-22.873033	139.761917	155	BBMT
IEB0462	-22.873267	139.7815	173	BBMT
IEB0463R	-22.873367	139.800933	165	BBMT
IEB0464	-22.8734	139.820467	154	BBMT
IEB0465	-22.873617	139.839933	146	BBMT
IEB0466	-22.873783	139.859433	144	BBMT
IEB0467	-22.873933	139.878967	148	BBMT
IEB0537A	-22.823722	139.294694	158	BBMT
IEB0538A	-22.823778	139.314278	159	BBMT
IEB0539A	-22.823972	139.333722	160	BBMT
IEB0540A	-22.824083	139.353	155	BBMT
IEB0541A	-22.824444	139.372639	159	BBMT
IEB0542A	-22.824611	139.392194	155	BBMT
IEB0543A	-22.824778	139.411694	153	BBMT
IEB0544A	-22.824972	139.431139	152	BBMT
IEB0545A	-22.825111	139.450667	151	BBMT
IEB0546A	-22.822639	139.470139	152	BBMT
IEB0547A	-22.823528	139.48975	157	BBMT
IEB0548A	-22.824806	139.509083	168	BBMT
IEB0549A	-22.825361	139.527806	168	BBMT
IEB0550A	-22.826111	139.548028	160	BBMT
IEB0551A	-22.826222	139.567556	154	BBMT
IEB0552A	-22.826444	139.587	152	BBMT
IEB0553A	-22.826583	139.606472	156	BBMT
IEB0554A	-22.826806	139.626	159	BBMT
IEB0555B	-22.826306	139.646194	155	BBMT
IEB0556A	-22.827139	139.664972	166	BBMT
IEB0557A	-22.827222	139.6845	179	BBMT
IEB0558A	-22.827417	139.703917	186	BBMT
IEB0559A	-22.827583	139.723333	177	BBMT
IEB0560A	-22.827722	139.742833	168	BBMT
IEB0561A	-22.827972	139.762417	169	BBMT
IEB0562A	-22.828056	139.781889	163	BBMT
IEB0563A	-22.828222	139.801306	158	BBMT
IEB0564A	-22.828389	139.820861	156	BBMT
IEB0565A	-22.8285	139.840333	160	BBMT
IEB0566A	-22.828611	139.858917	153	BBMT
IEB0567A	-22.827222	139.6845	179	BBMT

IEB0636A	-22.778194	139.275861	159	BBMT
IEB0637A	-22.778444	139.295333	158	BBMT
IEB0638A	-22.778639	139.314778	163	BBMT
IEB0639A	-22.778917	139.334556	181	BBMT
IEB0640A	-22.779028	139.353722	184	BBMT
IEB0641A	-22.779278	139.373222	173	BBMT
IEB0642A	-22.779417	139.392694	172	BBMT
IEB0643A	-22.779778	139.412278	170	BBMT
IEB0644A	-22.779861	139.431639	160	BBMT
IEB0645A	-22.780056	139.451167	159	BBMT
IEB0646A	-22.780194	139.470639	159	BBMT
IEB0647A	-22.780389	139.490111	168	BBMT
IEB0648A	-22.780556	139.509528	172	BBMT
IEB0649A	-22.780778	139.529056	173	BBMT
IEB0650A	-22.780944	139.548528	162	BBMT
IEB0651A	-22.781111	139.568056	156	BBMT
IEB0652A	-22.781444	139.587694	163	BBMT
IEB0653A	-22.781389	139.606944	167	BBMT
IEB0654A	-22.781389	139.625722	171	BBMT
IEB0655A	-22.781778	139.646194	175	BBMT
IEB0656A	-22.781944	139.665556	176	BBMT
IEB0657A	-22.781944	139.684306	178	BBMT
IEB0658A	-22.782944	139.704694	193	BBMT
IEB0659A	-22.782444	139.723833	175	BBMT
IEB0660B	-22.782694	139.743222	170	BBMT
IEB0661A	-22.782917	139.762583	166	BBMT
IEB0662A	-22.782944	139.782306	156	BBMT
IEB0663A	-22.781444	139.802806	166	BBMT
IEB0664A	-22.783194	139.821222	166	BBMT
IEB0665A	-22.783333	139.840694	163	BBMT
IEB0735A	-22.732889	139.257056	165	BBMT
IEB0736A	-22.732889	139.276222	182	BBMT
IEB0737A	-22.733278	139.295889	165	BBMT
IEB0738A	-22.733361	139.315056	163	BBMT
IEB0739A	-22.734278	139.335	159	BBMT
IEB0740A	-22.734333	139.355194	190	BBMT
IEB0741A	-22.734306	139.373806	192	BBMT
IEB0742A	-22.734222	139.393139	188	BBMT
IEB0743B	-22.734556	139.412972	193	BBMT
IEB0744A	-22.734444	139.432056	204	BBMT
IEB0745A	-22.734694	139.451417	174	BBMT
IEB0746A	-22.735028	139.471139	165	BBMT
IEB0747A	-22.735361	139.490333	174	BBMT
IEB0748A	-22.735444	139.510083	172	BBMT
IEB0749A	-22.735639	139.529639	172	BBMT
IEB0750A	-22.735722	139.549028	169	BBMT
IEB0751A	-22.736083	139.568417	172	BBMT
IEB0752C	-22.735861	139.587472	175	BBMT
IEB0753A	-22.736194	139.607167	190	BBMT
IEB0754A	-22.736778	139.626639	197	BBMT
IEB0755A	-22.737056	139.647417	200	BBMT
IEB0756A	-22.738306	139.666806	191	BBMT

IEB0757A	-22.737333	139.685306	185	BBMT
IEB0758A	-22.737778	139.704778	178	BBMT
IEB0759A	-22.735944	139.724306	176	BBMT
IEB0760A	-22.736389	139.744	174	BBMT
IEB0761A	-22.737778	139.763556	170	BBMT
IEB0762A	-22.73775	139.782694	174	BBMT
IEB0763B	-22.738	139.802528	178	BBMT
IEB0764A	-22.738056	139.821611	175	BBMT
IEB0834A	-22.687889	139.238694	188	BBMT
IEB0835A	-22.687667	139.257611	180	BBMT
IEB0836A	-22.687917	139.276	187	BBMT
IEB0837A	-22.687778	139.296528	174	BBMT
IEB0838A	-22.688306	139.316028	178	BBMT
IEB0839A	-22.688444	139.335417	175	BBMT
IEB0840A	-22.688778	139.354833	169	BBMT
IEB0841A	-22.689	139.374722	165	BBMT
IEB0842A	-22.689083	139.393806	175	BBMT
IEB0843A	-22.689528	139.413222	191	BBMT
IEB0844B	-22.689389	139.432667	192	BBMT
IEB0845A	-22.689611	139.452306	195	BBMT
IEB0846A	-22.689861	139.4715	187	BBMT
IEB0847A	-22.690111	139.491111	176	BBMT
IEB0848A	-22.690306	139.510528	192	BBMT
IEB0849B	-22.690694	139.529972	180	BBMT
IEB0850A	-22.690694	139.549444	183	BBMT
IEB0851A	-22.690806	139.568944	187	BBMT
IEB0852A	-22.691194	139.589861	190	BBMT
IEB0853A	-22.690861	139.607167	210	BBMT
IEB0854A	-22.691472	139.627472	209	BBMT
IEB0855A	-22.691556	139.647444	197	BBMT
IEB0856A	-22.690889	139.666056	197	BBMT
IEB0857A	-22.691972	139.686222	196	BBMT
IEB0858A	-22.691378	139.70504	181.11	BBMT
IEB0859A	-22.691805	139.724707	174.01	BBMT
IEB0860A	-22.693072	139.743647	182.12	BBMT
IEB0861A	-22.691695	139.763482	202.27	BBMT
IEB0862A	-22.692553	139.78329	195.16	BBMT
IEB0863A	-22.692075	139.801943	190.27	BBMT
IEB0933A	-22.642056	139.219222	183	BBMT
IEB0934A	-22.642278	139.238694	194	BBMT
IEB0935A	-22.642556	139.258111	191	BBMT
IEB0936A	-22.642528	139.277861	192	BBMT
IEB0937A	-22.643	139.296306	190	BBMT
IEB0938A	-22.642667	139.316556	201	BBMT
IEB0939A	-22.644278	139.335028	191	BBMT
IEB0940A	-22.643611	139.355361	188	BBMT
IEB0941A	-22.643861	139.374778	179	BBMT
IEB0942A	-22.643972	139.394278	174	BBMT
IEB0943A	-22.644194	139.413722	173	BBMT
IEB0944A	-22.644389	139.433167	183	BBMT
IEB0945A	-22.644028	139.452583	184	BBMT
IEB0946A	-22.64475	139.472111	185	BBMT

IEB0947A	-22.644944	139.491583	191	BBMT
IEB0948A	-22.645528	139.511333	192	BBMT
IEB0949A	-22.645083	139.530917	213	BBMT
IEB0950A	-22.645361	139.550056	207	BBMT
IEB0951A	-22.645889	139.569722	200	BBMT
IEB0952A	-22.645639	139.58925	219	BBMT
IEB0953B	-22.646194	139.608556	215	BBMT
IEB0954A	-22.646278	139.627972	207	BBMT
IEB0955A	-22.644942	139.648433	200.8	BBMT
IEB0956A	-22.64595	139.666808	212.73	BBMT
IEB0957A	-22.646345	139.68614	203.45	BBMT
IEB0958A	-22.646687	139.705698	190.94	BBMT
IEB0959A	-22.646982	139.72656	195.61	BBMT
IEB0960A	-22.647111	139.744528	182	BBMT
IEB0961A	-22.646772	139.763887	186.27	BBMT
IEB0962A	-22.647183	139.783592	180.87	BBMT
IEB1003A	-22.588806	138.63675	166	BBMT
IEB1004A	-22.589556	138.655694	166	BBMT
IEB1005B	-22.590056	138.675222	172	BBMT
IEB1006A	-22.590417	138.695056	162	BBMT
IEB1007B	-22.590556	138.714139	163	BBMT
IEB1008B	-22.59075	138.733556	158	BBMT
IEB1009A	-22.591028	138.753139	154	BBMT
IEB1010A	-22.590083	138.772222	151	BBMT
IEB1011A	-22.591194	138.791444	148	BBMT
IEB1012A	-22.591917	138.811361	147	BBMT
IEB1013A	-22.592056	138.830778	141	BBMT
IEB1014A	-22.592444	138.850222	145	BBMT
IEB1015A	-22.592722	138.869694	149	BBMT
IEB1016A	-22.593472	138.889194	146	BBMT
IEB1017B	-22.593111	138.908806	152	BBMT
IEB1018A	-22.593694	138.927972	153	BBMT
IEB1019A	-22.593639	138.947472	162	BBMT
IEB1020A	-22.594194	138.967	165	BBMT
IEB1021A	-22.594167	138.986389	175	BBMT
IEB1022A	-22.594806	139.005667	181	BBMT
IEB1023A	-22.594694	139.025417	185	BBMT
IEB1024A	-22.594972	139.044889	196	BBMT
IEB1025A	-22.595278	139.063889	194	BBMT
IEB1026A	-22.595472	139.083722	198	BBMT
IEB1027A	-22.595472	139.103278	196	BBMT
IEB1028A	-22.596194	139.122472	203	BBMT
IEB1029A	-22.596056	139.142611	190	BBMT
IEB1030A	-22.596444	139.161694	195	BBMT
IEB1031A	-22.594694	139.180278	187	BBMT
IEB1032A	-22.596889	139.2005	198	BBMT
IEB1033A	-22.596917	139.219889	192	BBMT
IEB1034A	-22.598778	139.239167	189	BBMT
IEB1035A	-22.597306	139.258389	192	BBMT
IEB1036A	-22.597556	139.277889	196	BBMT
IEB1037A	-22.597833	139.297417	197	BBMT
IEB1038A	-22.598194	139.317056	209	BBMT

IEB1039A	-22.598389	139.336778	214	BBMT
IEB1040A	-22.597556	139.356083	209	BBMT
IEB1041A	-22.598472	139.375278	196	BBMT
IEB1042A	-22.599	139.395278	190	BBMT
IEB1043A	-22.599028	139.414306	179	BBMT
IEB1044A	-22.599083	139.433583	188	BBMT
IEB1045A	-22.599306	139.453472	186	BBMT
IEB1046A	-22.599528	139.472611	187	BBMT
IEB1047A	-22.599444	139.492389	204	BBMT
IEB1048A	-22.599944	139.511694	200	BBMT
IEB1049A	-22.600306	139.530972	204	BBMT
IEB1050A	-22.599889	139.550417	211	BBMT
IEB1051A	-22.600222	139.569806	213	BBMT
IEB1052A	-22.600722	139.589083	225	BBMT
IEB1053A	-22.601306	139.607972	219	BBMT
IEB1054A	-22.600194	139.628972	214	BBMT
IEB1055A	-22.599833	139.647639	223	BBMT
IEB1056A	-22.601361	139.667139	210	BBMT
IEB1057A	-22.6015	139.686583	209	BBMT
IEB1058A	-22.600972	139.706028	200	BBMT
IEB1059A	-22.601861	139.725528	199	BBMT
IEB1060A	-22.600944	139.744833	192	BBMT
IEB1061A	-22.602806	139.76475	192	BBMT
IEB1102A	-22.544028	138.617917	164	BBMT
IEB1103A	-22.543083	138.638333	163	BBMT
IEB1104A	-22.544806	138.656361	178	BBMT
IEB1105A	-22.544944	138.676028	170	BBMT
IEB1106A	-22.545111	138.695639	162	BBMT
IEB1107A	-22.545389	138.714833	159	BBMT
IEB1108A	-22.545861	138.734278	156	BBMT
IEB1109A	-22.546583	138.754194	158	BBMT
IEB1110A	-22.546222	138.77325	156	BBMT
IEB1111A	-22.546444	138.792667	147	BBMT
IEB1112A	-22.546778	138.812028	149	BBMT
IEB1113A	-22.546944	138.831528	145	BBMT
IEB1114A	-22.546694	138.851028	149	BBMT
IEB1115A	-22.546778	138.870444	144	BBMT
IEB1116A	-22.547444	138.889972	150	BBMT
IEB1117A	-22.548306	138.909111	148	BBMT
IEB1118A	-22.548139	138.928861	154	BBMT
IEB1119A	-22.5485	138.948194	163	BBMT
IEB1120A	-22.549111	138.967306	162	BBMT
IEB1121A	-22.549	138.986694	167	BBMT
IEB1122A	-22.549556	139.00625	167	BBMT
IEB1123A	-22.551389	139.025694	179	BBMT
IEB1124A	-22.549556	139.045444	183	BBMT
IEB1125A	-22.549889	139.064889	193	BBMT
IEB1126A	-22.55075	139.084389	202	BBMT
IEB1127A	-22.551611	139.103889	208	BBMT
IEB1128A	-22.550889	139.12325	215	BBMT
IEB1129A	-22.551139	139.142194	222	BBMT
IEB1130A	-22.550694	139.161972	223	BBMT

IEB1131A	-22.551722	139.181611	208	BBMT
IEB1132A	-22.551611	139.200528	201	BBMT
IEB1133A	-22.550944	139.220194	209	BBMT
IEB1134A	-22.552778	139.240056	210	BBMT
IEB1135A	-22.552306	139.259222	204	BBMT
IEB1136A	-22.552389	139.2785	207	BBMT
IEB1137A	-22.552722	139.297944	213	BBMT
IEB1138A	-22.552139	139.317889	202	BBMT
IEB1139A	-22.553556	139.337	192	BBMT
IEB1140a	-22.553333	139.356472	191	BBMT
IEB1141A	-22.552972	139.375833	193	BBMT
IEB1142A	-22.553722	139.395389	191	BBMT
IEB1143A	-22.553889	139.414806	183	BBMT
IEB1144A	-22.554111	139.434194	190	BBMT
IEB1145A	-22.554278	139.453667	193	BBMT
IEB1146b	-22.554361	139.473306	201	BBMT
IEB1147A	-22.554806	139.492528	215	BBMT
IEB1148A	-22.554861	139.511861	212	BBMT
IEB1149A	-22.555306	139.531472	209	BBMT
IEB1150A	-22.555	139.550528	207	BBMT
IEB1151A	-22.555028	139.569944	258	BBMT
IEB1152A	-22.555778	139.589472	243	BBMT
IEB1153A	-22.556111	139.609389	254	BBMT
IEB1154A	-22.555139	139.628028	223	BBMT
IEB1155A	-22.556028	139.648167	211	BBMT
IEB1156A	-22.557194	139.667639	202	BBMT
IEB1157A	-22.555111	139.68725	199	BBMT
IEB1158A	-22.556583	139.706194	201	BBMT
IEB1159A	-22.556472	139.725861	202	BBMT
IEB1160A	-22.55775	139.745861	198	BBMT
IEB1201A	-22.498306	138.601111	170	BBMT
IEB1202A	-22.498944	138.619389	174	BBMT
IEB1203A	-22.499472	138.638694	167	BBMT
IEB1204B	-22.499556	138.657472	181	BBMT
IEB1205A	-22.500333	138.676944	179	BBMT
IEB1206A	-22.502806	138.695694	182	BBMT
IEB1207A	-22.502056	138.715528	186	BBMT
IEB1208A	-22.500361	138.735306	168	BBMT
IEB1209A	-22.501444	138.754472	170	BBMT
IEB1210A	-22.501111	138.773556	163	BBMT
IEB1211A	-22.501222	138.793222	151	BBMT
IEB1212A	-22.501611	138.812833	150	BBMT
IEB1213A	-22.502111	138.832222	146	BBMT
IEB1214A	-22.502028	138.851861	150	BBMT
IEB1215A	-22.502861	138.872306	146	BBMT
IEB1216A	-22.502694	138.890528	150	BBMT
IEB1217A	-22.503056	138.909528	155	BBMT
IEB1218A	-22.503139	138.929472	156	BBMT
IEB1219A	-22.503444	138.948833	152	BBMT
IEB1220A	-22.503556	138.968361	170	BBMT
IEB1221A	-22.503972	138.987722	178	BBMT
IEB1222A	-22.504333	139.007194	175	BBMT

IEB1223A	-22.504389	139.02675	178	BBMT
IEB1224A	-22.504611	139.046222	181	BBMT
IEB1225A	-22.504889	139.065361	187	BBMT
IEB1226A	-22.505056	139.084861	190	BBMT
IEB1227A	-22.504611	139.104389	205	BBMT
IEB1228A	-22.506	139.123639	214	BBMT
IEB1229A	-22.504972	139.14475	214	BBMT
IEB1230A	-22.505028	139.162444	215	BBMT
IEB1231A	-22.505361	139.183222	212	BBMT
IEB1232A	-22.506278	139.201389	206	BBMT
IEB1233A	-22.506667	139.220889	208	BBMT
IEB1234A	-22.506278	139.240361	204	BBMT
IEB1235A	-22.505611	139.259944	220	BBMT
IEB1236A	-22.507667	139.279306	222	BBMT
IEB1237A	-22.507306	139.298833	213	BBMT
IEB1238A	-22.506972	139.317528	209	BBMT
IEB1239A	-22.507889	139.337139	209	BBMT
IEB1240A	-22.507722	139.357111	194	BBMT
IEB1241A	-22.508306	139.376389	207	BBMT
IEB1242A	-22.508111	139.395472	213	BBMT
IEB1243A	-22.50975	139.415778	198	BBMT
IEB1244B	-22.508833	139.435028	189	BBMT
IEB1245A	-22.509306	139.454389	196	BBMT
IEB1246A	-22.509111	139.474028	193	BBMT
IEB1247A	-22.509722	139.493417	213	BBMT
IEB1248A	-22.51	139.511611	203	BBMT
IEB1249A	-22.509694	139.531917	210	BBMT
IEB1250A	-22.508833	139.551361	225	BBMT
IEB1251A	-22.510056	139.570694	228	BBMT
IEB1252A	-22.510306	139.590389	252	BBMT
IEB1253A	-22.510444	139.609472	228	BBMT
IEB1254B	-22.510722	139.629194	213	BBMT
IEB1255B	-22.510806	139.648944	210	BBMT
IEB1256A	-22.510806	139.668278	218	BBMT
IEB1257A	-22.511139	139.687111	222	BBMT
IEB1258A	-22.511306	139.706889	219	BBMT
IEB1259A	-22.510889	139.726583	214	BBMT
IEB1300A	-22.453056	138.580417	177	BBMT
IEB1301A	-22.453556	138.599722	185	BBMT
IEB1302A	-22.453694	138.6205	208	BBMT
IEB1303A	-22.454056	138.639889	208	BBMT
IEB1304A	-22.454389	138.658111	193	BBMT
IEB1305A	-22.4545	138.677778	176	BBMT
IEB1306A	-22.454694	138.696972	178	BBMT
IEB1307A	-22.456083	138.716778	165	BBMT
IEB1308A	-22.453944	138.735806	163	BBMT
IEB1309A	-22.455667	138.755278	158	BBMT
IEB1310A	-22.456056	138.774778	155	BBMT
IEB1311A	-22.455139	138.793917	153	BBMT
IEB1312A	-22.456472	138.813583	144	BBMT
IEB1313A	-22.456528	138.832861	147	BBMT
IEB1314A	-22.456972	138.852361	157	BBMT

IEB1315A	-22.457361	138.871444	156	BBMT
IEB1316A	-22.457833	138.891444	156	BBMT
IEB1317A	-22.458083	138.91075	157	BBMT
IEB1318A	-22.45775	138.930056	153	BBMT
IEB1319A	-22.458222	138.949556	151	BBMT
IEB1320A	-22.458444	138.969361	155	BBMT
IEB1321A	-22.458528	138.987861	163	BBMT
IEB1322A	-22.459	139.007056	168	BBMT
IEB1323A	-22.459944	139.027611	172	BBMT
IEB1324A	-22.459444	139.046694	175	BBMT
IEB1325A	-22.459778	139.066139	176	BBMT
IEB1326A	-22.460056	139.085389	178	BBMT
IEB1327A	-22.461222	139.1045	195	BBMT
IEB1328A	-22.459639	139.124306	190	BBMT
IEB1329A	-22.460778	139.143778	202	BBMT
IEB1330A	-22.461028	139.162944	196	BBMT
IEB1331A	-22.461306	139.182444	197	BBMT
IEB1332A	-22.461111	139.202028	202	BBMT
IEB1333B	-22.461361	139.221278	199	BBMT
IEB1334A	-22.461222	139.239694	206	BBMT
IEB1335A	-22.462806	139.260333	204	BBMT
IEB1336A	-22.46175	139.279667	213	BBMT
IEB1337A	-22.462056	139.29925	218	BBMT
IEB1338A	-22.463056	139.318917	225	BBMT
IEB1339A	-22.462694	139.338111	212	BBMT
IEB1339B	-22.462806	139.338111	211	BBMT
IEB1340A	-22.463806	139.357444	209	BBMT
IEB1341A	-22.463167	139.376917	219	BBMT
IEB1342A	-22.463306	139.396778	211	BBMT
IEB1343A	-22.463361	139.416222	202	BBMT
IEB1344A	-22.464361	139.434528	192	BBMT
IEB1345A	-22.464306	139.454583	196	BBMT
IEB1346A	-22.464056	139.473722	204	BBMT
IEB1347A	-22.46525	139.492528	230	BBMT
IEB1348A	-22.464667	139.512722	226	BBMT
IEB1349A	-22.465139	139.532417	216	BBMT
IEB1350A	-22.468778	139.552194	215	BBMT
IEB1351A	-22.463611	139.570528	228	BBMT
IEB1352A	-22.465139	139.590444	247	BBMT
IEB1353A	-22.466028	139.611361	234	BBMT
IEB1354A	-22.465528	139.629556	224	BBMT
IEB1355A	-22.465722	139.648972	225	BBMT
IEB1356A	-22.465389	139.668139	224	BBMT
IEB1357A	-22.466083	139.687778	226	BBMT
IEB1358A	-22.466361	139.708	220	BBMT
IEB1400A	-22.40875	138.581028	202	BBMT
IEB1401A	-22.408722	138.600056	188	BBMT
IEB1402A	-22.408583	138.619889	182	BBMT
IEB1403A	-22.409444	138.640056	198	BBMT
IEB1404A	-22.407889	138.659722	187	BBMT
IEB1405A	-22.409222	138.678083	165	BBMT
IEB1406A	-22.409194	138.698028	161	BBMT

IEB1407A	-22.410222	138.717194	154	BBMT
IEB1408B	-22.410278	138.736778	158	BBMT
IEB1409A	-22.4105	138.755861	142	BBMT
IEB1410A	-22.410861	138.775389	157	BBMT
IEB1411A	-22.411028	138.795	151	BBMT
IEB1412A	-22.411389	138.814139	150	BBMT
IEB1413C	-22.411694	138.834306	157	BBMT
IEB1414A	-22.411917	138.853056	154	BBMT
IEB1415A	-22.411778	138.872444	159	BBMT
IEB1416A	-22.412278	138.891806	154	BBMT
IEB1417A	-22.412639	138.911222	157	BBMT
IEB1418A	-22.412944	138.930778	158	BBMT
IEB1419A	-22.414167	138.949861	158	BBMT
IEB1420A	-22.413361	138.969611	165	BBMT
IEB1421A	-22.413556	138.98875	165	BBMT
IEB1422A	-22.414056	139.008278	170	BBMT
IEB1423A	-22.414111	139.027722	165	BBMT
IEB1424A	-22.414194	139.047167	168	BBMT
IEB1425A	-22.414444	139.066444	170	BBMT
IEB1426A	-22.414806	139.086194	169	BBMT
IEB1427A	-22.414944	139.105583	167	BBMT
IEB1428A	-22.415389	139.125028	185	BBMT
IEB1429A	-22.415528	139.1445	184	BBMT
IEB1430A	-22.415222	139.163194	198	BBMT
IEB1431A	-22.415667	139.183167	206	BBMT
IEB1432A	-22.417222	139.201944	200	BBMT
IEB1433A	-22.416222	139.222194	200	BBMT
IEB1434A	-22.417	139.241306	207	BBMT
IEB1435A	-22.416556	139.260639	200	BBMT
IEB1436B	-22.415361	139.279417	218	BBMT
IEB1437A	-22.417194	139.299889	232	BBMT
IEB1438A	-22.417806	139.319583	213	BBMT
IEB1439A	-22.417833	139.338528	225	BBMT
IEB1440A	-22.417556	139.357972	224	BBMT
IEB1441B	-22.418194	139.377583	211	BBMT
IEB1442A	-22.418417	139.397333	222	BBMT
IEB1443A	-22.417639	139.415778	208	BBMT
IEB1444A	-22.420139	139.435778	207	BBMT
IEB1445A	-22.417917	139.455806	194	BBMT
IEB1446A	-22.418944	139.474806	197	BBMT
IEB1447A	-22.418444	139.493778	208	BBMT
IEB1448A	-22.417889	139.512944	218	BBMT
IEB1449A	-22.419056	139.532778	229	BBMT
IEB1450A	-22.418417	139.552611	231	BBMT
IEB1451A	-22.419333	139.572056	250	BBMT
IEB1452A	-22.420278	139.590361	242	BBMT
IEB1453A	-22.420278	139.610694	235	BBMT
IEB1454A	-22.421	139.629611	235	BBMT
IEB1455A	-22.420417	139.649222	227	BBMT
IEB1456A	-22.420528	139.668972	223	BBMT
IEB1457A	-22.421722	139.688278	228	BBMT
IEB1500A	-22.363167	138.581806	167	BBMT

IEB1501A	-22.363417	138.598611	175	BBMT
IEB1502A	-22.36275	138.616694	162	BBMT
IEB1503A	-22.363556	138.640139	157	BBMT
IEB1504A	-22.363778	138.659111	161	BBMT
IEB1505A	-22.364361	138.679	156	BBMT
IEB1506A	-22.364972	138.698833	153	BBMT
IEB1507A	-22.366194	138.717806	146	BBMT
IEB1508A	-22.366056	138.737083	146	BBMT
IEB1509A	-22.365361	138.756639	152	BBMT
IEB1510A	-22.365667	138.776222	143	BBMT
IEB1511A	-22.362528	138.797583	151	BBMT
IEB1512A	-22.366111	138.814611	155	BBMT
IEB1513A	-22.366472	138.834389	149	BBMT
IEB1514A	-22.366306	138.853972	153	BBMT
IEB1515A	-22.367194	138.873083	155	BBMT
IEB1516A	-22.366944	138.893194	159	BBMT
IEB1517A	-22.367583	138.911972	152	BBMT
IEB1518A	-22.367722	138.931306	152	BBMT
IEB1519A	-22.368056	138.950833	169	BBMT
IEB1520A	-22.368667	138.970361	169	BBMT
IEB1521A	-22.368278	138.990028	175	BBMT
IEB1522A	-22.368639	139.009139	176	BBMT
IEB1523A	-22.368778	139.028611	174	BBMT
IEB1524A	-22.367194	139.048361	177	BBMT
IEB1525A	-22.369306	139.066972	191	BBMT
IEB1526A	-22.369444	139.086722	178	BBMT
IEB1527A	-22.369861	139.106194	187	BBMT
IEB1528A	-22.370111	139.125389	187	BBMT
IEB1529A	-22.370556	139.145083	206	BBMT
IEB1530A	-22.370694	139.164472	206	BBMT
IEB1531b	-22.370667	139.183667	191	BBMT
IEB1532A	-22.370861	139.203333	201	BBMT
IEB1533A	-22.371417	139.222639	215	BBMT
IEB1534A	-22.371528	139.262056	222	BBMT
IEB1535A	-22.37125	139.241556	226	BBMT
IEB1536A	-22.372278	139.280611	224	BBMT
IEB1537A	-22.372111	139.300972	233	BBMT
IEB1538A	-22.372306	139.319778	233	BBMT
IEB1539A	-22.372306	139.338972	253	BBMT
IEB1540A	-22.372361	139.358361	229	BBMT
IEB1541A	-22.372694	139.378056	234	BBMT
IEB1542A	-22.372694	139.397278	232	BBMT
IEB1543A	-22.373444	139.416472	214	BBMT
IEB1544A	-22.373556	139.436333	203	BBMT
IEB1545A	-22.371444	139.455306	202	BBMT
IEB1546A	-22.374472	139.474944	206	BBMT
IEB1547A	-22.375722	139.494472	213	BBMT
IEB1548A	-22.374417	139.514222	207	BBMT
IEB1549A	-22.37475	139.533111	217	BBMT
IEB1550A	-22.374444	139.552778	222	BBMT
IEB1551A	-22.375417	139.572639	231	BBMT
IEB1552a	-22.376028	139.592028	245	BBMT

IEB1553A	-22.374889	139.610972	243	BBMT
IEB1554A	-22.375111	139.631361	230	BBMT
IEB1555A	-22.375556	139.649667	239	BBMT
IEB1556A	-22.375167	139.669333	242	BBMT
IEB1557A	-22.375639	139.687611	238	BBMT
IEB1600A	-22.318056	138.581889	180	BBMT
IEB1601A	-22.318639	138.602333	174	BBMT
IEB1602A	-22.319639	138.621444	169	BBMT
IEB1603A	-22.318667	138.640972	165	BBMT
IEB1604A	-22.318944	138.660389	157	BBMT
IEB1605A	-22.319222	138.679778	160	BBMT
IEB1606A	-22.3195	138.699194	156	BBMT
IEB1607B	-22.319778	138.718611	152	BBMT
IEB1608A	-22.319889	138.737889	152	BBMT
IEB1610A	-22.320694	138.777278	155	BBMT
IEB1611A	-22.321222	138.796556	151	BBMT
IEB1612A	-22.321111	138.815417	156	BBMT
IEB1613A	-22.321944	138.834944	157	BBMT
IEB1614A	-22.321639	138.854417	157	BBMT
IEB1615A	-22.321889	138.873806	161	BBMT
IEB1616B	-22.322194	138.893222	165	BBMT
IEB1617A	-22.322417	138.912639	165	BBMT
IEB1618A	-22.322639	138.932056	171	BBMT
IEB1619A	-22.322833	138.951389	176	BBMT
IEB1620A	-22.323194	138.970806	176	BBMT
IEB1621A	-22.323361	138.990667	179	BBMT
IEB1622A	-22.323556	139.00975	178	BBMT
IEB1623A	-22.324361	139.028944	181	BBMT
IEB1624A	-22.324389	139.048722	184	BBMT
IEB1625A	-22.325083	139.067861	182	BBMT
IEB1626A	-22.324917	139.087222	192	BBMT
IEB1627A	-22.324722	139.106806	196	BBMT
IEB1628A	-22.325444	139.126083	197	BBMT
IEB1629A	-22.325528	139.145583	206	BBMT
IEB1630A	-22.325722	139.165306	202	BBMT
IEB1631A	-22.325667	139.184444	214	BBMT
IEB1632A	-22.325361	139.203111	226	BBMT
IEB1633A	-22.326111	139.223472	234	BBMT
IEB1634A	-22.326444	139.241806	228	BBMT
IEB1635A	-22.323111	139.262028	247	BBMT
IEB1636A	-22.326611	139.281722	248	BBMT
IEB1637A	-22.327111	139.300944	241	BBMT
IEB1638A	-22.325	139.320694	250	BBMT
IEB1639A	-22.327417	139.340444	264	BBMT
IEB1640A	-22.326472	139.358444	265	BBMT
IEB1641A	-22.328028	139.378389	235	BBMT
IEB1642A	-22.328333	139.397806	222	BBMT
IEB1643A	-22.328278	139.417306	219	BBMT
IEB1644A	-22.328139	139.436639	212	BBMT
IEB1645A	-22.328556	139.455861	213	BBMT
IEB1646A	-22.328028	139.475556	228	BBMT
IEB1647A	-22.330222	139.494889	229	BBMT

IEB1648A	-22.330389	139.516889	228	BBMT
IEB1649A	-22.329472	139.535056	238	BBMT
IEB1650A	-22.329194	139.553083	226	BBMT
IEB1651A	-22.328972	139.572806	244	BBMT
IEB1652A	-22.329611	139.591556	253	BBMT
IEB1653A	-22.331222	139.611139	243	BBMT
IEB1654A	-22.330306	139.630833	248	BBMT
IEB1655A	-22.328111	139.651111	248	BBMT
IEB1656A	-22.329667	139.670444	249	BBMT
IEB1702A	-22.27325	138.622333	193	BBMT
IEB1703A	-22.273528	138.641722	179	BBMT
IEB1704A	-22.273806	138.661139	174	BBMT
IEB1705A	-22.274111	138.680528	168	BBMT
IEB1706A	-22.274389	138.699944	164	BBMT
IEB1707A	-22.274833	138.719361	161	BBMT
IEB1708A	-22.274806	138.738722	153	BBMT
IEB1709A	-22.274444	138.757583	155	BBMT
IEB1710A	-22.275389	138.777694	158	BBMT
IEB1711A	-22.275694	138.796694	163	BBMT
IEB1712A	-22.276028	138.816306	158	BBMT
IEB1713A	-22.276222	138.835722	162	BBMT
IEB1714A	-22.276472	138.855139	160	BBMT
IEB1715A	-22.276722	138.874528	159	BBMT
IEB1716A	-22.277	138.893972	161	BBMT
IEB1717A	-22.277222	138.913111	166	BBMT
IEB1718A	-22.277417	138.932806	171	BBMT
IEB1719A	-22.277722	138.952556	180	BBMT
IEB1720A	-22.277278	138.971472	189	BBMT
IEB1721A	-22.278333	138.990833	185	BBMT
IEB1722A	-22.278639	139.010361	185	BBMT
IEB1723A	-22.279444	139.030111	187	BBMT
IEB1724A	-22.278722	139.049083	188	BBMT
IEB1725A	-22.279	139.068417	192	BBMT
IEB1726A	-22.279333	139.087944	190	BBMT
IEB1727A	-22.279639	139.107444	199	BBMT
IEB1728A	-22.279694	139.12675	201	BBMT
IEB1729A	-22.279556	139.146222	201	BBMT
IEB1730A	-22.280444	139.165528	211	BBMT
IEB1731C	-22.279139	139.185222	215	BBMT
IEB1732A	-22.280278	139.204361	242	BBMT
IEB1733a	-22.280889	139.223611	247	BBMT
IEB1734a	-22.280917	139.243639	250	BBMT
IEB1735A	-22.280389	139.261917	250	BBMT
IEB1736A	-22.285583	139.283139	257	BBMT
IEB1737A	-22.281861	139.301056	262	BBMT
IEB1738A	-22.281306	139.320833	261	BBMT
IEB1739A	-22.282139	139.340139	242	BBMT
IEB1740A	-22.28275	139.359417	243	BBMT
IEB1741A	-22.282361	139.378889	238	BBMT
IEB1742A	-22.282694	139.398639	221	BBMT
IEB1743A	-22.283167	139.417861	217	BBMT
IEB1744a	-22.283361	139.437528	230	BBMT

IEB1745A	-22.283889	139.456611	222	BBMT
IEB1746A	-22.283444	139.475944	230	BBMT
IEB1747a	-22.283833	139.495389	235	BBMT
IEB1748A	-22.283778	139.514972	239	BBMT
IEB1749A	-22.284417	139.533278	233	BBMT
IEB1750a	-22.284389	139.554028	244	BBMT
IEB1751A	-22.284194	139.572694	269	BBMT
IEB1752A	-22.285056	139.591972	261	BBMT
IEB1753a	-22.285278	139.611861	259	BBMT
IEB1754A	-22.285694	139.631306	268	BBMT
IEB1755A	-22.285167	139.650667	258	BBMT
IEB1801A	-22.227861	138.603778	206	BBMT
IEB1803B	-22.228389	138.6425	167	BBMT
IEB1804A	-22.229194	138.66225	163	BBMT
IEB1805A	-22.228694	138.681222	164	BBMT
IEB1806A	-22.228194	138.700694	159	BBMT
IEB1807A	-22.229028	138.720472	162	BBMT
IEB1808A	-22.231111	138.739889	160	BBMT
IEB1809A	-22.233306	138.760389	151	BBMT
IEB1810A	-22.229528	138.777889	163	BBMT
IEB1811A	-22.230889	138.798333	165	BBMT
IEB1812A	-22.230722	138.817139	175	BBMT
IEB1813A	-22.231028	138.836417	162	BBMT
IEB1814A	-22.231333	138.85575	167	BBMT
IEB1815A	-22.231667	138.875278	169	BBMT
IEB1816A	-22.231111	138.892694	164	BBMT
IEB1817A	-22.231389	138.913139	171	BBMT
IEB1818A	-22.233361	138.933194	176	BBMT
IEB1819A	-22.233306	138.953333	190	BBMT
IEB1820A	-22.233083	138.971972	191	BBMT
IEB1821A	-22.233028	138.991583	192	BBMT
IEB1822A	-22.233306	139.010778	200	BBMT
IEB1823A	-22.232556	139.030389	210	BBMT
IEB1824A	-22.234028	139.049722	206	BBMT
IEB1825A	-22.234278	139.069278	200	BBMT
IEB1826A	-22.234111	139.088806	198	BBMT
IEB1827B	-22.234194	139.108083	202	BBMT
IEB1828A	-22.234528	139.127389	201	BBMT
IEB1829A	-22.235361	139.146806	203	BBMT
IEB1830A	-22.235056	139.166194	209	BBMT
IEB1831A	-22.235167	139.185444	227	BBMT
IEB1832A	-22.235556	139.204889	222	BBMT
IEB1833A	-22.234611	139.224556	238	BBMT
IEB1834A	-22.236389	139.243694	247	BBMT
IEB1835A	-22.233889	139.263194	261	BBMT
IEB1836A	-22.234611	139.282556	252	BBMT
IEB1837A	-22.233667	139.30175	261	BBMT
IEB1838A	-22.237111	139.321222	244	BBMT
IEB1839A	-22.236972	139.340778	239	BBMT
IEB1840A	-22.23675	139.359778	231	BBMT
IEB1841A	-22.237806	139.379611	230	BBMT
IEB1842A	-22.237639	139.399028	230	BBMT

IEB1843A	-22.237694	139.418333	227	BBMT
IEB1844a	-22.237889	139.437333	235	BBMT
IEB1845A	-22.23725	139.457194	247	BBMT
IEB1846A	-22.237556	139.476639	262	BBMT
IEB1847a	-22.239611	139.495444	251	BBMT
IEB1848A	-22.236611	139.515972	273	BBMT
IEB1849A	-22.239639	139.534444	250	BBMT
IEB1850b	-22.239139	139.554139	253	BBMT
IEB1851A	-22.239389	139.573472	272	BBMT
IEB1852A	-22.240972	139.593194	264	BBMT
IEB1853A	-22.238083	139.611861	262	BBMT
IEB1854A	-22.239722	139.630694	255	BBMT
IEB1855A	-22.239778	139.651583	247	BBMT

APPENDIX B

B.1 Descriptions of coarse inversion results

B1.1 Starting model variants

The UNC100 inversion achieved an overall RMS of 1.13. The Tzx and Zyx components have the poorest data fits (Figure B.1). The Tzx misfit is localized in the south-east and north-west of the data array, while the Zyx RMS is more evenly distributed across all sites. The Ty data has a small area of high misfit along the eastern edge of the array. RMS misfit for all data components is variable with period for UNC100 (Figure 2.9). Between periods of 4 s and 500 s all impedance components fit the data well. At periods less than 4 s, Zyx and Zxy have significantly higher RMS. At periods longer than 500 s impedance RMS increases for all components. The inversion model fits the Tzx data poorly for between 1 s and 200 s. The Tzy data has similar misfits to the impedance data, but is more consistent across all periods than the impedance or Tzx data.

UNC100 has three conductive features (C1, C2, C3; Figure B.1 and 2.8). The three conductors are present from approximately 15 km depth and have variable intensities. C3 is an elongate feature with an approximate north-south strike direction. There is a localized area of higher misfit for the Zxx data in the area around the south extent of C3 (Figure B.1). C2 has the highest conductivity of the three features and has a slightly more westerly strike than C3. C1 is a broad area of moderately high conductivity which deepens to the north-west (Figure 2.8). C1 and C2 become a single condor in the north-west of the survey area.

The overall misfit for UNC10 was 1.16, with the tipper components having a higher misfit than the impedance components. Both Tzx and Tzy have increased misfit along the eastern edge of the survey with but the Tzx data fit is significantly worse than the Tzy fit. Zxy, Zyx and Zyy have even misfit distributions with the Zyx component having higher overall misfit. The Zxx component has elevated misfit in the centre of the survey (Figure B.1). Misfits for the Zxy and Zyy components have similar trends, with misfits deteriorating outside the range of 2 s – 200 s (Figure 2.9). The model fits the Zxx and Zyx components slightly more poorly, with fits deteriorating outside the range of 4 s – 100 s. The Tzy component has an even misfit across all periods, but the Tzx data RMS is high between 10 s and 500 s.

UNC10 has four highly conductive features with a consistent north-north-west strike (C1, C2, C3, C4; Figure 2.8). C1, C2 and C3 are present from approximately 10 km depth while C4 is present from approximately 15 km depth. Some along strike variability in conductivity is evident for these features (Figure B.1).

The overall RMS misfit for UNC1000 was 1.05, with a tipper RMS of 0.99 and an impedance RMS of 1.15. The Tzx component has poor data fits in the south-east and north-west parts of the array. The impedance misfit is even across all sites except for the Zyx component, which has higher RMS in the south (Figure B.1). The overall misfit for Zyx is also slightly elevated for most periods (Figure 2.9).

A single, broad lower crustal conductor is present in the UNC1000 model (Figures B.1 and 2.8). This feature is in approximately the location of C1 in the other models but may be an amalgamation of C1 and C2. The cross section and profile plots of the UNC1000 model have subtle features in the middle of the survey area which may be C2 and C3. They are not well developed and it is unclear what, if any, impact they have on overall model RMS. In addition to these conductors a number of very small, shallow conductors are evident in the isosurface (Figure 2.8). Some of these features coincide with the location of C3 in other models but they are not restricted to the location of condors in other models and also occur exclusively between MT sites.

The overall misfit achieved by the UNC2 inversion was 1.04, with elevated misfit visible predominantly on the Tzx component, and to a lesser extent of the Zxx and Zyx components (Figure B.1). Poorer data fits are evident in the impedance components below periods of 3 s and above 500 s (Figure 2.9). The Tzx component fits poorest below a period of 500 s. The misfit distributions for all components and periods for UNC2 is strikingly similar to UNC100.

C1, C2 and C3 are all present in the UNC2 model, and their expressions are almost identical to the corresponding features in UNC100 (Figure B.1; see also Figure 2.8), with the exception that C2 and C1 are not joined in the north of UNC2.

GEO1 has a high overall misfit with an RMS of 2.43. The misfit is distributed across all periods (Figure 2.9) and data components, with the poorest fits on the Tzx, Zyx and Zxy components (Figure B.1). The Zxx component has the best data fits for the model, however even this component has localized areas of high misfit.

The C1 and C2 low-resistivity features are both present in the GEO1 model, however C2 is clearly aligned along a domain boundary where the roughness penalty was absent (Figure B.1). Additionally, there are resistivity contrasts localized along the Moho interface at approximately 45 km depth. Shallow inversion artefacts created between data sites are present in the central domain for the model (Figure 2.8).

The GEO2 model has an RMS misfit of 1.24 and most of this misfit is accommodated in the Tzx and Zyx components (Figure B.2 and 2.9).The Tzx component has elevated RMS concentrated in the centre of the data array, while the Zyx misfit is more evenly distributed across the entire dataset. RMS for all components is fairly evenly distributed across the full period range, with relatively elevated RMS in the Zyx component at periods <5 s and in the Tzx component between 10 – 200 s.

The inverted model has little variation from the starting model (compare Figures 2.7 and B.2). A lot of the variability between the starting and final models is confined to the low-resistivity layer in the top 500 m of the model. Some separation of the C1 and C3 structures is evident in the isosurfaces but they are not discrete feature as they area in other models (Figure 2.8).

The GEO3 inversion achieved a total RMS of 1.05, with slightly elevated RMS on the Zyx and Tzx components (Figure 2.9). Significantly elevated RMS values are present in the Zxy and Zyx components at periods <3 s, and all Z components at periods higher than 500 s (Figure 2.9). Both tipper components have reasonably even misfit distribution across all periods, decreasing slightly at longer periods.

The C1 and C3 features are both present in the final model for GEO3 (Figure B.2 and 2.8). C3 in this model has the largest expression of any of the coarse models, while the C1 extent is among the smallest of any model (Figure 2.8). Removal of the shallow low-resistivity layer appears to lead to a significant change in deep structures for this model when compared to the GEO2 model. However, as their misfit levels aren’t entirely comparable (Figure B.2), it is not possible to determine if the change is due to the removal of the shallow layer influencing the deeper features or if the higher misfit in GEO2 is due to these missing deeper features.

B1.2 Spatial data distribution models

The RAND1 model has an overall RMS misfit of 3.09, with the majority of this misfit accommodated in the tipper components (Figure B.2 and 2.9). There is some indication of a variable misfit distribution for the Zxx component, with lower misfits in the north-east. The other impedance components have an even misfits distribution across the area (Figure B.2). Despite the higher overall misfit when compared to other inversions in the coarse suite, the RMS with period distribution has similar characteristic for the impedance components with better data fits between 4 s and 400 s (Figure 2.9). The poor tipper component misfits are present in the longer period data, starting at 30 s.

Only the C1 conductors is present in the isosurface model for the RAND1 inversion. C1 is present from approximately 15 km and dips to the west (Figure 2.8). Subtle resistivity features which may correspond to C2 and C3 are visible in the map and profile for RAND1 (Figure 2.9).

The RAND2 model has an overall RMS was 3.27 for this inversion. Despite the higher overall RMS, spatial distribution of RMS for individual components is lower than the RAND1 inversion result. The bulk of misfit for the RAND2 inversion is accommodated in the Tzx and Tzy data at periods longer than 200 s. Between periods of 4 s and 400s the RMS for the impedance components is comparable to inversions with lower overall RMS with the exception of the Zyx component which has higher RMS misfits (Figure 2.9).

C1 and C3 are both present in the in the inversion model but C2 is absent within the data array (Figure B.2 and 2.8). C3 is a small north-north-west striking feature present between 15 km and 35 km depth. C1 is a north-south striking feature present from 20km that dips to the west. There is a feature in the south central part the RAND2 model in Figure 2.8 which may correspond to C2, however the feature is unconstrained by the data.

B1.3 Inverted data component model

The IMP100 model achieved an overall misfit of 1.05. The elevated misfits are present at periods less than 3 s and periods above 200 s (Figure 2.9). The misfit is evenly distributed across all four impedance components (Figure B.3) and have reasonably even spatial distributions. There are slightly elevated RMS misfit values for the Zxx and Zxy components for the area near the southern part of the C3 conductor (Figure 2.11).

C1, C3 and C3 are all present in the IMP100 inversion model (Figures B.3 and 2.8). C3 strikes approximately north-south and is present below a depth of 15 km (Figure B.3). C1 is also present from approximately 15 km depth and dips to the west (Figure 2.8). C2 is a comparatively small weak conductor which strikes north-west and joins with C1 in the north of the survey area. There is an additional, very small conductive features in the north of the study area between C2 and C3 (Figure 2.8). This feature only underlays a single MT site.

The TIP model achieved an overall misfit of 1.03, with most of the elevated RMS accommodated on the Tzx Component. The Tzx component RMS is elevated in the south and east of the data array (Figure B.2) and is largely confined to periods below 600 s (Figure 2.9). The Tzy component data has consistent RMS misfit across all sites and periods.

Only the C1 conductor is present in the Tipp model (Figure 2.8); it is located further east than the other coarse model C1 structures. The only other feature in the Tipp model is a broad gradient from high resistivity in the north-east to low resistivity in the south-west (Figures B.2 and 2.8). This trend is subtle but consistent at all depths.

The IMP10 inversion achieved an overall RMS misfit of 1.08. The Zxx and Zyx components have higher overall misfits, which is distributed across the entire area for the Zyx component, but is concentrated in the middle of the array for the Zxx component (Figure B.3). The RMS for the Zxx component is consistent across the full period range but has an overall higher misfit than the other components (Figure 2.9).

Four, approximately north-south striking low-resistivity features are present in the IMP10 model (C1, C2, C3 and C4; Figures B.3 and 2.8). Similar to UNC10, C1, C2 and C3 are present from approximately 10 km depth while C4 is present from approximately 15 km depth (Figure 2.8). The four low-resistivity features have shorter north-south strike extents and are slightly narrower than the corresponding features in UNC10 (Figure 2.8).

The overall RMS misfit for the IMP1000 model is 1.06. The misfits are evenly distributed spatially, with the Zyx component having the highest overall RMS misfit (Figures B.3 and 2.9). The model fits the data well between periods of 4 – 200 s but RMS values increase outside this range, particularly on the Zxy and Zyx components (Figure 2.9).

Similar to UNC1000, only C1 is present in the IMP1000 model and may be an amalgamation of C1 and C2 (Figures B.3 and 2.8). C21 in IMP1000 has a smaller north-south extent than the same features in UNC1000 (Figure 2.8). The cross section and profile plots of the IMP1000 model have subtle features in the middle of the survey area which may be C2 and C3, however similar to UNC1000 they are not well developed. In addition to C1, a number of very small, shallow conductors are evident in the isosurface (Figure 2.8).

B1.4 Covariance models

The COVX inversion achieved an RMS misfit of 1.04. Zyx and Zxx have slightly higher RMS than Zxy and Zyy, with the Zxx misfit localized in the centre of the array and the Zyx misfit more evenly distributed across all sites (Figure B.3). All components fit the data well between periods of 3 s and 100 s with misfits increasing outside this range (Figure 2.9).

C1 and C3 are both present in the COVX model (Figure 2.11), however the resistivity of these features is higher than other models, leading to the features being largely absent from the isosurface (Figure 2.8). The map and profile slices from the model indicate C3 is present from approximately 10 km depth and C1 present from 20 km.

The overall RMS misfit for COVY was 1.04. The misfit has a reasonably even spatial distribution for all components across the entire data array (Figure B.3). RMS for the Zxx and Zyx components is slightly elevated compared to Zxy and Zyy between periods of 100 s and 500 s, but general misfits across all four impedance components is relatively even between 4 s and 400 s (Figure 2.9).

C1, C2 and C3 are all present in the COVY model. The strike of all three features is strongly north-south and C2 and C3 are narrow and exist largely between sites (Figures B.3 and 2.11). All three low-resistivity features occur below depths of 15 km (Figure B.3).

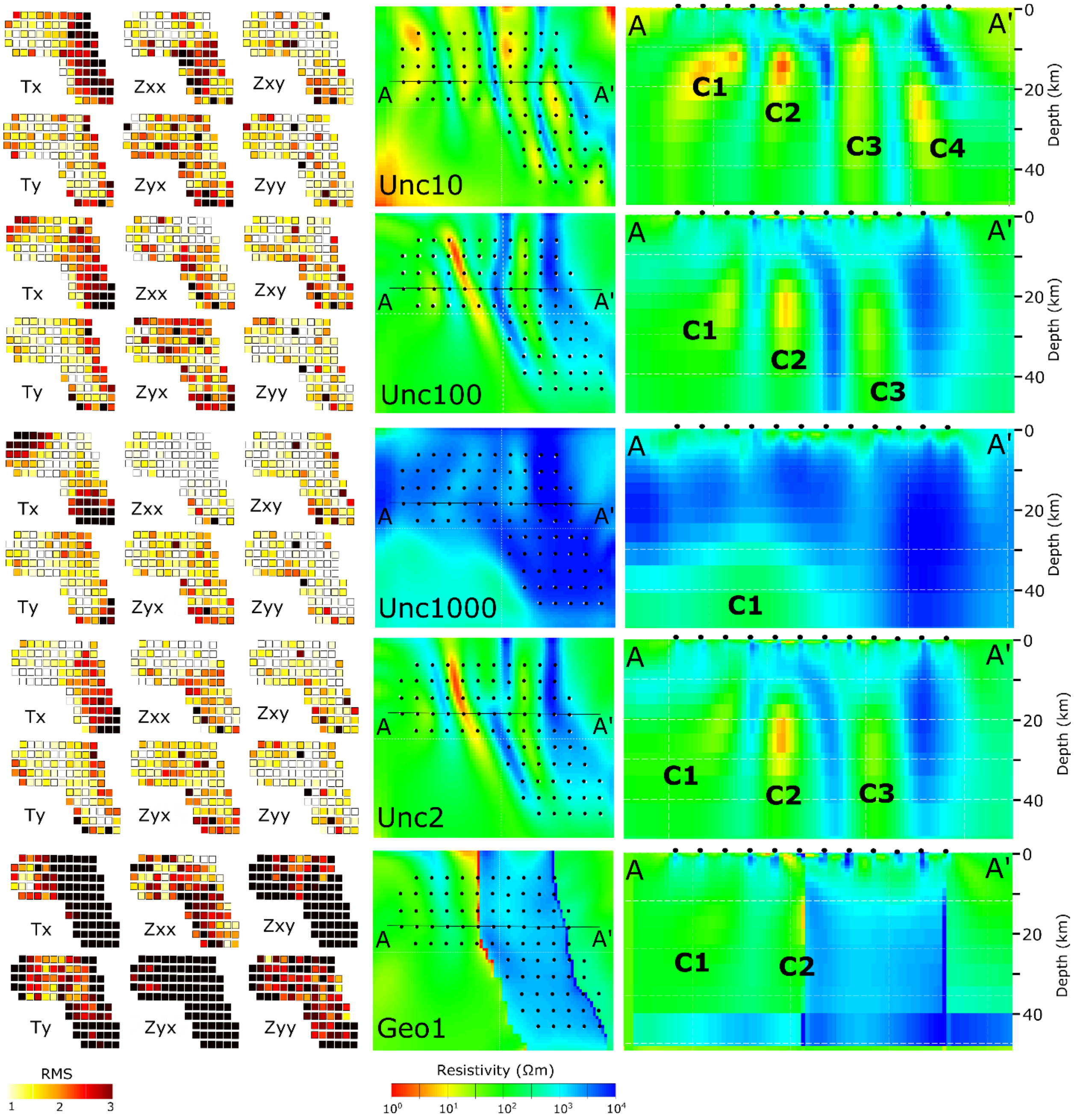

Figure B.1. Comparison of results from UNC10, UNC 100, UNC1000, UNC2 and GEO1 inversions. Left to right, spatial RMS distribution all inverted data components, 20km depth slice, and model section (location indicated on depth slice).

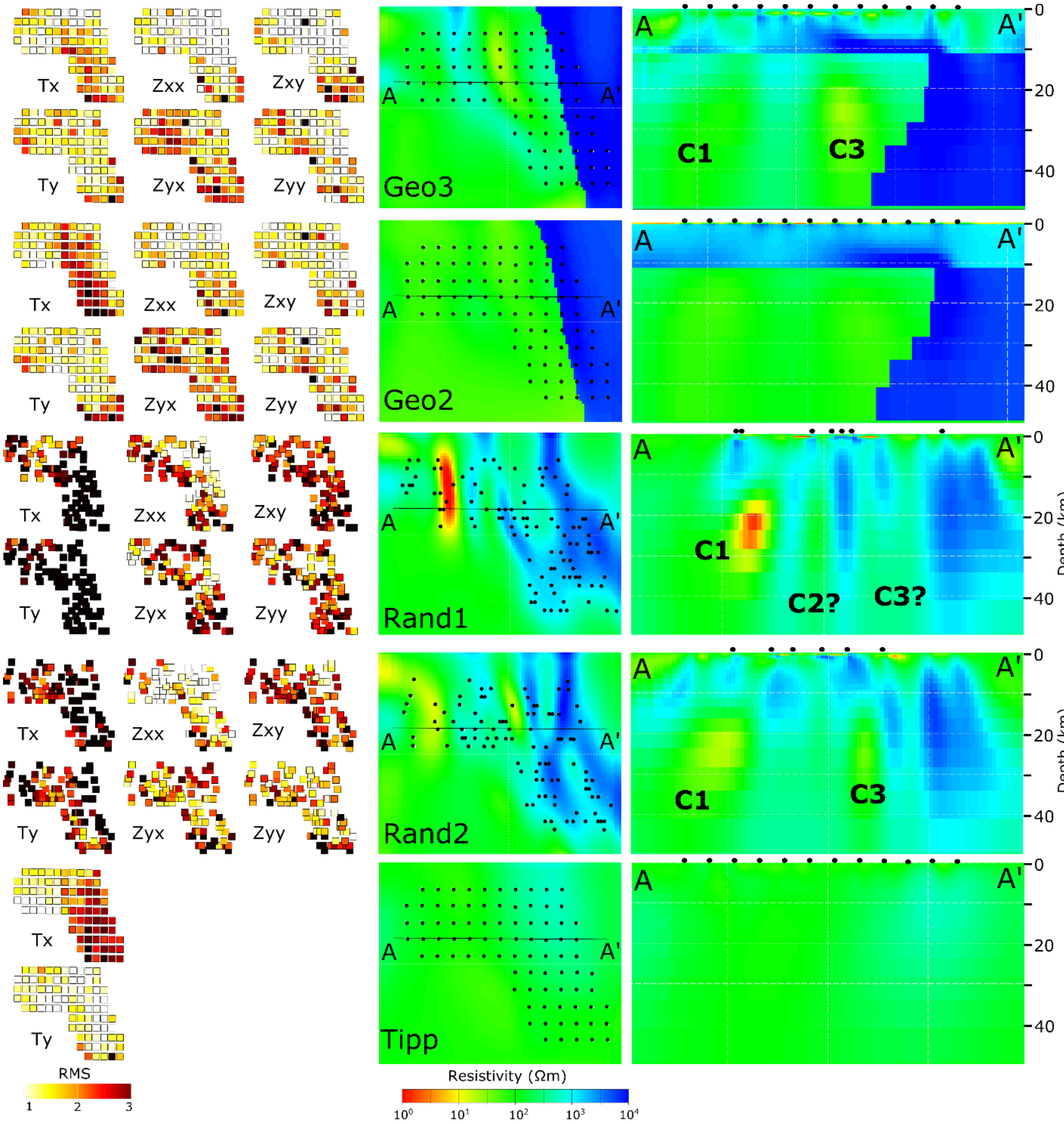

Figure B.2. Comparison of results from GEO3, GEO2, RAND1, RAND2 and Tipp inversions. Left to right, spatial RMS distribution for all inverted data components, 20km depth slice, and model section (location indicated on depth slice).

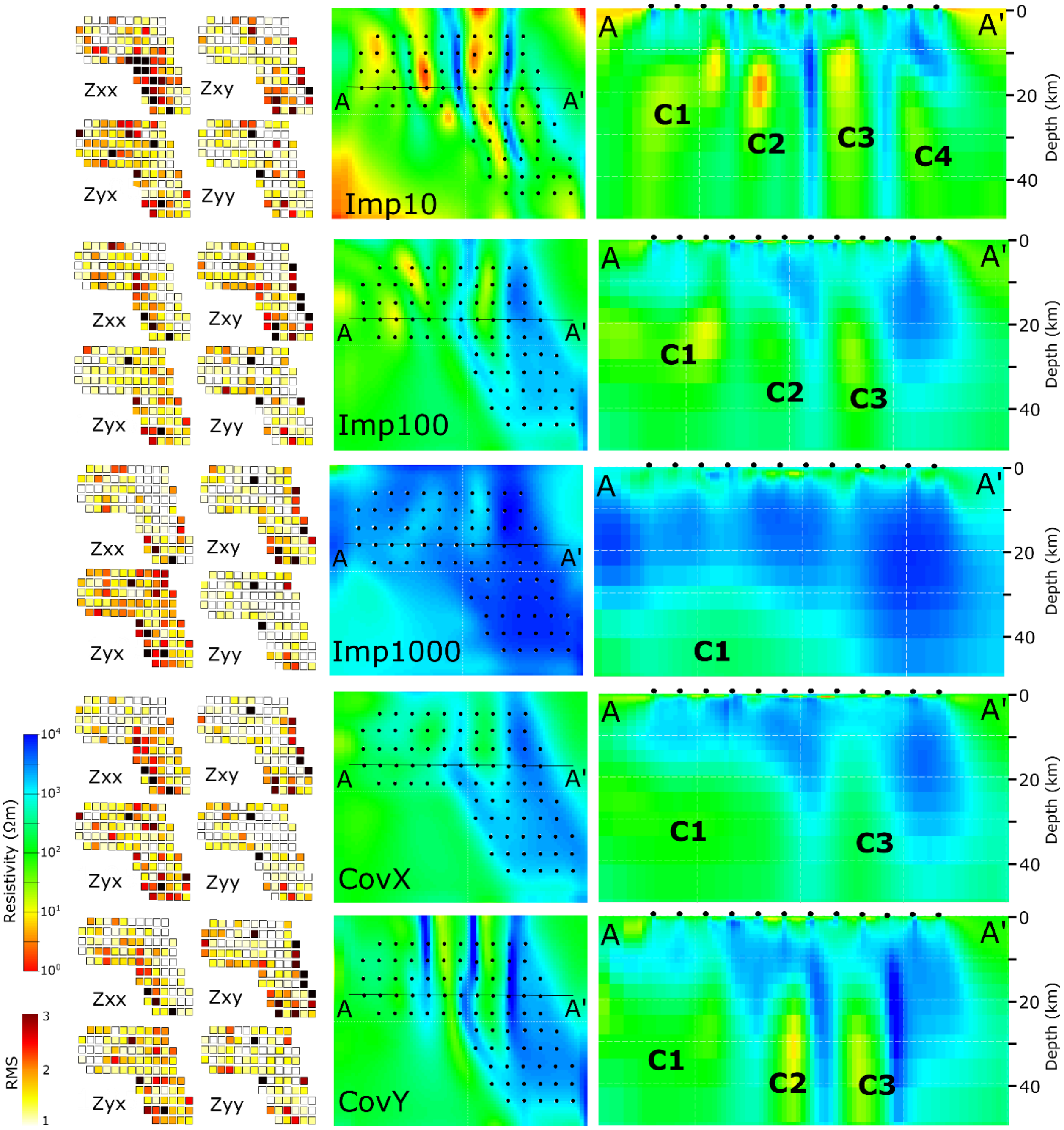

Figure B.3. Comparison of results from IMP10, IMP100, IMP1000, COVX and COVY inversions. Left to right, spatial RMS distribution for all inverted data components, 20km depth slice, and model section (location indicated on depth slice).

B1.5 Comparison between C3 and MT data

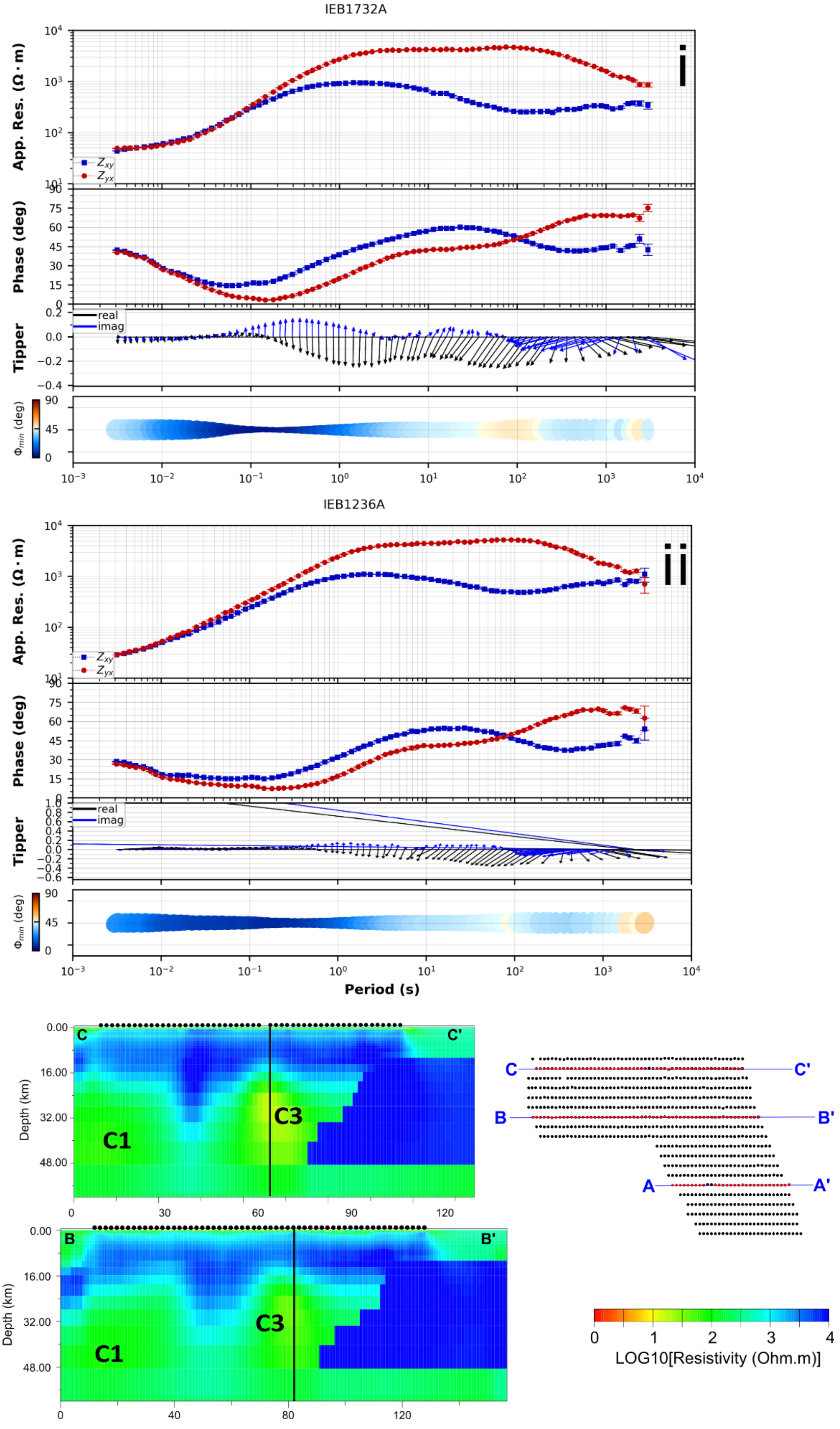

Figure B.4. Apparent resistivity, phase and tipper plots for two sites which are on top of the C3 conductor from the FINE inversion. i) site IEB1732A from indicated location on profile C-C'. ii) Site IEB1236A from indicated location in profile B-B'.

B.2 Variability analysis depth slices for each model

Figures B.5, B.6 and B.7 display results from variability analysis for each model grouped by four version parameter suites.

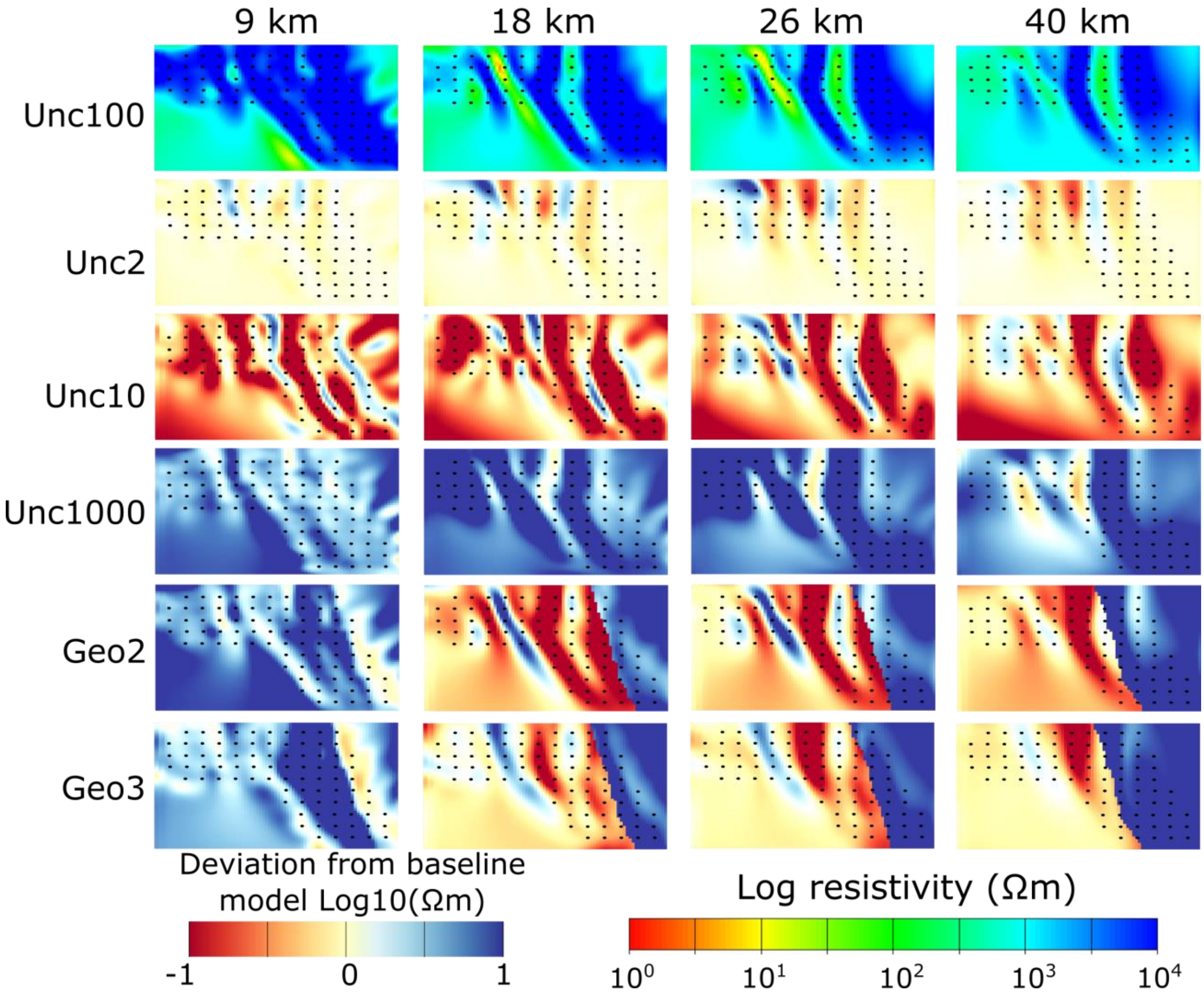

Figure B.5. Comparison of variability for models which only differ in their starting model, the UNC100 model is used as the baseline model for this analysis. Dark red or blue areas indicate a difference of more than one order of magnitude from the baseline model. Red areas indicate the model being analysed in more conductive than the baseline model, dark blue indicates the model is more resistive than the baseline, and yellow colours are indicative of similar resistivity values to the baseline model.

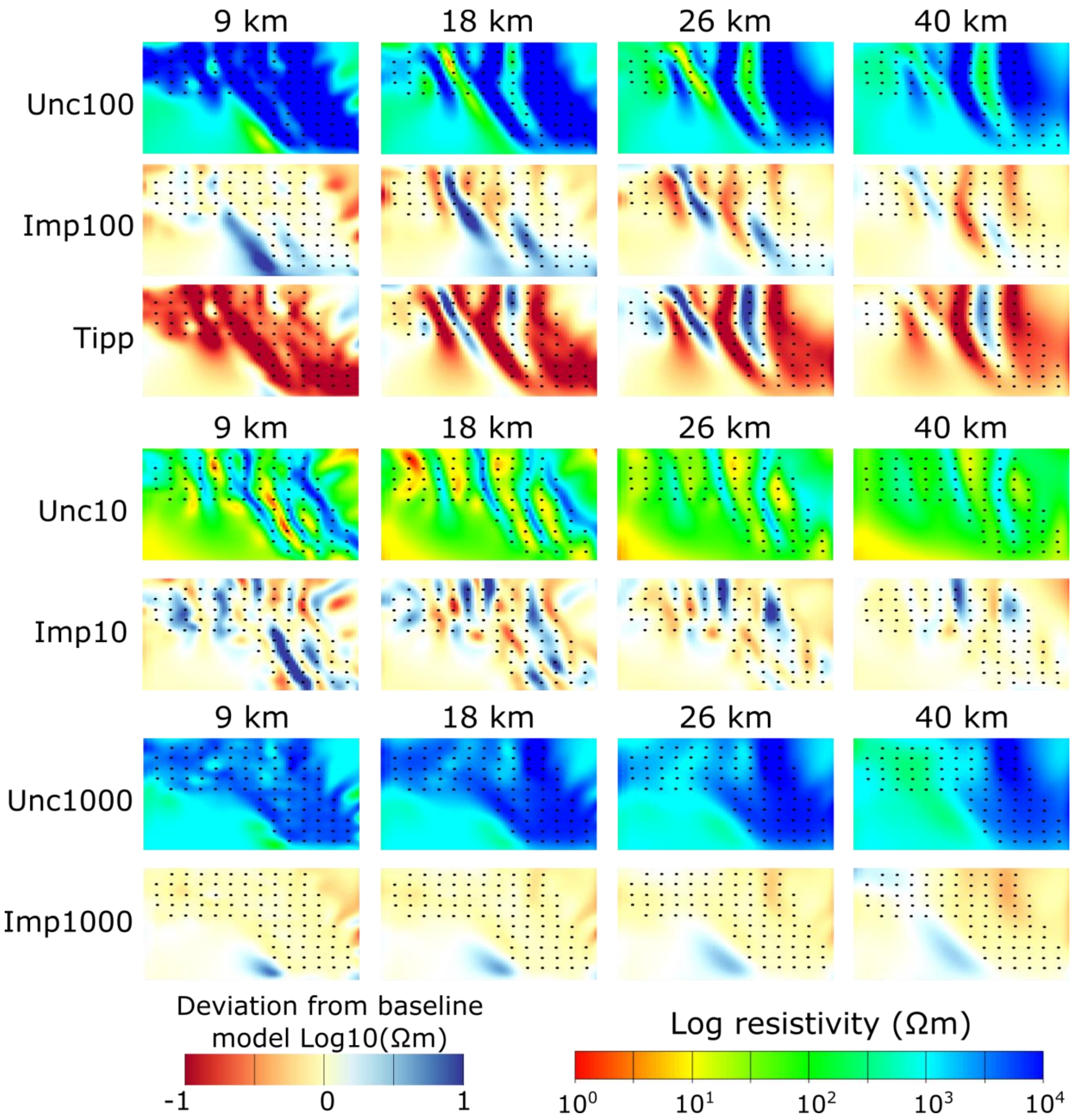

Figure B.6. Comparison of variability for models which only differ in their inverted data components. Comparison was conducted using UNC10, UNC100, and UNC1000 as baseline models. These three models were compared to their corresponding impedance only inversions, IMP10, IMP100 and IMP1000 respectively and the tipper only inversion, Tipp. Dark red or blue areas indicate a difference of more than one order of magnitude from the baseline model. Red areas indicate the model being analysed in more conductive than the baseline model, dark blue indicates the model is more resistive than the baseline, and yellow colours are indicative of similar resistivity values to the baseline model.

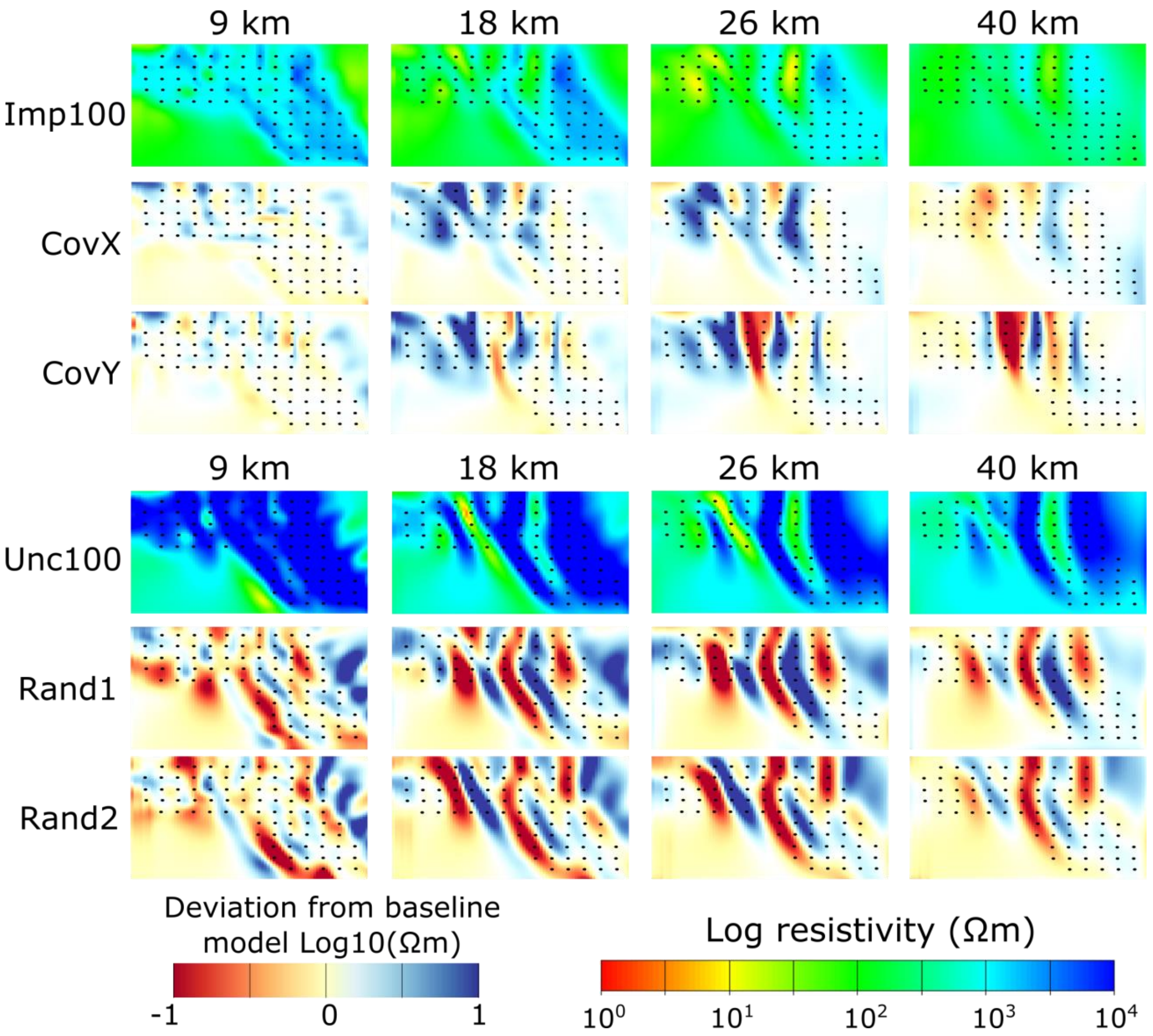

Figure B.7. Comparison of variability for models which only differ in their smoothing parameter (top three panels) and models which differ in their MT site distribution (bottom three panels). The IMP100 model is used as a baseline for the smoothing models and the UNC100 model is used as the baseline for the site distribution analysis. Dark red or blue areas indicate a difference of more than one order of magnitude from the baseline model. Red areas indicate the model being analysed in more conductive than the baseline model, dark blue indicates the model is more resistive than the baseline, and yellow colours are indicative of similar resistivity values to the baseline model.

APPENDIX C

C.1 Appendix for Chapter 3

Table C.1 Inversion parameters and names for all initial inversion tests and associated RMS achieved during inversion. Variation in starting model, inverted data component, covariance and data spacing were tested. Covariance listed in x, y, z directions according to ModEM standard orientations (Kelbert et al., 2014). Rand dataset is a randomly selected subset of the full dataset with 99 sites. Z data type indicates impedance data and T indicates tipper data. More information about this inversion testing is in Simpson and Heinson (in prep).

Model name	Dataset		Data type		Starting model (values represent Ωm half spaces)					Covariance			RMS
	10 km	Rand	Z	T	10	100	1000	Geo	Other	0.2, 0.2, 0.2	0.4, 0.1, 0.2	0.1, 0.4, 0.2	
Unc10	x		x	x	x					x			1.16
Unc100	x		x	x		x				x			1.13
Unc1000	x		x	x			x			x			1.05
Unc2	x		x	x					x	x			1.04
Geo1	x		x	x				x		x			2.43
Geo2	x		x	x				x		x			1.24
Geo3	x		x	x				x		x			1.05
Imp100	x		x			x				x			1.05
Tipp	x			x		x				x			1.03
Imp10	x		x		x					x			1.08
Imp1000	x		x				x			x			1.06
Rand1		x	x	x		x				x			3.09
Rand2		x	x	x		x				x			3.27
CovX	x		x			x						x	1.04
CovY	x		x			x					x		1.04

APPENDIX D

D.1 Additional files for Chapter 4

D.1.1 1D rj-McMC inversion record

Table D.1. A record of which 1D rj-McMC inversion result (BBMT, reduced frequency AMT or full frequency AMT) was used for the final interpretation.

Station ID	Latitude (GDA 94)	Longitude (GDA 94)	AMT_ 10Hz	AMT_ 1000to 10Hz	Questionable result	Unusable	BBMT
15125A	-22.37080556	139.1886389		x			
15126A	-22.37063889	139.1935		x			
15127A	-22.37102778	139.1984167		x	x		
15128A	-22.37086111	139.2033056		x	x		
15129A	-22.37108333	139.2080833	x				
15130A	-22.37122222	139.2129722		x			
15131A	-22.37113889	139.2178333		x			
15132A	-22.37141667	139.2226389		x			
15133A	-22.3715	139.2275278		x			
15134A	-22.37144444	139.2326389	x				
15135A	-22.37105556	139.2368056	x				
15136A	-22.37125	139.2415278		x			
15137A	-22.37122222	139.2468056		x			
15138A	-22.37102778	139.2513611		x			
15139A	-22.37177778	139.2562222		x			
15140A	-22.37152778	139.2621111	x				
15141A	-22.37147222	139.2665556		x	x		
15142A	-22.37188889	139.2715		x			
15143A	-22.37186111	139.2759722				x	
15144A	-22.37227778	139.2806667	x				
15145A	-22.37205556	139.2857778	x				
15146A	-22.37172222	139.2911944		x			
15147A	-22.37183333	139.2954444		x			
15148A	-22.37208333	139.3009722		x			
15149A	-22.37216667	139.3051944	x				
15150A	-22.37230556	139.31		x			
15151A	-22.37230556	139.3149167		x			
15152A	-22.37227778	139.3198056		x			
15153A	-22.37227778	139.3245556				x	
15154A	-22.37230556	139.3293333		x			
15155A	-22.37241667	139.3343611	x				
15156A	-22.37252778	139.3390833	x				
15157A	-22.37252778	139.3440556	x				
15158A	-22.37261111	139.3488889		x			
15159A	-22.37261111	139.3537222				x	
15160A	-22.37269444	139.3585833	x				
15161A	-22.37272222	139.3635	x				
15162A	-22.37272222	139.3682778		x			
15163A	-22.37283333	139.3731944		x			

Station ID	Latitude (GDA 94)	Longitude (GDA 94)	AMT_10Hz	AMT_1000to10Hz	Questionable result	Unusable	BBMT
15164A	-22.37288889	139.3779722		x			
15165B	-22.373	139.3830556		x			
15166A	-22.37302778	139.3877222	x				
15167A	-22.37308333	139.3926111	x				
15168A	-22.37269444	139.3973056	x		x		
15169B	-22.37322222	139.4022778				x	
15170A	-22.37311111	139.4073611	x		x		
15171A	-22.37322222	139.4120278				x	
15172A	-22.37327778	139.4168889				x	
15173A	-22.37330556	139.4217778		x			
15174A	-22.37338889	139.4265278		x			
15175A	-22.37336111	139.4314722		x			
15176A	-22.37344444	139.4362778				x	
15177B	-22.37347222	139.4411667		x			
15178A	-22.37347222	139.446				x	
15179A	-22.37358333	139.4508333		x			
15180B	-22.37355556	139.4551111				x	
15181B	-22.37363889	139.4605556		x			
15182A	-22.37363889	139.4653611		x			
15183A	-22.37377778	139.4702778	x				
15184A	-22.37377778	139.4750556				x	
15185B	-22.37386111	139.4799444		x	x		
15186A	-22.37394444	139.4848611				x	
15187B	-22.37397222	139.4896944				x	
15188A	-22.37572222	139.4944722				x	
15189A	-22.37411111	139.4993611		x			
15190A	-22.37411111	139.5041389		x			
15191A	-22.37413889	139.5088056		x			
15192A	-22.37413889	139.5139444				x	
15193B	-22.37422222	139.5188056				x	
15194A	-22.37422222	139.5236111		x			
15195A	-22.37430556	139.5286111		x			
15196A	-22.37472222	139.5331389		x			
15197A	-22.37438889	139.5381944		x			
15198A	-22.37447222	139.5431111		x			
15199A	-22.37447222	139.548				x	
15200A	-22.37458333	139.5527778	x				
15201A	-22.37461111	139.5576111	x				
15202A	-22.37463889	139.5625	x				
15203A	-22.37469444	139.5673333		x	x		
15204A	-22.37544444	139.5726667	x				
15205A	-22.37477778	139.5770556		x			
15206A	-22.37483333	139.5819167		x			
15207A	-22.37486111	139.5868056		x			
15208C	-22.37602778	139.5920556		x	x		
15209A	-22.37494444	139.5964722		x			

Station ID	Latitude (GDA 94)	Longitude (GDA 94)	AMT_ 10Hz	AMT_ 1000to 10Hz	Questionable result	Unusable	BBMT
15210A	-22.37491667	139.6013889	x				
15211A	-22.37502778	139.6062778	x				
15212A	-22.37488889	139.6109722				x	
15213A	-22.37511111	139.6158611		x			
16122A	-22.32561111	139.1743611		x			
16123A	-22.32555556	139.1790556		x			
16124A	-22.32569444	139.1844722		x			
16125A	-22.32575	139.1893056		x			
16126A	-22.32580556	139.194		x			
16127A	-22.32588889	139.1988611		x			
16128A	-22.32538889	139.2031389	x				
16129A	-22.32658333	139.2088611	x				
16130A	-22.32608333	139.2133889		x			
16131A	-22.32602778	139.2186111		x			
16132A	-22.32616667	139.2231389		x			
16133A	-22.32641667	139.22825	x				
16134A	-22.32605556	139.2330278		x			
16135A	-22.32622222	139.2375		x			
16136A	-22.32641667	139.2418056		x			
16137A	-22.32622222	139.2473889	x				
16138A	-22.32652778	139.2529444		x			
16139A	-22.32661111	139.2571389		x	x		
16140A	-22.32711111	139.2625278		x			
16141A	-22.32625	139.2666944		x			
16142A	-22.32688889	139.2716111	x				
16143A	-22.32663889	139.2763889		x			
16144A	-22.32661111	139.2817778	x				
16145A	-22.32647222	139.2861667		x			
16146A	-22.32669444	139.2908889		x			
16147A	-22.32691667	139.2958333		x			
16148A	-22.32705556	139.3009444	x				
16149A	-22.32680556	139.3053889	x				
16150A	-22.32669444	139.3104167	x				
16151A	-22.32694444	139.3154444	x				
16152A	-22.32497222	139.3206389	x				
16153A	-22.32713889	139.3255278		x			
16154A	-22.32708333	139.33		x			
16155B	-22.32697222	139.335		x			
16156A	-22.32741667	139.3403889	x				
16157A	-22.32730556	139.3447778		x			
16158A	-22.32766667	139.3496111		x			
16159A	-22.32797222	139.3546667				x	
16160A	-22.32644444	139.3583889	x				
16161A	-22.32761111	139.3639722	x				
16162A	-22.3275	139.3689444		x			
16163A	-22.32819444	139.3735556	x				

Station ID	Latitude (GDA 94)	Longitude (GDA 94)	AMT_ 10Hz	AMT_ 1000to 10Hz	Questionable result	Unusable	BBMT
16164A	-22.328	139.3784167	x				
16165A	-22.327	139.3836944				x	
16166A	-22.32797222	139.3882778		x			
16167A	-22.32797222	139.3933611	x				
16168A	-22.32833333	139.3978056	x				
16169A	-22.32802778	139.403		x			
16170A	-22.32794444	139.4076111		x			
16171A	-22.32813889	139.4123611	x				
16172A	-22.32827778	139.4172778		x			
16173A	-22.32822222	139.4223056				x	
16174A	-22.32830556	139.4272778				x	
16175A	-22.32822222	139.4318889				x	
16176A	-22.32813889	139.4366389	x				
16177A	-22.32838889	139.4416389	x				
16178A	-22.32838889	139.4463611		x			
16179A	-22.32841667	139.4511667		x			
16180A	-22.32847222	139.4564167		x			
16181A	-22.32866667	139.4612222	x				
16182A	-22.32866667	139.4657222	x				
16183B	-22.32863889	139.4707778		x			
16184A	-22.32802778	139.4755556				x	
16185A	-22.32872222	139.4801944		x			
16186B	-22.32869444	139.4852778		x			
16187A	-22.32877778	139.4900278		x			
16188A	-22.33025	139.4948889		x			
16189A	-22.32872222	139.4999444				x	
16190A	-22.32908333	139.505		x			
16191A	-22.32905556	139.5095278				x	
16192A	-22.32897222	139.5143611				x	
16193B	-22.33038889	139.5169444				x	
16194A	-22.32936111	139.5241667	x				
16195A	-22.32922222	139.5288056		x			
16196A	-22.32944444	139.5350833				x	
16197A	-22.32897222	139.5389444		x			
16198A	-22.32902778	139.5438056		x			
16199A	-22.32944444	139.5484444				x	
16200a	-22.32919444	139.5530278	x				
16201B	-22.32872222	139.5581111				x	
16202A	-22.32947222	139.5634722		x			
16203A	-22.32802778	139.5675556		x			
16204A	-22.329	139.5727778		x			
16205A	-22.32988889	139.5778056		x			
16206A	-22.32922222	139.5820556		x			
16207A	-22.32947222	139.5870278				x	
16208A	-22.32958333	139.5915833	x				
16209A	-22.32972222	139.5970278		x			

Station ID	Latitude (GDA 94)	Longitude (GDA 94)	AMT_ 10Hz	AMT_ 1000to 10Hz	Questionable result	Unusable	BBMT
16210A	-22.32944444	139.6018611	x				
16211A	-22.32986111	139.6066389		x			
17119A	-22.28019444	139.1606389		x			
17120A	-22.28036111	139.1656111		x			
17121A	-22.28038889	139.1703611		x			
17122A	-22.28047222	139.1753056		x			
17123A	-22.28055556	139.1804167		x			
17124A	-22.28052778	139.1850833		x			
17125A	-22.28005556	139.1898333		x			
17126A	-22.28061111	139.1945278		x			
17127A	-22.28102778	139.2004444		x			
17128A	-22.28055556	139.2043056		x			
17129A	-22.28086111	139.2091389		x			
17130A	-22.28080556	139.2141389		x			
17131A	-22.28091667	139.2190556		x			
17132A	-22.28088889	139.2235556		x			
17133A	-22.28366667	139.2281944		x			
17134A	-22.27938889	139.2341111		x			
17135A	-22.28113889	139.2393056	x				
17136A	-22.28088889	139.2436667	x				
17137A	-22.28136111	139.2482222		x			
17138A	-22.28122222	139.2528889		x			
17139A	-22.28136111	139.2576667	x				
17140A	-22.28055556	139.2619722		x			
17141A	-22.28244444	139.2674722		x			
17142A	-22.28155556	139.2730556				x	
17143A	-22.2815	139.2772778		x			
17144A	-22.28002778	139.2819444	x				
17145A	-22.28163889	139.2867222		x			
17146A	-22.28197222	139.2913611		x			
17147A	-22.28158333	139.2968333		x			
17148A	-22.28191667	139.3011111		x			
17149A	-22.28186111	139.30625		x			
17150A	-22.28186111	139.3110833		x			
17151A	-22.28191667	139.3160278		x			
17152A	-22.28138889	139.3208333		x			
17153A	-22.28211111	139.3257778		x			
17154A	-22.28213889	139.3305833		x			
17155A	-22.28216667	139.3353889		x			
17156A	-22.28213889	139.34025		x			
17157A	-22.28230556	139.3452778	x				
17158A	-22.28222222	139.3495556		x			
17159A	-22.28236111	139.3546111		x	x		
17160A	-22.28272222	139.3593889		x			
17161A	-22.28180556	139.3648889	x				
17162A	-22.28230556	139.3697222		x			

Station ID	Latitude (GDA 94)	Longitude (GDA 94)	AMT_ 10Hz	AMT_ 1000to 10Hz	Questionable result	Unusable	BBMT
17163A	-22.28238889	139.3742778				x	
17164A	-22.28236111	139.3789444		x			
17165B	-22.28263889	139.3838889				x	
17166A	-22.28269444	139.3888333	x				
17167A	-22.28286111	139.3938333	x				
17168A	-22.28266667	139.3986111	x				
17169B	-22.28280556	139.4033056				x	
17170A	-22.28286111	139.4080556	x				
17171A	-22.28294444	139.4130556		x			
17172A	-22.28313889	139.4178333		x	x		
17173A	-22.28302778	139.4228056		x			
17174A	-22.28327778	139.4276944		x			
17175A	-22.28305556	139.4323611	x				
17176A	-22.28338889	139.4375556	x				
17177A	-22.28305556	139.4416944		x			
17178A	-22.28336111	139.4466111		x	x		
17179A	-22.28336111	139.4519167	x				
17180A	-22.28391667	139.4566944	x				
17181A	-22.28333333	139.4615556	x				
17182A	-22.28352778	139.4663333	x				
17183A	-22.28358333	139.4712778		x			
17184A	-22.28344444	139.4759722		x			
17185A	-22.28352778	139.4809444	x				
17186A	-22.28372222	139.4856944	x				
17187A	-22.28363889	139.4906389		x			
17188B	-22.28369444	139.4954167	x				
17189A	-22.28377778	139.5003333		x	x		
17190A	-22.28383333	139.5051667	x				
17191A	-22.28386111	139.5100278	x				
17192A	-22.28377778	139.5149722				x	
17193B	-22.28386111	139.5197222				x	
17194A	-22.284	139.5245556	x				
17195A	-22.284	139.5294444	x				
17196A	-22.28430556	139.5333611		x			
17197A	-22.28411111	139.5391389	x				
17198A	-22.28405556	139.5440278		x			
17199A	-22.28405556	139.5488611				x	
17200A	-22.28430556	139.5536944		x			
17201A	-22.28430556	139.5586111	x				
17202A	-22.28433333	139.5633333	x				
17203A	-22.28430556	139.5678611		x			
17204A	-22.28419444	139.5726944		x			
17205A	-22.28438889	139.5779722		x			
17206A	-22.28461111	139.5828889		x			
17207A	-22.28447222	139.5876389	x				
17208A	-22.28505556	139.592	x				

Station ID	**Latitude (GDA 94)**	**Longitude (GDA 94)**	**AMT_ 10Hz**	**AMT_ 1000to 10Hz**	**Questionable result**	**Unusable**	**BBMT**
17209A	-22.28463889	139.5973333	x				
18116A	-22.23536111	139.1466944		x			
18117A	-22.23497222	139.1515278		x			
18118A	-22.23511111	139.1563889	x				
18119A	-22.23511111	139.1613056	x				
18120A	-22.23508333	139.1662222		x			
18121A	-22.23525	139.1709722		x			
18122A	-22.23533333	139.1758889		x			
18123A	-22.23530556	139.1806944		x			
18124A	-22.23513889	139.1854722				x	
18125A	-22.23536111	139.1903889		x			
18126A	-22.23547222	139.19525	x				
18127A	-22.23561111	139.2002222	x				
18128A	-22.23561111	139.2050278		x			
18129A	-22.23566667	139.2098056		x			
18130A	-22.23569444	139.2146389		x			
18131A	-22.23572222	139.2195556				x	
18132A	-22.23461111	139.2245833	x				
18133A	-22.23594444	139.2293056	x				
18134A	-22.23577778	139.2345556	x				
18135A	-22.23594444	139.2389167				x	
18136A	-22.23644444	139.2436944				x	
18137A	-22.23569444	139.24825		x			
18138A	-22.23611111	139.2534722		x			
18139A	-22.23647222	139.2583611	x		x		
18140A	-22.23619444	139.2631389		x			
18141A	-22.23627778	139.268	x				
18142A	-22.23633333	139.2728611				x	
18143A	-22.23638889	139.2777222		x			
18144A	-22.23458333	139.2825556		x			
18145A	-22.23644444	139.2874167	x				
18146A	-22.23652778	139.2922778	x				
18147A	-22.23672222	139.2967778	x				
18148A	-22.23663889	139.3019444		x			
18149A	-22.23661111	139.3066389		x	x		
18150A	-22.23675	139.3116111		x			
18151A	-22.23680556	139.3165278	x				
18152A	-22.23711111	139.3212222	x				
18153A	-22.23688889	139.3261389		x			
18154A	-22.23691667	139.3310556		x			
18155A	-22.23697222	139.3358889		x			
18156A	-22.23702778	139.3406944	x				
18157A	-22.23702778	139.3456944	x				
18158A	-22.23725	139.3505278	x				
18159A	-22.23713889	139.3552778		x			
18160A	-22.23722222	139.3601389		x			

Station ID	Latitude (GDA 94)	Longitude (GDA 94)	AMT_ 10Hz	AMT_ 1000to 10Hz	Questionable result	Unusable	BBMT
18161A	-22.23727778	139.3649722		x			
18162A	-22.23727778	139.3696944		x			
18163A	-22.23738889	139.3747778		x			
18164A	-22.23775	139.3796667		x			
18165A	-22.23738889	139.3844444				x	
18166A	-22.23752778	139.3892222				x	
18167A	-22.23777778	139.3939722	x				
18168A	-22.23763889	139.3990556	x				
18169A	-22.23744444	139.40375		x	x		
18170A	-22.23777778	139.4084444		x	x		
18171A	-22.23769444	139.4133056		x	x		
18172A	-22.23769444	139.4183611	x				
18173A	-22.23766667	139.4233056	x				
18174A	-22.23802778	139.4276667		x			
18175A	-22.23797222	139.4329167		x			
18176A	-22.23786111	139.4373056		x			
18177A	-22.23769444	139.4428056	x				
18178A	-22.23819444	139.4475833				x	
18179A	-22.23788889	139.4513056		x			
18180A	-22.23719444	139.4571389		x	x		
18181A	-22.23805556	139.4627222	x				
18182A	-22.23769444	139.4670278	x				
18183A	-22.23702778	139.4708611		x			
18184A	-22.23755556	139.4766389		x			
18185A	-22.23894444	139.4812778		x			
18186A	-22.23827778	139.48625		x			
18187A	-22.23861111	139.4909444				x	
18188A	-22.23961111	139.4954444		x			
18189A	-22.23905556	139.5013056		x			
18190A	-22.23863889	139.50575	x				
18191A	-22.23847222	139.5106667	x				
18192A	-22.23658333	139.5160278				x	
18193A	-22.2375	139.5204444		x			
18194A	-22.23905556	139.5250833		x	x		
18195A	-22.23844444	139.5296944		x			
18196A	-22.23961111	139.5344722	x				
18197A	-22.23883333	139.5396389		x			
18198A	-22.23902778	139.5437778				x	
18199A	-22.23911111	139.5490278		x			
18200A	-22.23911111	139.5541389		x			
18201A	-22.23919444	139.5589444	x				
18202A	-22.23938889	139.5638333	x		x		
18203A	-22.23855556	139.5690556	x				
18204A	-22.23936111	139.5735556	x				
18205A	-22.23936111	139.5787222		x			
18206A	-22.23961111	139.5832222	x				

Station ID	Latitude (GDA 94)	Longitude (GDA 94)	AMT_ 10Hz	AMT_ 1000to 10Hz	Questionable result	Unusable	BBMT
IEA00184	-23.05113333	139.4675333	x				
IEA00185	-23.05118333	139.47245	x				
IEA00186	-23.05113333	139.47725	x				
IEA00187	-23.05118333	139.4820667	x				
IEA00188	-23.05128333	139.48705	x				
IEA00189	-23.05128333	139.4920333		x			
IEA00190	-23.05145	139.4968667	x				
IEA00191	-23.0514	139.5017	x				
IEA00192	-23.05143333	139.5065833	x				
IEA00193	-23.05151667	139.5114833	x				
IEA00194	-23.0515	139.5163333		x			
IEA00195	-23.0517	139.5212333	x				
IEA00196	-23.05143333	139.5261	x				
IEA00197	-23.05171667	139.5310833		x	x		
IEA00198	-23.0518	139.5358833		x			
IEA00199	-23.05178333	139.5407333		x			
IEA00200	-23.05158333	139.5452	x				
IEA00201	-23.05198333	139.5506833		x			
IEA00202	-23.05181667	139.55535		x			
IEA00203	-23.05195	139.5602	x				
IEA00204	-23.05183333	139.5651333	x				
IEA00205	-23.0521	139.5700167		x			
IEA00206	-23.05223333	139.57495		x			
IEA00207	-23.05211667	139.5797167		x			
IEA00208	-23.05215	139.5846667	x				
IEA00209	-23.05225	139.5895667		x			
IEA00210	-23.05226667	139.5943667		x			
IEA00211	-23.05226667	139.5992667		x			
IEA00212	-23.05236667	139.6041	x				
IEA00213	-23.05241667	139.6089667	x				
IEA00214	-23.05251667	139.6140167	x				
IEA00215	-23.05243333	139.6188833		x			
IEA00216	-23.0524	139.6238167	x				
IEA00217	-23.0525	139.6286	x				
IEA00218	-23.05266667	139.6335167	x				
IEA00219	-23.05265	139.63835		x			
IEA00220	-23.05268333	139.6431833		x			
IEA00221	-23.05271667	139.6480167		x			
IEA00222	-23.05278333	139.6529333		x			
IEA00223	-23.05281667	139.65795	x				
IEA00224	-23.0528	139.6627667				x	
IEA00225	-23.05291667	139.6676167	x				
IEA00226	-23.05293333	139.6723333		x			
IEA00227	-23.05308333	139.6770833	x				
IEA00228	-23.05303333	139.6821167	x				
IEA00229	-23.05308333	139.6870833	x				

Station ID	Latitude (GDA 94)	Longitude (GDA 94)	AMT_ 10Hz	AMT_ 1000to 10Hz	Questionable result	Unusable	BBMT
IEA00230	-23.05318333	139.69195	x				
IEA00231	-23.05305	139.6967833	x				
IEA00232	-23.05315	139.7015833	x				
IEA00233	-23.0533	139.70665	x				
IEA00234	-23.0532	139.7115		x			
IEA00235	-23.05333333	139.7163833	x				
IEA00236	-23.05335	139.7211333		x			
IEA00237	-23.05341667	139.7261667		x			
IEA00238	-23.05338333	139.7309833		x			
IEA00239	-23.05338333	139.7359167		x			
IEA00240	-23.05346667	139.7406833	x				
IEA00241	-23.05351667	139.7457333	x				
IEA00242	-23.05355	139.7506		x			
IEA00243	-23.05373333	139.75545		x			
IEA00244	-23.05365	139.76035	x				
IEA00245	-23.05365	139.7651667	x				
IEA00246	-23.05393333	139.7702833	x				
IEA00247	-23.05375	139.77495		x			
IEA00248	-23.054	139.7799667	x				
IEA00249	-23.0538	139.7842667		x			
IEA00250	-23.05395	139.7896667	x				
IEA00251	-23.05405	139.7947167	x				
IEA00252	-23.05393333	139.7996333	x				
IEA00253	-23.054	139.8042667		x			
IEA00254	-23.05385	139.8091167		x			
IEA00255	-23.05423333	139.8139667	x				
IEA00256	-23.05376667	139.8185		x			
IEA00257	-23.05406667	139.8238333	x				
IEA00258	-23.05416667	139.8285833	x				
IEA00259	-23.05415	139.83345	x				
IEA00260	-23.05416667	139.8384	x				
IEA00261	-23.05423333	139.8432167		x			
IEA00262	-23.05426667	139.8481833	x				
IEA00263	-23.0543	139.8529333	x				
IEA00264	-23.05435	139.8577	x				
IEA00265	-23.05443333	139.8628333				x	
IEA00266	-23.05445	139.8679		x			
IEA00267	-23.0545	139.8725167	x				
IEA00268	-23.05451667	139.8773667	x				
IEA00269	-23.05461667	139.8822	x				
IEA00270	-23.0545	139.88705	x				
IEA00271	-23.05456667	139.8920333		x			
IEA00272	-23.05468333	139.8968833	x				
IEA00273	-23.05475	139.90165		x			
IEA00274	-23.05476667	139.9067167		x			
IEA00275	-23.05478333	139.9115833		x			

Station ID	Latitude (GDA 94)	Longitude (GDA 94)	AMT_ 10Hz	AMT_ 1000to 10Hz	Questionable result	Unusable	BBMT
IEA00276	-23.0548	139.9164667	x				
IEA00277	-23.0548	139.9213167		x			
IEA00278	-23.05501667	139.9263167		x			
IEA00279	-23.05486667	139.93105	x				
IEA00280	-23.05493333	139.9360333		x			
IEA01179	-23.00563333	139.4436667		x			
IEA01180	-23.00576667	139.4483667	x				
IEA01181	-23.00581667	139.4534167		x			
IEA01182	-23.00591667	139.45835	x				
IEA01183	-23.00583333	139.4632	x				
IEA01184	-23.00593333	139.4679833		x			
IEA01185	-23.006	139.47295	x				
IEA01186	-23.00606667	139.4777833	x				
IEA01187	-23.0061	139.4827167	x				
IEA01188	-23.00613333	139.4876	x				
IEA01189	-23.0062	139.49245	x				
IEA01190	-23.00628333	139.4973833	x				
IEA01191	-23.00625	139.5022167		x			
IEA01192	-23.00621667	139.5070667	x				
IEA01193	-23.00633333	139.51185		x			
IEA01194	-23.00641667	139.51685	x				
IEA01195	-23.00653333	139.5217333		x			
IEA01196	-23.00646667	139.5265833	x				
IEA01197	-23.00648333	139.53145		x			
IEA01198	-23.0066	139.5363167	x				
IEA01199	-23.00658333	139.5412167		x	x		
IEA01200	-23.00666667	139.54615	x				
IEA01201	-23.00666667	139.5509	x				
IEA01202	-23.00676667	139.5558833	x				
IEA01203	-23.00685	139.56075		x			
IEA01204	-23.00683333	139.5656333	x				
IEA01205	-23.0069	139.5705333	x				
IEA01206	-23.00693333	139.5753833		x			
IEA01207	-23.00703333	139.5802	x				
IEA01208R	-23.00681667	139.5851167	x				
IEA01209	-23.00711667	139.59	x				
IEA01210	-23.00711667	139.59485	x				
IEA01211	-23.00713333	139.5997833	x				
IEA01212	-23.00715	139.60455		x			
IEA01213	-23.00723333	139.60955	x				
IEA01214	-23.00726667	139.6144333	x				
IEA01215	-23.00733333	139.6192833		x			
IEA01216	-23.00728333	139.6241333				x	
IEA01217	-23.0074	139.62905	x				
IEA01218	-23.00745	139.6338833	x				
IEA01219	-23.00748333	139.6388333		x			

Station ID	Latitude (GDA 94)	Longitude (GDA 94)	AMT_ 10Hz	AMT_ 1000to 10Hz	Questionable result	Unusable	BBMT
IEA01220	-23.0075	139.6436667	x				
IEA01221	-23.00798333	139.6483667	x				
IEA01222	-23.00766667	139.6534		x			
IEA01223	-23.00768333	139.6582667	x				
IEA01224	-23.00768333	139.6631333		x			
IEA01225	-23.00753333	139.6684333	x				
IEA01226	-23.00781667	139.6729167		x			
IEA01227	-23.00793333	139.6774167	x				
IEA01228	-23.00783333	139.68265	x				
IEA01229	-23.00788333	139.6876167	x				
IEA01230	-23.00795	139.69245	x				
IEA01231	-23.00801667	139.69715	x				
IEA01232	-23.00805	139.70215	x				
IEA01233R	-23.00801667	139.7069833		x			
IEA01234R	-23.00805	139.71185	x				
IEA01235	-23.00813333	139.7168333	x				
IEA01236	-23.00835	139.7214	x				
IEA01237	-23.00818333	139.7266167	x				
IEA01238	-23.00825	139.7315	x				
IEA01239	-23.00828333	139.7363333		x			
IEA01240	-23.00828333	139.7411833	x				
IEA01241	-23.00833333	139.7460833	x				
IEA01242	-23.00841667	139.7509667		x			
IEA01243	-23.00865	139.7556	x				
IEA01244	-23.00851667	139.7607667		x			
IEA01245	-23.0086	139.76565		x			
IEA01246	-23.00858333	139.77045		x			
IEA01247	-23.00865	139.77525		x			
IEA01248	-23.0088	139.7799167		x			
IEA01249	-23.00868333	139.7851	x				
IEA01250	-23.00878333	139.7899833		x			
IEA01251	-23.00833333	139.7949667	x				
IEA01252	-23.00873333	139.79975	x				
IEA01253	-23.00885	139.8046167	x				
IEA01254	-23.00891667	139.80955		x			
IEA01255	-23.00875	139.8139167	x				
IEA01256	-23.00893333	139.8192833	x				
IEA01257	-23.00901667	139.8241333		x			
IEA01258	-23.009	139.8296		x			
IEA01259	-23.00898333	139.8339	x				
IEA01260	-23.00908333	139.8387667	x				
IEA01261	-23.00913333	139.84365	x				
IEA01262	-23.00918333	139.8485667	x				
IEA01263	-23.0092	139.85345	x				
IEA01264	-23.00923333	139.8583333	x				
IEA01265	-23.0092	139.8632167		x			

Station ID	Latitude (GDA 94)	Longitude (GDA 94)	AMT_ 10Hz	AMT_ 1000to 10Hz	Questionable result	Unusable	BBMT
IEA01266	-23.0093	139.8680833	x				
IEA01267	-23.00933333	139.8729667		x			
IEA01268R	-23.00936667	139.87775	x				
IEA01269	-23.00938333	139.8825667		x			
IEA01270	-23.0094	139.8875167		x			
IEA01271	-23.0095	139.8924333				x	
IEA01272	-23.00948333	139.8972833	x				
IEA01273	-23.00958333	139.90225		x			
IEA01274	-23.00955	139.9070333	x				
IEA01275	-23.00956667	139.9119167	x				
IEA01276	-23.0097	139.9168667		x			
IEA02173	-22.96035	139.4149333	x				
IEA02174	-22.96035	139.41985	x				
IEA02175	-22.96026667	139.4247167	x				
IEA02176	-22.96046667	139.4295	x				
IEA02177	-22.9604	139.4346333		x			
IEA02178	-22.96048333	139.4393833	x				
IEA02179	-22.9606	139.4442333		x			
IEA02180	-22.96056667	139.4491	x				
IEA02181	-22.96071667	139.4539833		x			
IEA02182	-22.96083333	139.4589333	x				
IEA02183	-22.96075	139.4637167	x				
IEA02184	-22.96076667	139.4685833	x				
IEA02185	-22.96086667	139.4734833	x				
IEA02186	-22.96091667	139.4783167	x				
IEA02187	-22.96093333	139.4831667	x				
IEA02188	-22.96095	139.4881	x				
IEA02189	-22.96103333	139.493	x				
IEA02190	-22.96111667	139.4984	x				
IEA02191	-22.96116667	139.5027333	x				
IEA02192	-22.9612	139.5075833	x				
IEA02193	-22.96121667	139.5124333	x				
IEA02194	-22.96141667	139.5174833		x			
IEA02195	-22.9613	139.5222				x	
IEA02196	-22.96135	139.5271	x				
IEA02197	-22.96166667	139.5320333		x			
IEA02198	-22.9614	139.53685	x				
IEA02199	-22.9615	139.5417333	x				
IEA02200	-22.96153333	139.5466333	x				
IEA02201	-22.9616	139.5514167	x				
IEA02202	-22.96156667	139.5563	x				
IEA02203	-22.96165	139.56125	x				
IEA02204	-22.96171667	139.56605	x				
IEA02205	-22.96146667	139.5712333		x			
IEA02206	-22.96183333	139.57585	x				
IEA02207	-22.96183333	139.5807	x				

Station ID	Latitude (GDA 94)	Longitude (GDA 94)	AMT_ 10Hz	AMT_ 1000to 10Hz	Questionable result	Unusable	BBMT
IEA02208	-22.96193333	139.5855833		x			
IEA02209	-22.96185	139.5904667	x				
IEA02210R	-22.962	139.5953333	x				
IEA02211	-22.96186667	139.6002833	x				
IEA02212	-22.96206667	139.60505	x				
IEA02213	-22.96201667	139.6101	x				
IEA02214	-22.96218333	139.6149		x			
IEA02215	-22.96218333	139.6196833	x				
IEA02216	-22.96228333	139.62455	x				
IEA02217	-22.96193333	139.6295833	x				
IEA02218R	-22.96233333	139.6343333		x			
IEA02219	-22.96233333	139.6392333	x				
IEA02220	-22.96235	139.6440333	x				
IEA02221	-22.96243333	139.64895	x				
IEA02222	-22.96248333	139.65385		x			
IEA02223	-22.9625	139.6586667		x			
IEA02224	-22.96255	139.6636167	x				
IEA02225	-22.96261667	139.6684833	x				
IEA02226	-22.96261667	139.6733333	x				
IEA02227	-22.96273333	139.6782333	x				
IEA02228	-22.96265	139.68315	x				
IEA02229	-22.96276667	139.6880333		x			
IEA02230	-22.96285	139.6929167	x				
IEA02231	-22.96283333	139.6978833	x				
IEA02232	-22.96286667	139.7026167	x				
IEA02233	-22.96286667	139.7075833	x				
IEA02234	-22.96298333	139.7124333		x			
IEA02235	-22.9631	139.7179	x				
IEA02236	-22.96305	139.7221167		x			
IEA02237	-22.96305	139.727	x				
IEA02238	-22.96305	139.7319167		x			
IEA02239	-22.96318333	139.7368		x			
IEA02240	-22.96316667	139.74155		x			
IEA02241	-22.96328333	139.7465667	x				
IEA02242	-22.9633	139.7513	x				
IEA02243	-22.96338333	139.7563167		x			
IEA02244	-22.96335	139.76115		x			
IEA02245	-22.96361667	139.7662667		x			
IEA02246	-22.96346667	139.7709833		x			
IEA02247	-22.96343333	139.7758		x			
IEA02248	-22.96343333	139.7802833	x				
IEA02249	-22.9636	139.78565	x				
IEA02250	-22.96363333	139.7904333		x			
IEA02251	-22.96365	139.7953333	x				
IEA02252	-22.9635	139.8001		x			
IEA02253	-22.96355	139.8051667	x				

Station ID	Latitude (GDA 94)	Longitude (GDA 94)	AMT_ 10Hz	AMT_ 1000to 10Hz	Questionable result	Unusable	BBMT
IEA02254	-22.96373333	139.8097167		x			
IEA02255	-22.9638	139.81475		x			
IEA02256	-22.96385	139.8194667	x				
IEA02257	-22.96386667	139.8245667	x				
IEA02258	-22.96378333	139.8295	x				
IEA02259	-22.96378333	139.8342833	x				
IEA02260	-22.96393333	139.8391833		x			
IEA02261	-22.96398333	139.8442	x				
IEA02262	-22.96405	139.849	x				
IEA02263	-22.964	139.8538167	x				
IEA02264	-22.96405	139.8586	x				
IEA02265	-22.96406667	139.8635667		x			
IEA02266	-22.9643	139.8686667		x			
IEA02267	-22.96403333	139.8736667		x			
IEA02268	-22.96391667	139.8780833		x			
IEA02269	-22.96401667	139.8829333	x				
IEA02270	-22.96428333	139.8879833	x				
IEA02271	-22.96436667	139.8928667		x			
IEA03168	-22.91483333	139.3911	x				
IEA03169	-22.9149	139.3959333	x				
IEA03170R	-22.915	139.40085	x				
IEA03171	-22.91503333	139.4057	x				
IEA03172	-22.91503333	139.4105167		x			
IEA03173R	-22.91513333	139.4154667	x				
IEA03174R	-22.91521667	139.4203	x				
IEA03175	-22.9152	139.4251333	x				
IEA03176	-22.91521667	139.4300833	x				
IEA03177	-22.91531667	139.4349	x				
IEA03178	-22.9154	139.4397833	x				
IEA03179	-22.91545	139.4447	x				
IEA03180	-22.91543333	139.4496333	x				
IEA03181	-22.91553333	139.4544167		x			
IEA03182	-22.91551667	139.4593	x				
IEA03183	-22.91556667	139.4642167		x			
IEA03184	-22.91563333	139.4690167	x				
IEA03185	-22.91568333	139.4738833		x			
IEA03186	-22.9157	139.4788		x			
IEA03187	-22.91581667	139.4836667	x				
IEA03188	-22.91583333	139.4884833	x				
IEA03189	-22.91595	139.4934333	x				
IEA03190	-22.91595	139.4982833	x				
IEA03191	-22.91596667	139.50315		x			
IEA03192	-22.91598333	139.50805	x				
IEA03193	-22.91608333	139.5128833	x				
IEA03194	-22.9161	139.5178	x				
IEA03195	-22.91616667	139.5226833		x			

Station ID	Latitude (GDA 94)	Longitude (GDA 94)	AMT_ 10Hz	AMT_ 1000to 10Hz	Questionable result	Unusable	BBMT
IEA03196	-22.91623333	139.5275833	x				
IEA03197	-22.91621667	139.53245		x			
IEA03198	-22.91641667	139.53695	x				
IEA03199	-22.9163	139.5422333		x			
IEA03200	-22.91635	139.5469833		x			
IEA03201R	-22.91655	139.5518	x				
IEA03202	-22.9163	139.5571167	x				
IEA03203	-22.9166	139.5620167	x				
IEA03204	-22.91661667	139.5664833	x				
IEA03205	-22.91666667	139.5718	x				
IEA03206	-22.91658333	139.57645		x			
IEA03207	-22.9167	139.581		x			
IEA03208	-22.9167	139.5864667	x				
IEA03209	-22.91685	139.5908833	x				
IEA03210	-22.9164	139.5959833	x				
IEA03211	-22.91686667	139.6008		x			
IEA03212	-22.91681667	139.6056333	x				
IEA03213	-22.91695	139.61035		x			
IEA03214	-22.91698333	139.6154333		x			
IEA03215	-22.91691667	139.6201667	x				
IEA03216	-22.91708333	139.6250667	x				
IEA03217	-22.91715	139.6299667		x			
IEA03218	-22.91716667	139.6347833		x			
IEA03219	-22.91691667	139.64	x				
IEA03220	-22.91716667	139.64475	x				
IEA03221	-22.91738333	139.6493333	x				
IEA03222	-22.91728333	139.65425		x			
IEA03223	-22.91743333	139.6591667	x				
IEA03224	-22.91748333	139.664		x			
IEA03225	-22.91755	139.6689333		x			
IEA03226	-22.9175	139.6737667	x				
IEA03227	-22.91743333	139.6783167	x				
IEA03228	-22.91763333	139.6833333	x				
IEA03229	-22.91755	139.6884333		x	x		
IEA03230	-22.9176	139.6928		x			
IEA03231	-22.91785	139.6981667	x				
IEA03232	-22.91761667	139.7030167		x			
IEA03233	-22.91765	139.70805	x				
IEA03234	-22.91813333	139.7128167	x				
IEA03235	-22.91785	139.7177167	x				
IEA03236R	-22.91788333	139.72255		x			
IEA03237	-22.9179	139.7274333	x				
IEA03238R	-22.9181	139.7322667	x				
IEA03239	-22.91801667	139.7371333	x				
IEA03240	-22.91805	139.74205	x				
IEA03241	-22.91798333	139.7469333	x				

Station ID	Latitude (GDA 94)	Longitude (GDA 94)	AMT_ 10Hz	AMT_ 1000to 10Hz	Questionable result	Unusable	BBMT
IEA03242	-22.91815	139.7516667	x				
IEA03243	-22.91811667	139.7567333	x		x		
IEA03244	-22.9186	139.7615	x				
IEA03245	-22.91821667	139.7662167	x				
IEA03246	-22.9184	139.77135		x			
IEA03247	-22.91826667	139.7761833		x			
IEA03248	-22.91835	139.7810333	x				
IEA03249R	-22.91835	139.7858	x				
IEA03250	-22.91848333	139.7906833	x				
IEA03251	-22.91821667	139.7956667	x				
IEA03252R	-22.91851667	139.8006	x				
IEA03253R	-22.91851667	139.80545		x			
IEA03254	-22.9187	139.8101167	x				
IEA03255R	-22.91868333	139.8150667	x				
IEA03256R	-22.91865	139.8200333	x				
IEA03257	-22.91863333	139.8252167		x			
IEA03258	-22.91893333	139.8298167		x	x		
IEA03259	-22.91856667	139.83475	x				
IEA03260	-22.91883333	139.83955		x			
IEA03261	-22.91888333	139.8446833	x				
IEA03262	-22.91886667	139.8493833		x			
IEA03263	-22.9189	139.8542167		x			
IEA03264	-22.91896667	139.8589333	x				
IEA03265	-22.91891667	139.8639	x				
IEA03266	-22.91896667	139.8688333		x			
IEA04162	-22.8694	139.3624333		x			
IEA04163	-22.86943333	139.36725		x			
IEA04164	-22.86951667	139.3721333	x				
IEA04165	-22.86955	139.377		x			
IEA04166	-22.86958333	139.38185	x				
IEA04167	-22.8697	139.3867167	x				
IEA04168	-22.86971667	139.3916167	x				
IEA04169	-22.86975	139.3964833	x				
IEA04170	-22.8698	139.4013333		x			
IEA04171	-22.86988333	139.4062333	x				
IEA04172	-22.8699	139.4110667	x				
IEA04173	-22.86991667	139.4159833		x			
IEA04174	-22.87001667	139.4208833		x			
IEA04175	-22.8701	139.4257333	x				
IEA04176	-22.87008333	139.4305833	x				
IEA04177	-22.87018333	139.43545	x				
IEA04178	-22.87021667	139.44035		x			
IEA04179	-22.87016667	139.4451667		x			
IEA04180	-22.87025	139.4500667	x				
IEA04181RR	-22.87033333	139.45495	x				
IEA04182	-22.87038333	139.4598333		x			

Station ID	Latitude (GDA 94)	Longitude (GDA 94)	AMT_ 10Hz	AMT_ 1000to 10Hz	Questionable result	Unusable	BBMT
IEA04183	-22.87046667	139.46465		x			
IEA04184	-22.87043333	139.46955		x			
IEA04185R	-22.87056667	139.4744667		x			
IEA04186	-22.87061667	139.4793667		x			
IEA04187	-22.87065	139.4842333		x			
IEA04188	-22.87071667	139.48905	x				
IEA04189R	-22.87076667	139.4939167	x				
IEA04190	-22.87078333	139.4988333		x			
IEA04191	-22.8708	139.50365		x			
IEA04192R	-22.87088333	139.50855		x			
IEA04193	-22.87088333	139.51345	x				
IEA04194	-22.87098333	139.5183	x				
IEA04195	-22.87098333	139.5231833		x			
IEA04196	-22.87103333	139.5280667	x				
IEA04197	-22.8711	139.5329333		x			
IEA04198	-22.87113333	139.5377667		x			
IEA04199	-22.8712	139.5427167		x			
IEA04200	-22.8712	139.5475167	x				
IEA04201	-22.87126667	139.5524167		x			
IEA04202	-22.87136667	139.5573		x			
IEA04203	-22.87125	139.5622167	x				
IEA04204	-22.87131667	139.5671167		x			
IEA04205	-22.87148333	139.5719833	x				
IEA04206	-22.87145	139.5767833		x			
IEA04207	-22.87158333	139.5816167	x				
IEA04208	-22.87143333	139.5863833	x				
IEA04209	-22.87161667	139.59125	x				
IEA04210	-22.8716	139.5966	x				
IEA04211	-22.87178333	139.6012	x				
IEA04212	-22.87175	139.60595		x			
IEA04213	-22.87181667	139.6110167		x			
IEA04214	-22.87185	139.6157333	x				
IEA04215	-22.8719	139.6207		x			
IEA04216	-22.87181667	139.6255167	x				
IEA04217	-22.87195	139.6304333	x				
IEA04218	-22.87208333	139.6353333	x				
IEA04219	-22.87216667	139.6400833	x				
IEA04220	-22.87196667	139.64495	x				
IEA04221	-22.87218333	139.6498667	x				
IEA04222	-22.87225	139.6546667	x				
IEA04223	-22.87223333	139.6595833	x				
IEA04224	-22.87216667	139.6644833	x				
IEA04225	-22.87228333	139.66905	x				
IEA04226	-22.87226667	139.6743333		x			
IEA04227	-22.87245	139.67915	x				
IEA04228	-22.87235	139.68395	x				

Station ID	Latitude (GDA 94)	Longitude (GDA 94)	AMT_10Hz	AMT_1000to10Hz	Questionable result	Unusable	BBMT
IEA04229	-22.8724	139.6888667		x			
IEA04230	-22.87245	139.6937833				x	
IEA04231	-22.8724	139.6985167	x				
IEA04231_wLF	-22.8724	139.6985167	x				
IEA04232	-22.87256667	139.7033667		x			
IEA04233	-22.87258333	139.7083667	x				
IEA04234	-22.87265	139.7131833	x				
IEA04235	-22.87266667	139.7180667	x				
IEA04236	-22.87271667	139.7229	x				
IEA04237	-22.87273333	139.7278167	x				
IEA04238	-22.8728	139.7326667	x				
IEA04239	-22.87285	139.7375833	x				
IEA04240	-22.87285	139.7424333		x			
IEA04241R	-22.87288333	139.7474		x			
IEA04242	-22.87291667	139.7522		x			
IEA04243R	-22.87306667	139.7570667	x				
IEA04244	-22.87303333	139.7619167	x				
IEA04245	-22.873	139.7666167	x				
IEA04246	-22.87308333	139.7717833	x				
IEA04247	-22.87315	139.7765		x			
IEA04248	-22.87326667	139.7815	x				
IEA04249	-22.87315	139.7863833		x			
IEA04250	-22.87316667	139.79125	x				
IEA04251	-22.87343333	139.79595	x				
IEA04252R	-22.87336667	139.8009333	x				
IEA04253	-22.87338333	139.8059167		x			
IEA04254	-22.8734	139.8107667	x				
IEA04255	-22.8734	139.8156333		x			
IEA04256	-22.8734	139.8204667	x				
IEA04257	-22.8735	139.8254		x			
IEA04258	-22.87355	139.8302667	x				
IEA04259	-22.87355	139.83505	x				
IEA04260	-22.87361667	139.8399333	x				
IEA04261	-22.87361667	139.84485		x			
IEB0044	-23.05071667	139.4285					**x**
IEB0045	-23.05093333	139.4479833					**x**
IEB0046	-23.05113333	139.4675333					**x**
IEB0047	-23.05128333	139.48705					**x**
IEB0048	-23.05143333	139.5065833					**x**
IEB0049	-23.05143333	139.5261					**x**
IEB0050	-23.05158333	139.5452					**x**
IEB0051	-23.05183333	139.5651333					**x**
IEB0052	-23.05215	139.5846667					**x**
IEB0053	-23.05236667	139.6041					**x**
IEB0054	-23.0524	139.6238167					**x**
IEB0055	-23.05268333	139.6431833					**x**

Station ID	Latitude (GDA 94)	Longitude (GDA 94)	AMT_ 10Hz	AMT_ 1000to 10Hz	Questionable result	Unusable	BBMT
IEB0056	-23.0528	139.6627667					x
IEB0057	-23.05303333	139.6821167					x
IEB0058	-23.05315	139.7015833					x
IEB0059	-23.05335	139.7211333					x
IEB0060	-23.05346667	139.7406833					x
IEB0061	-23.05365	139.76035					x
IEB0062	-23.054	139.7799667					x
IEB0063	-23.05393333	139.7996333					x
IEB0064	-23.05376667	139.8185					x
IEB0065	-23.05416667	139.8384					x
IEB0066	-23.05435	139.8577					x
IEB0067	-23.05451667	139.8773667					x
IEB0068	-23.05468333	139.8968833					x
IEB0069	-23.0548	139.9164667					x
IEB0070	-23.05493333	139.9360333					x
IEB0143	-23.00531667	139.4095167					x
IEB0144	-23.00558333	139.4291					x
IEB0145	-23.00576667	139.4483667					x
IEB0146	-23.00593333	139.4679833					x
IEB0147	-23.00613333	139.4876					x
IEB0148	-23.00621667	139.5070667					x
IEB0149	-23.00646667	139.5265833					x
IEB0150	-23.00666667	139.54615					x
IEB0151	-23.00683333	139.5656333					x
IEB0152R	-23.00681667	139.5851167					x
IEB0153	-23.00715	139.60455					x
IEB0154	-23.00728333	139.6241333					x
IEB0155	-23.0075	139.6436667					x
IEB0156	-23.00768333	139.6631333					x
IEB0157	-23.00783333	139.68265					x
IEB0158	-23.00805	139.70215					x
IEB0159	-23.00835	139.7214					x
IEB0160	-23.00828333	139.7411833					x
IEB0161	-23.00851667	139.7607667					x
IEB0162	-23.0088	139.7799167					x
IEB0163	-23.00873333	139.79975					x
IEB0164	-23.00893333	139.8192833					x
IEB0165	-23.00908333	139.8387667					x
IEB0166	-23.00923333	139.8583333					x
IEB0167R	-23.00936667	139.87775					x
IEB0168	-23.00948333	139.8972833					x
IEB0169	-23.0097	139.9168667					x
IEB0241	-22.95986667	139.3710167					x
IEB0242	-22.96003333	139.3906					x
IEB0243	-22.96025	139.41005					x
IEB0244	-22.96046667	139.4295					x

Station ID	Latitude (GDA 94)	Longitude (GDA 94)	AMT_ 10Hz	AMT_ 1000to 10Hz	Questionable result	Unusable	BBMT
IEB0245	-22.96056667	139.4491					**x**
IEB0246	-22.96076667	139.4685833					**x**
IEB0247	-22.96095	139.4881					**x**
IEB0248	-22.9612	139.5075833					**x**
IEB0249	-22.96135	139.5271					**x**
IEB0250	-22.96153333	139.5466333					**x**
IEB0251	-22.96171667	139.56605					**x**
IEB0252	-22.96193333	139.5855833					**x**
IEB0253	-22.96206667	139.60505					**x**
IEB0254	-22.96228333	139.62455					**x**
IEB0255	-22.96235	139.6440333					**x**
IEB0256	-22.96255	139.6636167					**x**
IEB0257	-22.96265	139.68315					**x**
IEB0258	-22.96286667	139.7026167					**x**
IEB0259	-22.96305	139.7221167					**x**
IEB0260	-22.96316667	139.74155					**x**
IEB0261	-22.96335	139.76115					**x**
IEB0262	-22.96343333	139.7802833					**x**
IEB0263	-22.9635	139.8001					
IEB0264	-22.96385	139.8194667					**x**
IEB0265	-22.96393333	139.8391833					**x**
IEB0266	-22.96405	139.8586					**x**
IEB0267	-22.96391667	139.8780833					**x**
IEB0268	-22.96438333	139.8976					**x**
IEB0269	-22.96445	139.9172333					**x**
IEB0341	-22.9147	139.3716833					**x**
IEB0342	-22.91483333	139.3911					**x**
IEB0343	-22.91503333	139.4105167					**x**
IEB0344	-22.91521667	139.4300833					**x**
IEB0345	-22.91543333	139.4496333					**x**
IEB0346	-22.91563333	139.4690167					**x**
IEB0347	-22.91583333	139.4884833					**x**
IEB0348	-22.91598333	139.50805					**x**
IEB0349	-22.91623333	139.5275833					**x**
IEB0350	-22.91635	139.5469833					**x**
IEB0351	-22.91661667	139.5664833					**x**
IEB0352	-22.9167	139.5864667					**x**
IEB0353	-22.91681667	139.6056333					**x**
IEB0354	-22.91708333	139.6250667					**x**
IEB0355	-22.91716667	139.64475					**x**
IEB0356	-22.91748333	139.664					**x**
IEB0357	-22.91763333	139.6833333					**x**
IEB0358	-22.91761667	139.7030167					**x**
IEB0359R	-22.91788333	139.72255					**x**
IEB0360	-22.91805	139.74205					**x**
IEB0361	-22.9186	139.7615					**x**

Station ID	**Latitude (GDA 94)**	**Longitude (GDA 94)**	**AMT_ 10Hz**	**AMT_ 1000to 10Hz**	**Questionable result**	**Unusable**	**BBMT**
IEB0362	-22.91835	139.7810333					x
IEB0363R	-22.91851667	139.8006				x	
IEB0364R	-22.91865	139.8200333					x
IEB0365	-22.91883333	139.83955					x
IEB0366	-22.91896667	139.8589333					x
IEB0367	-22.91911667	139.8785833					x
IEB0368	-22.9191	139.8980667					x
IEB0439	-22.86916667	139.3331333					x
IEB0440	-22.86935	139.35265					x
IEB0441	-22.86951667	139.3721333					x
IEB0442	-22.86971667	139.3916167					x
IEB0443	-22.8699	139.4110667					x
IEB0444	-22.87008333	139.4305833					x
IEB0445	-22.87025	139.4500667					x
IEB0446	-22.87043333	139.46955					x
IEB0447	-22.87071667	139.48905					x
IEB0448R	-22.87088333	139.50855					x
IEB0449	-22.87103333	139.5280667					x
IEB0450	-22.8712	139.5475167					x
IEB0451	-22.87131667	139.5671167					x
IEB0452	-22.87143333	139.5863833					x
IEB0453	-22.87175	139.60595					x
IEB0454	-22.87181667	139.6255167					x
IEB0455	-22.87196667	139.64495					x
IEB0456	-22.87216667	139.6644833					x
IEB0457	-22.87235	139.68395					x
IEB0458	-22.87256667	139.7033667					x
IEB0459	-22.87271667	139.7229					x
IEB0460	-22.87285	139.7424333					x
IEB0461	-22.87303333	139.7619167					x
IEB0462	-22.87326667	139.7815					x
IEB0463R	-22.87336667	139.8009333					x
IEB0464	-22.8734	139.8204667					x
IEB0465	-22.87361667	139.8399333					x
IEB0466	-22.87378333	139.8594333					x
IEB0467	-22.87393333	139.8789667					x
IEB0537A	-22.82372222	139.2946944					x
IEB0538A	-22.82377778	139.3142778					x
IEB0539A	-22.82397222	139.3337222					x
IEB0540A	-22.82408333	139.353					x
IEB0541A	-22.82444444	139.3726389					x
IEB0542A	-22.82461111	139.3921944					x
IEB0543A	-22.82477778	139.4116944					x
IEB0544A	-22.82497222	139.4311389					x
IEB0545A	-22.82511111	139.4506667					x
IEB0546A	-22.82263889	139.4701389					x

Station ID	Latitude (GDA 94)	Longitude (GDA 94)	AMT_ 10Hz	AMT_ 1000to 10Hz	Questionable result	Unusable	BBMT
IEB0547A	-22.82352778	139.48975					**x**
IEB0548A	-22.82480556	139.5090833					**x**
IEB0549A	-22.82536111	139.5278056					**x**
IEB0550A	-22.82611111	139.5480278					**x**
IEB0551A	-22.82622222	139.5675556					**x**
IEB0552A	-22.82644444	139.587					**x**
IEB0553A	-22.82658333	139.6064722					**x**
IEB0554A	-22.82680556	139.626					**x**
IEB0555B	-22.82630556	139.6461944					**x**
IEB0556A	-22.82713889	139.6649722					**x**
IEB0557A	-22.82722222	139.6845					**x**
IEB0558A	-22.82741667	139.7039167					**x**
IEB0559A	-22.82758333	139.7233333					**x**
IEB0560A	-22.82772222	139.7428333			x		**x**
IEB0561A	-22.82797222	139.7624167					**x**
IEB0562A	-22.82805556	139.7818889				x	
IEB0563A	-22.82822222	139.8013056				x	
IEB0564A	-22.82838889	139.8208611				x	
IEB0565A	-22.8285	139.8403333					**x**
IEB0566A	-22.82861111	139.8589167					**x**
IEB0567A	-22.82722222	139.6845					**x**
IEB0636A	-22.77819444	139.2758611					**x**
IEB0637A	-22.77844444	139.2953333					**x**
IEB0638A	-22.77863889	139.3147778					**x**
IEB0639A	-22.77891667	139.3345556					**x**
IEB0640A	-22.77902778	139.3537222					**x**
IEB0641A	-22.77927778	139.3732222					**x**
IEB0642A	-22.77941667	139.3926944					**x**
IEB0643A	-22.77977778	139.4122778					**x**
IEB0644A	-22.77986111	139.4316389					**x**
IEB0645A	-22.78005556	139.4511667					**x**
IEB0646A	-22.78019444	139.4706389					**x**
IEB0647A	-22.78038889	139.4901111					**x**
IEB0648A	-22.78055556	139.5095278					**x**
IEB0649A	-22.78077778	139.5290556					**x**
IEB0650A	-22.78094444	139.5485278					**x**
IEB0651A	-22.78111111	139.5680556					**x**
IEB0652A	-22.78144444	139.5876944					**x**
IEB0653A	-22.78138889	139.6069444					**x**
IEB0654A	-22.78138889	139.6257222					**x**
IEB0655A	-22.78177778	139.6461944					**x**
IEB0656A	-22.78194444	139.6655556					**x**
IEB0657A	-22.78194444	139.6843056					**x**
IEB0658A	-22.78294444	139.7046944					**x**
IEB0659A	-22.78244444	139.7238333				x	
IEB0660B	-22.78269444	139.7432222				x	

Station ID	Latitude (GDA 94)	Longitude (GDA 94)	AMT_ 10Hz	AMT_ 1000to 10Hz	Questionable result	Unusable	BBMT
IEB0661A	-22.78291667	139.7625833				x	
IEB0662A	-22.78294444	139.7823056				x	
IEB0663A	-22.78144444	139.8028056				x	
IEB0664A	-22.78319444	139.8212222				x	
IEB0665A	-22.78333333	139.8406944			x		**x**
IEB0735A	-22.73288889	139.2570556					**x**
IEB0736A	-22.73288889	139.2762222					**x**
IEB0737A	-22.73327778	139.2958889					**x**
IEB0738A	-22.73336111	139.3150556					**x**
IEB0739A	-22.73427778	139.335					**x**
IEB0740A	-22.73433333	139.3551944					**x**
IEB0741A	-22.73430556	139.3738056					**x**
IEB0742A	-22.73422222	139.3931389					**x**
IEB0743B	-22.73455556	139.4129722					**x**
IEB0744A	-22.73444444	139.4320556					**x**
IEB0745A	-22.73469444	139.4514167					**x**
IEB0746A	-22.73502778	139.4711389					**x**
IEB0747A	-22.73536111	139.4903333					**x**
IEB0748A	-22.73544444	139.5100833					**x**
IEB0749A	-22.73563889	139.5296389					**x**
IEB0750A	-22.73572222	139.5490278					**x**
IEB0751A	-22.73608333	139.5684167					**x**
IEB0752C	-22.73586111	139.5874722					**x**
IEB0753A	-22.73619444	139.6071667					**x**
IEB0754A	-22.73677778	139.6266389					**x**
IEB0755A	-22.73705556	139.6474167					**x**
IEB0756A	-22.73830556	139.6668056					**x**
IEB0757A	-22.73733333	139.6853056					**x**
IEB0758A	-22.73777778	139.7047778			x		**x**
IEB0759A	-22.73594444	139.7243056			x		**x**
IEB0760A	-22.73638889	139.744				x	
IEB0761A	-22.73777778	139.7635556				x	
IEB0762A	-22.73775	139.7826944			x		**x**
IEB0763B	-22.738	139.8025278					**x**
IEB0764A	-22.73805556	139.8216111				x	
IEB0834A	-22.68788889	139.2386944					**x**
IEB0835A	-22.68766667	139.2576111					**x**
IEB0836A	-22.68791667	139.276					**x**
IEB0837A	-22.68777778	139.2965278					**x**
IEB0838A	-22.68830556	139.3160278					**x**
IEB0839A	-22.68844444	139.3354167					**x**
IEB0840A	-22.68877778	139.3548333					**x**
IEB0841A	-22.689	139.3747222					**x**
IEB0842A	-22.68908333	139.3938056					**x**
IEB0843A	-22.68952778	139.4132222					**x**
IEB0844B	-22.68938889	139.4326667					**x**

Station ID	Latitude (GDA 94)	Longitude (GDA 94)	AMT_ 10Hz	AMT_ 1000to 10Hz	Questionable result	Unusable	BBMT
IEB0845A	-22.68961111	139.4523056					**x**
IEB0846A	-22.68986111	139.4715					**x**
IEB0847A	-22.69011111	139.4911111					**x**
IEB0848A	-22.69030556	139.5105278					**x**
IEB0849B	-22.69069444	139.5299722					**x**
IEB0850A	-22.69069444	139.5494444					**x**
IEB0851A	-22.69080556	139.5689444					**x**
IEB0852A	-22.69119444	139.5898611					**x**
IEB0853A	-22.69086111	139.6071667					**x**
IEB0854A	-22.69147222	139.6274722					**x**
IEB0855A	-22.69155556	139.6474444					**x**
IEB0856A	-22.69088889	139.6660556					**x**
IEB0857A	-22.69197222	139.6862222					**x**
IEB0858A	-22.69137833	139.70504					**x**
IEB0859A	-22.691805	139.7247067					**x**
IEB0860A	-22.69307167	139.7436467				x	
IEB0861A	-22.691695	139.7634817				x	
IEB0862A	-22.69255333	139.78329					**x**
IEB0863A	-22.692075	139.8019433					**x**
IEB0933A	-22.64205556	139.2192222					**x**
IEB0934A	-22.64227778	139.2386944					**x**
IEB0935A	-22.64255556	139.2581111					**x**
IEB0936A	-22.64252778	139.2778611					**x**
IEB0937A	-22.643	139.2963056					**x**
IEB0938A	-22.64266667	139.3165556					**x**
IEB0939A	-22.64427778	139.3350278					**x**
IEB0940A	-22.64361111	139.3553611					**x**
IEB0941A	-22.64386111	139.3747778					**x**
IEB0942A	-22.64397222	139.3942778					**x**
IEB0943A	-22.64419444	139.4137222					**x**
IEB0944A	-22.64438889	139.4331667					**x**
IEB0945A	-22.64402778	139.4525833					**x**
IEB0946A	-22.64475	139.4721111					**x**
IEB0947A	-22.64494444	139.4915833					**x**
IEB0948A	-22.64552778	139.5113333					**x**
IEB0949A	-22.64508333	139.5309167					**x**
IEB0950A	-22.64536111	139.5500556					**x**
IEB0951A	-22.64588889	139.5697222					**x**
IEB0952A	-22.64563889	139.58925					**x**
IEB0953B	-22.64619444	139.6085556					**x**
IEB0954A	-22.64627778	139.6279722					**x**
IEB0955A	-22.64494167	139.6484333				x	
IEB0956A	-22.64595	139.6668083					**x**
IEB0957A	-22.646345	139.68614					**x**
IEB0958A	-22.64668667	139.7056983					**x**
IEB0959A	-22.64698167	139.72656				x	

Station ID	Latitude (GDA 94)	Longitude (GDA 94)	AMT_ 10Hz	AMT_ 1000to 10Hz	Questionable result	Unusable	BBMT
IEB0960A	-22.64711111	139.7445278				x	
IEB0961A	-22.64677167	139.7638867					**x**
IEB0962A	-22.64718333	139.7835917					**x**
IEB1003A	-22.58880558	138.63675					**x**
IEB1004A	-22.58955558	138.6556944					**x**
IEB1005B	-22.59005558	138.6752222					**x**
IEB1006A	-22.59041669	138.6950556					**x**
IEB1007B	-22.59055558	138.7141389					**x**
IEB1008B	-22.59075003	138.7335556					**x**
IEB1009A	-22.59102781	138.7531389					**x**
IEB1010A	-22.59008336	138.7722222					**x**
IEB1011A	-22.59119447	138.7914444					**x**
IEB1012A	-22.59191667	138.8113611					**x**
IEB1013A	-22.59205556	138.8307778					**x**
IEB1014A	-22.59244444	138.8502222					**x**
IEB1015A	-22.59272222	138.8696944					**x**
IEB1016A	-22.59347222	138.8891944					**x**
IEB1017B	-22.59311111	138.9088056					**x**
IEB1018A	-22.59369444	138.9279722					**x**
IEB1019A	-22.59363889	138.9474722					**x**
IEB1020A	-22.59419444	138.967					**x**
IEB1021A	-22.59416667	138.9863889					**x**
IEB1022A	-22.59480556	139.0056667					**x**
IEB1023A	-22.59469444	139.0254167					**x**
IEB1024A	-22.59497222	139.0448889					**x**
IEB1025A	-22.59527778	139.0638889					**x**
IEB1026A	-22.59547222	139.0837222					**x**
IEB1027A	-22.59547222	139.1032778					**x**
IEB1028A	-22.59619444	139.1224722					**x**
IEB1029A	-22.59605556	139.1426111					**x**
IEB1030A	-22.59644444	139.1616944					**x**
IEB1031A	-22.59469444	139.1802778					**x**
IEB1032A	-22.59688889	139.2005					**x**
IEB1033A	-22.59691667	139.2198889					**x**
IEB1034A	-22.59877778	139.2391667					**x**
IEB1035A	-22.59730556	139.2583889					**x**
IEB1036A	-22.59755556	139.2778889					**x**
IEB1037A	-22.59783333	139.2974167					**x**
IEB1038A	-22.59819444	139.3170556					**x**
IEB1039A	-22.59838889	139.3367778					**x**
IEB1040A	-22.59755556	139.3560833					**x**
IEB1041A	-22.59847222	139.3752778					**x**
IEB1042A	-22.599	139.3952778					**x**
IEB1043A	-22.59902778	139.4143056					**x**
IEB1044A	-22.59908333	139.4335833					**x**
IEB1045A	-22.59930556	139.4534722					**x**

Station ID	Latitude (GDA 94)	Longitude (GDA 94)	AMT_ 10Hz	AMT_ 1000to 10Hz	Questionable result	Unusable	BBMT
IEB1046A	-22.59952778	139.4726111					**x**
IEB1047A	-22.59944444	139.4923889					**x**
IEB1048A	-22.59994444	139.5116944					**x**
IEB1049A	-22.60030556	139.5309722					**x**
IEB1050A	-22.59988889	139.5504167					**x**
IEB1051A	-22.60022222	139.5698056					**x**
IEB1052A	-22.60072222	139.5890833					**x**
IEB1053A	-22.60130556	139.6079722					**x**
IEB1054A	-22.60019444	139.6289722					**x**
IEB1055A	-22.59983333	139.6476389					**x**
IEB1056A	-22.60136111	139.6671389					**x**
IEB1057A	-22.6015	139.6865833					**x**
IEB1058A	-22.60097222	139.7060278					**x**
IEB1059A	-22.60186111	139.7255278					**x**
IEB1060A	-22.60094444	139.7448333			x		**x**
IEB1061A	-22.60280556	139.76475			x		**x**
IEB1102A	-22.54402781	138.6179167					**x**
IEB1103A	-22.54308336	138.6383333					**x**
IEB1104A	-22.54480558	138.6563611					**x**
IEB1105A	-22.54494447	138.6760278					**x**
IEB1106A	-22.54511114	138.6956389					**x**
IEB1107A	-22.54538892	138.7148333					**x**
IEB1108A	-22.54586114	138.7342778					**x**
IEB1109A	-22.54658336	138.7541944					**x**
IEB1110A	-22.54622225	138.77325					**x**
IEB1111A	-22.54644447	138.7926667					**x**
IEB1112A	-22.54677778	138.8120278					**x**
IEB1113A	-22.54694444	138.8315278					**x**
IEB1114A	-22.54669444	138.8510278					**x**
IEB1115A	-22.54677778	138.8704444					**x**
IEB1116A	-22.54744444	138.8899722					**x**
IEB1117A	-22.54830556	138.9091111					**x**
IEB1118A	-22.54813889	138.9288611					**x**
IEB1119A	-22.5485	138.9481944					**x**
IEB1120A	-22.54911111	138.9673056					**x**
IEB1121A	-22.549	138.9866944					**x**
IEB1122A	-22.54955556	139.00625					**x**
IEB1123A	-22.55138889	139.0256944					**x**
IEB1124A	-22.54955556	139.0454444					**x**
IEB1125A	-22.54988889	139.0648889					**x**
IEB1126A	-22.55075	139.0843889					**x**
IEB1127A	-22.55161111	139.1038889					**x**
IEB1128A	-22.55088889	139.12325					**x**
IEB1129A	-22.55113889	139.1421944					**x**
IEB1130A	-22.55069444	139.1619722					**x**
IEB1131A	-22.55172222	139.1816111					**x**

Station ID	**Latitude (GDA 94)**	**Longitude (GDA 94)**	**AMT_ 10Hz**	**AMT_ 1000to 10Hz**	**Questionable result**	**Unusable**	**BBMT**
IEB1132A	-22.55161111	139.2005278					**x**
IEB1133A	-22.55094444	139.2201944					**x**
IEB1134A	-22.55277778	139.2400556					**x**
IEB1135A	-22.55230556	139.2592222					**x**
IEB1136A	-22.55238889	139.2785					**x**
IEB1137A	-22.55272222	139.2979444					**x**
IEB1138A	-22.55213889	139.3178889					**x**
IEB1139A	-22.55355556	139.337					**x**
IEB1140a	-22.55333333	139.3564722					**x**
IEB1141A	-22.55297222	139.3758333					**x**
IEB1142A	-22.55372222	139.3953889					**x**
IEB1143A	-22.55388889	139.4148056					**x**
IEB1144A	-22.55411111	139.4341944					**x**
IEB1145A	-22.55427778	139.4536667					**x**
IEB1146b	-22.55436111	139.4733056					**x**
IEB1147A	-22.55480556	139.4925278					**x**
IEB1148A	-22.55486111	139.5118611					**x**
IEB1149A	-22.55530556	139.5314722					**x**
IEB1150A	-22.555	139.5505278					**x**
IEB1151A	-22.55502778	139.5699444			x		**x**
IEB1152A	-22.55577778	139.5894722					**x**
IEB1153A	-22.55611111	139.6093889					**x**
IEB1154A	-22.55513889	139.6280278					**x**
IEB1155A	-22.55602778	139.6481667					**x**
IEB1156A	-22.55719444	139.6676389					**x**
IEB1157A	-22.55511111	139.68725					**x**
IEB1158A	-22.55658333	139.7061944					**x**
IEB1159A	-22.55647222	139.7258611				x	
IEB1160A	-22.55775	139.7458611				x	
IEB1201A	-22.49830558	138.6011111					**x**
IEB1202A	-22.49894447	138.6193889					**x**
IEB1203A	-22.49947225	138.6386944					**x**
IEB1204A	-22.49955558	138.6574722					**x**
IEB1204B	-22.49955558	138.6574722					**x**
IEB1205A	-22.50033336	138.6769444					**x**
IEB1206A	-22.50280558	138.6956944					**x**
IEB1207A	-22.50205558	138.7155278					**x**
IEB1208A	-22.50036114	138.7353056					**x**
IEB1209A	-22.50144447	138.7544722					**x**
IEB1210A	-22.50111114	138.7735556					**x**
IEB1211A	-22.50122225	138.7932222					**x**
IEB1212A	-22.50161111	138.8128333					**x**
IEB1213A	-22.50211111	138.8322222					**x**
IEB1214A	-22.50202778	138.8518611					**x**
IEB1215A	-22.50286111	138.8723056					**x**
IEB1216A	-22.50269444	138.8905278					**x**

Station ID	Latitude (GDA 94)	Longitude (GDA 94)	AMT_ 10Hz	AMT_ 1000to 10Hz	Questionable result	Unusable	BBMT
IEB1217A	-22.50305556	138.9095278					x
IEB1218A	-22.50313889	138.9294722					x
IEB1219A	-22.50344444	138.9488333					x
IEB1220A	-22.50355556	138.9683611					x
IEB1221A	-22.50397222	138.9877222					x
IEB1222A	-22.50433333	139.0071944					x
IEB1223A	-22.50438889	139.02675					x
IEB1224A	-22.50461111	139.0462222					x
IEB1225A	-22.50488889	139.0653611					x
IEB1226A	-22.50505556	139.0848611					x
IEB1227A	-22.50461111	139.1043889					x
IEB1228A	-22.506	139.1236389					x
IEB1229A	-22.50497222	139.14475					x
IEB1230A	-22.50502778	139.1624444					x
IEB1231A	-22.50536111	139.1832222					x
IEB1232A	-22.50627778	139.2013889					x
IEB1233A	-22.50666667	139.2208889					x
IEB1234A	-22.50627778	139.2403611					x
IEB1235A	-22.50561111	139.2599444					x
IEB1236A	-22.50766667	139.2793056					x
IEB1237A	-22.50730556	139.2988333					x
IEB1238A	-22.50697222	139.3175278					x
IEB1239A	-22.50788889	139.3371389					x
IEB1240A	-22.50772222	139.3571111					x
IEB1241A	-22.50830556	139.3763889					x
IEB1242A	-22.50811111	139.3954722					x
IEB1243A	-22.50975	139.4157778					x
IEB1244B	-22.50883333	139.4350278					x
IEB1245A	-22.50930556	139.4543889					x
IEB1246A	-22.50911111	139.4740278					x
IEB1247A	-22.50972222	139.4934167					x
IEB1248A	-22.51	139.5116111					x
IEB1249A	-22.50969444	139.5319167					x
IEB1250A	-22.50883333	139.5513611					x
IEB1251A	-22.51005556	139.5706944					x
IEB1252A	-22.51030556	139.5903889					x
IEB1253A	-22.51044444	139.6094722					x
IEB1254B	-22.51072222	139.6291944					x
IEB1255B	-22.51080556	139.6489444					x
IEB1256A	-22.51080556	139.6682778					x
IEB1257A	-22.51113889	139.6871111					x
IEB1258A	-22.51130556	139.7068889					x
IEB1259A	-22.51088889	139.7265833					x
IEB1300A	-22.45305558	138.5804167					x
IEB1301A	-22.45355558	138.5997222					x
IEB1302A	-22.45369447	138.6205					x

Station ID	Latitude (GDA 94)	Longitude (GDA 94)	AMT_ 10Hz	AMT_ 1000to 10Hz	Questionable result	Unusable	BBMT
IEB1303A	-22.45405558	138.6398889					**x**
IEB1304A	-22.45438892	138.6581111					**x**
IEB1305A	-22.45450003	138.6777778			x		**x**
IEB1306A	-22.45469447	138.6969722					**x**
IEB1307A	-22.45608336	138.7167778					**x**
IEB1308A	-22.45394447	138.7358056					**x**
IEB1309A	-22.45566669	138.7552778					**x**
IEB1310A	-22.45605558	138.7747778					**x**
IEB1311A	-22.45513892	138.7939167					**x**
IEB1312A	-22.45647222	138.8135833					**x**
IEB1313A	-22.45652778	138.8328611				x	
IEB1314A	-22.45697222	138.8523611					**x**
IEB1315A	-22.45736111	138.8714444					**x**
IEB1316A	-22.45783333	138.8914444				x	
IEB1317A	-22.45808333	138.91075					**x**
IEB1318A	-22.45775	138.9300556					**x**
IEB1319A	-22.45822222	138.9495556					**x**
IEB1320A	-22.45844444	138.9693611					**x**
IEB1321A	-22.45852778	138.9878611					**x**
IEB1322A	-22.459	139.0070556					**x**
IEB1323A	-22.45994444	139.0276111					**x**
IEB1324A	-22.45944444	139.0466944					**x**
IEB1325A	-22.45977778	139.0661389					**x**
IEB1326A	-22.46005556	139.0853889					**x**
IEB1327A	-22.46122222	139.1045					**x**
IEB1328A	-22.45963889	139.1243056					**x**
IEB1329A	-22.46077778	139.1437778					**x**
IEB1330A	-22.46102778	139.1629444					**x**
IEB1331A	-22.46130556	139.1824444					**x**
IEB1332A	-22.46111111	139.2020278					**x**
IEB1333B	-22.46136111	139.2212778					**x**
IEB1334A	-22.46122222	139.2396944					**x**
IEB1335A	-22.46280556	139.2603333					**x**
IEB1336A	-22.46175	139.2796667					**x**
IEB1337A	-22.46205556	139.29925					**x**
IEB1338A	-22.46305556	139.3189167					**x**
IEB1339A	-22.46269444	139.3381111					**x**
IEB1339B	-22.46280556	139.3381111					**x**
IEB1340A	-22.46380556	139.3574444					**x**
IEB1341A	-22.46316667	139.3769167					**x**
IEB1342A	-22.46330556	139.3967778					**x**
IEB1343A	-22.46336111	139.4162222					**x**
IEB1344A	-22.46436111	139.4345278					**x**
IEB1345A	-22.46430556	139.4545833					**x**
IEB1346A	-22.46405556	139.4737222					**x**
IEB1347A	-22.46525	139.4925278					**x**

Station ID	**Latitude (GDA 94)**	**Longitude (GDA 94)**	**AMT_ 10Hz**	**AMT_ 1000to 10Hz**	**Questionable result**	**Unusable**	**BBMT**
IEB1348A	-22.46466667	139.5127222					**x**
IEB1349A	-22.46513889	139.5324167					**x**
IEB1350A	-22.46877778	139.5521944					**x**
IEB1351A	-22.46361111	139.5705278					**x**
IEB1352A	-22.46513889	139.5904444					**x**
IEB1353A	-22.46602778	139.6113611					**x**
IEB1354A	-22.46552778	139.6295556					**x**
IEB1355A	-22.46572222	139.6489722					**x**
IEB1356A	-22.46538889	139.6681389					**x**
IEB1357A	-22.46608333	139.6877778					**x**
IEB1358A	-22.46636111	139.708					**x**
IEB1400A	-22.40875003	138.5810278					**x**
IEB1401A	-22.40872225	138.6000556					**x**
IEB1402A	-22.40858336	138.6198889					**x**
IEB1403A	-22.40944447	138.6400556					**x**
IEB1404A	-22.40788892	138.6597222					**x**
IEB1405A	-22.40922225	138.6780833					**x**
IEB1406A	-22.40919447	138.6980278					**x**
IEB1407A	-22.41022225	138.7171944					**x**
IEB1408B	-22.41027781	138.7367778					**x**
IEB1409A	-22.41050003	138.7558611					**x**
IEB1410A	-22.41086114	138.7753889					**x**
IEB1411A	-22.41102778	138.795					**x**
IEB1412A	-22.41138889	138.8141389					**x**
IEB1413C	-22.41169444	138.8343056					**x**
IEB1414A	-22.41191667	138.8530556			x		**x**
IEB1415A	-22.41177778	138.8724444				x	
IEB1416A	-22.41227778	138.8918056					**x**
IEB1417A	-22.41263889	138.9112222					**x**
IEB1418A	-22.41294444	138.9307778					**x**
IEB1419A	-22.41416667	138.9498611					**x**
IEB1420A	-22.41336111	138.9696111					**x**
IEB1421A	-22.41355556	138.98875					**x**
IEB1422A	-22.41405556	139.0082778					**x**
IEB1423A	-22.41411111	139.0277222					**x**
IEB1424A	-22.41419444	139.0471667					**x**
IEB1425A	-22.41444444	139.0664444					**x**
IEB1426A	-22.41480556	139.0861944					**x**
IEB1427A	-22.41494444	139.1055833					**x**
IEB1428A	-22.41538889	139.1250278					**x**
IEB1429A	-22.41552778	139.1445					**x**
IEB1430A	-22.41522222	139.1631944					**x**
IEB1431A	-22.41566667	139.1831667					**x**
IEB1432A	-22.41722222	139.2019444					**x**
IEB1433A	-22.41622222	139.2221944					**x**
IEB1434A	-22.417	139.2413056					**x**

Station ID	Latitude (GDA 94)	Longitude (GDA 94)	AMT_ 10Hz	AMT_ 1000to 10Hz	Questionable result	Unusable	BBMT
IEB1435A	-22.41655556	139.2606389					**x**
IEB1436B	-22.41536111	139.2794167					**x**
IEB1437A	-22.41719444	139.2998889					**x**
IEB1438A	-22.41780556	139.3195833					**x**
IEB1439A	-22.41783333	139.3385278					**x**
IEB1440A	-22.41755556	139.3579722					**x**
IEB1441B	-22.41819444	139.3775833					**x**
IEB1442A	-22.41841667	139.3973333					**x**
IEB1443A	-22.41763889	139.4157778					**x**
IEB1444A	-22.42013889	139.4357778					**x**
IEB1445A	-22.41791667	139.4558056					**x**
IEB1446A	-22.41894444	139.4748056					**x**
IEB1447A	-22.41844444	139.4937778					**x**
IEB1448A	-22.41788889	139.5129444					**x**
IEB1449A	-22.41905556	139.5327778					**x**
IEB1450A	-22.41841667	139.5526111					**x**
IEB1451A	-22.41933333	139.5720556					**x**
IEB1452A	-22.42027778	139.5903611					**x**
IEB1453A	-22.42027778	139.6106944					**x**
IEB1454A	-22.421	139.6296111					**x**
IEB1455A	-22.42041667	139.6492222					**x**
IEB1456A	-22.42052778	139.6689722					**x**
IEB1457A	-22.42172222	139.6882778					**x**
IEB1500A	-22.36316669	138.5818056			x		**x**
IEB1501A	-22.36341669	138.5986111					**x**
IEB1502A	-22.36275003	138.6166944					**x**
IEB1503A	-22.36355558	138.6401389					**x**
IEB1504A	-22.36377781	138.6591111				x	
IEB1505A	-22.36436114	138.679					**x**
IEB1506A	-22.36497225	138.6988333					**x**
IEB1507A	-22.36619447	138.7178056					**x**
IEB1508A	-22.36605558	138.7370833				x	
IEB1509A	-22.36536114	138.7566389			x		**x**
IEB1510A	-22.36566669	138.7762222			x		**x**
IEB1511A	-22.36252778	138.7975833					**x**
IEB1512A	-22.36611111	138.8146111			x		**x**
IEB1513A	-22.36647222	138.8343889					**x**
IEB1514A	-22.36630556	138.8539722			x		**x**
IEB1515A	-22.36719444	138.8730833					**x**
IEB1516A	-22.36694444	138.8931944					**x**
IEB1517A	-22.36758333	138.9119722					**x**
IEB1518A	-22.36772222	138.9313056					**x**
IEB1519A	-22.36805556	138.9508333					**x**
IEB1520A	-22.36866667	138.9703611					**x**
IEB1521A	-22.36827778	138.9900278					**x**
IEB1522A	-22.36863889	139.0091389					**x**

Station ID	Latitude (GDA 94)	Longitude (GDA 94)	AMT_ 10Hz	AMT_ 1000to 10Hz	Questionable result	Unusable	BBMT
IEB1523A	-22.36877778	139.0286111					**x**
IEB1524A	-22.36719444	139.0483611			x		**x**
IEB1525A	-22.36930556	139.0669722					**x**
IEB1526A	-22.36944444	139.0867222					**x**
IEB1527A	-22.36986111	139.1061944					**x**
IEB1528A	-22.37011111	139.1253889					**x**
IEB1529A	-22.37055556	139.1450833					**x**
IEB1530A	-22.37069444	139.1644722					**x**
IEB1531b	-22.37066667	139.1836667					**x**
IEB1532A	-22.37086111	139.2033333					**x**
IEB1533A	-22.37141667	139.2226389					**x**
IEB1534A	-22.37152778	139.2620556					**x**
IEB1535A	-22.37125	139.2415556					**x**
IEB1536A	-22.37227778	139.2806111			x		**x**
IEB1537A	-22.37211111	139.3009722					**x**
IEB1538A	-22.37230556	139.3197778					**x**
IEB1539A	-22.37230556	139.3389722					**x**
IEB1540A	-22.37236111	139.3583611					**x**
IEB1541A	-22.37269444	139.3780556					**x**
IEB1542A	-22.37269444	139.3972778					**x**
IEB1543A	-22.37344444	139.4164722					**x**
IEB1544A	-22.37355556	139.4363333					**x**
IEB1545A	-22.37144444	139.4553056					**x**
IEB1546A	-22.37447222	139.4749444					**x**
IEB1547A	-22.37572222	139.4944722					**x**
IEB1548A	-22.37441667	139.5142222			x		**x**
IEB1549A	-22.37475	139.5331111					**x**
IEB1550A	-22.37444444	139.5527778					**x**
IEB1551A	-22.37541667	139.5726389					**x**
IEB1552a	-22.37602778	139.5920278					**x**
IEB1553A	-22.37488889	139.6109722					**x**
IEB1554A	-22.37511111	139.6313611					**x**
IEB1555A	-22.37555556	139.6496667					**x**
IEB1556A	-22.37516667	139.6693333					**x**
IEB1557A	-22.37563889	139.6876111					**x**
IEB1600A	-22.31805558	138.5818889					**x**
IEB1601A	-22.31863892	138.6023333					**x**
IEB1602A	-22.31963892	138.6214444					**x**
IEB1603A	-22.31866669	138.6409722					**x**
IEB1604A	-22.31894447	138.6603889					**x**
IEB1605A	-22.31922225	138.6797778					**x**
IEB1606A	-22.31950003	138.6991944					**x**
IEB1607B	-22.31977781	138.7186111					**x**
IEB1608A	-22.31988892	138.7378889					**x**
IEB1610A	-22.32069447	138.7772778					**x**
IEB1611A	-22.32122222	138.7965556			x		**x**

Station ID	Latitude (GDA 94)	Longitude (GDA 94)	AMT_ 10Hz	AMT_ 1000to 10Hz	Questionable result	Unusable	BBMT
IEB1612A	-22.32111111	138.8154167					**x**
IEB1613A	-22.32194444	138.8349444					**x**
IEB1614A	-22.32163889	138.8544167				x	
IEB1615A	-22.32188889	138.8738056					**x**
IEB1616B	-22.32219444	138.8932222			x		**x**
IEB1617A	-22.32241667	138.9126389					**x**
IEB1618A	-22.32263889	138.9320556			x		**x**
IEB1619A	-22.32283333	138.9513889				x	
IEB1620A	-22.32319444	138.9708056					**x**
IEB1621A	-22.32336111	138.9906667			x		**x**
IEB1622A	-22.32355556	139.00975			x		**x**
IEB1623A	-22.32436111	139.0289444					**x**
IEB1624A	-22.32438889	139.0487222					**x**
IEB1625A	-22.32508333	139.0678611					**x**
IEB1626A	-22.32491667	139.0872222					**x**
IEB1627A	-22.32472222	139.1068056					**x**
IEB1628A	-22.32544444	139.1260833					**x**
IEB1629A	-22.32552778	139.1455833					**x**
IEB1630A	-22.32572222	139.1653056					**x**
IEB1631A	-22.32566667	139.1844444					**x**
IEB1632A	-22.32536111	139.2031111					**x**
IEB1633A	-22.32611111	139.2234722					**x**
IEB1634A	-22.32644444	139.2418056					**x**
IEB1635A	-22.32311111	139.2620278					**x**
IEB1636A	-22.32661111	139.2817222					**x**
IEB1637A	-22.32711111	139.3009444					**x**
IEB1638A	-22.325	139.3206944					**x**
IEB1639A	-22.32741667	139.3404444					**x**
IEB1640A	-22.32647222	139.3584444					**x**
IEB1641A	-22.32802778	139.3783889					**x**
IEB1642A	-22.32833333	139.3978056					**x**
IEB1643A	-22.32827778	139.4173056					**x**
IEB1644A	-22.32813889	139.4366389					**x**
IEB1645A	-22.32855556	139.4558611					**x**
IEB1646A	-22.32802778	139.4755556					**x**
IEB1647A	-22.33022222	139.4948889					**x**
IEB1648A	-22.33038889	139.5168889					**x**
IEB1649A	-22.32947222	139.5350556					**x**
IEB1650A	-22.32919444	139.5530833					**x**
IEB1651A	-22.32897222	139.5728056					**x**
IEB1652A	-22.32961111	139.5915556					**x**
IEB1653A	-22.33122222	139.6111389					**x**
IEB1654A	-22.33030556	139.6308333					**x**
IEB1655A	-22.32811111	139.6511111					**x**
IEB1656A	-22.32966667	139.6704444					**x**
IEB1702A	-22.27325003	138.6223333					**x**

Station ID	**Latitude (GDA 94)**	**Longitude (GDA 94)**	**AMT_ 10Hz**	**AMT_ 1000to 10Hz**	**Questionable result**	**Unusable**	**BBMT**
IEB1703A	-22.27352781	138.6417222					**x**
IEB1704A	-22.27380558	138.6611389					**x**
IEB1705A	-22.27411114	138.6805278					**x**
IEB1706A	-22.27438892	138.6999444					**x**
IEB1707A	-22.27483336	138.7193611					**x**
IEB1708A	-22.27480558	138.7387222					**x**
IEB1709A	-22.27444447	138.7575833					**x**
IEB1710A	-22.27538892	138.7776944					**x**
IEB1711A	-22.27569444	138.7966944					**x**
IEB1712A	-22.27602778	138.8163056			x		**x**
IEB1713A	-22.27622222	138.8357222				x	
IEB1714A	-22.27647222	138.8551389			x		**x**
IEB1715A	-22.27672222	138.8745278					**x**
IEB1716A	-22.277	138.8939722					**x**
IEB1717A	-22.27722222	138.9131111					**x**
IEB1718A	-22.27741667	138.9328056			x		**x**
IEB1719A	-22.27772222	138.9525556			x		**x**
IEB1720A	-22.27727778	138.9714722			x		**x**
IEB1721A	-22.27833333	138.9908333			x		**x**
IEB1722A	-22.27863889	139.0103611					**x**
IEB1723A	-22.27944444	139.0301111					**x**
IEB1724A	-22.27872222	139.0490833			x		**x**
IEB1725A	-22.279	139.0684167					**x**
IEB1726A	-22.27933333	139.0879444					**x**
IEB1727A	-22.27963889	139.1074444					**x**
IEB1728A	-22.27969444	139.12675					**x**
IEB1729A	-22.27955556	139.1462222					**x**
IEB1730A	-22.28044444	139.1655278					**x**
IEB1731C	-22.27913889	139.1852222					**x**
IEB1732A	-22.28027778	139.2043611			x		**x**
IEB1733a	-22.28088889	139.2236111					**x**
IEB1734a	-22.28091667	139.2436389					**x**
IEB1735A	-22.28038889	139.2619167					**x**
IEB1736A	-22.28558333	139.2831389					**x**
IEB1737A	-22.28186111	139.3010556					**x**
IEB1738A	-22.28130556	139.3208333					**x**
IEB1739A	-22.28213889	139.3401389					**x**
IEB1740A	-22.28275	139.3594167					**x**
IEB1741A	-22.28236111	139.3788889					**x**
IEB1742A	-22.28269444	139.3986389			x		**x**
IEB1743A	-22.28316667	139.4178611			x		**x**
IEB1744a	-22.28336111	139.4375278					**x**
IEB1745A	-22.28388889	139.4566111					**x**
IEB1746A	-22.28344444	139.4759444					**x**
IEB1747a	-22.28383333	139.4953889					**x**
IEB1748A	-22.28377778	139.5149722					**x**

Station ID	Latitude (GDA 94)	Longitude (GDA 94)	AMT_ 10Hz	AMT_ 1000to 10Hz	Questionable result	Unusable	BBMT
IEB1749A	-22.28441667	139.5332778			x		**x**
IEB1750a	-22.28438889	139.5540278					**x**
IEB1751A	-22.28419444	139.5726944					**x**
IEB1752A	-22.28505556	139.5919722					**x**
IEB1753a	-22.28527778	139.6118611					**x**
IEB1754A	-22.28569444	139.6313056					**x**
IEB1755A	-22.28516667	139.6506667					**x**
IEB1801A	-22.22786114	138.6037778					**x**
IEB1803B	-22.22838892	138.6425					**x**
IEB1804A	-22.22919447	138.66225				x	
IEB1805A	-22.22869447	138.6812222					**x**
IEB1806A	-22.22819447	138.7006944					**x**
IEB1807A	-22.22902781	138.7204722					**x**
IEB1808A	-22.23111114	138.7398889					**x**
IEB1809A	-22.23330558	138.7603889					**x**
IEB1810A	-22.22952781	138.7778889				x	
IEB1811A	-22.23088889	138.7983333					**x**
IEB1812A	-22.23072222	138.8171389					**x**
IEB1813A	-22.23102778	138.8364167					**x**
IEB1814A	-22.23133333	138.85575					**x**
IEB1815A	-22.23166667	138.8752778					**x**
IEB1816A	-22.23111111	138.8926944					**x**
IEB1817A	-22.23138889	138.9131389					**x**
IEB1818A	-22.23336111	138.9331944			x		**x**
IEB1819A	-22.23330556	138.9533333			x		**x**
IEB1820A	-22.23308333	138.9719722					**x**
IEB1821A	-22.23302778	138.9915833			x		**x**
IEB1822A	-22.23330556	139.0107778					**x**
IEB1823A	-22.23255556	139.0303889			x		**x**
IEB1824A	-22.23402778	139.0497222				x	
IEB1825A	-22.23427778	139.0692778					**x**
IEB1826A	-22.23411111	139.0888056					**x**
IEB1827B	-22.23419444	139.1080833					**x**
IEB1828A	-22.23452778	139.1273889					**x**
IEB1829A	-22.23536111	139.1468056					**x**
IEB1830A	-22.23505556	139.1661944					**x**
IEB1831A	-22.23516667	139.1854444			x		**x**
IEB1832A	-22.23555556	139.2048889			x		**x**
IEB1833A	-22.23461111	139.2245556				x	
IEB1834A	-22.23638889	139.2436944			x		**x**
IEB1835A	-22.23388889	139.2631944					**x**
IEB1836A	-22.23461111	139.2825556					**x**
IEB1837A	-22.23366667	139.30175					**x**
IEB1838A	-22.23711111	139.3212222					**x**
IEB1839A	-22.23697222	139.3407778					**x**
IEB1840A	-22.23675	139.3597778					**x**

Station ID	Latitude (GDA 94)	Longitude (GDA 94)	AMT_ 10Hz	AMT_ 1000to 10Hz	Questionable result	Unusable	BBMT
IEB1841A	-22.23780556	139.3796111					**x**
IEB1842A	-22.23763889	139.3990278					**x**
IEB1843A	-22.23769444	139.4183333					**x**
IEB1844a	-22.23788889	139.4373333					**x**
IEB1845A	-22.23725	139.4571944					**x**
IEB1846A	-22.23755556	139.4766389					**x**
IEB1847a	-22.23961111	139.4954444					**x**
IEB1848A	-22.23661111	139.5159722					**x**
IEB1849A	-22.23963889	139.5344444				x	
IEB1850b	-22.23913889	139.5541389					**x**
IEB1851A	-22.23938889	139.5734722					**x**
IEB1852A	-22.24097222	139.5931944					**x**
IEB1853A	-22.23808333	139.6118611					**x**
IEB1854A	-22.23972222	139.6306944					**x**
IEB1855A	-22.23977778	139.6515833					**x**

D.1.2 1D rj-McMC inversion results

See digital submission for Inversion summary figures for all rj-McMT inversions run. Files are grouped by input site type and frequency band: BBMT (10^1 Hz to 3 x 10^2 Hz), reduced frequency AMT (10^1 Hz to 10^3 Hz) or full frequency AMT (10^1 Hz to 10^4 Hz).